ISSN 0915-6348

NATIONAL INSTITUTE FOR FUSION SCIENCE

# Proceedings of the Japan-US Workshop on Plasma Polarization Spectroscopy and The International Seminar on Plasma Polarization Spectroscopy January 26-28, 1998, Kyoto

( Eds.)T. Fujimoto, P. Beiersdorfer

(Received - May 15, 1998 )

NIFS-PROC-37 June 1998



**RESEARCH REPORT**
**NIFS-PROC Series**

NAGOYA, JAPAN

Proceedings
of
The Japan-US Workshop on Plasma Polarization Spectroscopy
and
The International Seminar on Plasma Polarization Spectroscopy

January 26-28, 1998, Kyoto

edited by
Takashi Fujimoto
Peter Beiersdorfer

Abstract

The international meeting on Plasma Polarization Spectroscopy (PPS) was held in Kyoto during January 26-28, 1998. This Proceedings book includes the papers of the talks given at the meeting. These include: overviews of PPS from the aspects of atomic physics, and of plasma physics; several PPS and MSE (motional Stark effect) experiments on magnetically confined plasmas and a laser-produced plasma; polarized laser-induced fluorescence spectroscopy, several experiments on EBITs (electron beam ion trap) and their theoretical interpretations; polarized profiles of spectral lines, basic formulation of PPS; inelastic and elastic electron collisions leading to polarized atomic states; polarization in recombining plasma; relationship between the collisional polarization relaxation and the line broadening; and characteristics of the plasma produced by very short pulse and high power laser irradiation.

Key words;
PPS (Plasma Polarization Spectroscopy), tokamak, CHS, laser-induced fluorescence spectroscopy, electron collisions, excitation, alignment,disalignment, x-ray, vacuum spark, spectral line profile, EBIT

## Preface

The Japan-US Workshop on Plasma Polarization Spectroscopy and The International Seminar on Plasma Polarization Spectroscopy was held during January 26 - 28, 1998, in Kyoto. This was the second meeting of its kind following the first US-Japan Workshop at Los Alamos four years earlier. It was attended by 6 US and 17 Japanese participants and 9 participants from Russia, France and Germany. During the two and a half day workshop, various facets of Plasma Polarization Spectroscopy (PPS) were reviewed, new results were presented, new ideas were exchanged and intensive discussions were made. As organizers we feel that the Workshop and Seminar marks a milestone in the progress in Plasma Polarization Spectroscopy and demonstrates the vitality of this new research field.

The various polarization phenomena are divided into three classes: Class 1 contains the effects of electric and/or magnetic fields. The atomic excitation is isotropic. The present status of the MSE (motional Stark effect) diagnostics of magnetically confined plasmas were reviewed and a new experimental result was presented. Fields may be static or dynamic, or we may even have coherent superposition of dynamic fields due to, *e.g.*, plasma turbulence, to a static field. A variety of polarization dependent emission line profiles emerge owing to these fields.

Class 2 phenomena involve spatially anisotropic excitation by plasma particles. Polarization measurements of emission lines and continuum were conducted on gas discharge plasmas, tokamak plasmas, laser produced plasmas, Z-pinch and a vacuum spark plasmas. The anisotropy of the electron velocity distribution function (EDF) was discussed. Atomic physics is particularly important in this class; progress in theoretical calculations of excitation cross section relevant to PPS was reviewed and new results presented, including treatments of radiative cascades, dielectronic recombination, or charge transfer reactions. EBIT is a powerful tool in anisotropic collision spectroscopy, and recent experimental results and theoretical interpretation were presented. Moreover, the first experimental evidence was reported which clearly indicates that alignment can be created by elastic electron impact; this process applied to the ground state atoms may be called collisional pumping.

Class 3 phenomena are combinations of Class 1 and Class 3, and sometimes pose a very difficult problem, especially when the directions of the electric and magnetic fields are different. A basic framework was presented in terms of the density matrix formalism.

Polarized laser induced fluorescence spectroscopy (LIFS) also constitutes a part of PPS. Electric-field diagnostics based on polarized LIFS was presented. Spectral line broadening and disalignment of the excited atoms, both by atomic collisions, were investigated, and it

was confirmed that the rate coefficients for these processes have nearly the same values.

PPS is still in the process of development and has a broad area of possible applications. This is true for the Class 1 polarization. This is even more so true for Class 2; for magnetically confined plasmas PPS can play a decisive role in determining the EDF, especially in plasmas with current drive. Industrial plasmas are another field for PPS; the presence of an anisotropic EDF or IDF (ion velocity distribution function) is important for the performance of the plasma, for example, during etching of circuits. Anisotropies have been suggested by simulations, but until now with no experimental means for detecting them. PPS could substantiate these simulation results and may help improve the performance of these plasmas. Plasma display panel research and development is another field that might benefit from PPS. Several anomalies, or one might even call them mysteries, of the observed line intensities were noted for otherwise well understood solar and tokamak plasmas. It was suggested that PPS research on these plasmas may solve some of them and provide new insight into the physical processes underlying these plasmas. Recent progress in producing a plasma with very high power and short pulse laser irradiation has opened an entirely new class of plasmas. PPS can be a powerful tool in investigating physics of these plasmas, and several such investigations are now underway.

The above is only a brief and incomplete summary of the presentations and discussions during the workshop. The details are given in papers included in these Proceedings. It would be to our great pleasure, if the reader were to find the topics in these papers interesting and stimulating.

Finally, we would like to acknowledge the following companies for their support of our meeting: Rohm Co., Ltd.; Toshiba Lighting and Technology Corporation; Matsushita Electric Works, Ltd.; Ricoh Co., Ltd.; Ushio Inc.; Hitachi, Ltd.; and Matsushita Electric Industrial Co., Ltd.

May, 1998

Peter Beiersdorfer
Takashi Fujimoto

**List of Participants**

P. Beiersdorfer: Lawrence Livermore National Laboratory, P.O.Box 808, L-421, Livermore, California 94551-9900 USA; beiersdorfer1@llnl.gov

G. Csanak: Los Alamos National Laboratory, Los Alamos, New Mexico 87545 USA; gc@t4.lanl.gov

D.W. Savin: Columbia Astrophysics Laboratory, Mail Code 5247, 550 W113th st., NY, NY 10027; savin@astro.columbia.edu

V.L. Jacobs: Complex Systems Theory Branch, Code 6693, Condensed Matter and Radiation Sciences Division, Naval Research Laboratory, Washington, D.C. 20375, USA; jacobs@dave.nrl.navy.mil

E. Oks: Physics Department, Auburn University, 206 Allison Lab. Auburn, Alabama 36849-5311, USA; goks@physics.auburn.edu

R. Mancini: Department of Physics, University of Nevada-Reno, Reno, Nevada 89557, USA; rcman@physics.unr.edu

A. Shlyaptseva: Department of Physics 220(Mail Stop), University of Nevada-Reno, Reno, Nevada 89557, USA; alla@arrayan.physics.unr.edu

S.A. Kazantsev; Institute of Physics, St. Petersburg State University, 7/9 Universitetskaya nab. 199034 St. Petersburg, Russia; DASOP-L.P.S.M. Observatoire de Paris, Section Meudon, 5 Place Jules Janssen, 92195 Meudon, France; Fax+33-1-4507-79-59; GUEST326%MESOPH@MESIOB.OBSPM.FR

A.M. Urnov; Department of Optics, P.N. Lebedev Physics Institute of The Russian Academy of Sciences, 119146 Moscow, Russia; urnov@sci.lpi.msk.su

V. Helbig; Institut fuer Experimentelle und Angewandte Physik, Universitaet Kiel, D24098 Kiel, Germany; helbig@physik.uni-kiel.de

O. Herzog: Inst. Exp. Phys. V, Ruhr-Universitat, Bochum, 44785 Bochum, Germany; olaf.herzog@ep5.ruhr-uni-bochm.de

J. Dubau: Paris Observatory, 5 place Jules Janssen, 92195 Meudon Cedex, France; dubau@delacroix.obspm.fr

M. Cornille: Paris Observatory, 5 place Jules Janssen, 92195 Meudon Cedex, France; cornille@turner.obspm.fr

C. Chenais-Popovics: Laboratoire pour l'Utilisation des Lasers Intenses, Ecole Polytechnique, 91128 Palaiseau Cedex, France; claude@greco2.polytechnique.fr

K. Ida: National Institute for Fusion Science, Toki 509-5292, Japan; ida@ms.nifs.ac.jp

T. Kato: National Institute for Fusion Science, Toki 509-5292, Japan; takako@nifs.ac.jp

T. Oda: Faculty of Engineering, Hiroshima University, Higashi-Hiroshima 739, Japan; tshoda@ipc.hiroshima-u.ac.jp

H. Yoneda: Institute for Laser Science, University of Electro-communications, Chofu 182, Japan; yoneda@ils.uec.ac.jp

S. Ohtani: University of Electro-communications, Chofu 182, Japan; ohtani@ils.uec.ac.jp

Y. Kato: Instutute of Laser Engineering, Osaka University, Suita 565, Japan; kato@ile.osaka-u.ac.jp

T. Makabe: Department of Electrical Engineering, Faculty of Science and Technology, Keio University, Hiyoshi, Kita-ku, Yokohama 223, Japan; makabe@mkbe.elec.keio.ac.jp

T. Fujimoto: Department of Engineering Physics and Mechanics, Graduate School of Engineering, Kyoto University, Kyoto 606-8501, Japan; a53080@sakura.kudpc.kyoto-u.ac.jp

I. Murakami: National Institute for Fusion Science, Toki 509-5292, Japan; mizumi@nifs.ac.jp

T. Kagawa: Department of Physics, Nara Women's University, Nara 630, Japan; kagawa@cc.nara-wu.ac.jp

K. Itoh: National Institute for Fusion Science, Toki 509-5292, Japan

M. Hirsch: Max-Planck-Institute fur Plasmaphysik, EURATOM Ass., Boltzmann str. 2, D-85748 Garching, FRG; matthius.hirsch@ipp.mgp.de

M. Hasuo; Department of Engineering Physics and Mechanics, Graduate School of Engineering, Kyoto University, Kyoto 606-8501, Japan; hasuo@jasmine.scphys.kyoto-u.ac.jp

T. Kawachi: The Institute of Physical and Chemical Research, RIKEN, Wako 351-01, Japan; kawachi@postman.riken.go.jp

M. Watanabe: Faculty of Engineering, Hiroshima University, Higashi-Hiroshima 739, Japan; magico@ipc.hiroshima-u.ac.jp

H. Watanabe: Department of Engineering Physics and Mechanics, Graduate School of Engineering, Kyoto University, Kyoto 606-8501; Institute for Laser Science, University of Electro-communications, Chofu 182; h_watana@ils.uec.ac.jp

T. Furukubo: Department of Engineering Physics and Mechanics, Graduate School of Engineering, Kyoto University, Kyoto 606-8501, Japan;
furukubo@jasmine.scphys.kyoto-u.ac.jp

M.Yoshikawa: Plasma Research Center, University of Tsukuba, Tsukuba, Ibaraki 305, Japan; yosikawa@prc.tsukuba.ac.jp

**Contents**

# Historical Overview of Plasma Polarization Spectroscopy

A.M.Urnov
*P.N.Lebedev Physical Institute of Russian Academy of Sciences, 53 Leninskii Prospect, 117924 Moscow, Russia*

**Introduction**

Polarization is the key word to describe a specific field of spectroscopic research named Plasma Polarization Spectroscopy (PPS). Being one of the main concepts of the light theory it has a long way of history. The idea to consider the phenomena of double ray refraction, discovered in 1669 by Bartholin, by means of the property pertinent to light corpuscules belongs to Newton. The term "polarization" in application to light phenomena was introduced by Malus in 1808 who discovered the manifistation of this property in light reflection. Since that during about a century the concept of light polarization developed along with an evolution of theoretical concepts of light nature until the modern understanding of this phenomena was founded. Each fundamental discovery in this field such as those made by Zeeman (1996), Stark (1913), and Hanle (1924) opened new possibilities for later applications of polarization spectroscopy or spectropolarimetry to a remote sensing of matter in the presence of external fields in astrophysical and laboratory conditions.

First detailed investigations of impact polarization caused by collisions were carried out in 1920's in a series of experiments with Na (Kossel & Gerthsen, 1925), Hg (Skinner, 1926), He and Ne (Steiner, 1928)[1-3]. The theory of polarization of impact radiation was first developed by Oppenheimer in 1927 [4,5]. The first detailed calculation was made by Penney (1932) who also showed the importance of account for hyperfine structure [6]. Further

development of the collisional approach of Oppenheimer-Penney to the problem of line polarization as well as the calculations in the Born approximation were given in the paper of Percival & Seaton (1958) [7]. In this paper the polarized photon was considered as being emitted by the complete system of atom+electron.

For about 30 years following aforementioned observations line polarization has been observed in various discharges, however only qualitative analysis was given.

The modern period in exploration of the light polarization phenomena connected with plasma spectroscopy was started in the 1950s by the work of Fano [8] and later by Fano & Macek [9] who provided a new approach to the problem in the frame of the formalisms of density matrix in irreducible tensorial set representation of the rotation symmetry group (see [10]). A crucial point in the development of experimental studies in the frame of PPS is connected with the discovery in the mid of 1960s of self-alignment phenomena caused by the anisotropy properties of plasma sources.

Polarization state of emission and absorption lines could be considered as the consequence of polarization of atomic ansembles related to nonequilibrium populations of magnetic sublevels or in other words to the ordering of angular momenta of atomic particles in plasma. The alignment effect described by the quadrupole polarization momentum of atomic density matrix may be a result of different processes arising in plasma due to external or inner interactions. The self-alignment of atomic ansembles reflecting the limited spatial dimensions and the energy exchange processes in plasma became a subject of intensive investigations both experimental and theoretical in the 1970s. The application of the quantum kinetic equations happened to be an adequate approach to various problems of plasma spectroscopy including interference of atomic states, line broadening, polarization and many others. Fundamental results had since been obtained were described in detail in many monographs and reviews. We refere the reader to the recent book of Kazantsev & Henoux [11] and the review of Fujimoto & Kazantsev [12] where the survey for physical and historical aspects of the PPS is given along with a complete set of relevant references.

Below we will restrict ourself by a consideretion of X-ray Line Polarization Spectrosopy (XRLPS) - a new trend in the PPS, developed for last decade and focused at the specific properties of polarized emission from higly charged ions in plasma. A short survey of the main results obtained for the impact polarization due electron-ion interactions in plasma is presented.

**The role of non-Maxwellian electrons.**

Among various macroparamerters characterizing the state of high-temperature plasmas there are those which are connected with so called nonthermal or suprathermal electrons. The distortions of Maxwellian distribution function (DF) or presence in plasma of electron beams, in spite of relatively low densities may play a substantial role in the processes of energy balance, thermal conductivity and others as well as for the formation of emission spectra. There are many physical mechanisms for creation of nonthermal electrons, for example, the presence in plasma of the electric field, temperature gradients, parametric instabilities. Such runaway electrons were directly registered in laser produced plasma; their presence in laboratory (laser produced, tokamak, and vacuum spark) as well as in astrophysical (solar corona) plasmas was established by observing the bremsstralung radiation (see [13]).

A significant role of nonMaxwellian electrons in formation of short wavelength spectra and thus the importance of their account in a theoretical approach to spectroscopic diagnostics of plasma parameters such as an electron temperature and density was pointed out in a series of papers devoted to the plasma of solar corona [14-17], pinch plasma [18,19] and plasma focus [20-22]. A strong impetus to a research activity in this field was given by the appearance of current drive on tokamaks by the lower hybrid heating (see, for example, [23]), and, from other side, by the results of polarization measurements for continuous [24] and line spectra [25,26] of solar flares (see also reviews [27,28]).

The information about the DF for electrons is important because of two main reasons. One is connected with a necessity to study physical conditions in plasma which lead to formation of nonMaxwellian DF, the other concerns the methods of spectroscopic diagnostics of plasma. An account for nonthermal electrons in calculations of emission spectra may considerably change such characteristics of plasma as electron temperature and density, ionization equilibrium, and others (e.g.[14-22],[29]). The short wavelength emission is a main source of direct information on the processes in hot plasma. For majority of laboratory and astrophysical plasmas the electron-ion interaction is the dominate mechanism for formation of this emission. Measurements of its spectroscopic characteristics provide a unique possibility for diagnostics of electron and ion DF with high accuracy. The most natural way to study the anisotropic DF, electron beams in particular, seems to be the polarization measurements.

**Main results of XRLPS.**

First investigations of X-ray line polarization as far as we are aware were made in the papers [30,31] in connection with the problem of anisotropic nonthermal electrons in solar flares. These calculations carried out for [H] iron ions were based on a theory for dipole transitions in neutral atoms [7]. Non-relativistic calculations of polarization for [H] and [He] ions lines and their satellites using the Coulomb-Born-Exchange method with account for intermediate coupling due to relativistic perturbic interactions were firstly presented in [32,33]. The results of calculations were applied to the interpretation of the results of polarization measurements made for the first time for solar flares by means of Bragg spectrometers with high resolution in [16,24,26]. The method of diagnostics for anisotropic suprathermal electrons based on the polarization measurements, first suggested in [34] was used in these papers. The computer codes ATOM and MZ [35-36] developed at the Lebedev Physical Institute (FIAN) were used in these calculations.

Similar calculations for iron ions by means of well known University College London program [37,38] adopted to the problem under consideration were given in papers [39,40].In the papers [41,42] a nonrelativistic LS coupling approach was used in calculations of the cross sections for electron impact excitation of ion target magnetic sublevels. The polarization degree as it was already shown in [33,39] is expressed trough these values. A relativistic distorted wave approach on the basis of Dirac-Fock- Slater potential was used in the paper [43] for calculations of cross sections of excitation to specific magnetic sublevels of ions with high charge z.

First direct measurements of line polarization excited by electron beams by means of the EBIT source were made for [He] ions of Sc [44] and Fe [45]. A fail of a theory to predict the polarization degree for the lines due to forbidden transitions in elements with nonzero nuclear spin was understood in [44,46] by an account for the fine structure interactions. First EBIT mesurements of polarization of satellite lines emitted from [Li] and [Be] ions of Fe were carried out in [47].

The experiments with line polarization measurements were firstly carried out for laboratory plasmas of Z-pinch and laser produced plasma in [48] and [49], respectively. In both cases the results showed the presence in plasma of nonMaxwellian anisotropic electrons directed perpendicular to the symmetry axes.

First measurements of line polarization from tokamak plasma were made for C and O in [50].

The review of atomic processes and the compilation of atomic data rel-

evant to polarization plasma spectroscopy is given in [51]. Theoretical approach to a discription of an ansemble of ions in terms of two quantities, population and alignnment, signed to each atomic level is given in [52] on the basis of kinetic equations for atomic density matrix.

The approach based on the desity matrix was used in [53] where the equations for low density (astrophysical) plasma were derived for a plasma in external electrical and magnetic fields in the Born approximation for exitation amplitudes. General expressions for a similar case are given in [54] with a future application to the tokamak plasma.

In conclusion it should be noted that the results of the present International Simposium and US/Japan Workshop will considerably increase the list of experimental and theoretical acheavments in the field of PPS.

Acknowledgments

I would like to thank the Organizing committee, in particular Prof. T.Fujimoto and Dr. P.Beiersdorfer for the invitation to participate at the Simposium and Workshop on PPS. The works presented were supported by grants of the INTAS-RFBR 95-0875 and RFBR 97-02-16919.

References

1. Kossel W, and Gerthsen C, 1925, Ann.Phys., Lpz., 77, 273.
2. Skinner H W B, 1926, Proc.Roy.Soc.A, 11, 642.
3. Steiner K, 1928, Z.Phys., 52, 1002.
4. Oppenheimer J R, 1927, Z.Phys., 43, 27; Proc.Nat.Acad.Sci., 13, 800.
5. Oppenheimer J R, 1928, Phys.Rev., 32, 361.
6. Penney W G, 1932, Proc.Nat.Acad.Sci., 18, 231.
7. Percival I C, and Seaton M J, 1957, Phil.Trans.R.Soc.A, 251, 113.
8. Fano U, 1957, Rev.Mod.Phys., 29, 74.
9. Fano U, and Macek J H, 1973, Rev.Mod.Phys., 45, 553.
10. Blum K, 1981, Density matrix theory and applications, NY, London, Plenum Press.
11. Kazantsev S A, and Henoux J-C, 1995, Polarization spectroscopy of ionized gases, Dordrecht, Boston, London, Kluwer Academic Publ.
12. Fujimoto T, and Kazantsev S, 1997, Plasma polarization Spectroscopy, Plasma Phys.Control.Fusion, 39, 1267.
13. Lamourex M, 1993, Atomic Physics and Non-Maxwellian Plasmas in "Advances in Atomic, Molecular, and Optical Physics, V.31 (D.Bates and B Bederson, eds) Academic Press, New York, 233.
14. Karev V I, Korneev V V, Krutov V V, Lomkova M, Oparin S N, Urnov A M, Vasilyev B N, Zhitnik I A, Gilvarg A B, Belicova T S, 1980,

Preprint FIAN No 81, Moscow.

15. Siarkowski M, Sylwester I, Bromboszcz G, Korneev V V, Mandelshtam S L, Oparin S N, Urnov A M, and Zhitnik I A, 1982, Solar Phys. 81, 63.

16. Korneev V V, Mandelshtam S L, Oparin S N, Urnov A M, and Zhitnik I A, 1983, Adv. Space Res. 2, No 11, 139.

17. Mandelshtam S L, Urnov A M, and Zhitnik I A, 1984, Adv. Space Res., 4, No 7, 87.

18. Kania D R, and Jones L A, 1984, Phys. Rev. Lett., 53, 166.

19. Kania D R, and Jones L A, 1985, ibid, 55, 1993.

20. Schneider R R, Lee M J, Gullicson R L, and Smith, 1985, "Characteristics of charged particle beams produced by a plasma focus" in Proc. of the Fourth Int. Workshop on Plasma Focus and Z-pinch Resaerch, p.108, Warsaw, Poland.

21. Czekaj S, Denus S, Szydlowski A, and Sledzinski S, 1985, "Characteristics of ion and electron emission from PF-150 and PF-20 plasma focus devices", ibid,p.116.

22. Noll R, Lebert R, Ruel F, and Herzinger G, 1985, "suprathermal IR-emission and bidirectional electron beams at the plasma focus", ibid, p.120.

23.Von Goeller S Stevens J, Stodiek W, Bernabet S, Bitter M, Chu T K, Hill K W, Hillis D, Hooke W, Jobes F, Lenner G, Meservey E, Motley R, Sauthoff N, Sesnic S, and Tenney F, 1983, Report PPPL-2010, Princeton, USA.

24. Krutov V V, Korneev V V, Mandelshtam S L, Urnov A M, and Zhitnik I A, 1981, Preprint FIAN No 133, Moscow.

25. Akida K, Tanaka K, and Watanabe T, 1983, Solar Phys., 88, 101.

26. Zhitnik I A, Korneev V V, Krutov V V, Oparin S N, and Urnov A M, 1987, Russian: Trudi FIAN, 179, 39. English translation:Proceedings of P N lebedev Physical Institute (N G Basov, edt), v. 179(I I Sobelman, edt), p.51, Nova Science publ. co., New York.

27. Zhitnik I A, Tindo I P, and Urnov A M, 1989, Russian: Trudi FIAN, 195, 3. English translation: Proceedings of P N Lebedev Physical Institute(N G Basov, edt), v.192 (I I Sobelman, edt), Nova Science publ. co., New York.

28. Urnov A M, 1994, Solar spectroscopy in the Russian space programme; past results and future prospects, J.Phys. B: Atom.,Mol. Opt.Phys., 28, 1.

29. Rosmej F B, 1994, JQSRT, 51, 319.

30. Haug E, 1979, Solar Phys., 61, 129.

31. Haug E, 1981, Solar Phys., 71, 77.

32. Shlyaptseva A S, Urnov A M, and Vinogradov A V, 1981, Preprint FIAN No 194, Moscow, Russia.

33. Vinogradov A V, Urnov A M, and Shlyaptseva A S, 1989, Russian: Trudi FIAN, 195, 89. English translation: Proceedings of P N Lebedev Physical Institute (N G Basov, edt), v.192 (I I Sobelman, edt), Nova Science publ. co., New York.

34. Shlyaptseva A S, Urnov A M, and Vinogradov A V, 1981, Preprint FIAN No 193, Moscow, Russia.

35. Vainshtein L A, and Shevelko V P, 1986, Structure and characteristics of ions in hot plasma, NAUKA, Moscow.

36. Shevelko V P, and Vainshtein L A, 1993, Atomic physics for hot plasmas, Institute of Physics Publishing, Bristol & Philadelphia.

37. Eissner W, and Seaton M J, 1972, J. Phys. B: At. Mol. Phys., 5, 2187.

38. Saraph H E, 1978, Comput. Phys. Commun., 15, 247.

39. Inal M K, and Dubau J, 1987, J. Phys. B: Atom. Mol. Phys., 20, 4221.

40. Inal M K, and Dubau J, 1989, ibid, 22, 3329.

41. Mitroy J, 1988, Phys. Rev. A, 37, 649.

42. Mitroy J, and Norcross D W, 1988, Phys. Rev. A, 37,3755.

43. Zhang H L, Sampson D H, and Clark R E H, 1990, Phys. Rev. A, 41, 198.

44. Henderson J R, Beiersdorfer P, Bennet C L, Chantrenna S, Knapp D A, Marrs R E, Doschek G A, Seely J F, Brown C M, LaVilla R E, Dubau J, and Levine M A, 1990, Phys. Rev. Lett., 65, 705.

45.Beiersdorfer P, Vogel D A, Reed K J, Decaux V, Scofield H, Widmann K, Holzer G, Forster E, Wehrhan O, Savin D W, Schweikhard L, 1996 Phys.Rev A, 53, N 6, 3974.

46. Dubau J, Garbuzov Y, and Urnov A, 1994, Physica Scripta, 49, 39.

47. Biersdorfer P, Slyaptseva A S, Mancini R C, and Neil P, 1997, Rev.SC.Instrum., 68(1), 1095.

48.Veretennikov V A, Gurei A E, Dolgov A N, Korneev V V, and Semenov O G, Russian: Pis"ma v Zh. Exp.Teor. Fiz., 47,29.

49. Kieffer J C, Matte J P, Pepin H, Chaker M, Beaudon Y, Johnston T W, Chien C Y, Coe S, Mourou G, and Dubau J, Phys. Rev. Lett., 68, 480.

50.Fujimoto T, Sahara H, Kawachi T, Kallsteenius T, Goto M, Kawase H, Furukubo T, Maekawa T, Terumichi Y, 1996, Phys.Rev. E, 544, 53.

51.Fujimoto T, Koike F, Sakimoto K, Okasawa R, Kawasaki K, Takiyama K, Oda T, and Kato T, 1992, Research Report NIFS-DATA-16, Nagoya 464-01, Japan.

52. Fujimoto T, Sahara H, Csanak, and Grabbe, 1996, Research Report NIFS-DATA-38, Nagoya 464-01, Japan.

53. Fineschi S, and Degl'Innocenti E L, 1992, Aph.J., 392, 337.

54. Jacobs V L, and Filuk A B, 1995 Laser and Particle Beams, 13(2) 303.

# Overview on Atomic Physics of Plasma Polarization Spectroscopy

**J. Dubau**, Observatoire de Paris, 92195 Meudon-Cedex, France

**Abstract**

An introduction to the Atomics Physics for Plasma Polarization Spectroscopy is given. It is stressed that, in general, atomic-electron collisions can not be approximated by a simple electric dipole transition. This is a consequence of the complexity of the electron-electron interaction ($1/r_{ij}$), which is not as simple as photon interactions which usually are dominated by E1 transitions.

## 1. Introduction

The radiation emitted or absorbed by a plasma gives very important informations concerning the physical parameters of this plasma. In Astrophysics, it is usually the unique way to get such informations. For laboratory, more direct measurement methods (electrical voltage and current intensity, different laser interactions, ...) can be used, in particular, to test the results deduced from spectroscopic diagnostics.

Plasmas have usually very complex geometries and many inhomogeneities can occur, which make spectroscopic analyses very difficult. Any temporal or spatial resolution improvement of experimental setup, as well as spectroscopical resolution, increases greatly the quality of the diagnostics. In particular for short life plasmas, such as laser produced plasmas or pinch plasmas, until very recently, it was necessary to cumulate many data obtained during different discharges to extract a resolved spectra from its statistical background. Nowadays, the situation is more promising and more refined atomic data become necessary to do better plasma theoretical modellings. Fortunately, parallel to technological progresses in experimental technics, great improvements have been done on fast and powerful computors, which give now huge amounts of accurate atomic data.

Although radiation polarization has been discovered almost two centuries ago, it has been relunctaly used for plasma analysis. A century ago, for reasons already mentioned, the astronomers have thought it could contribute to a better understanding of the Universe : reflexion of the solar light by the planets, measurement of the Sun magnetic field using Zeeman effect, etc. In laboratory, the plasmas being apparently more instable than in Astronomy, the polarization is often destroyed by many random collisional processes, except if some strong anisotropy dominates. If now we combine the fact that polarization can be weak, to the difficulty to get a resolvable spectra, we can understand why Plasma Polarization Spectroscopy is still a very modern subject.

## 2. Introduction to the Density Matrix

In Quantum Mechanics text-books, the density matrix concept is usually shortly described and leaves the impression of a very complex theoretical tool. It is often possible to avoid it but, in the case of energy sublevel populations and radiation polarization, it helps to easily formulate the excitation and desexcitation process mechanisms.

The wavefunction (or ket) contains all the informations concerning a system of $N$ particles interacting one with the other, at a time $t$.

$$\Phi(x_1, x_2, ...x_N; t) = \langle x_1, x_2, ...x_N; t \,|\Phi\rangle \tag{1}$$

where $\mathbf{x}_i = (\vec{r}_i, \sigma_i)$ are the spatial and spin coordinates of the particle $i$.

The *observable* informations (energy, momenta, ... ) concerning the system can be obtained by applying some appropriate operator $\tilde{A}$.

$$\langle \tilde{A} \rangle = \langle \Phi | \tilde{A} | \Phi \rangle \qquad \text{with} \qquad \langle \Phi | \Phi \rangle = 1 \tag{2}$$

Except if the particles do not interact, it is impossible to factorize $\Phi$

$$\Phi(x_1, x_2, ...x_N; t) \neq \phi_1(x_1; t)\phi_2(x_2; t)...\phi_N(x_N; t) \tag{3}$$

In particular, it is usually not possible to separate $p$ particles from $N - p$ particles, for example, to separate some observed atomic system from the surrounding plasma.

If we can indentify some lines emitted from a plasma, it means that the coupling between the emitting atomic system ($p$ particles) and the other particles ($N - p$) is relatively weak. We can then asumme the $p$ particle system to be in a statistical *mixture* of unperturbed states, i.e. a mixture of energy eigenstates of the $p$ particle sytem, $\Psi_1, \Psi_2, ...\Psi_n$.

$$\Psi_i(x_1, x_2, ...x_p) = \langle x_1, x_2, ...x_p | \Psi_i \rangle \tag{4}$$

(we have chosen the coordinates 1, 2, ... $p$ to belong to the observed atomic system, the other coordinates $p + 1$, ... $N$ are for the other plasma particles). We shall suppose the $\Psi_i$ forms a complete basis :

$$\sum_{i=1,n} |\Psi_i\rangle\langle\Psi_i| = 1 \qquad \text{(closure formula)} \tag{5}$$

The density matrix elements $\rho_{mn}$ are defined as

$$\rho_{mn} = \int \langle \Phi | \Psi_m \rangle \langle \Psi_n | \Phi \rangle \, dx_{p+1} ... dx_N \tag{6}$$

the $\rho$ matrix is hermitian, i.e. $\rho_{mn} = \rho^*_{nm}$. We see that if we could factorize $\Phi$ such as $|\Phi\rangle = |\Psi_i\rangle\,|\chi\rangle$ (and $\langle\chi|\chi\rangle = 1$), we should have

$$\rho_{ij} = \delta_{ij}$$

($\delta$ Kronecker symbol). The $p$-particle system is only in one eigenstate $\Psi_i$, i.e. it is a *pure* state.

Using the closure formula, any operator $\tilde{A}(p)$, acting only on the $p$ particle system can be expanded as follow :

$$\langle \tilde{A}(p) \rangle = \sum_{mn} \int \langle \Phi | \Psi_m \rangle \langle \Psi_m | \tilde{A}(p) | \Psi_n \rangle \langle \Psi_n | \Phi \rangle \, dx_{p+1} ... dx_N = \sum_{mn} \rho_{mn} \langle \Psi_m | \tilde{A}(p) | \Psi_n \rangle \quad (7)$$

which shows that the density matrix $\rho$ contains all the informations concerning the interaction of the $p - N$ particles. The main problem is that we can not calculate $\Phi$ for $N$ large. But, since the interactions are weak and occurs usually in a very short time, it is possible to consider the interactions as a one-perturber interaction. Some time, it is necessary to go further to two-perturber approximation, etc. For very dense plasmas, it is possible to try to represent the collective interaction as a static or dynamic microfield. In the case of the one-perturber approximation, a statistic on all the possible situation ($\alpha$) of the $p+1$ particle system is done :

$$\rho_{mn} = \sum_{\alpha} g_\alpha \langle \Phi^\alpha_{(p+1)} | \Psi_m \rangle \langle \Psi_n | \Phi^\alpha_{(p+1)} \rangle \quad (8)$$

$g_\alpha$ being the probability to be in the situation $\alpha$, which can be a (continuous) probability density (for example, an energy electron distribution). In this case, the summation over $\alpha$ becomes an integral.

### 3. Level and sublevels

An atomic level ($aJ$) is a set of atomic sublevels $m = |aJM\rangle$ (or magnetic sublevels, or Zeeman sublevels), all of them being *degenerate in energy* (no electric field, no magnetic field are considered). For example, the Ne-like atomic level $1s^2 2s^2 2p^5 3d\ ^3D_2$, corresponding to $S = 1, L = 2$ and $J = 2$, has 5 sublevels $M$=-2, -1, 0, +1, +2, $M$ being the projection of the total angular momentum $J$, on the quantization axis $z$. The choice of these degenerate states depends therefore on the choice of the quantization axis. If the quantization axis is rotated, 5 new sublevels are redefined, which are a linear combination of the first 5 sublevels. The transformation matrix passing from one set to the other is called the *rotation matrix*.

If the atomic system is excited only by *isotropic* processes, the choice of the quantization axis is arbitrary and the results must not depend on any angle. Therefore the corresponding $\rho$ matrix between these sublevels must be the unit matrix multiplied by some constant :

$$\rho_{-2-2} = \rho_{-1-1} = \rho_{00} = \rho_{+1+1} = \rho_{+2+2}$$

($\rho_{mn} = 0$ if $m \neq n$). On the $\rho$ matrix diagonal, the matrix elements will only be different for different levels, all the out-diagonal elements being zero. The diagonal elements are the *populations* of the sublevels, divided by the total atomic population.

The most usual case in laboratory plasmas corresponds to axial symmetry excitation processes by unpolarized particles (Fujimoto and Kazantzev, 1997). The evident choice of

quantization axis is then the axis of symmetry. With this choice, the $\rho$ matrix is expected to be diagonal and does not depend on any rotation of the azimutal angle $\phi$, i.e. :

$$\rho_{-2-2} = \rho_{+2+2} \neq \rho_{-1-1} = \rho_{+1+1} \neq \rho_{00}$$

It is said that the collision has produced an **alignment** of the sublevels.

Another experimental case is when there is also a symmetry axis but the atomic system is excited by polarized electrons, i.e. with a spin projection $m_s = \pm 1/2$ on the symmetry axis, then

$$\rho_{-2-2} \neq \rho_{+2+2} \neq \rho_{-1-1} \neq \rho_{+1+1} \neq \rho_{00}$$

but the non-diagonal density matrix elements are still zero. The atomic system is said to be both oriented and aligned, the alignment part corresponding to :

$$\frac{1}{2}(\rho_{-2-2} + \rho_{+2+2}) \neq \frac{1}{2}(\rho_{-1-1} + \rho_{+1+1}) \neq \rho_{00}$$

## 4. Collisional-radiative model

We shall consider the case of axial symmetry and take the axis of symmetry for quantization axis $z$. The density matrix is therefore diagonal. We renormalize the diagonal elements to correspond to the populations of the sublevels, i.e. $N_m = \rho_{mm}$. The time evolution of the populations is obtained by assuming the different excitation and desexcitation processes are Markovian, i.e. each interaction occurs in a very short time one after the other so that the memory of the former interaction is lost :

$$\frac{dN_m}{dt} = \sum_n B_{mn} N_n \tag{9}$$

These equations are the same equations used for levels : the excitation rates from (sub) level $n \neq m$ are $B_{mn}N_n$ and the desexcitation rate from (sub) level $m$ is $B_{mm}N_m$. If we consider that only electron excitation and spontaneous radiative probabilities are the important population and depopulation processes, and we assume the electron to be thermal (i.e. isotropic and maxwellian), we obtain the following collisional-radiative model :

$$n < m \qquad B_{mn} = N_e q_{nm}(T_e) \tag{10a}$$

$$n > m \qquad B_{mn} = N_e q_{nm}(T_e) + A^r_{nm} \tag{10b}$$

$$B_{mm} = -\left( \sum_{n \neq m} N_e q_{mn}(T_e) + \sum_{n<m} A^r_{mn} \right) \tag{10c}$$

$T_e$ and $N_e$ being respectively the electron temperature and density of the plasma. $A^r_{mn}$ is the spontaneous radiative probability from sublevel $m$ to sublevel $n$ and $q_{nm}(T_e)$, the electron

collisional excitation (or desexcitation) rate coefficient, from $n$ to $m$, satisfies the *detailed balance principle* :

$$q_{nm}(T_e) = q_{mn}(T_e) \exp\left(\frac{E_m - E_n}{kT_e}\right) \tag{11}$$

$E_m$ and $E_n$ are respectively the energies of sublevels $m$ and $n$, and $k$ is the Boltzmann constant. For non-thermal electron collision, the former equation is **no more valid**, e.g. for axial symmetry excitations.

When only one type of radiation (E1, E2, ...., M1, M2, ....) is involved the radiative probability between sublevels is directly related to the radiative probability between levels using a Clebsch-Gordan coefficient $C^{j_1\, j_2\, J}_{m_1\, m_2\, M}$. For example for electric dipole (E1) transitions

$$A^r_{(aJM)(a'J'M')} = A^r_{(aJ)(a'J')} \left| C^{J'\, 1\, J}_{M'\, \mu\, M} \right|^2 \tag{12}$$

with $\mu = M - M'$

## 5. Angular tensor operator representation of the density matrix

Angular tensor operators play a very important role in Atomic Physics : the total angular momentum of the $N$ particle system is conserved during the interactions between the $p$ particle atomic system and the other $N - p$ particles; the choice of the quantization axis depends on an angle; atomic systems have a spherical symmetry around the nucleus. All these properties are taken into account when developping the different interaction operators on *angular tensor operators*. The definition of the $\rho$ matrix, contains the (dyadic) operator $|\Psi_m\rangle\langle\Psi_n|$, i.e. $|aJM\rangle\langle a'J'M'|$. Since we shall not considered any $J$ mixing by some electric field, we shall discuss only the case $J' = J$, i.e. $|aJM\rangle\langle aJM'|$. Fano and Racah (1959) defined a set of irreducible tensorial operators $T^k_q(aJ)$ :

$$T^k_q(aJ) = \sum_{MM'} (-1)^{J-M'} C^{J\, J\, k}_{M\, -M'\, q}\ |aJM\rangle\langle aJM'| \tag{13}$$

We can redefine the $\rho$ density matrix on the $T^k_q(aJ)$ basis:

$$\tilde{\rho}^k_q(aJ) = \sum_{MM'} (-1)^{J-M'} C^{J\, J\, k}_{M\, -M'\, q}\ \rho_{(aJM)(aJM')} = \int \langle\Phi|T^k_q(aJ)|\Phi\rangle\, dx_{p+1}...dx_N \tag{14}$$

$$\text{with} \qquad 0 \le k \le 2J \qquad -k \le q \le +k$$

It is a unitary matrix transformation. Of course, there are as many $\tilde{\rho}^k_q(aJ)$ as $\rho_{(aJM)(aJM')}$.

$$\rho_{(aJM)(aJM')} = \sum_{k\,q} (-1)^{J-M'} C^{J\, J\, k}_{M\, -M'\, q}\ \tilde{\rho}^k_q(aJ) \tag{15}$$

In the case of axial symmetry and unpolarized particles, we saw that there are three different non-zero $\rho$ matrix elements for $J = 2$, i.e. $N_2 = \rho_{+2+2} = \rho_{-2-2}$; $N_1 = \rho_{+1+1} = \rho_{-1-1}$ and $N_0 = \rho_{00}$. There are also three non-zero $\tilde{\rho}^k_q(a2)$ values :

$$\tilde{\rho}_0^0 = \frac{1}{\sqrt{5}}(2N_2 + 2N_1 + N_0) \qquad (16a)$$

$$\tilde{\rho}_0^2 = \frac{1}{\sqrt{14}}(4N_2 - 2N_1 - 2N_0) \qquad (16b)$$

$$\tilde{\rho}_0^4 = \frac{1}{\sqrt{70}}(2N_2 - 8N_1 + 6N_0) \qquad (16c)$$

In the case of polarized particles, there are 2 more independent values ($\rho_{-2-2} \neq \rho_{+2+2}$ and $\rho_{-1-1} \neq \rho_{+1+1}$). There are also 2 more $\tilde{\rho}_0^k$ : $\tilde{\rho}_0^1$ and $\tilde{\rho}_0^3$.

Of course, $\tilde{\rho}_0^0$ is usually non-zero since it is proportional to the population of the level. $\tilde{\rho}_0^2$ is often called the "alignment of the level" and $\tilde{\rho}_0^1$ the "orientation of the level". Usually $\tilde{\rho}_0^2$ is also non-zero. But, we have to be careful that $\tilde{\rho}_0^4$, $\tilde{\rho}_0^6$, ... $\tilde{\rho}_0^{2J}$ do also contribute partly to the effective alignment of the level and $\tilde{\rho}_0^3$, $\tilde{\rho}_0^5$, ... $\tilde{\rho}_0^{2J-1}$ do contribute partly to the effective orientation of the level. For example, for Ne-like Germanium, with a collisional radiative model including only the ground state $(1s^2 2s^2)2p^6$ and $(...)2p^5 3d$, calculations have been done (Inal and Dubau, 1998). The upper state was assumed to be directly excited from the ground state by an electron beam of 2.3 keV, along the quantization axis, this upper state decaying to the ground state by radiative cascades via several intermediate excited states.

The following values were obtained for $2p^5 3d\ ^3D_3$, for example:

$$\frac{\tilde{\rho}_0^2}{\tilde{\rho}_0^0} = -0.19 \qquad \frac{\tilde{\rho}_0^4}{\tilde{\rho}_0^0} = -0.33 \qquad \frac{\tilde{\rho}_0^6}{\tilde{\rho}_0^0} = -0.11$$

and for $2p^5 3d\ ^1D_2$

$$\frac{\tilde{\rho}_0^2}{\tilde{\rho}_0^0} = -0.22 \qquad \frac{\tilde{\rho}_0^4}{\tilde{\rho}_0^0} = -0.54 \qquad \text{i.e.} \qquad \tilde{\rho}_0^4 >> \tilde{\rho}_0^2$$

The time evolution of $\tilde{\rho}_0^k(aJ)$ can be deduced from section 4 :

$$\frac{d\tilde{\rho}_0^k(aJ)}{dt} = \sum_{a'J'k'} B_{k\ k'}^{aJ\,a'J'}\ \tilde{\rho}_0^{k'}(a'J') \qquad (17)$$

using formulae (9), (14) and (15) :

$$B_{k\ k'}^{aJ\,aJ'} = \sum_{M\,M'} (-1)^{J+J'-M-M'}\ B_{(aJM)(a'J'M')}\ C_{M-M\,0}^{J\ J\ k}\ C_{M'-M'\,0}^{J'\ J'\ k} \qquad (18)$$

## 6. Linear polarization

All the radiative observables from the atomic system can be deduced from the $\tilde{\rho}_0^k$, i.e. intensity, linear and circular polarization. In the case where only one radiation type (E1,E2,...,M1,M2) exists between the 2 levels $aJ$ and $a'J'$, the linear polarization of the line $aJ \rightarrow a'J'$ is given by:

$$\eta_3(\theta,\phi) = \pm \frac{\sum_{k=2,2J}^{(even)} \begin{pmatrix} \lambda & \lambda & k \\ 1 & 1 & -2 \end{pmatrix} \begin{Bmatrix} k & J & J \\ J' & \lambda & \lambda \end{Bmatrix} \tilde{\rho}_0^k(aJ)\, Y_k^2(\theta,\phi)}{\sum_{k=0,2J}^{(even)} \begin{pmatrix} \lambda & \lambda & k \\ 1 & -1 & 0 \end{pmatrix} \begin{Bmatrix} k & J & J \\ J' & \lambda & \lambda \end{Bmatrix} \tilde{\rho}_0^k(aJ)\, Y_k^0(\theta,\phi)} \tag{19}$$

where $\lambda = 1$ for dipole radiative transitions (E1,M1) and $\lambda = 2$ for quadrupole radiative transitions (E2,M2). The angles $\theta$ and $\phi$ are relative to the quantization axis. The sign $\pm$ varies for electric (+) and magnetic (-) transition. The $\sum_k^{(even)}$ means a summation on even $k$ values.

For E1 and M1, we see that the linear polarization ($\eta_3(\theta,\phi)$) contains only $\tilde{\rho}_0^0$ and $\tilde{\rho}_0^2$, even if $J > 1$. For E2 and M2, $\eta_3(\theta,\phi)$ contains also $\tilde{\rho}_0^4$. Of course, $\tilde{\rho}_0^4$ can be zero as illustrated by the following example : the magnetic quadrupole line 1s2p $^3P_2$ - 1s$^2$ $^1S_0$. Using a non-relativistic distorted wave approximation and a 2 level collisional-radiative model, it can be proved (Inal and Dubau, 1987) that :

$$N_0 = \frac{4}{3} N_1 - \frac{1}{3} N_2$$

($N_n = \rho_{+n+n} = \rho_{-n-n}$) therefore $\tilde{\rho}_0^4 = 0$. It is nevertheless a M2-transition.

Radiative cascades from 1s$nl$ ($n \geq 3$) upper levels were included in the collisional-radiative model (Inal and J. Dubau, 1993) It was found that 1s3d $^3D_3$ had an important contribution by cascades to 1s2p $^3P_2$ sublevel populations. This produces that $\tilde{\rho}_0^4$ of 1s2p$^3$P$_2$ is no more zero. Radiative cascades are very important for large energy, E, of the projectile on the target 1s$^2$ $^1S_0$. For He-like Fe, at E=27 keV (2000 Ryd), the cascades from upper levels decrease the polarization of this quadrupole line by 23 %, compared to a model including no radiative cascade.

### 7. Electron distribution

The projectile electron distribution in angle $\theta$ and velocity $v$ can be expanded on the Legendre polynomials (or spherical harmonics) ($\int f(v,\theta)\, v^2 \sin\theta\, dv\, d\theta = 1$) :

$$f(v,\theta) = \sum_{K=0}^{\infty} f_K(v) P_K(\cos\theta) \qquad \left( = \sum_{K=0}^{\infty} f_K(v) \sqrt{\frac{4\pi}{2K+1}}\, Y_K^0(\theta,\phi) \right) \tag{20}$$

Similarly it is interesting to develop the excitation rate coefficient (i.e. integrated on angle and energy) $q_{nm}$ by separating the angular part :

$$q_{nm} = \langle v_n \sigma_{nm} \rangle = \int dv_n v_n \left( \sum_{K=0,K_{max}}^{(even)} f_K(v_n) \sigma_{nm}^K(v_n) \right) = \sum_{K=0,K_{max}}^{(even)} q_{nm}^K \tag{21}$$

$\sigma_{nm}^K(v_n)$ is the cross section for the transition between the sublevels $n$ and $m$ ($n = |a'J'M'\rangle$ and $m = |aJM\rangle$) for a velocity $v_n$ and averaged on the projectile angular distribution $P_K(\cos\theta)$. From Quantum Mechanics selection rules (see Inal and Dubau (1987), formula (1)), only the even $K$ contributes to $q_{nm}$. $K_{max}$ depends on the values of $J$ and $J'$. For unpolarized projectile, $q^K_{(aJM)(a'J'M')} = q^K_{(aJ-M)(a'J'-M')}$. For K=0, we have a stronger relation :

$$v_n^2 \sigma_{nm}^0(v_n) = v_m^2 \sigma_{mn}^0(v_m) \tag{22}$$

$$\text{where} \qquad E_n + \frac{v_n^2}{2} = E_m + \frac{v_m^2}{2} \qquad \text{(atomic unit)}$$

Therefore, if $f_0(v_n)$ is a maxwellian distribution of temperature $T_e$, multiplied by some normalisation constant, $q^0_{nm}$ satisfies equation (11) :

$$q^0_{nm}(T_e) = q^0_{mn}(T_e) \exp\left(\frac{E_m - E_n}{kT_e}\right) \tag{23}$$

The development of an electron beam of velocity $v_0$ coming along the quantization axis $z$ is :

$$f_K(v) = \frac{(2K+1)}{2v_0^2}\,\delta(v - v_0) \tag{24}$$

For the transition between $1s^2\ {}^1S$ and $1s3d\,{}^1D$, $K_{max} = 4$, we see that only $\sigma^0_{mn}$, $\sigma^2_{mn}$, $\sigma^4_{mn}$ contributes to $q_{mn}$, i.e $f_0(v)$, $f_2(v)$, $f_4(v)$ even if the Legendre polymonial expansion of the electron distribution is infinite, for an electron beam.

## 8. Conclusion

This chapter did not try to be a review but an overview keeping in mind that it was done for a workshop. It was shown that, in general, atomic-electron collisions can not be approximated by a simple electric dipole transition. This is a consequence of the complexity of the electron-electron interaction ($1/r_{ij}$), which is not as simple as photon interactions which usually are dominated by E1 transitions. We did not speak about electric or magnetic field effects or radiative transfert of polarized light. Some of these effects will be discussed in other papers. For the radiative redistribution, we refer to the 2 recent papers by Bommier (1997). For the readers who would like to go deeper in the knowledge of impact excitation and polarization of emitted lines, they can look at the review paper of Fano and Macek (1973) and the book of Kazantsev and Henoux (1995).

## References


V. Bommier, Astron. Astrophys., **328**, 706 (1997)

V. Bommier, Astron. Astrophys., **328**, 726 (1997)

U. Fano and J.H. Macek, Rev. Mod. Phys., **45**, 553 (1973)

U. Fano and G. Racah, *Irreducible Tensorial Sets* (Academic Press Inc., New York, 1959)

T. Fujimoto and S. A. Kazantzev, Plasma Phys. Control. Fusion **39**, 1267 (1997)

M. K. Inal and J. Dubau, J.Phys. B, **20**, 4221 (1987)

M. K. Inal and J. Dubau, Phys. Rev, **A 47**, 4794 (1993)

M. K. Inal and J. Dubau, private communication, (1998)

S. A. Kazantzev and J-C. Henoux, *Polarization Spectroscopy of Inonized Gases* (Astrophysics and Space Science Library, vol 200, Kluwer Academic Pub., Dordrecht/Boston/London, 1995)

**39**, 1267 (1997)

# Polarization Plasma Spectroscopy (PPS) viewed from plasma physics and fusion research

Katsumi Ida

National Institute for Fusion Science, 322-6, Oroshi-cho, Toki, 509-52 Japan
322-6 Oroshi-cho, Toki, 509-52 Japan

Abstract

Recently the measurements of poloidal magnetic field become important in plasma physics and nuclear fusion research, since an improved confinement mode associating with a negative magnetic shear has been found. The polarization plasma spectroscopy is recognized to be a useful tool to measure poloidal magnetic field and pitch angle of magnetic field.

## 1. Zeeman spectroscopy

At the weak magnetic field the energy levels of ion is split into 2J + 1 sublevels with energy shift given by

$$\Delta E = MgB_0\mu \qquad (1)$$

where M has values from -J to +J , J is the total angular momentum number, $\mu$ is Bohr magnetron factor,the g is standard Lande splitting factor, and B is the magnetic field strength[1]. A spectral lines is composed a number of component due to the energy splitting of the upper and lower levels. The selection rules for electric dipole and magnetic dipole transition are $\Delta J = 0, \pm 1$, $\Delta M = 0$ ($\pi$ component) and $\Delta M = \pm 1$ ($\sigma$ component). When observed from the direction parallel to the magnetic field, the intensity of $\Delta M = 0$ line (linearly polarized) is zero and only $\Delta M = +1$ (clockwise [right-hand] circularly polarized) line and $\Delta M = -1$(counterclockwise [left-hand] circularly polarized) lines are present. When observed from the direction perpendicular to the magnetic field, the radiations of $\Delta M = 0, \pm 1$ transition are linearly polarized parallel ($\Delta M = 0$) and perpendicular ($\Delta M = \pm 1$) to the magnetic field. The Zeeman splitting in angstrom measured from zero-field wavelength $\lambda_0$ for the circularly polarized component is given by

$$\Delta\lambda_B = \pm 4.67 \times 10^{-13}\, zB\lambda_0^2 \qquad (2)$$

where $\pm$ refers to the clockwise and counterclockwise circularly polarized component. B is the strength of the magnetic field in Gauss and z is unity for a normal Zeeman triplet. In the high temperature plasma, the Zeeman splitting is much smaller than the the Doppler broadening with the full width of half maximum (FWHM),

$$\Delta\lambda_D = 7.71 \times 10^{-5}\, \lambda_0 (T_i/A)^{1/2} \qquad (3)$$

The intensity of right-hand and left-hand circularly polarized component, $I_R$ and $I_L$ , observed from the direction with the angle of $\gamma$ with respect to the magnetic field, is given by

$$I_{R,L} = \frac{(1\pm\cos\gamma)^2}{4} I_{\pi+} + \frac{(1\mp\cos\gamma)^2}{4} I_{\pi-} + \frac{\sin^2\gamma}{2} I_{\pi} \qquad (4)$$

where $I_{\sigma+}$ [ = $I(\lambda + \Delta\lambda_B)$ ]and $I_{\sigma-}$ [ = $I(\lambda - \Delta\lambda_B)$ ]are right-hand and left-hand circularly polarized $\sigma$ component and $I_{\pi}$ [ = $I(\lambda)$ ] is linear polarized $\pi$ component. Because of Doppler broadening, the intensity $I(\lambda)$ has Gaussian profile as

$$I(\lambda) = I_0 \exp\left[ - \left( \frac{\lambda - \lambda_0}{\Delta\lambda_D/2\sqrt{\ln 2}} \right)^2 \right] \qquad (5)$$

Then the difference in intensity between $I_R$ and $I_L$ is proportinal to $\cos\gamma$ as,

$$I_R - I_L = \cos\gamma \left[ I_0 \exp\left[ - \left( \frac{(\lambda + \Delta\lambda_B - \lambda_0)}{(\Delta\lambda_D/2\sqrt{\ln 2})} \right)^2 \right] - I_0 \exp\left[ - \left( \frac{(\lambda - \Delta\lambda_B - \lambda_0)}{(\Delta\lambda_D/2\sqrt{\ln 2})} \right)^2 \right] \right] \qquad (6)$$

Right-hand ($I_R$ ) and left-hand ($I_L$) polarized profiles contain contribution from all Zeeman components but due to their partial circular polarization, the $\sigma$ components do not contribute evenly, which results in a small shift (~ $\Delta\lambda_B\cos\gamma$)between the polarized profiles as shown in Fig.1. The magnitude of difference between the circularly polarized profiles is proportional to the magnetic field component in the direction of observation in magnetic field [$\Delta\lambda_B/\Delta\lambda_D << 1$]. The circularly polarized component of Ti XVII 383.4nm was measured in Texas Experimental Tokamak (TEXT) using Fabry-Perot interferometer and photoelastic modulator (PEM)[2]. Figure 2(a) shows the normalized difference of $I_+$ and $I_-$, $(I_+ - I_-)/I_0$, at four position near the plasma axis. The solid lines is least-squares fit to the measured signal (dotted line). The coordinate r is the distance of the line of sight from the center of vacuum vessel. The reversal of the modulation signal indicates null in the poloidal magnetic field. The radial profile of poloidal magnetic field derived with this technique is plotted in Fig.2(b). This data clearly shows the position of magnetic axis (poloidal field is zero) at r = 3cm. The position of magnetic axis is an important issue in plasma physics. Since the shift of magnetic axis is related to the spontaneous current driven by the plasma pressure gradient, the plasma pressure can be estimated from the shift of magnetic axis.

## 2. MSE spectroscopy

The polarization spectroscopy techniques is applied to emission ($H_\alpha$ lines ) from a high energy atomic hydrogen beam injected into a magnetically confined plasma. A strong Lorentz field, E = v x B, ( v : neutral beam velocity, B : magnetic field in the plasma) observed in the reference frame of the beam particle produces splitting and polarization of line emissions via the Stark effect. The Doppler shifted wavelength of the beam emission including the first-order Stark effect is obtained from

$$\lambda = \lambda_0 (1 + (v/c)\cos\beta)(1 + a_i\lambda_0 vB\sin\zeta) \qquad (7)$$

Here, $\zeta$ is the intersecting angle of the injected beam and the magnetic field, and $\beta$ is the angle between the beam and the line of sight.'a(i)' is the coefficient for the line splitting, $\lambda_0$ is the $H_\alpha$ wavelength (6562.8 Å) and c is the light velocity.

When observed in the direction perpendicular to the electric field, the Stark $\sigma$ and $\pi$ component are linearly polarized, respectively perpendicular ($\sigma$ component) and parallel ($\pi$ component) to the direction of the Lorentz field. The spectral intensity through the optics transmitting at $\phi$ degree with respect to the mid-plane at the wavelength $\lambda$ is expressed as

$$I(\phi,\lambda) = I_{\pi l}(\lambda)\cos^2(\alpha_\pi-\phi) + I_{\sigma l}(l)\cos^2(\alpha_\sigma-\phi) + \frac{1}{2} I_{\sigma c}(\lambda) \qquad (8)$$

where $\alpha_\pi=\alpha_\sigma+90$, $I_{\pi l}(\lambda)$ [ $= I_\pi(\lambda)(\sin^2\theta)/2$ ]and $I_{\sigma l}(\lambda)$ [ $= I_\sigma(\lambda)(\sin^2\theta)/2$ ] are the linearly polarized $\pi$ component and the $\sigma$ component, respectively, $I_{\sigma c}(\lambda)$ [ $= I_\sigma(\lambda)(\cos^2\theta)$ ] is the circularly polarized $\sigma$ component, $\theta$ is the angle between Lorentz field vector and viewing line. When the excitation is isotropic, the total intensity of $\sigma$ and $\pi+$ plus $\pi-$ component become equal as $I_{\pi+} = I_{\pi-} =(1/2)I_\sigma$. By using the intensity ratio measured with four different optic transmitting angle $\phi$, regardless the intensity ratio between $I_\pi$ and $I_\sigma$ and angle $\theta$, the polarization angle of the $\sigma$ (or $\pi$ ) component $\alpha_\sigma$ (= $\alpha_\pi - 90$ ) is given by

$$\tan(2\alpha_\sigma) = \frac{\left(I(135,\lambda)-I(45,\lambda)\right)}{\left(I(90,\lambda)-I(0,\lambda)\right)} \qquad (9)$$

The pitch angle $\gamma$ is derived from the polarization angle of $\alpha_\sigma$ or $\alpha_\pi$ as

$$\tan\gamma = \frac{\tan\alpha_\sigma}{\cos\beta} = \frac{\cot\alpha_\pi}{\cos\beta} \qquad (10)$$

When the pitch angle is derived from $\pi$ component alone (when $\pi$ component is completely isolated from $\sigma$ component), the polarization angle or $\alpha_\pi$ can be measured from the ratio of $I(45,\lambda)$ to $I(135,\lambda)$ as $\tan^2(\alpha_\pi - 45) = I(45,\lambda)/I(135,\lambda)$[3]. However, in many cases, there is a overlap of spectra between $\pi$ component and $\sigma$ component as shown in Fig.3[4]. When the magnetic field is weak, the overlapping problem becomes serious and $\pi$ component and $\sigma$ components looks like one peak. Therefore the technique to solve the overlapping problems. There are two technique to separate $\pi$ component from overlapping $\sigma$ component or linearly polarized $\sigma$ component from circular polarized $\sigma$ component. One is the set of four linear polarizer[5] and the other is set of linear polarizer and photo elastic modulator (PEM), which functions as oscillating (~ 50kHz) quarter-wave plate (retardation from $-\lambda/4$ to $+\lambda/4$). The axes of the PEM are at +22.5 and -22.5 to the transmission axis of the linear polarizer and modulated with different frequency $\omega_1$ and $\omega_2$. The intensity ratio of the modulation amplitude at $2\omega_1$ to that at $2\omega_2$ gives polarization angle as $\tan[2(\alpha_\sigma-22.5)] = I(2\omega_1)/I(2\omega_2)$. The pitch angle measurements using PEM has been widely used in many tokamaks[4,6,7]. The pitch angle measurements with high time resolution was demonstrated in DIII-D tokamak as seen in Fig.4. The periodic oscillations with 10Hz are so-called sawtooth oscillation. The correlation between MSE measurements and soft x-ray (SXR) emission signal, which indicates the change of plasma electron temperature and density, shows that the magnetic field changes at the sawtooth instability as well as temperature. The good correlation between MSE and SXR measurements supports that sawtooth instability is due to the reconnection of magnetic field in the plasma. The measurements of local magnetic field inside the plasma is essential in the research of

MHD activity in the plasma.

Another application of MSE is measurement of radial electric field. When the radial electric field is large enough to comparable to 1% of Lorentz electric field (> 100kV/m), change of polarization angle due to radial electric field will be measurerable[8].

## 3. Possible application of polarization spectroscopy to plasma diagnostics

In magnetically confined plasma, the polarization of emission is due to the existence of magnetic field through Zeeman and Motional stark effect as described above. Therefore the most application of polarization plasma spectroscopy is the measurements of strength and direction of magnetic field. Another possible application of polarization plasma spectroscopy is the measurement of electron tail using the effect of the anisotropic electron impact on polarization characteristics such as the ratio of $\pi$ component to $\sigma$ component. The electron tail appears in the plasma, where the plasma current is driven by waves in the range of lower hybrid resonance[9]. Conventional approach is that the energy of electron tail is estimated from the angular dependence of hard X-ray intensity in the range of 100 - 400 keV measured with sodium iodide NaI detector. However, the parameters fitting the measured hard X-ray are not determined in a unique fashion[10,11]. Then the estimated energy of electron tail has large uncertainty in general.

A preliminary experiment to study the polarization of impurity emission due to electron tail was done for the plasma with lower hybrid resonance current drive (LHCD) in WT-3 tokamak. The ratio of $\pi$ component to $\sigma$ component is above unity when LHCD is applied, while it is around unity before the LHCD[12]. This experiment suggests the possibility of measurement of electron tail with polarization plasma spectroscopy. Preliminary experiments to measure the polarization due to anisotropic charge exchange at the beam energy of 30 - 40 keV have been done in JFT-2M[13], JIPP T-IIU[14] tokamaks and CHS heliotron/torsatron devices. However, the intensity ratio of $\pi$ component to $\sigma$ component is $1.03 \pm 0.02$ (in JFT-2M), $0.95 \pm 0.03$ (in JIPP TII-U), $1.05 \pm 0.02$ (in CHS) [the error bar is only due to the scatter of data and not including systematic error bar in the measurements], and there is no results that shows the the polarization due to anisotropic charge exchange. The beam energy for these experiments seems to be too low to produce enough polarization to be measured. Higher beam energy using negative ion source will be required for further study.

## References


[1] U.Feldman, J.F.Seely, N.R.Sheeley, Jr., S.Suckewer, A.M.Title, J.Appl. Phys. **56** (1984) 2512.

[2] D.Wroblewski, L.K.Huang, H.W.Moos, Rev.Sci.Instrum. **59**, (1988) 2341.

[3] W.Mandl, R.C.Wolf, M.G.von Hellermann, H.P.Summers, Plasma Phys. Control. Fusion 35 (1993) 1373.

[4] D.Wroblewski, L.L.Lao, Rev.Sci.Instrum. **63**, (1992) 5140.

[5] J.Xu, K.Ida , et al., Fusion Engineering and Design, B23 (1997) 293.

[6] F. M. Levinton, Rev.Sci.Instrum. **63**, (1992) 5157.

[7] F. M. Levinton, G. M. Gammel, R. Kaita, H. W. Kugel, D. W. Roberts, Rev.Sci.Instrum. **61**, (1990) 2914.

[8] B.W.Rice, K.H.Burrell, L.L.Lao, Nucl. Fuion 37 (1997) 517.

[9] S.Bernabei, et al., Phys. Rev. Lett. 49 (1982) 1255.

[10] S.VonGoeler, et al., Nucl. Fusion 25 (1985) 1515.

[11] S.Texter, et al., Nucl. Fusion 26 (1986) 1279.
[12] T.Fujimoto, et al.Phys. Rev. E 54 (1996) 2240.,
[13] J.Xu, K.Ida, T.Kawachi, H.Ogawa, J.Fujita, JFT-2M group, in Controlled Fusion and Plasma Physics, (Proc. 22th Europ. Conf., Bournemouth 1995), 19C, Part III, European physical Society (1995) p417
[14] K.Ida, J.Xu, et al., UV and X-ray Spectroscopy of Astrophysical and Laboratory Plasmas, (Proc. 11th Colloquium on UV and X-ray Spectroscopy of Astrophysical and Laboratory Plasmas, May 29 - June 2, 1995, Nagoya), Edited by K.Yamashita T.Watanabe, University Academy Press, Tokyo, (1996).p503

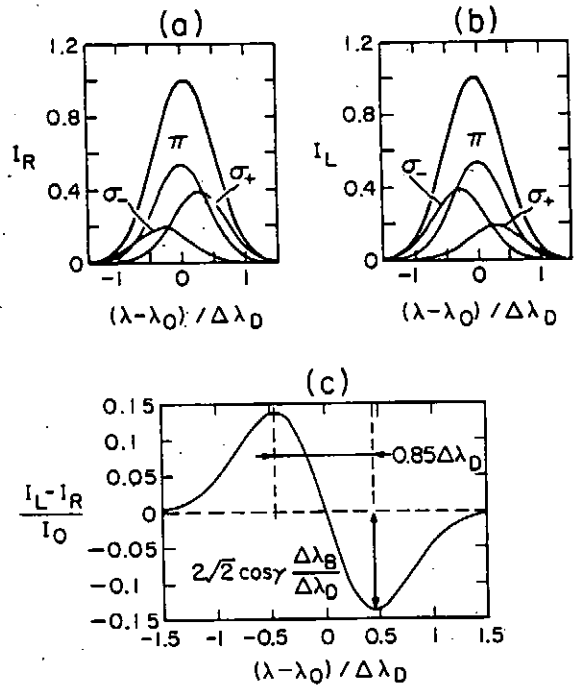


Fig.1.(a),(b) right-hand ($I_R$) and left-hand ($I_L$) polarized profiles of a Doppler broadened spectral line and (c) The magnitude of difference between the circularly polarized profiles (quoted from [2]).

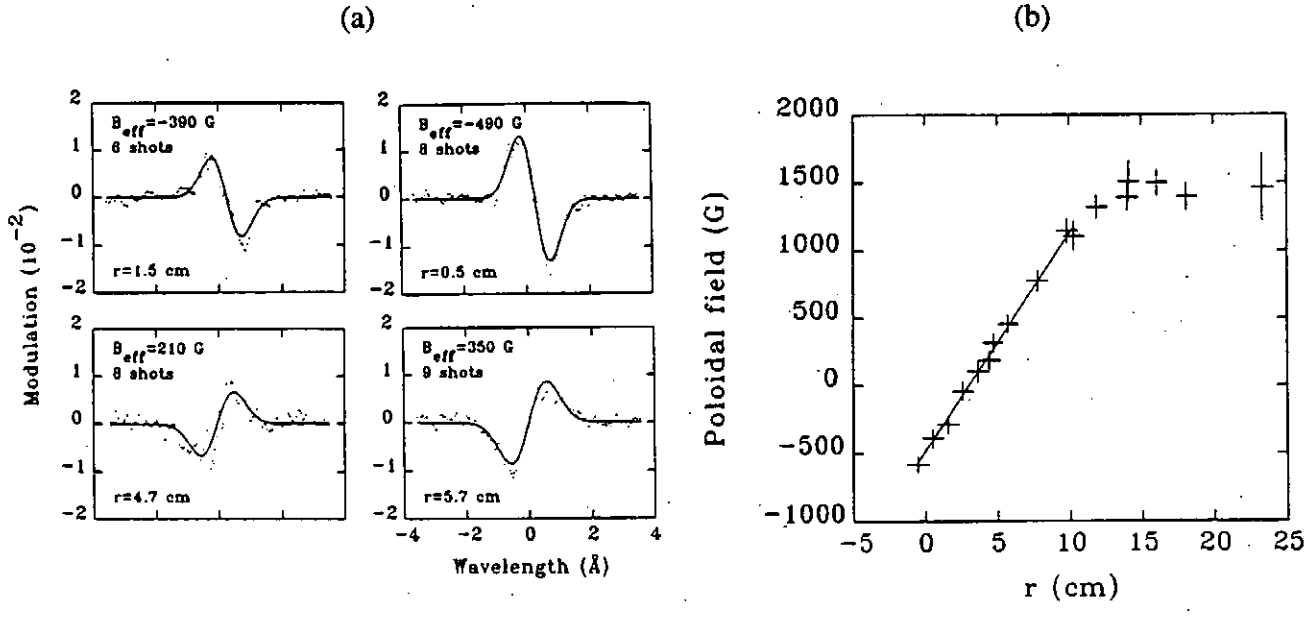


Fig.2 (a) Difference of intensity between clockwise ($\Delta M = +1$) and counterclockwise ($\Delta M = -1$) circularly polarized spectral line of Ti XVII 383.4nm. Solid line is the least squares fit to the measured signal (dotted line). (b) Measured poloidal magnetic field profile. Toroidal field B= 2.0T, plasma current, producing poloidal magnetic field, $I_p$ = 200kA. Solid line is the least squares liner fit to central points (quoted from [2]).

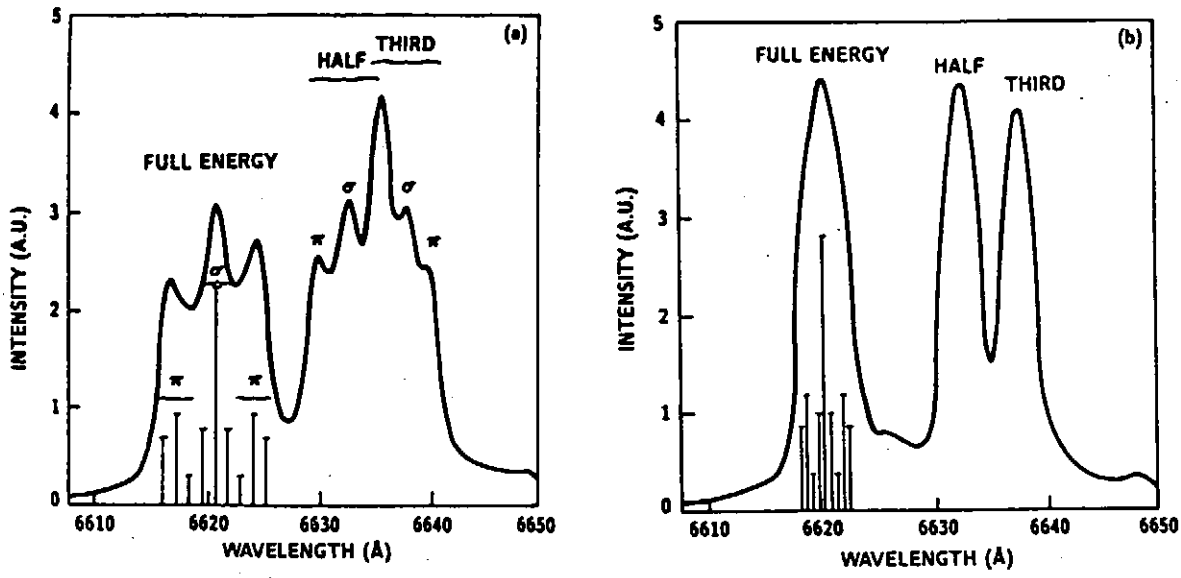


Fig.3. Spectrum of Balmer-α line emitted by the DIII-D neutral beam. Beam energy is 74keV; (a) B = 2.1T, (b) B = 0.9T (quoted from [4]).

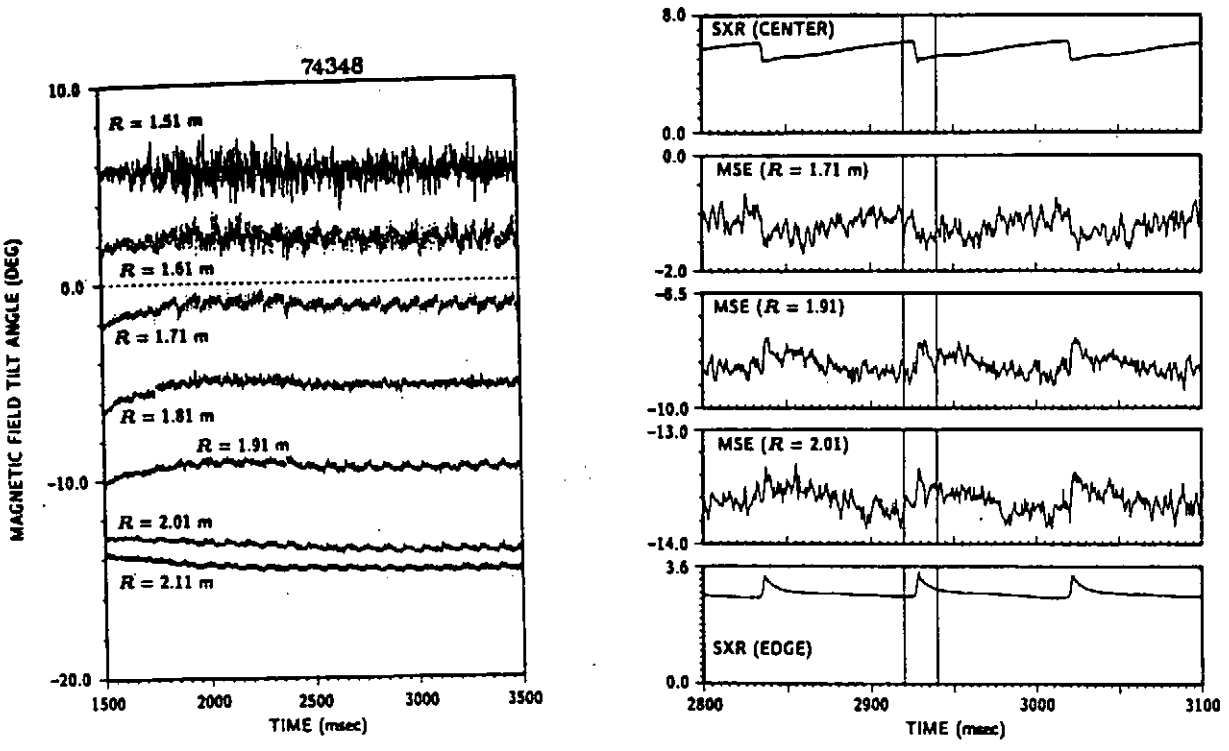


Fig.4. The magnetic field tilt angle measured by the MSE polarimeter at seven spatial locations and correlation between magnetic field tilt angle measured in the plasma interior (MSE) and the soft x-ray emission signal (SXR) during the sawtooth instability (quoted from [4]).

# PLASMA POLARIZATION SPECTROSCOPY ON GAS DISCHARGES AND ASTROPHYSICS

S.A.KAZANTSEV

Institute of Physics, St.Petersburg State University, RUSSIA;
DASOP-L.P.S.H. Section Meudon, Observatoire de Paris
5 place Jules Janssen, 92195 Meudon Cedex, FRANCE

## INTRODUCTION

Polarization of radiation is an universal feature of every real emiting ionized gas entity. The spectropolarimetry, based on a measurement of the polarization parameters of radiation, offers principally new means for sensing of ionized media. Polarimetric remote sensing, being closely connected to the general methods, the computational techniques of the atomic collision theory and kinetics is an actively developing field, because many contemporary principle problems of atomic, collisional physics, plasma diagnostic, solar physics require new diagnostic approaches and practical techniques[1,2,3].

The polarization of a spectral line is effectively a basic spectroscopic characteristic, which, within the most simple approach, stems from a nonequilibrium distribution of populations of the magnetic substates of excited atomic particles (atoms, ions, molecules) and reflects an ordering of the angular momenta of electron shells in an ensemble, or, in other words, the polarization of an ensemble[3]. In many cases the polarization of an emission spectrum is directly connected to the stucture of an ionized entity, which was out of possibilities of the well developed intensity methods of the spectroscopic sensing. Structural features of an ionized medium, such as anisotropy of the resonance optical field, distribution of electric and magnetic fields, energy transport by precipitating particles or by heat conduction, gradients of parameters and boundary effects give rise to the spatial anysotropy of momenta of the excited atomic particles inside the medium[4].

Analysing in more detail an energy aspect of maintenance of an ionized gas entity, as a principle factor of its structure it is possible to conclude, that the energy transport into an ionized medium is implemented, as a rule, in a nonthertmal form, accompanied by gradients of parameters and the spatialy located anisotropies of the light fast charged particles. Collisional interaction of these mobile particles with other plasma components, provide a transformation of energy, associated to the ordered motion into the energy of the chaotic thermal motion. An energy dissipation at the boundaries and the mechanisms, responsible for a self-sustenance of an ionized entity are also reflected in an anisotropy of motion of the plasma components. All these anisotropies in the velocity space, directly connected to the structural features of an

ionized entity as a whole, are thereby reflected in the impact polarization of ensembles of atomic particles and, as a result, in the degree of the radiation polarization.

These new attractive diagnostic opportunities of the polarization spectroscopy are accompanied by a complexity of mechanisms of the spectral line polarization, even for a simple gas discharge, difficulties in experimental observation and correct measurements of the Stokes parameters, lack of the theoretical relations between the polarization of radiation and the kinetic characteristics of the plasma components, specific field effects in case of the magneticaly sustained hot plasmas, as well as indispensable cross sections and polarization parameters for many atomic and ionic states. These difficulties have been successively overcome during last decade in course of development of the quantum collision theory, deep analysis of the elementary polarization process, kinetics of polarization and solutions of the practical problems of the spectropolarimetric sensing under different conditions[2,5].

This report reviews some results of the plasma polarization spectroscopy on gas discharges and non-thermal phenomena in the solar atmosphere in regard to many prospective developments for the ground based or satelite born optical polarization studies of the outer ionosphere and the hot plasmas, which could be expected in a near future.

## GAS DISCHARGES

The first qualitative studies in the simple laboratory gas discharges, performed since the middle of the 70th, indicated, that the observed polarization effects, created by the direct electron impact excitation, or relaxation processes inside an ionized gas are deteremined by the selfalignment of particles or the quadrupole orientation of momenta[6]. The principle result of these initial laboratory studies in view of the new contribution of the spectropolarimetry to the quantitative remote sensing of ionized gases is that the electron impact selfalignment of atomic states and the resulting Stokes parameters of the emission spectral lines are expressed in terms of the quadrupole moment of the velocity distribution function of fast electrons $f^{(2)}(v,\vec{r})$[7]. The quadrupole moment is the third coefficient of the multipole representation of the velocity distribution function in the velocity space:

$$f(\vec{v},\vec{r}) = \sum_{k=0}^{\infty} \sum_{q=-k}^{k} Y_q^{(k)}(\vec{n}) f_q^{(k)}(v,\vec{r})$$

where $Y_q^{(k)}(\vec{n})\,(\vec{n} = \vec{v}/v,\ v = \mid \vec{v} \mid)$ are spherical harmonics determined in the velocity space of electrons.

By its nature, the quadrupole momenmt of the velocity distribution function, being the anisotropic pressure tensor of the electron component, characterizes the local value of the momentum flow density of electrons and, as a result, the quantitative characteristic of the local energy exchange. Indeed, the principle process, indespensable for understanding of a nature of a low temperature plasma of a gas discharge, as well as for many other ionized gas entities, such as an energy exchange with the

environment specifies the kinetics of the most mobile electron component. The polarization of atomic particles in a plasma, created by the electron impact excitation, or the impact selfalignment of the ensemble $\rho_q^{(2)}(J,\vec{r})$, is directly connected to the quadrupole moment of the velocity distribution function via a basic relation:

$$\rho_q^{(2)}(J,\vec{r}) \sim \int_0^\infty dv v^3 \sigma^{(2)}(J,v)\, f_q^{(2)}(v,\vec{r})$$

where $\sigma^{(2)}(J,v)$ is the alignment creation parameter.

Historically, the most simple object to analyse the selfalignment under the direct excitation of atomic particles by fast electrons and to demonstrate new practical potentialities of this thechnique was the positive column of a simple laboratory d.c. gas discharge. The spectropolarimetric studies of the impact selfalignment, caused by anisotropies in the space of the relative velocities of the colliding particles allowed to detect a very fine kinetic effect of the formation of the loss cones in the velocity distribution of fast electrons, resulting from an interaction of the low temperature diluted plasma with the wall of a discharge tube. Moreover, it was possible to sense an orientation of these loss cones and the radial profile of the internal plasma electric field[3].

The high frequency discharge in different forms is a well known laboratory source of the low temperature plasma with the well expressed structural features. The capacitive high frequency discharge, which is formed inside the capacitor of the oscillating circuit of the high frequency generator due to the potential high frequency alternative electric field is a very important object, because it could bring understanding and even simulate processes of the energy deposition into many plasmas under different conditions.

In spite of a long history of experimental and theoretical studies, the physical processes in the high frequency discharge still remain a subject of detailed interest. An interest in this discharge is determined by its wide applications as a light source with high spectral efficiency for the emission lines of the majority of elements, in quantum standards, quantum magnetometers, spectral analysis and as an active medium of gas lasers[8]. Spectral light sources on the basis of the high frequency discharge are usually spherical or cylindric lamps filled with a buffer gas and the studied element, which are excited by a high frequency oscillator inside the inductive coil or the capacitor (capacitive discharge).

Boundary electrode processes in the capacitive discharge are very important because, at certain conditions, the stochastic Fermi process of heating of electrons, which is of a fundamental physical significance, takes place. If the frequency of the electric field is between the ion and electron plasma frequencies, the potential barrier of the boundary of the electrode sheath is modulated with the high amplitude at the frequency of the external field. For conditions of the low temperature diluted plasma, when the velocity of this boundary is comparable to the mean electron velocity, most of the bulk plasma electrons will be reflected from this boundary with an enrichment of their energy, due to the Fermi acceleration. These concept have been confirmed by an anamalous polarization effect detected at the boundary of the electrode sheath for

the low pressure discharges in noble gases. In course of spectropolarimetric studies of the high frequency discharge, polarization spectroscopy enabled to undertake for the first time a remote sensing of the most important structural parameter: the energy deposition into the plasma through the electrode sheath and the alternative electric field strength in the middle of the discharge, maintaining the low temperature plasma[3,8].

Collisions between free atomic particles in ionized media play an important role in the kinetics of polarization. Collisions between isotropically moving particles play purely destructive role, destroying orderings of the angular momenta. In this case an isotropic relaxation of atomic polarization moments takes place. This relaxation is represented by an exponential decay of the polarization moments with different ranks or by different relaxation rates. Experimetaly observable process of the collisional depolarization of the linearly and circularly polarized light, emited by an ensemble, is characterized, in turn, by different rate constants.

For anisotropic velocity distribution of atomic particles, with a preferential direction of collisions, the collisional relaxation of the atomic polarization moments undergoes crucial changes. In this case inelastic collisions play a constructive role by creating an ordering of the angular momenta. Mathematically, it stems from a change of the type of symmetry of interaction from a spherical to an axial one. As a result, a multiexponential temporal decay and a mutual transformation of the polarization moments may take place. Anisotropic collisional relaxation leads to the collisional creation of the quadrupole orientation of the momenta from the nonequilibrium population of atomic and ionic states[9].

In gas discharges with the drift of ions, different probabilities of collisions along the radial ion drift velocity and in the perpendicular directions provide a preferential direction of collisional interaction within a plasma. Such a partial anisotropy of collisional interaction of ions with an isotropic atomic environment is a reason for the anisotropic collisional relaxation within the system of the closely spaced fine structure levels of an energy structure, which is the case for most of the atomic ions. The polarization moments of an ensemble of ions, undergoing anisotropic collisional relaxation are described by the kinetic equation:

$$\frac{d}{dt}\rho_0^k(J,\vec{r}) = \sum_{k_1} \frac{4a^{3/2}}{\sqrt{\pi}} e^{-av^2} \sum_{q,l} (-1)^q \begin{bmatrix} k & k_1 & l \\ 0 & 0 & 0 \end{bmatrix} \begin{bmatrix} k & k_1 & l \\ q & -q & 0 \end{bmatrix} \cdot$$

$$\cdot \int dv\, \tilde{R}_q^{kk_1}(JJ_1v,\vec{r}) v^2 e^{-av^2} \left(\frac{v}{2av_0}\right)^l \left(\frac{1}{v}\frac{d}{dv}\right)^l \frac{sh\ 2avv_0}{2avv_0} \rho_0^{k_1}(J_1,\vec{r})$$

where:

$$a = \frac{m_i m_a}{2k(m_i T_a + m_a T_i)},$$

$m_a, m_i$, $T_a, T_i$ are masses and temperatures of atoms and ions, $\tilde{R}_Q^{kk_1}(JJ_1v)$ is the matrix of the total anisotropic collisional relaxation.

Due to a linkage of momenta with different ranks under the anisotropic collisional relaxation, the drift of ions is accompanied by a creation of the longitudinal alignment from the populations of the fine structure levels with the axis parallel to the drift velocity vector, known as the drift selfalignment. Naturally, this process is only possible if the kinetic energy exceeds the multiplet spliting:

$$m_1 v_1^2/2 > \Delta E.$$

An efficiency of the drift selfalignment is dependent on the degree of anisotropy of motion and on the energy of an ion. The general requirement for the drift selfalignment creation is a deviation of the fine level populations from its equilibrium values. The process of the drift selfalignment is specific by the fact, that the projection of the momentum on the drift axis is conserved, but not the rank of the tensor $k$. This effect has a very high diagnostic significance. Polarization created by anisotropies of the slow collisions of atomic particles reflects internal anisotropies of the studied object, providing a tool for remote sensing of many plasma parameters. Study of the drift selfalignment of ions which was undertaken for the first time on the system of the close multiplets of the noble gase ions, excited in the hollow cathode discharge, allowed to measure the drift velocity of ions and the electric field profile inside the negative glow of the hollow cathode[10].

## SOLAR ATMOSPHERE PLASMA

A special place in a history of the spectropolarimetric sensing is taken by the contineous astrophysical studies of the solar flares, which, according to the present day concept, is a consequence of a liberation of the magnetic free energy in the outer coronal region due to the reconnection of the magnetic field lines. Usually secondary processes, resulting from the energy transformation and transport from the primary corona source of the flare are observed. The non-thermal chromospheric region of a solar flare, where optical emission lines are excited, was studied for a long time. Systematic observations, started in the beginning of 80th revealed the linear polarization of different chromospheric emission lines (hydrogen Balmer $\alpha$[11], $SI$, 1437 $\AA$[12]).

These first observations and the new principle possibilities provided by the linear polarization brought about an idea of the quantitative polarimetric sensing of the conductive flux at the top of the flaring chromospheric layers and, later on, some quantitative estimates for this flux have been obtained[12]. A successive analysis of the spectropolarimetric information enabled to reveal the second energy transport mode associated with accelerated particles. Orientation of the polarization direction was that important parameter, which could distinguish the energy transport modes[13]. Further on spectropolarimetric studies of the solar flares have been connected to the quantitative sensing of the corpuscular modes of the energy transport. Basing on the impulse relaxation creterium, protons were specified as the most probable energy carrier.

The degree of polarization, measured by the ground based observer is expressed as:

$$P = \sqrt{Q^2 + U^2} = \frac{|\tilde{Q}| \cos^2\beta}{1 - \tilde{Q} \sin^2\beta},$$

where $\beta$ is an angle, specifying a geometry of observation, the Stokes parameter $\tilde{Q}$ is determined in the collisional frame of reference with the quantization axis oriented along the velocity vector of the exciting protons:

$$\tilde{Q} = -\frac{3K_2\,\tilde{\rho}^2_0(j)}{2\sqrt{2}K_0\,\tilde{\rho}^0_0(j) - K_2\,\tilde{\rho}^2_0(j)}$$

in terms of the polarization moments $\tilde{\rho}^2_0(j)$ and $\tilde{\rho}^0_0(j)$ computed in the collision frame of reference as well, and the numerical constant

$$K_p = \left\{ \begin{array}{ccc} 1 & 1 & p \\ j & j & j_0 \end{array} \right\},$$

which depends upon the total angular momenta of the spectral transition $j \to j_0$ and the ranks of the polarization moment.

Computations of the polarization moments for $H_\alpha$ and $H_\beta$ hydrogen emission lines have been undertaken for the Born, Glauber and the impact parameter method approximations as functions of energy of the exciting proton beam[5]. Comparisons with the data of observations of the hydrogen line polarization during different solar flare events[15], allowed to estimate the energy of protons bombarding the upper opticaly active location of the solar chromosphere.

## CHARGE EXCHANGE

It is safe to say, that a significant part of the impact polarization phenomena of the opticaly active entities in the solar and terrestrial atmospheres, in which jets and swarms of the charged particles is the dominant energy transport mode, are created by the charge exchange collisions. Charge exchange process seems to be extremely important not only for various astrophysical or geophysical emissions, but also as a diagnostic tool for the hot plasmas. There exist a developed intensity spectroscopy technique for sensing of the local parameters and special laboratory installations, based on the beam-hot plasma interaction[16,17]. In this case, using the same technical means, the polarization spectroscopy could bring many principaly new data.

An ordering of momenta of colliding particles under the charge exchange process is described by the following equations:

$$A + B^{q+} \to A^{s+} + B^{(q-s)+}$$

An ion $B$ colliding with an atom $A$, captures one or several electrons of the last, changing its electric charge. A description of the multielectron charge exchange process is connected to considerable computational difficulties, typical for the two center multielectron problems, so we shall restrict ourselfs only to analysis of the one electron charge exchange process ($s = 1$).

In order to compute the cross sections of the collisional ordering of momenta of the excited states of the ensemble of the recharged ions $B^{(Z_b-1)+}$ a very effective pseudolevel method[18] could be exploited. The idea of this method is that the wave function of the electron in the field of two centers is constructed in a form of an expansion in terms of the full system of functions of $B^{(Z_b-1)+}$ ion, or $\psi_m(\vec{r}_b)$, as follows:

$$\Psi(\vec{r}_b\, t) = \sum_m C_m(t)\, \psi_m(\vec{r}_b)\, exp(i\varepsilon_m^{(b)} t)$$

where $m$ is the set of quantum numbers, specifying the state of the ion $B^{(Z_b-1)+}$, $\vec{r}$ and $\vec{R}$ are vectors, specifying coordinates of the electron, the atomic partice and $\varepsilon_m^{(b)} = E_m^{(b)}/\hbar$.

Under $t \to -\infty$ this function should be transformed into the wave function of the electron on the center $A$:

$$\psi_a(\vec{r}_a) exp(-i\frac{E_0^{(a)} t}{\hbar})$$

A consequence of this condition is the following assymptotic behavior of the coefficients:

$$C_m(t)\,|_{t\to-\infty} \sim\ exp(-i\omega_m t)\, S_m(t)$$

where

$$S_m(t) = \int d\vec{r}\, \psi_m(\vec{r} + \frac{m_a}{m_a+m_b}\vec{R})\, exp[im\frac{(\vec{v},\vec{r})}{\hbar}]\, \psi_a(\vec{r} - \frac{m_b}{m_a+m_b}\vec{R}),$$

$$\omega_m = \varepsilon_m^{(b)} - \frac{E_0^{(a)}}{\hbar}$$

and $E_0^{(a)}$ is the total energy of the electron on the center $A$, including the kinetic energy, associated with the relative motion $A-B$.

Selecting a particular state with $m = n$, an expression for the wave function will take the following form:

$$\Psi(\vec{r}_b, t) = \sum_{m\neq n} C_m(t)\, \psi_m(\vec{r}_b)\, exp(-i\varepsilon_m^{(b)} t) + C_n(t)\, \psi_n(\vec{r}_b)\, exp(-i\varepsilon_n^{(b)} t)$$

Representing the first term of this expression as a product

$$b_n(t)\, \phi_n(\vec{r}_b, \vec{R})\, exp(-\varepsilon_a t),$$

$$\langle \phi_n \mid \phi_n \rangle = 1,$$

we have:

$$\Psi(\vec{r}_b, t) = b_n(t)\phi_n(\vec{r}_b, \vec{R}) exp(-i\varepsilon_a t)\ +\ C_n(t)\psi_n(\vec{r}_b) exp(-i\varepsilon_n^{(b)} t)$$

It means, that the multilevel charge exchange problem is reduced to a two level one, including the real level $\mid n\rangle$ with the wave function $\psi_n(\vec{r}_b)$ and the pseudolevel

with the wave function $\phi_n(\vec{r}_b, \vec{R})$. The last, as it follows from the previous relations, should satisfy the following conditions:

$$C_m \, exp(-i\varepsilon_m^{(b)} t) \; = \; b_n \langle \psi_m \mid \phi_n \rangle exp(-i\varepsilon_a t), \quad m \neq n$$

$$b_n \langle \psi_n \mid \phi_n \rangle = 0$$

$$\langle \phi_n \mid \phi_n \rangle = 1$$

Seeking the function $\phi_n(\vec{r}_b, \vec{R})$ as a linear combination of $\psi_a(\vec{r}_a) = \psi_a(\vec{R} - \vec{r}_b)$ and $\psi_n(\vec{r}_b)$, as follows from the results of [18], the coefficients of this linear combination could be determined from the last two equations. Within an accuracy of a phase factor, one has:

$$\phi_n(\vec{r}_b, \vec{R}) = \frac{\psi_a(\vec{r}_a) - S_n \, \psi_n(\vec{r}_b)}{\sqrt{1 - \mid S_n \mid^2}}$$

whereas the relation between $C_m$ and $b_n$ is determined by:

$$C_m(t) = \frac{b_n(t) \, S_m(t) \, exp(i\omega_m t)}{\sqrt{1 - \mid S_n \mid^2}}, \quad m \neq n.$$

Computations of the polarization effects under the charge exchange reactions of the highly charged ions of noble gases in beams, using this technique, have been made in comparison to observations of the spectropolarimetric effects on many spectral lines of the recharged ions[19–21].

## REFERENCES


1. Fujimoto T and Kazantsev S A 1997 Plasma Phys. Control. Fusion 39, 1267

2. Fujimoto T, Sahara H, Csanak G and Grabbe S 1996 Atomic States and Collision Relaxation in Plasma Polarization Spectroscopy: Axially Symmetric Case (NIFS-DATA-38, Institute for Fusion Science, Nagoya)

3. Kazantsev S A and Hénoux J-C 1995 Polarization Spectroscopy of Ionized Gases. KLUWER Academic Publishers Dordrecht, Boston, London

4. Kazantsev S A, Polynovskaya N Ya, Piatnitsky L N and Edelman S A 1988 Sov. Phys. Uspekhi 31, 785

5. Kazantsev S A, Petrashen A G and Firstova N M 1998 Impact Spectropolarimetric Sensing. PLENUM Press, New York London

6. Kazantsev S A 1983 Sov. Phys. Uspekhi 26, 328

7. Kazantsev S A 1983 JETP Lett. 37, 159

8. Kazantsev S A, Khutorshchikov V I, Guthohrlein G and Windholz L 1998 Practical Spectroscopy of High Frequency Discharges. PLENUM Press, New York London

9. Kazantsev S A, Polezhaeva N T and Rebane V N 1985 Opt. Spectrosc. 63, 15

10. Kazantsev S A, Petrashen A G, Rebane V N, Rebane T K, Funtov V N, Neureiter Ch and Windholz L 1995 Phys. Scr. 52, 572

11. Hénoux J-C and M.Semel 1981 Proceedings of Solar Maximum Year Workshop, eds Obridko V N and Ivanov E V IZMIRAN 1, 207

12. Hénoux J-C, Herischi D, Chambe G, Machado M, Woodgate B, Shine R and Bakers J 1983 Astron. Astrophys. 119, 233

13. Hénoux J-C and Chambe G, JQSRT 44, 193 (1990)

14. Kazantsev S A and Petrashen A G 1994 Opt. Spectrosc. 77, 898

15. Bulatov V A, Firstova N M, Hénoux J-C and Kazantsev S A 1997 Solar Phys. 171, 123

16. Groebner R J, Brooks N H, Burrell K H and Rotter L 1983 Appl. Phys. Lett. 43, 920

17. Ida K and Hidekuma S 1989 Rev. Sci. Instr. 60, 867

18. Sobelman I I, Vainstein L A and Yukov E A 1995 Excitation of atoms and Broadening of Spectral Lines. SPRINGER, Berlin, Heidelberg, New York and
Vainstein L A, Sobelman I I and Yukov E A 1978 Excitation of Atoms and Spectral Line Broadening (In Russian) NAUKA, Moscow

19. Chantepie M, Jacquet E, Laulhe S, Kazantsev S A and Petrashen A G 1996 Opt. Spectrosc. (USA) 81, 30

20. Chantepie M, Jacquet E, Laulhe S, Kazantsev S A and Petrashen A G 1996 Opt. Spectrosc. (USA) 81, 164

21. Chantepie M, Jacquet E, Laulhe S, Kazantsev S A and Petrashen A G 1997 Opt. Spectrosc. (USA) 83, 201.

# *The Bragg – Polarimeter at TEXTOR 94*

O.Herzog*, G.Bertschinger**, M.Bitter***, J.Weinheimer*, A.Urnov****, F.B.Rosmej*, H.-J.Kunze*

* Institut für Experimentalphysik V, Ruhr-Universität – Bochum, Germany

** Institut für Plasmaphysik, Forschungszentrum Jülich GmbH, Germany

*** Institute of Plasmaphysics (PPPL), Princeton, USA

**** Lebedev Institute of Theoretical Physics, Moscow, Russia

## 1.) Instrumentation

At the tokamak TEXTOR 94 a Bragg-polarimeter has been installed. It consists of two x-ray crystal spectrometers in Johann-geometry which are orientated perpendicular to each other. One system is in the horizontal plane of the tokamak with a bending radius of $R_c$=3780 mm, the other system is orientated vertically with respect to the toroidal axis of the tokamak and has a bending radius of $R_c$=4620mm. The technical realisation is shown in figure 1. Both spectrometers are high resolution instruments. The resolution of the horizontal system is $\lambda/\Delta\lambda$=7200 and that of the vertical system $\lambda/\Delta\lambda$=8900. At present two quartz (110)-crystals with 2d=4.9130 Å are used. The detectors are one-dimensional multiwire-proportional-counters with $Kr/CO_2$ as the detector gas. The whole system is a vacuum system.

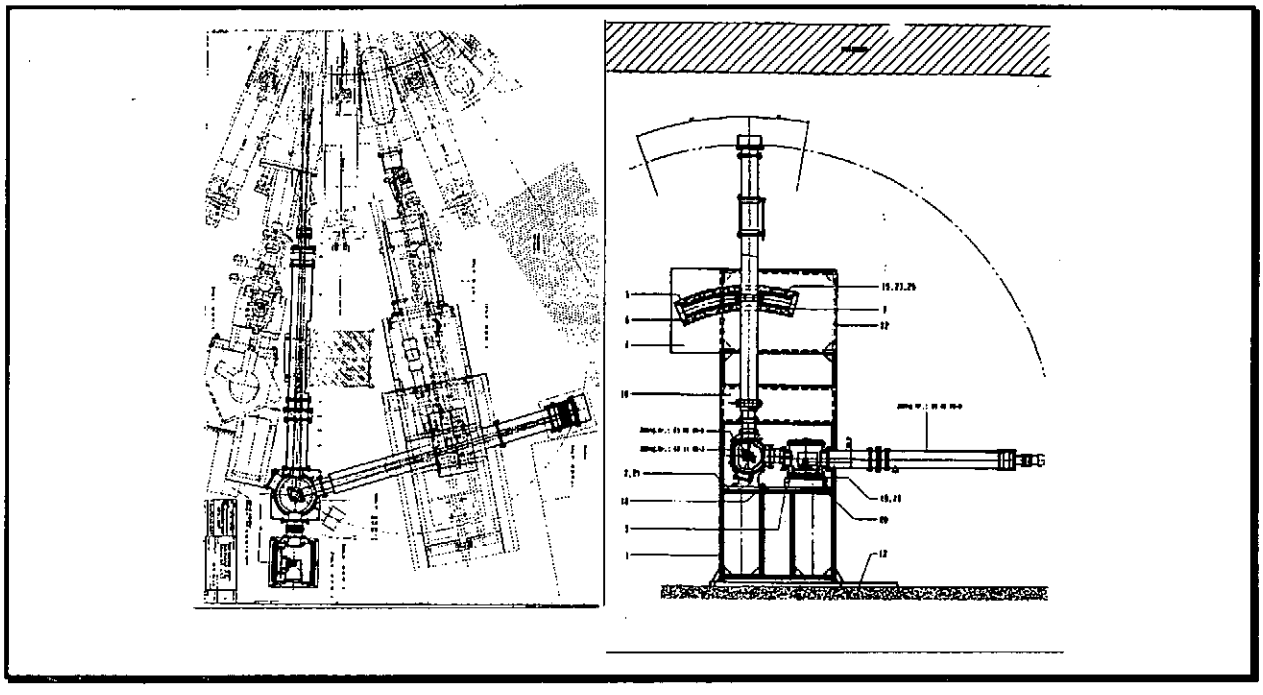

***Figure1:*** *Experimental setup of the Bragg – polarimeter at TEXTOR 94, horizontal plane (left) and vertical plane (right).*

The impurity studied here is argon. The spectral range presently covered is between the resonance line W ($\lambda$ = 3.9494 Å) and the forbidden line Z ($\lambda$ = 3.9944 Å) of [He]-like argon. A typical spectrum is shown in figure 2. Other typical spectroscopic features are the well resolved n=2-dielectronic satellites (r,a,k), the innershell excited satellite q, both intercombination lines (x,y), and not-resolved higher order n=3,n=4,...-dielectronic satellites.

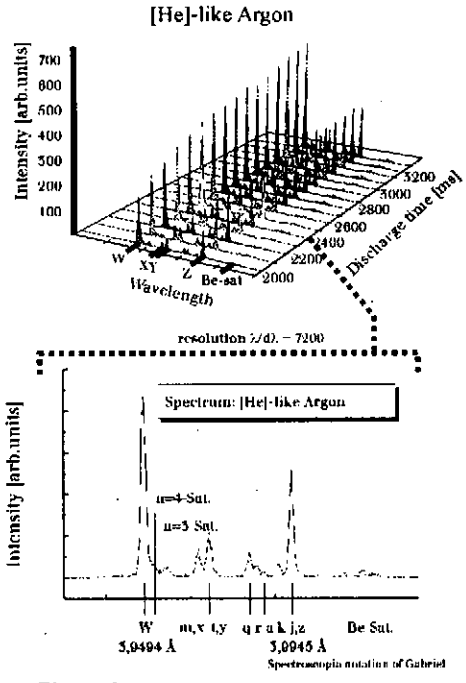


Figure 2

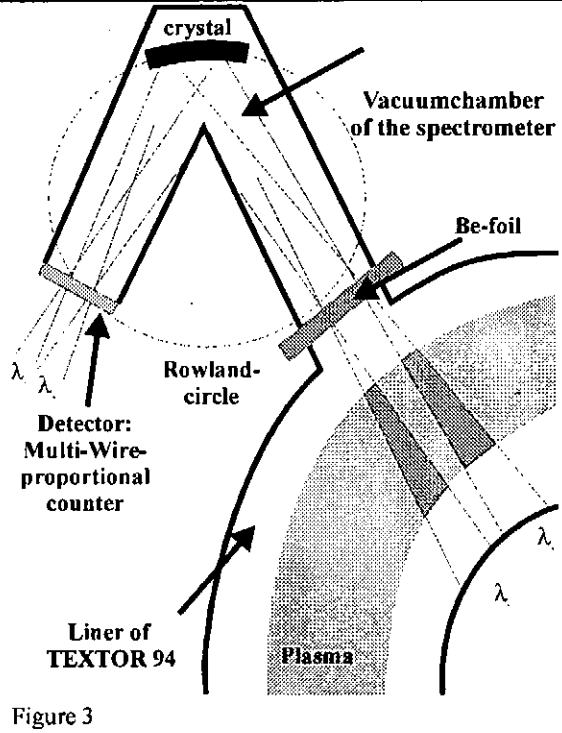


Figure 3

***Figure 2 (left):*** *Spectrum of [He]-like argon. The integrated time is $\Delta t$ = 100ms.*

***Figure 3 (right):*** *The geometry of a Johann type x-ray spectrometer at a tokamak.*

## 2.) Emissivity profiles

A x-ray spectrometer in typical Johann-geometry setup at a large plasma like that of a tokamak is shown in figure 3. For every wavelength Bragg angle $\vartheta$ (determined by Bragg's law: $2d\sin\vartheta=n\lambda$) and bent crystal define a solid angle, within the specific radiation is collected from the plasma and focused at one position on the Rowland-circle. Thus with a position sensitive detector like the multiwire-proportionalcounter, the respective spectrum can be detected.

It is evident from figure 3 that for each wavelength the plasma volume, from which the radiation is collected, is somewhat different. In the horizontal system the difference between the line of sight of the W-line and thatof the Z-line is 47 mm, and in the vertical system it is

55 mm. Thus it is crucial that the plasma is homogeneous, if line ratios are considered. They usually are used to derive the electron temperature. Here we used line ratios to determine line polarisation.

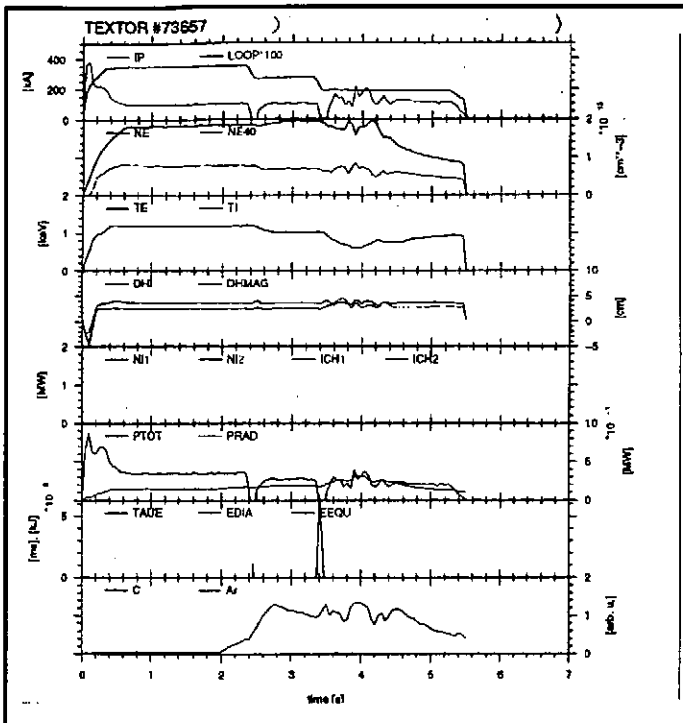


Figure 4

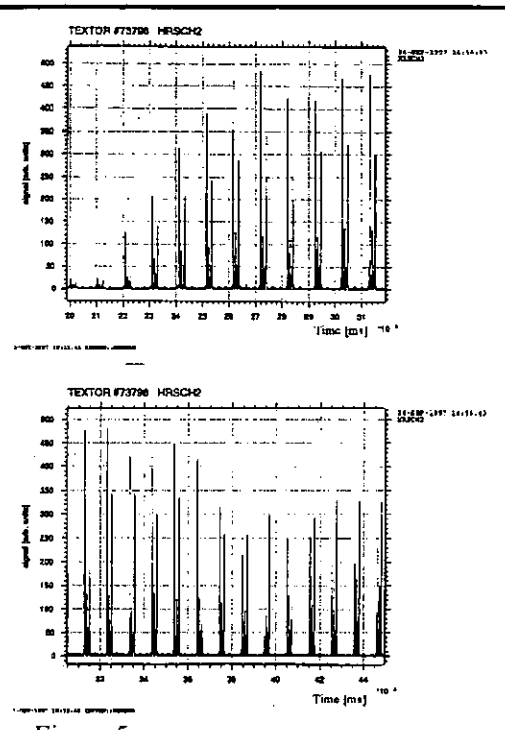


Figure 5

***Figure 4:*** *Parameter of an ohmic discharge with three current steps.*

***Figure 5 :*** *Spectra from this discharge with a time integration of 100 ms. The line ratios are shown in an early phase of the discharge (high current, high temperature) and in a later phase (lower current and lower temperature). In the second case (lower picture) the line ratios show unexpected values.*

In the horizontal system the homogeneity requirement poses no problem, because of the toroidal symmetry of the tokamak; however in the vertical system this indeed can be a problem. For an ohmic discharge the parameters are presented in figure 4 with three different phases during the discharge. Spectra from this discharge are shown in figure 5 for the vertical system. It is evident that in the beginning the line ratios are as expected but at the end of the discharge they change dramatically. This effect can be explained when the emissivity profiles of [He]-like argon are considered for these conditions. The emissivity is $I = n_e(r) \cdot n_{[He]}(r) \cdot \langle \sigma v \rangle(r)$ and thus it is determined by the temperature and density profiles of

TEXTOR 94 under the conditions of the discharge. The emissivity profiles were calculated and are shown in figure 6 for W and Z.

Especially in the last case the emissivity profile is very small (FWHM = 49 mm), and if the plasma moves a few cm in the vertical direction, radiation of the W- and Z-line is collected from different plasma regions resulting in a wrong intensity ratio. For the investigations of line polarisation it is crucial, therefore, that the described effect does not occur.

## 3.) Measurement of polarisation

For the investigation of line polarisation we used the discharge of figure 7 which is characterized by three current steps. To change the current, the loop voltage has to be changed and so electrons and ions are accelerated in toroidal direction. During the time of change the toroidal electric field produces an electron beam which excites different lines differently resulting in polarised emission.

Measurements are done with two crystals which are orientated perpendicular to each other. The reflectivity of the crystal is given by:

$$R(a) = \frac{I'(a)}{I(a)} = C(\lambda_a)\left[1 - \frac{\sin^2(2\theta_i)}{2}(1 - P(a)\cos(2\phi(a)\right]$$

The geometry is shown in figure 8. I(a) and I'(a) are the line intensities for the incoming and outcoming radiation fluxes; $C(\lambda_a)$ is a factor of the crystal. The reflectivity thus depends on the polarisation P(a) of the line. The best way to detect polarisation is to use the double ratio, i.e. the ratio of the ratio of lines from the vertical and the horizontal system. For linearly polarised lines the Stokes parameter $\xi_3$ determines the polarisation as $P=|\xi_3|$. The double line ratio depends on this parameter as:

$$\chi(a/b) = \frac{I'(a/b)}{I(a/b)} = \frac{R'(a/b)}{R(a/b)} = C'(a/b)\left[\frac{1 - K\xi_3(a)\cos(2\phi)}{1 - K\xi_3(b)\cos(2\phi)}\right]$$

K is a factor of geometry, and the double ratio $\chi$ is a function of line polarisation. Results of the discharge are shown in figure 9. During the current steps the line ratio has a higher or lower value than in the constant current phases. In the beginning of the discharge the effect is high because during this time argon is puffed. After 4 s the amount of argon is low. So the error bars become high and the effect is not as well seen as in the early phase of the discharge. Polarisation of the lines between 8,4% and 9,5% is measured.

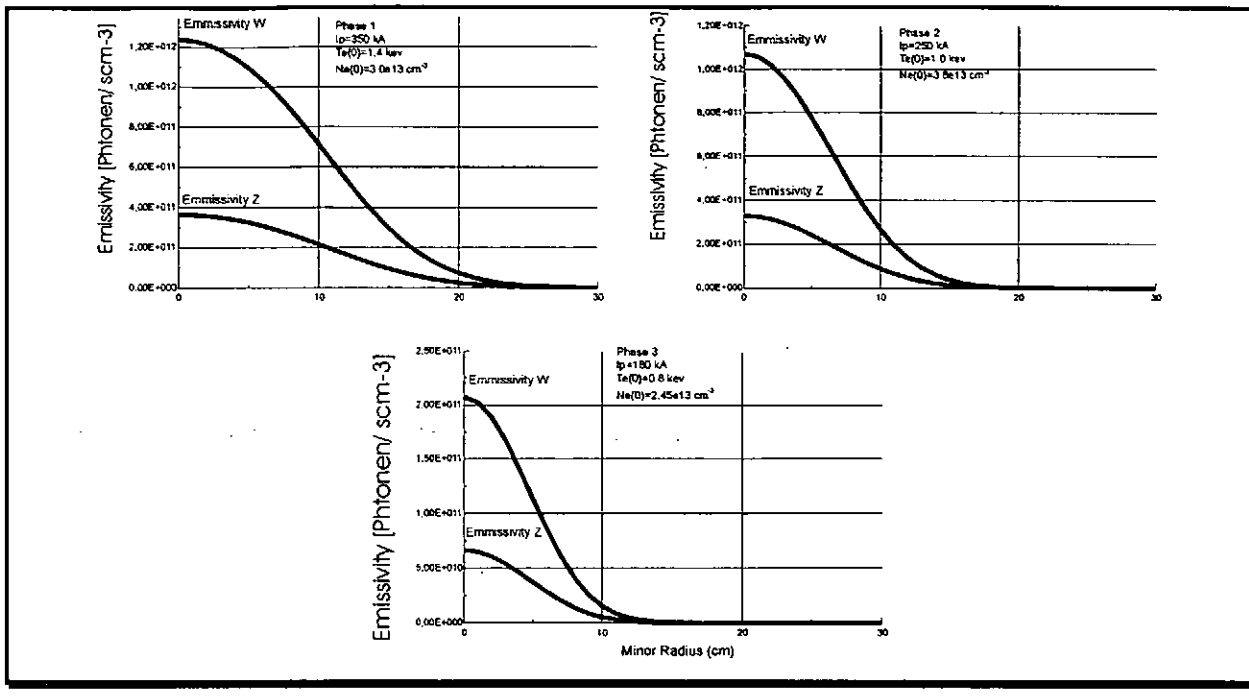


***Figure 6**: Calculated profiles of the emissivity of W and Z in the three current steps of the ohmic discharge #73796.*

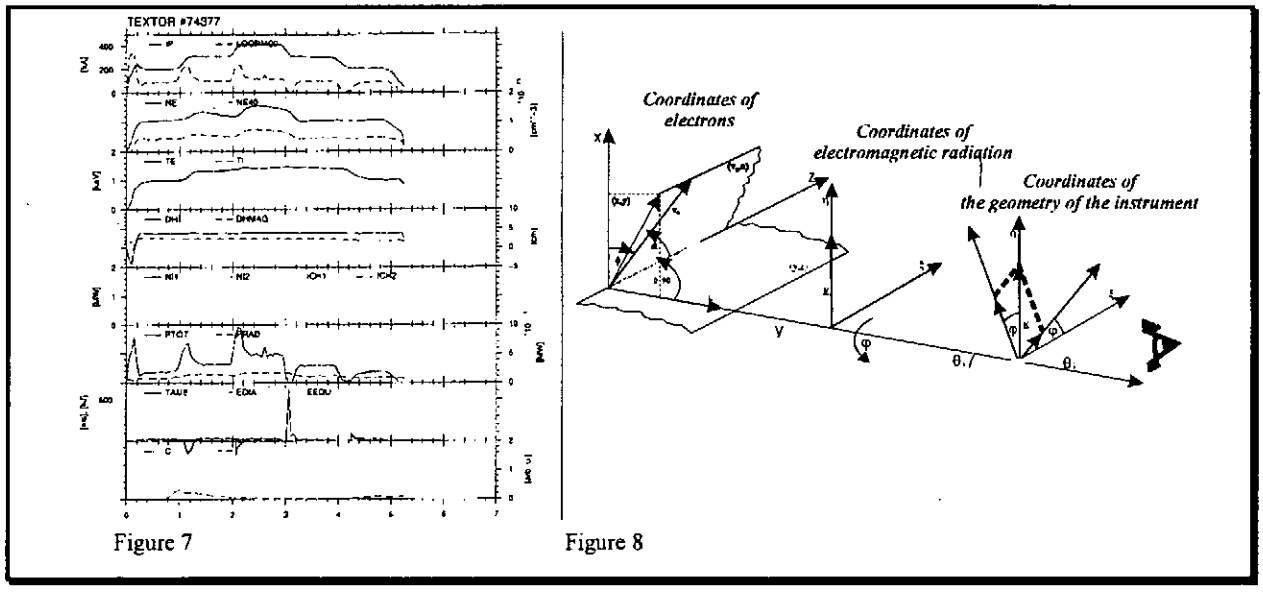


Figure 7 Figure 8

***Figure 7 (left)**: The parameters of an ohmic discharge for the investigation of polarisation.*

***Figure 8 (right)**: The geometry for the calculation of polarisation.*

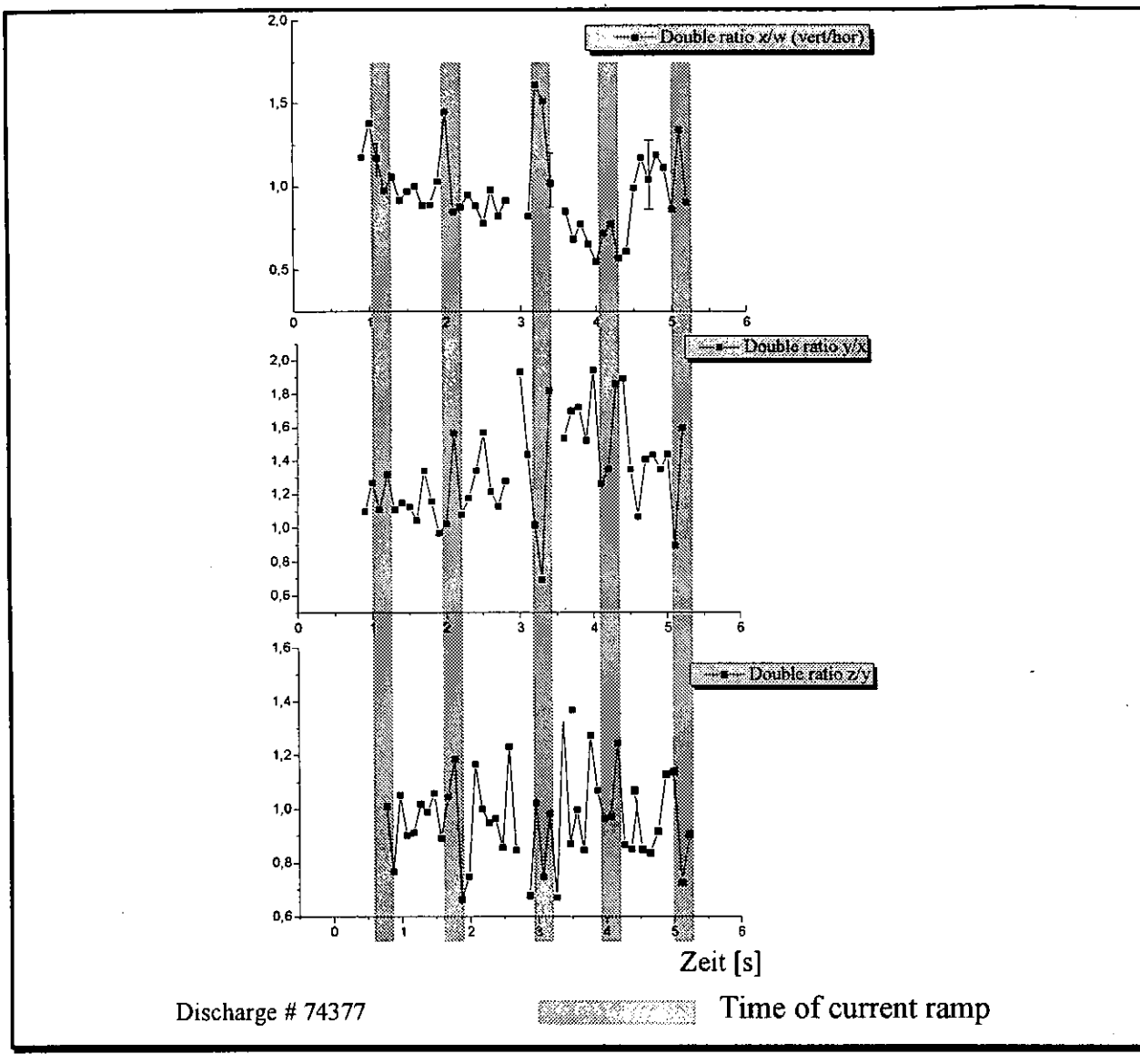


***Figure 8:*** *Double line ratio (vertical/horizontal). This value is a function of polarisation of the lines of the ratio.*

## 4.Conclusions and outlook

In TEXTOR 94 line polarisation was measured which shows that during current steps in ohmic discharges non-thermal electrons exist. The density and the energy have to be calculated by theoretical models. A systematical analysis especially for discharges with other heating scenarios like neutral beam heating, ion cyclotron heating or combinations of both is very important and will be done.

# Plasma polarization spectroscopy on the WT-3 tokamak

Takeo Furukubo and Takashi Fujimoto
*Department of Engineering Physics and Mechanics, Graduate School of Engineering*
*Kyoto University, Kyoto 606-8501, Japan*

By placing a calcite plate behind the entrance slit of the spectrometer we obtain polarization resolved spectra of impurity emission lines. We have obtained the intensity and the polarization degree (the longitudinal alignment) of the berylliumlike oxygen triplet lines. In a kinetic model, or the PACR model, the population and the alignment of the upper levels of these transitions are calculated for electrons with an anisotropic velocity distribution, and the result is compared with the experiment. We thus infer the distribution function of electrons in the velocity space to be of a "cigar" shape in our example.

## 1. Introduction

Plasma Polarization Spectroscopy (PPS) is a novel diagnostic technique which can give us structural information of a plasma, *e.g.*, anisotropy of the distribution function of electrons in the velocity space. This method has been applied to discharge plasmas and solar plasmas for some years.[1] The first application of PPS to a tokamak plasma was reported recently by our group,[2] in which polarization was detected in the heliumlike carbon lines and the berylliumlike oxygen lines. A kinetic model which relates the polarization characteristics to the electron velocity distribution function has been developed and named the population-alignment collisional-radiative (PACR) model.[3]

In the following, we present our recent experiment and its interpretation by a PACR model calculation.

## 2. Experiment

The WT-3 tokamak has the major radius of 0.65 m and the minor radius of 0.25 m. The electron *temperature* in the joule heating mode is estimated from ECE to be 100 - 300 eV, and the density is given from the CN laser interferometry to be typically 3 x $10^{18}$ $m^{-3}$. We observe the plasma with a uv-visible monochromator of the focal length of 1 m. Figure 1 shows the arrangement for separation of the two polarized components: a horizon-

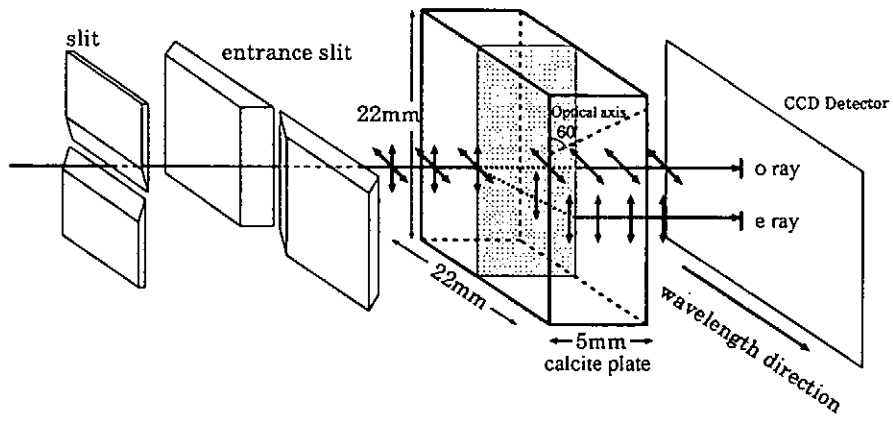


Fig. 1. Geometry of resolving polarization in spectometer.

tal slit in front of the vertical entrance slit of the monochromator tailors the image of the plasma to a 0.5 mm width, and this image goes through the entrance slit. The optical axis of the 5 mm thick calcite plate is at 30 degrees with respect the surface normal, and is directed upward. The o-ray, the $\pi$ light in our geometry, is transmitted without deflection, and the e-ray, the $\sigma$ light, is displaced owing to the anomalous refraction by 0.6 mm, parallel to the $\pi$ light. These light rays are dispersed by the grating and focused on the CCD detector. Thus, a pair of the spectra, one for the $\pi$ light and another for the $\sigma$ light, are obtained on the detector surface. The detector is operated in the kinetic mode: the spectra are recorded on the upper-most part of the detector, and the signal is accumulated, say over 10 ms in our case. After the accumulation, the charge is transferred downward to the adjacent area within a couple of microseconds. We repeat this procedure over the discharge period of 100 ms. We thus obtain a time sequence of the polarization resolved

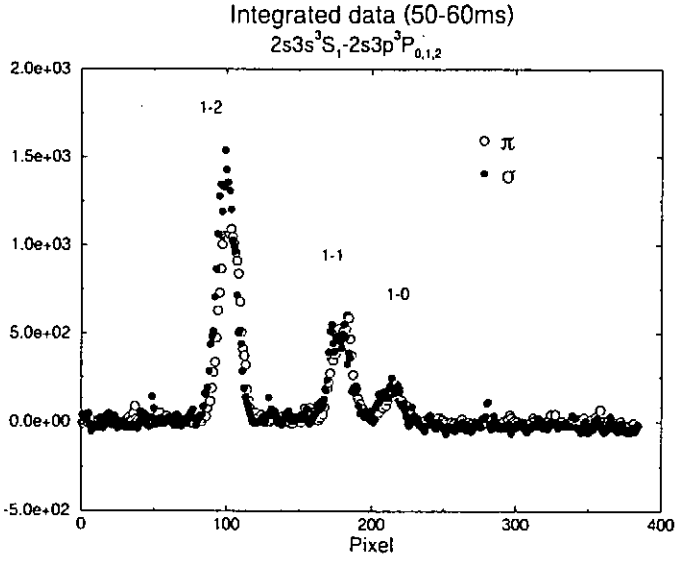


Fig. 2
Polarization resolved spectrum of berylliumlike oxygen lines for JH mode plasma.

spectra stored on the full area of the CCD detector. We collect the signals and obtain the results like Fig. 2. In this picture, the triplet lines of berylliumlike oxygen $3s^3S_1$ - $3p^3P_{0,1,2}$ are seen. The intensity ratio is approximately proportional to the statistical weight of the upper level, 1:3:5. See below for further details. It is obvious that the strongest line ($J$=1 ← $J$=2) is polarized.

The *intensity* that is proportional to the upper-level population is given in our case by $I = I_\pi + 2I_\sigma$, where $I_\pi$ and $I_\sigma$ are the intensities of the $\pi$ light and the $\sigma$ light, respectively. If the upper-levels of these three lines were populated according to the statistical weights, the relative intensities of the stronger lines with respect to the weakest line would be 3 and 5, as noted above. Figure 3 shows the result. Deviation is seen.

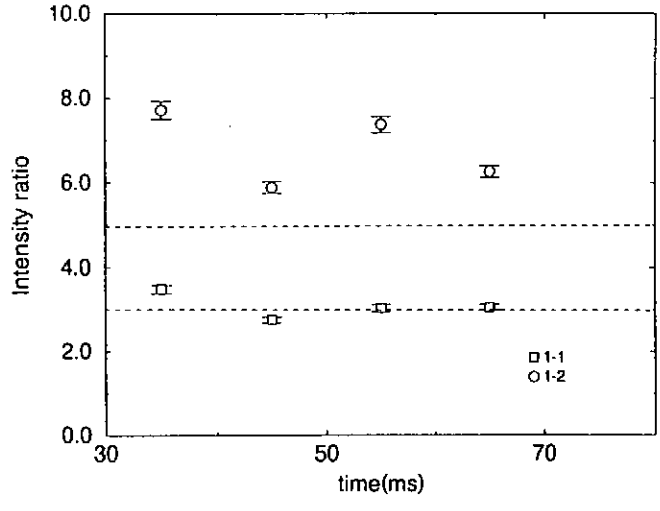


Fig. 3
Relative intensities of the stronger lines to the weakest line. Statistical populations would give values 3 and 5.

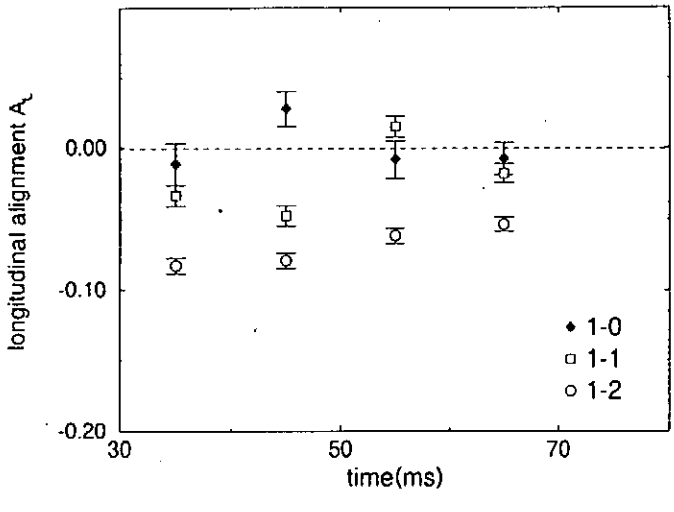


Fig. 4
The longitudinal alignment of the three lines. The weakest line, $J$ = 1 ← $J$ = 0, is never polarized.

Figure 4 shows the result of the longitudinal alignment, $A_L = (I_\pi - I_\sigma)/(I_\pi + 2I_\sigma)$. This figure includes the results for the weakest $J$=1 ← $J$=0 transition, which is never polarized.

Within the experimental uncertainty, our result is consistent with the absence of polarization. Other lines can be polarized, and the strongest line, $J$=1 ← $J$=2, is substantially polarized.

### 3. PACR calculation and comparison with experiment

For the velocity distribution of electrons, we assume a distribution function which is expressed by different temperatures in the troidal direction, $T_t$, and the poloidal direction, $T_p$. In the following calculation we assume 100 eV for $T_t$ in the case of $\alpha = T_p/T_t$ smaller than 1 and for $T_p$ for $\alpha$ larger than 1. The angular distribution function in the velocity space is expanded in terms of Legendre polynomials, and the expansion coefficients of even moments are given as functions of speed of electrons.

To each excited level two quantities are assigned, that is, the population and the alignment. For transitions between $2s^2\,{}^3S_1$, $2s2p\,{}^3P_{0,1,2}$ and $2s3p\,{}^3P_{0,1,2}$, Csanak and Grabbe[4] calculated the excitation cross sections between each of their magnetic sublevels. We combine these cross sections by the Clebsh-Gordan coefficients to obtain cross sections between these levels for transition of population-to-population, population-to-alignment, alignment-to-population and alignment-to-alignment. It is noted that the first cross section is nothing but the conventional excitation cross section or the deexcitation cross section. For transitions between other levels we adopt the recommended cross section by Kato *et al.* [5] as the cross section for population-to-population.

By combining the expansion coefficients and the relevant cross sections, we obtain transition rate coefficients to be used in the PACR model. We thus construct two sets of rate equations; one for the populations in the ground state and the excited levels and another for the alignments in the excited levels. We solve these equations by the method of quasi-

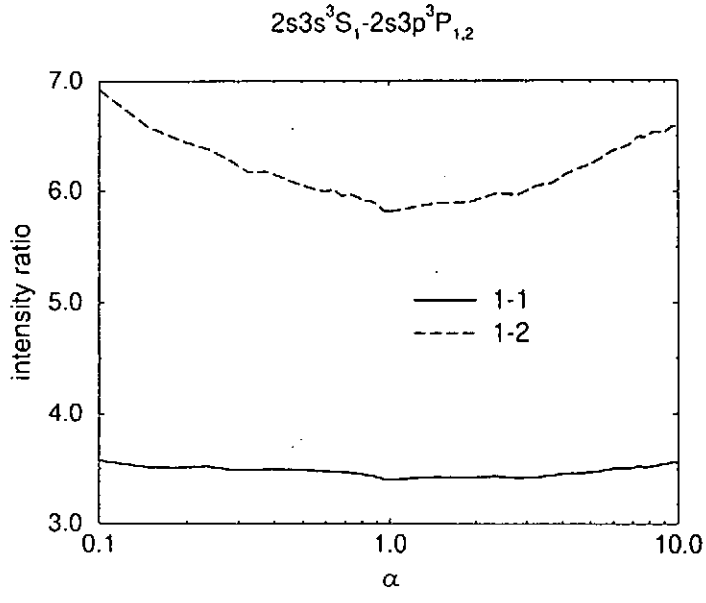


Fig. 5
The relative intensities corresponding to Fig. 3. $\alpha = T_p/T_t$.

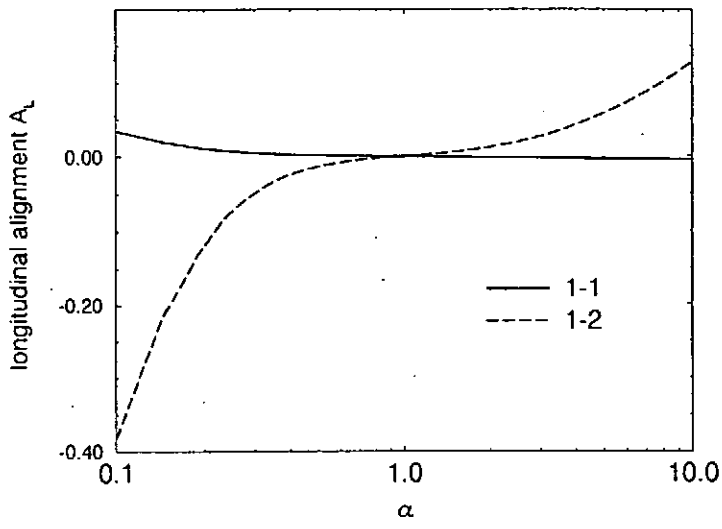


Fig. 6
The longitudinal alignment corresponding to Fig. 4.

steady-state solution in the framework of the ionizing plasma. Figure 5 and 6 show an example of the results to be compared with experiment; Figure 5 is for the intensity ratio or the population ratio corresponding to Fig. 3, and Fig. 6 is for the longitudinal alignment corresponding to Fig. 4.

If all of our assumptions above were correct, we should be able to obtain good agreement for a set of four quantities, *i.e.*, the two intensity ratios and the two alignments, by adjusting $\alpha$. For the majority of the data, however, we can fit only one or two quantities, the longitudinal alignment. We may thus only suggest that our distribution function is rather close to a cigar shape with $\alpha = 0.3$. At present, there remain substantial inconsistencies between the experiment and the calculation. One of the origins of the inconsistencies would be our too simple assumption of the "shape" of the velocity distribution function.

**references**

[1] S.A. Kazantsev and J.-C. Hénoux, *Polarization Spectroscopy of Ionized Gases* (Dortrecht: Kluwer, 1995).

[2] T. Fujimoto *et al.*, Phys. Rev. E **54**, R2240 (1996).

[3] T. Fujimoto and S.A. Kazantsev, Plasma Phys. Control. Fusion **39**, 1269 (1997).

[4] G. Csanak and S. Grabbe, (private communication).

[5] T. Kato, J. Lang and K.E. Berrington, NIFS-DATA-2 (Institute for Fusion Science, Nagoya, 1990).

# MSE Spectroscopy in CHS Heliotron/Torsatron

K.Ida, S.Takayama†, S.Kado, S.Hattori

National Institute for Fusion Science, 322-6, Oroshi-cho, Toki, 509-52 Japan
†Department of Fusion Science, The Graduate University for Advance Studies,
322-6 Oroshi-cho, Toki, 509-52 Japan

Abstract

The $H_\alpha$ spectrum with Motional Stark Effect (MSE) emitted from the fast hydrogen ion of a neutral beam is measured with polarization sensitive spectrometer in a CHS Heliotron/Torsatron.The measured MSE spectra is compared with the calculation. Application of MSE measurements to estimate the pitch angle of local magnetic field is demonstrated.

## 1. MSE spectroscopy

$H_\alpha$ lines emitted from the high energy atomic hydrogen beam injected into a magnetically confined plasma have a polarization due to the Motional Stark Effect. A strong Lorentz field, $E = v_b \times B$, ( $v_b$ : neutral beam velocity B : magnetic field in the plasma) observed in the reference frame of the beam particle produces splitting and polarization of line emissions via the Stark effect. When observed in the direction perpendicular to the electric field, the Stark $\sigma$ and $\pi$ component are linearly polarized, respectively perpendicular and parallel to the direction of the Lorentz field. The magnetic field in the magnetically confined plasma has two component; one is toroidal magnetic field $B_t$ and the other is poloidal magnetic field $B_p$. The pitch angle of magnetic field is defined as $\tan^{-1}(B_p/B_t)$. The MSE spectroscopy has been useful tool to measure the pitch angle in magnetic confined plasmas[1-6] The spectral intensity through the optics transmitting at $\phi$ degree with respect to the mid-plane at the wavelength $\lambda$ is expressed as

$$I(\phi,\lambda) = I_{\pi l}(\lambda)\cos^2(\alpha_\pi-\phi) + I_{\sigma l}(l)\cos^2(\alpha_\sigma-\phi) + \frac{1}{2} I_{\sigma c}(\lambda) \qquad (1)$$

where $\alpha_\pi=\alpha_\sigma+90$, $I_{\pi l}(\lambda)$ and $I_{\sigma l}(\lambda)$ are the linearly polarized $\pi$ component and the $\sigma$ component, respectively, $I_{\sigma c}(\lambda)$ is the circularly polarized $\sigma$ component. The polarization angle of the $\pi$ component $\alpha_\sigma$ is given by

$$\tan(2\alpha_\sigma) = \frac{(I(135,\lambda)-I(45,\lambda))}{(I(90,\lambda)-I(0,\lambda))} \qquad (2)$$

The pitch angle $\gamma$ is derived from the polarization angle of $\alpha_\sigma$ or $\alpha_\pi$ as

$$\tan\gamma = \frac{\tan\alpha_\sigma}{\cos\beta} = \frac{\cot\alpha_\pi}{\cos\beta} \qquad (3)$$

where $\beta$ is the intersection angle of the atomic hydrogen beam line and the sightline of fan array of optical fiber.The $\beta$ should be small enough (Doppler shift is large enough) to separate $H_\alpha$ emission of beam from background $H_\alpha$ and not be too small to achieve reasonable spatial resolution, the

integration along sightline within the beam width determines the spatial resolution. The intersection angle β is between 15.5 and 58.6 degrees in the experiment described here.

## 2. Polarization sensitive spectroscopy

Figure 1 shows a schematic view of the experimental arrangement of the MSE spectroscopy. The diagnostic neutral beam (DNB) is injected into the Compact Helical System (CHS) heliotron/torsatron devices almost perpendicularly in order to minimize the integration along the toroidal angle, where the poloidal magnetic field changes its sign every 22.5 degrees. The accelerated energy and extracted current of the injected hydrogen neutral beam are 45 keV and 3.7 A, respectively. The beam divergence angle is 0.65 degrees. The optical system consists of two sets of optics, each of them consisting of a polarizer and a ferroelectric liquid crystal (FLC) cell (Fig.1(b)). The FLC cell functions as switchable half-wave retarder. The retardation of the FLC is fixed to be -λ/2 but the axes can be rotated by 45 degree by applying voltage with respect to the transmission axis of the polarizer. By using two sets of the FLC, the spectral intensity having polarization angles of 0, 45, 90 and 135 degrees with respect to the mid-plane can be measured. Each set of optics has a 24 optical fiber-array viewing the plasma from R=0.72 to 1.13m along the beam line. Sightlines of the fiber-arrays are oriented with viewing angle 37.05±21.55 degrees with respect to the direction of the beam to yield enough Dopper shift and spatial resolution. The typical spatial resolution of each optical fiber is about 12 mm in the horizontally elongated poloidal cross section. The light from the fibers are simultaneously led to the entrance slit of the 0.5m spectrometer and the spectra for each fiber are detected with a two-dimensional (384 X 576 pixel) cooled charge-coupled device (CCD) detector system at the exit slit of the spectrometer. A 2160 line/mm grating is used and the wavelength resolution of the spectrometer is 1.7nm in the wavelength region of interest.

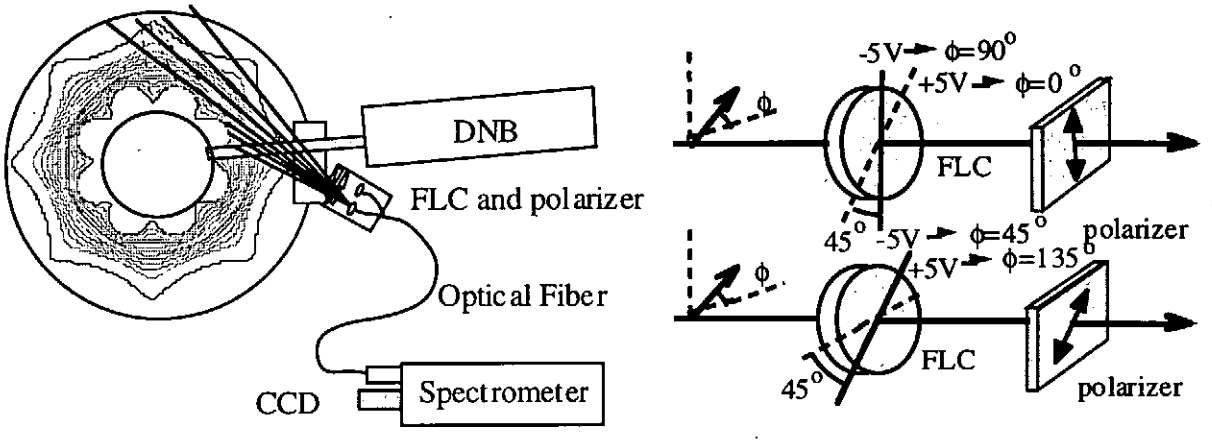


Fig.1 The experimental setup for $H_\alpha$ spectra measurements with the polarization sensitive spectroscopy.

## 3 Measurements of MSE spectra

The MSE spectrum are measured with polarization sensitive spectroscopy in CHS plasma with a magnetic field of 0.8 T. Figure 2 shows the spectra of σ and π component of $H_\alpha$ spectrum with Motional Stark Effect measured by inserting a linear polarizer in front of the object lens and tilting the effective polarizer angle by 90 degrees by applying +5 V for the major radius of 93.3cm, where the pitch angle is almost zero. The three peaks of correspond to the mission from atomic hydrogen beam with the full energy, the half energy and one-third energy beam components. The

solid lines are the calculated MSE spectrum using vacuum magnetic field with taking account of beam divergence, beam steering angle, integration effect along the sightline within beam width. The Doppler shift of spectrum is determined by the beam velocity and the intersection angle, $\beta$. The broadening of each spectrum is due to the finite beam divergence and steering angle. The integration effect along the sight line within the beam width of 6 cm, where the strength and pitch angle of magnetic field and varies. The ratio of injected neutral beam density n(E) : n(E/2) : n(E/3) is adjusted to get the best fit to the measured $I(0,\lambda)$ and $I(135,\lambda)$, respectively. The shape of the measured spectra shows reasonable agreement with the calculated ones.

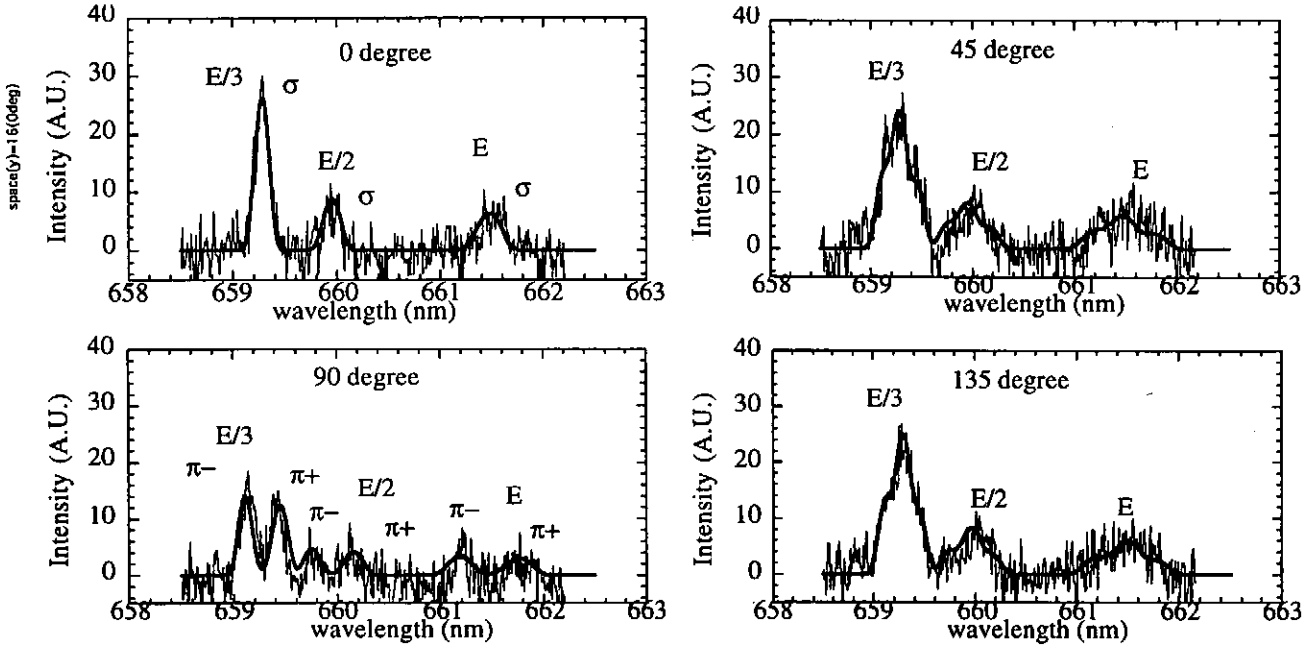


Fig.2 Comparison of measured and calculated MSE spectra with 0 degree (mainly $\sigma$ component), 90 degree (mainly $\pi$ component), 45 degree, and 135 degree polarizer at the major radius of 93cm

4. Pitch angle of magnetic field in CHS.

Although the full energy component has the largest motional Stark splitting and separation in wavelength between the $\sigma$ and the $\pi$ groups, the intensity of the full energy component is not sufficient to determine the pitch angle with a reasonable accuracy. Therefore, the one-third energy component which has the largest intensity is used to derive the pitch angle.The wavelength averaged polarization angle of $\sigma$ or $\pi$ components are given by

$$\overline{\alpha_i} = \frac{1}{2}\tan^{-1}\left( \frac{1}{2\Delta\lambda} \int_{\lambda_i-\Delta\lambda_i}^{\lambda_i+\Delta\lambda_i} \frac{\dfrac{(I(135,\lambda)-I(45,\lambda))}{(I(135,\lambda)+I(45,\lambda))}}{\dfrac{(I(90,\lambda)-I(0,\lambda))}{(I(90,\lambda)+I(0,\lambda))}} d\lambda \right) + \delta_i \qquad (4)$$

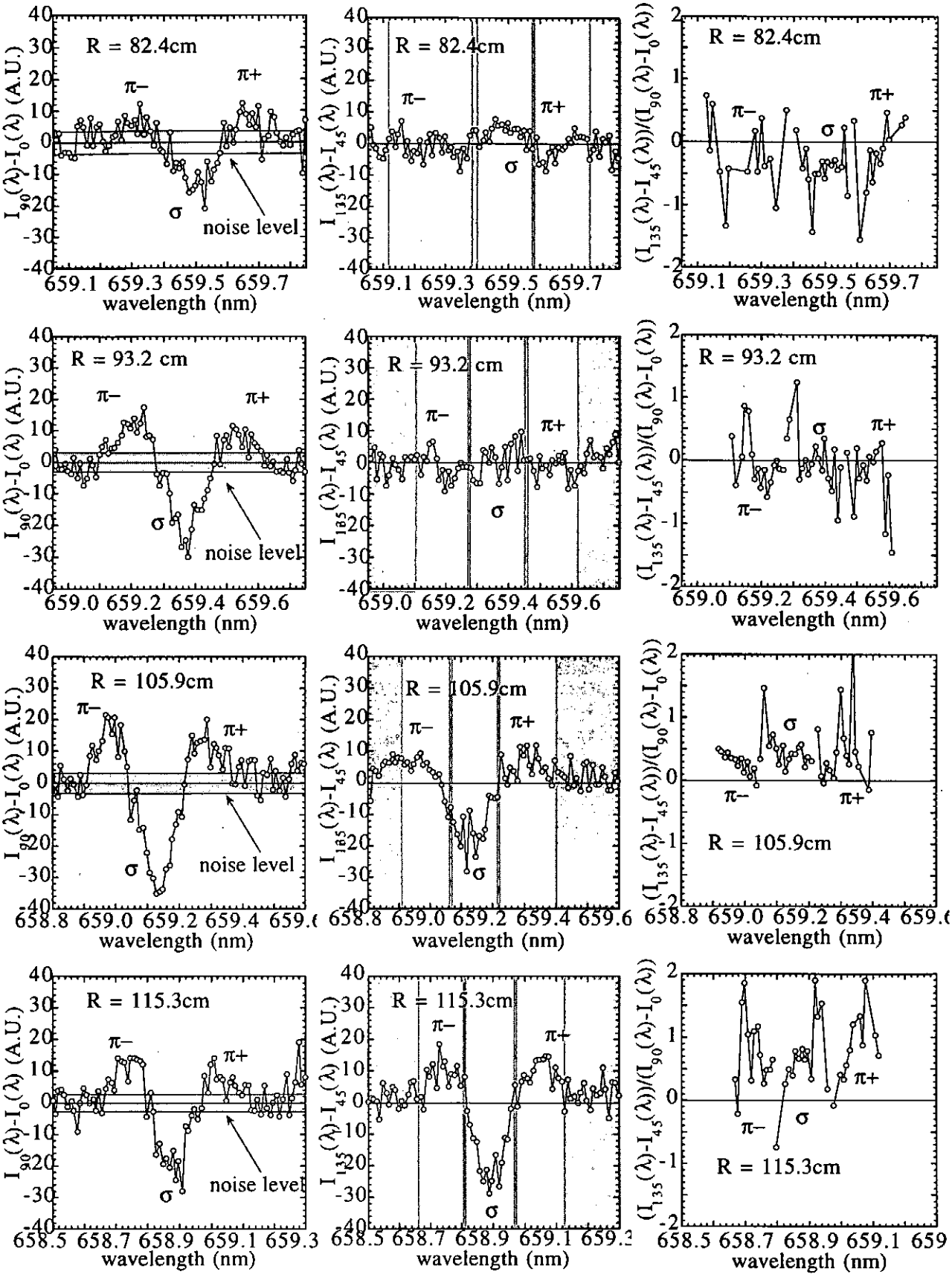


Fig.3 Intensity difference between 0 and 90 degree, ( I(90,λ)-I(0,λ), 45 and 135 degree, I(135,λ)-I(45,λ), and the intensity ratio, (I(135,λ)-I(45,λ))/( I(90,λ)-I(0,λ)), of $H_a$ emission for various position (R = 82.4, 93.2, 105.9, 115.3cm).

where i=π−, σ, π+. and $\delta_\sigma = 0$ and $\delta_{\pi+} = \delta_{\pi-} = 90$. $\Delta\lambda_i$ is the wavelength region for averaging.

Figure 3 shows the intensity difference between 0 and 90 degree, ( I(90,λ)-I(0,λ), 45 and 135 degree, I(135,λ)-I(45,λ), and the intensity ratio, (I(135,λ)-I(45,λ))/( I(90,λ)-I(0,λ)), of $H_a$ emission for one-third energy at various major radius. The major radius of magnetic axis is 94.9cm, where the pitch angle is almost zero. The data clearly shows that the pitch angle is negative for R < 94.49cm, while it is positive for R > 94.9cm. When the values of I(90,λ)-I(0,λ) is below the noise level (standard deviation of signal, where there is no spectrum), the polarization angle has large uncertainty. Therefore the data where I(90,λ)-I(0,λ) below the noise level (indicated in Fig as shadow region) is masked when the polarization angle is calculated

The radial profile of the magnetic field pitch angle estimated from the π- , σ and π+ groups are summarized in Fig.4. There is systematic differences between π- , σ and π+ groups. The pitch angle derived from σ component is larger than that derived from π- component. The values of the pitch angle derived from the π- agree with that of the vacuum magnetic field (solid line) calculated from the external coil current. However, the values of the pitch angle derived from σ and π+ groups shows less agreement with the calculation. The large scatter of π+ groups may be due to the overlap of spectra between one third and half energy peaks. The cause of offset of σ component is not clarified yet. One of the candidate of this offset is the change of polarization characteristics at the window, (for instance, mixture of circular polarization and linear polarization). This effect can be calibrated by installing calibration linear polarizer between window and the plasma inside the vacuum vessel.

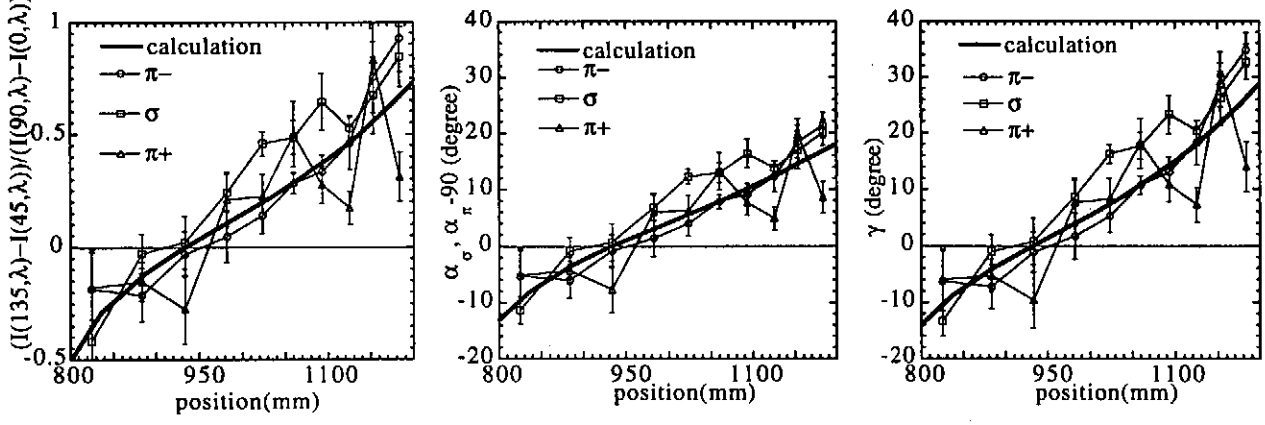


Fig.4 The radial profile of the averaged intensity rati, polarization angle of σ and π, and the magnetic field pitch angle γ estimated from the π- , σ and π+ groups.

References


[1] F. M. Levinton, Rev.Sci.Instrum. **63**, 5157 (1992)

[2] F. M. Levinton, G. M. Gammel, R. Kaita, H. W. Kugel, D. W. Roberts, Rev.Sci.Instrum. **61**(10), 2914 (1990)

[3] D.Wroblewski, K.H.Burrell, L.L.Lao,P.Politzer, W.P.West, Rev.Sci.Instrum. **61**, 3552 (1990)

[4] D.Wroblewski, L.L.Lao, Rev.Sci.Instrum. **63**(10), 5140 (1992).

[5] K.Ida, J.Xu, et al. (Proc. 11th Colloquium on UV and X-ray Spectroscopy of Astrophysical and Laboratory Plasmas, May 29 - June 2, 1995, Nagoya)

[6] J.Xu, K.Ida , et al., Fusion Engineering and Design, B23 293 (1997).

# Time dependent ionization and polarization of X-rays from solar flares

T. Kato, M. Kato and T. Fujimoto*

National Institute for Fusion Science, Toki, Japan
*Dep. Engineering Physics and Mechanics, Kyoto Univ., Kyoto, Japan

Abstract

We have analyzed the time evolution of solar flare X-ray spectra from He-like Fe, Ca and S ions measured by the Bragg Crystal Spectrometer (BCS) on the Yohkoh satellite[1]. We have derived time - dependent electron temperature, ion temperature, electron density as well as the ion density ratios such as n(Li-like)/n(He-like), n(Be-like)/n(He-like), n(B-like)/n(He-like) for Fe ions and n(He-like)/n(H) for Fe and Ca ions. The results show a deviation from ionization equilibrium. In this paper we investigate the origin of the deviation and make a time dependent ionization model assuming material flow in solar flares. We also estimate the effect of the polarization on the spectra.

## 1. X-ray spectra from Yohkoh

We have analyzed the time evolution of solar flare X-ray spectra from He-like Fe, Ca and S ions measured by the Bragg Crystal Spectrometer (BCS) on the Yohkoh satellite[1]. The Yohkoh BCS consists of four Bragg crystal spectrometers that cover narrow wavelength ranges including the resonance lines and associated satellite lines of H-like Fe XXVI (1.7636 - 1.8044A), He-like Fe XXV (1.8298 - 1.8942A), He-like Ca XIX (3.1631 - 3.1912A) and He-like S XV (5.0160 - 5.1143A). From the fit of the synthetic spectra to the observed spectra we can obtain several plasma parameters as described in the following. We did not assume ionization equilibrium in our fitting procedure. The electron temperature (Te) is obtained from the intensity ratio of the dielectronic satellite lines to the resonance line produced from the same ion. The ion density ratios of Li-like, Be-like and B-like ions to the He-like ion are obtained from the line intensity ratios of the inner shell satellite lines to the resonance line. The density

ratio of the He-like ions to the hydrogen, n(He-like)/n(H), is obtained from the intensity ratio of the resonance line to the continuum where n(He-like) is the density of He-like ions and n(H) is the density of hydrogen. The electron density is obtained from the emission measure assuming the volume measured by soft x-ray telescope (SXT) on Yohkoh. In this paper we discuss the results for a solar flare on 6th September 1992 at 05:05 (M2.4 class).

The spectrum of He-like Fe ions is shown in Fig.1 as an example. The contribution of the inner shell satellite lines is plotted by a dotted line in Fig.1. The spectrum for He-like S ions is shown in Fig.2. For the spectra of S ions we have included the contribution of H-like ions in the fit spectra and obtained the density ratio of n(H-like)/n(He-like) as well as n(Li-like)/n(He-like). The contribution of H-like ions is plotted by a dotted line in Fig.2. The energy level diagram corresponding to the He-like spectra is shown in Fig.3.

The electron temperature derived from the intensity ratios of dielectronic satellite lines to the resonance line is given in Fig. 4(a). The electron density derived from the emission measure assuming the flare volume to be $V = 2 \times 10^{27}$ cm$^3$ (20000 km x 10000 km x 10000 km) is shown in Fig.4 (b).

It has been previously found that the ion density ratios derived from the spectra deviate ionization equilibrium. However it has been said that this discrepancy may be a question about the atomic data. Therefore we employ reliable atomic data described by Itikawa et al[2] and by Kato et al[3] in our analysis. The ion density ratios derived from the intensity ratios are plotted as a function of the derived electron temperature in Fig.5 (a) for Fe ions and (b) for S ions. The dotted lines show the values in ionization equilibrium. In Fig.6 (a) and (b) the density ratios of He-like ions to hydrogen are shown for Fe and Ca ions respectively. This shows also the deviation from ionization equilibrium. The density ratios give the time dependent behaviour as shown in Fig.5 and 6; in the rising phase the ion density of He-like ions are smaller than those in the decay phase. The time dependent ion density ratios show the plasma is in an ionizing phase.

## 2. Flow model for time dependent ionization

In the rising phase of a flare unusually broad line width is often measured and the line center is shifted to the blue wavelength side. From the spectra of our flare on Sep. 6 1992, this phenomena is also measured at 05:14 for He-like Ca ion spectra. The velocity of the blue shift component is estimated as 140 km in our case[1]. Generally velocities of 100 - 300 km/s have

been measured in different flares. This phenomena supports the evaporation model of the flares. From the images of SXT of our flare the foot point was bright in early phase (05: 14) and the bright point moved to the loop top at the beginning of the maximum phase (05:17). This also indicates a movement of the plasma from the foot point to the loop top.

We make a time dependent model assuming a flow from the foot point to the loop top in a solar flare. We consider the highly ionized ions are produced at the loop top and they easily escape from the top of the flare. This idea can be expressed by a residence time $\tau$ of ions in the solar flare as follows,

The neutral atoms or low ionized ions enter the flow at foot point

$$dn(1)/dt = -S(1)\, n(1) + A(2)n(2) + n(1)/\tau$$

For M and L-shell ions,

$$dn(i)/dt = -(S(i) + A(i))n(i) + S(i-1)n(i-1) + A(i+1)n(i+1)$$

and K-shell ions (i = z-1, z, z+1) escape with a residence time $\tau$

$$dn(i)/dt = -(S(i) + A(i))n(i) + S(i-1)n(i-1) + A(i+1)n(i+1) - n(i)/\tau$$

where z is the nuclear charge of the ion. In our calculation we assumed

$$n(1)/\tau = n(z-1)/\tau + n(z)/\tau + n(z+1)/\tau$$

in order to exactly conserve the total density of ions. Using the time dependent electron temperature and the density derived from the observed spectra shown in Fig.4, we calculated the time dependent ion density for Fe, Ca and S ions. We assumed $\tau$ = 50 sec in our calculation. This corresponds to the value L/v = 10000 km / 200 km/s = 50 sec where L is the length of the flare and v is the velocity of the flow. The calculated results for time dependent ion density ratios are plotted as a function of the electron density in Fig.7 (a) for Fe ions and (b) for S ions. When we use the derived density in Fig. 4 (b) the deviation of the ion density ratios for L-shell ions to He-like ions (n(Li-like)/n(He-like), n(Be-like)/n(He-like) etc.) are obtained only in the rising phase but not obtained in the decay phase because the electron density is enough to reach equilibrium. We tentatively decreased the electron density more than factor 3 (by about factor 18 to 6 in the beginning of the flare to the maximum phase) as indicated in Fig.4 (b) by a dotted line, then a deviation of the density ratios from the equilibrium is obtained as shown in Fig.7 (a) by thick solid (for n(Li-like)/n(He-like)) and dot-dashed (for n(Be-like)/n(He-like)) lines. With the modified electron density, the agreements for n(Li-like)/n(He-like) are good for Fe and S ions, although the agreement for n(Be-like)/n(He-like) and n(B-like)/n(He-like) are not good. For the ion density ratios of n(He-like)/n(H) which are derived from the intensity ratio of the resonance line to the continuum, the calculated values change in the same sense as time

advances; the values in the rising phase are smaller than those in the decay phase. However the values in the rising phase and the decay phase are too close compared to the values derived from the spectra when we use the derived electron density. With the modified decreased electron density, we have better agreement as shown in Fig. 6 by thick dot-dashed lines. When we decrease the residence time $\tau$, then the deviation from equilibrium become larger for n(Li-like)/n(He-like). However for n(He-like)/n(H) the values in the rising phase and decay phase are almost the same.

## 3. Polarization by electron flow

The possible polarization of solar flares was reported in ref.4 for the Fe XXV - XXIII X-ray spectra measured by Intercosmos[5] . They reported a very large difference of the spectra with different BCS spectrometers which indicates a large polarization. However for Fe XXV spectra measured by Hinotori satellite[6] launched at 1981, Akita et al[7] showed that the average polarization is lower than 4%.

We want to know the effect of polarization on our analysis of X-ray spectra. As shown in Fig.1, the observed X-ray spectra show features of a one average temperature thermal plasma. The contribution of high energy electrons on the spectra is estimated less than 0.1% for the spectra after the maximum phase. However polarization is expected if there is a flow of electrons in a plasma even it is thermal.

We would like to estimate the polarization caused by electron flow in solar flares. Generally we measure the solar flares from the top side except for limb flares. If the direction of the measurement is the same as that of the electron flow, then we measure mainly only $\sigma$ component. In Table I we list the estimated intensity of $\pi$ component $I_\pi$ and $\sigma$ component $I_\pi$ for the energy at threshold from the polarization degree calculated by J. Dubau[8-10]. It is assumed that $I_\pi + 2\, I_\pi = 1.0$. The polarization of the He-like resonance line and the Be-like inner shell satellite line $\beta$ are almost the same. Therefore we can say that the intensity ratio of the resonance line $I_w$ and $I_\beta$ shows no effect of polarization. Consequently we can say that the deviation for n(Be-like)/n(He-like) derived by the intensity ratio of $I_\beta/I_w$ is not affected by polarization. On the contrary $I_q/I_w$ is affected by polarization. When only $\sigma$ component is measured, $I_q$ appears larger than $I_w$.

## 4. Summary and Discussion

The deviation from ionization equilibrium have been derived from X-ray spectra by Yohkoh satellite. We have explained this deviation by a flow model in solar flares with the residence time $\tau = 50$ sec. In our analysis the derived values for n(B-like ion)/n(He-like ion) of Fe ions is much smaller than other ions as shown in Fig.5(a). We do not know the reason for it yet. The wavelength of the strong dielectronic satellite line and that from the inner shell satellite line has the same wavelength of the same transition for B-like ions although for other ions those are different. It would be helpful to measure and study in more detail B-like and C-like dielectronic satellite lines as well as the inner shell satellite lines in laboratory plasmas such as EBIT in order to know more about the solar flare spectra.

We estimated the effect of the polarization for the resonance line of He-like ions and the inner shell satellite lines of Li, Be, B and C-like ions.

## References


1. T. Kato, T. Fujiwara and Y. Hanaoka, Ap. J., Jan. (1998)
2. Y. Itikawa, T. Kato and K. Sakimoto, The Institute of Space and Astronautical Science Report No. 657, ISSN 0285-6808, (1995)
3. T. Kato, U. Safronova, A. Shlyaptseva, M. Cornille and J. Dubau, Atomic Data and Nuclear Data Tables, 67., 225 (1997)
4. V.V. Krutov et al, Lebedev Physical Institute, no 133 (1981)
5. Y. I. Grineva et al, Space Research XIV - Akademie-Verlag, Berlin, 454 (1974)
6. K. Tanaka, Publ. Astron. Soc. Japan, 38, 225 (1986)
7. K. Akita , K. Tanaka and T. Watanabe, Solar Phys., 86, 101 (1983)
8. M.K. Inal and J. Dubau, J. Phys. B, 20, 4221 (1989)
9. M.K. Inal and J. Dubau, Phys. Rev. A47, 4794 (1993)
10. J. Dubau private communication (1997)

Table I

Polarization for the Resonance line and Inner shell excitation satellite lines for Fe ion spectra by electron excitation

| Transition | | $I_\sigma$ | $I_\pi$ | Polarization (at threshold energy) | Ref.No. |
|---|---|---|---|---|---|
| He-like (Fe XXV) | | | | | |
| w | $1s^2 2s\ ^1S - 1s2p\ ^1P_1$ | 0.16 | 0.67 | 0.6 | 8 |
| Li-like (Fe XXIV) | | | | | |
| q | $1s^2 2s\ ^2S_{1/2} - 1s2s2p\ ^2P_{3/2}$ | 0.25 | 0.5 | 0.3 | 9 |
| Be-like (Fe XXIII) | | | | | |
| β | $1s^2 2s^2\ ^1S - 1s2s^2 2p\ ^1P$ | 0.16 | 0.67 | 0.6 | 10 |
| B-like (Fe XXII) | | | | | |
| I4 | $1s^2 2s^2 2p\ ^2P_{1/2} - 1s2s^2 2p^2\ ^2D_{3/2}$ | 0.26 | 0.47 | 0.28 | 10 |
| I2 | $1s^2 2s^2 2p\ ^2P_{1/2} - 1s2s^2 2p^2\ ^2P_{1/2}$ | 0.33 | 0.33 | 0.0 | |
| I4 + I2 | | <0.3> | <0.4> | | |

Fig.1 He-like Fe spectra measured by Yohkoh. Dotted line indicates the contribution of the inner shell satelite lines.

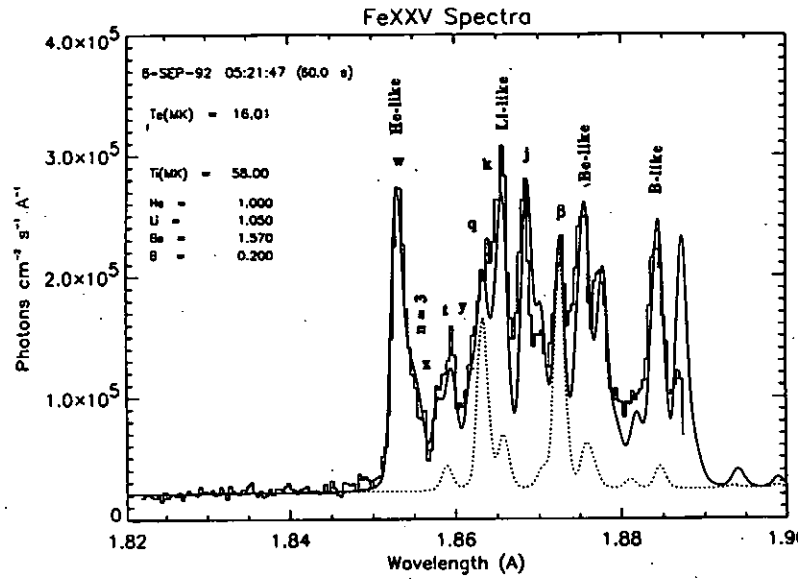


Fig.2 He-like S spectra measured by Yohkoh. Dotted line indicates the contribution of the recombination from H-like ions.

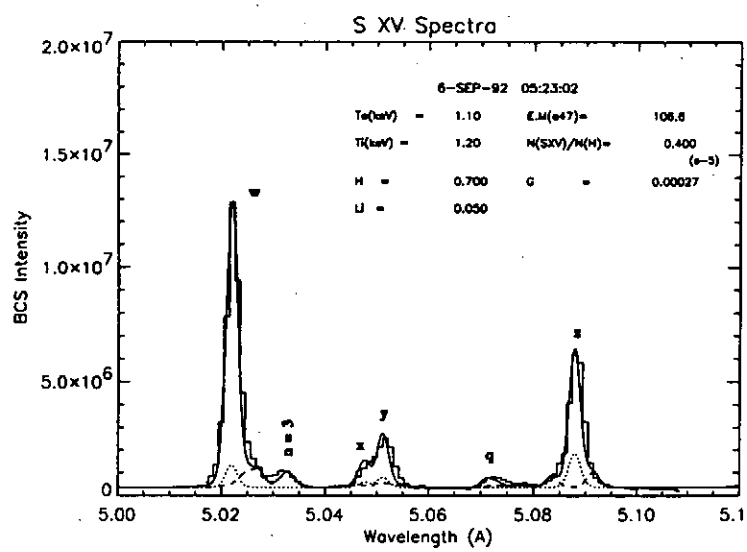


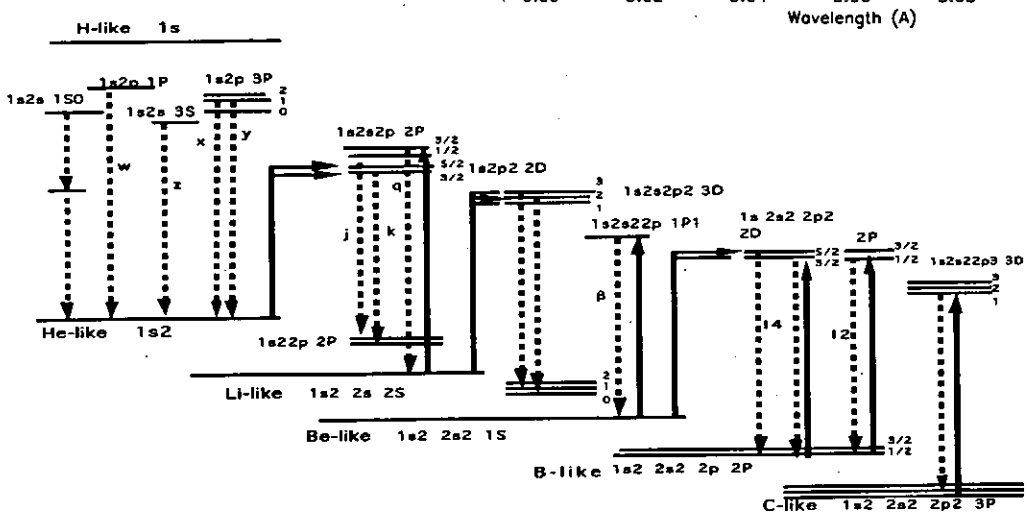


Fig.3 The energy level diagram corresponding to He-like spectra in Fig.1. contribution of recombination from H-like ions.

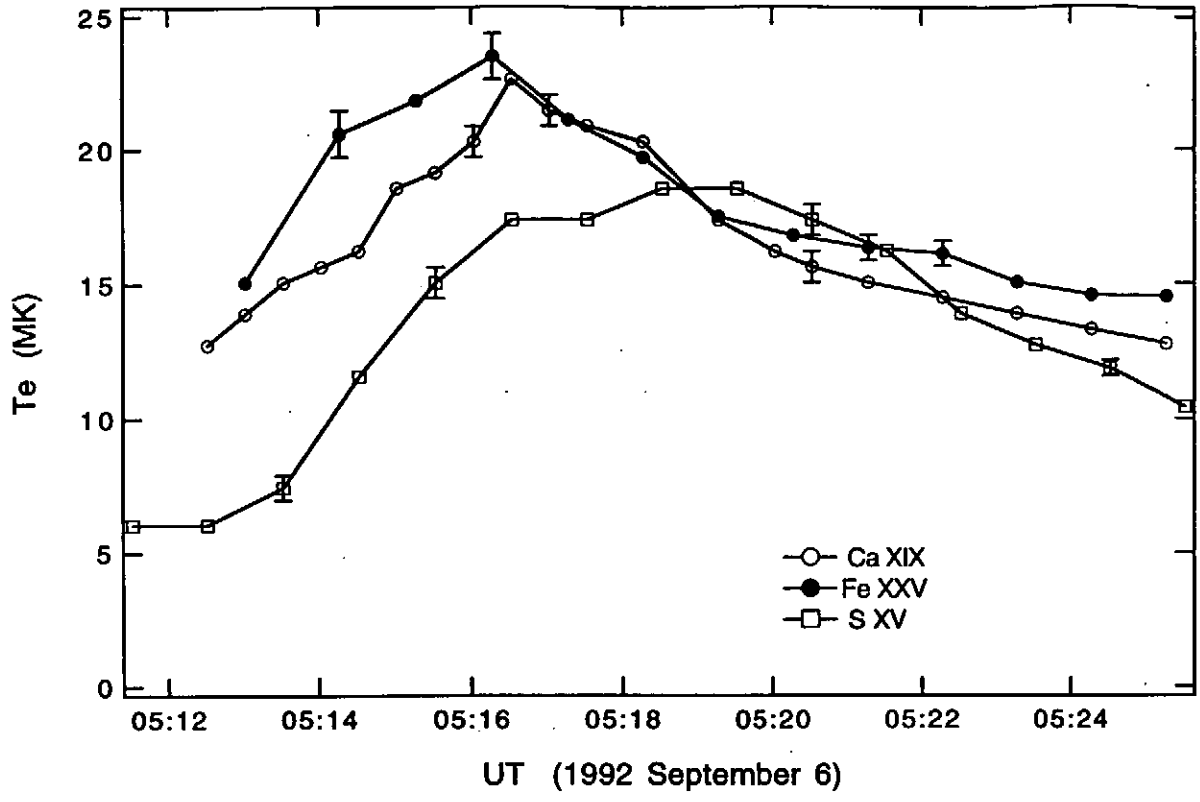


Fig. 4 (a) The electron temperature derived from the spectra of Fe, Ca and S ions

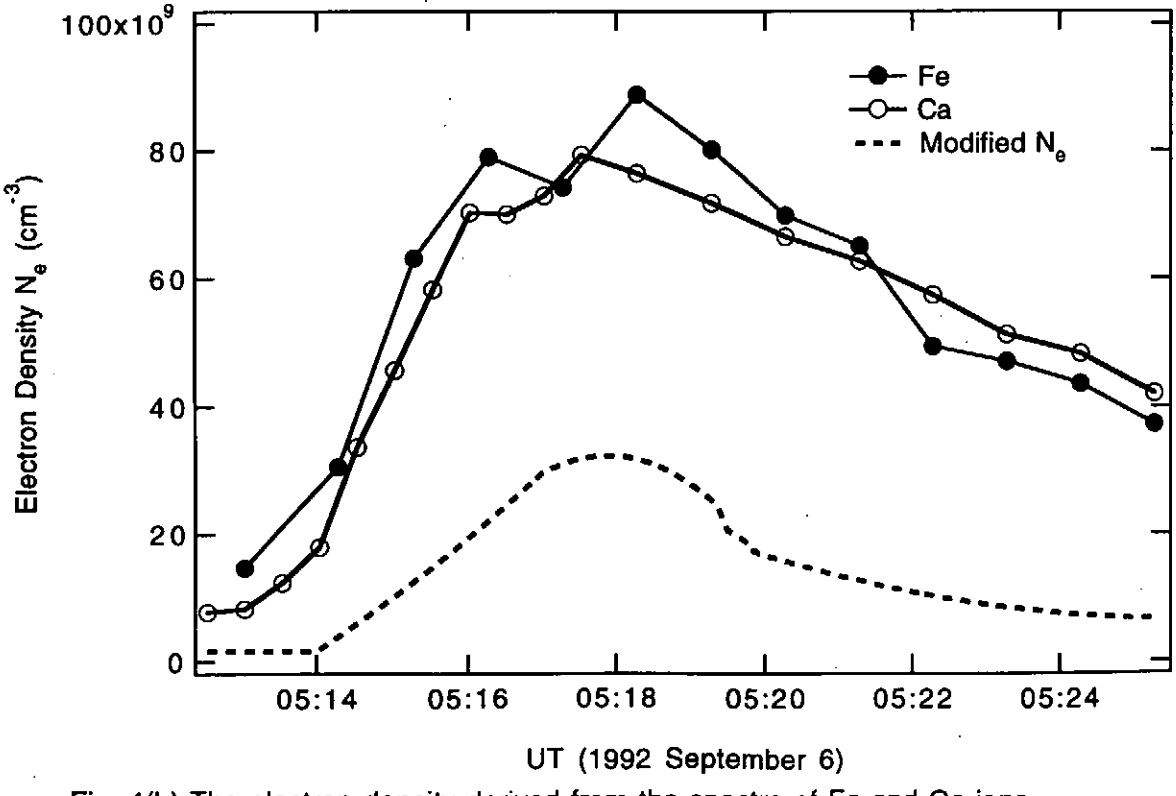


Fig. 4(b) The electron density derived from the spectra of Fe and Ca ions

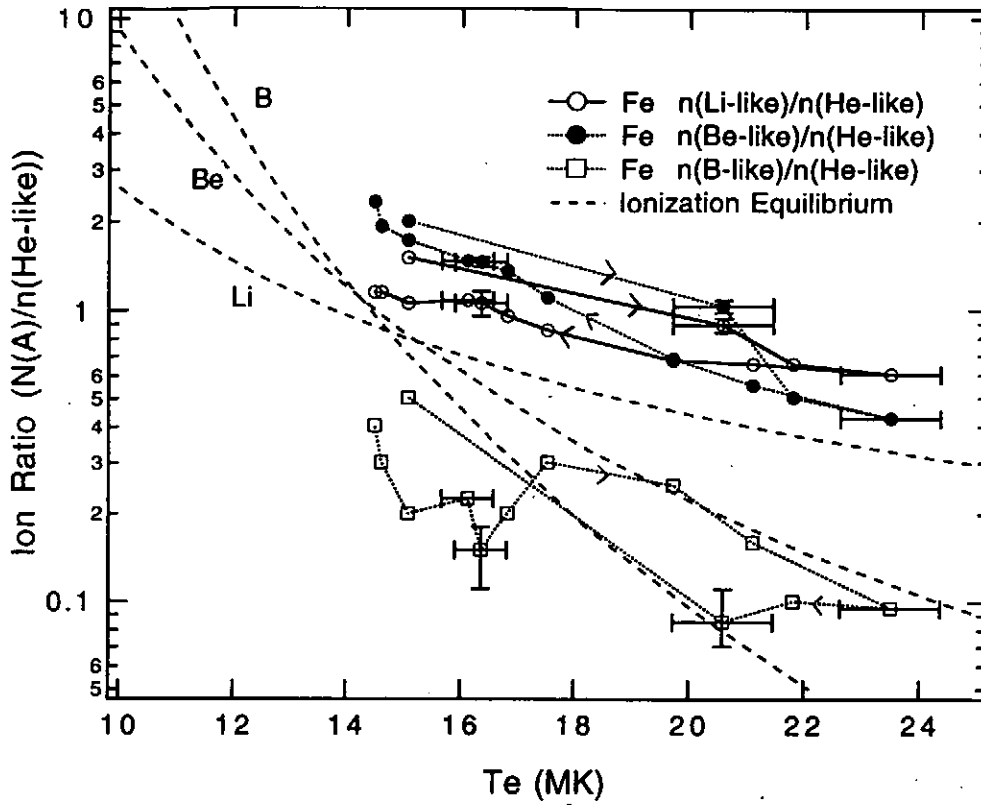


Fig.5 (a) The derived ion density ratios from the intensity ratios of Fe ion spectra

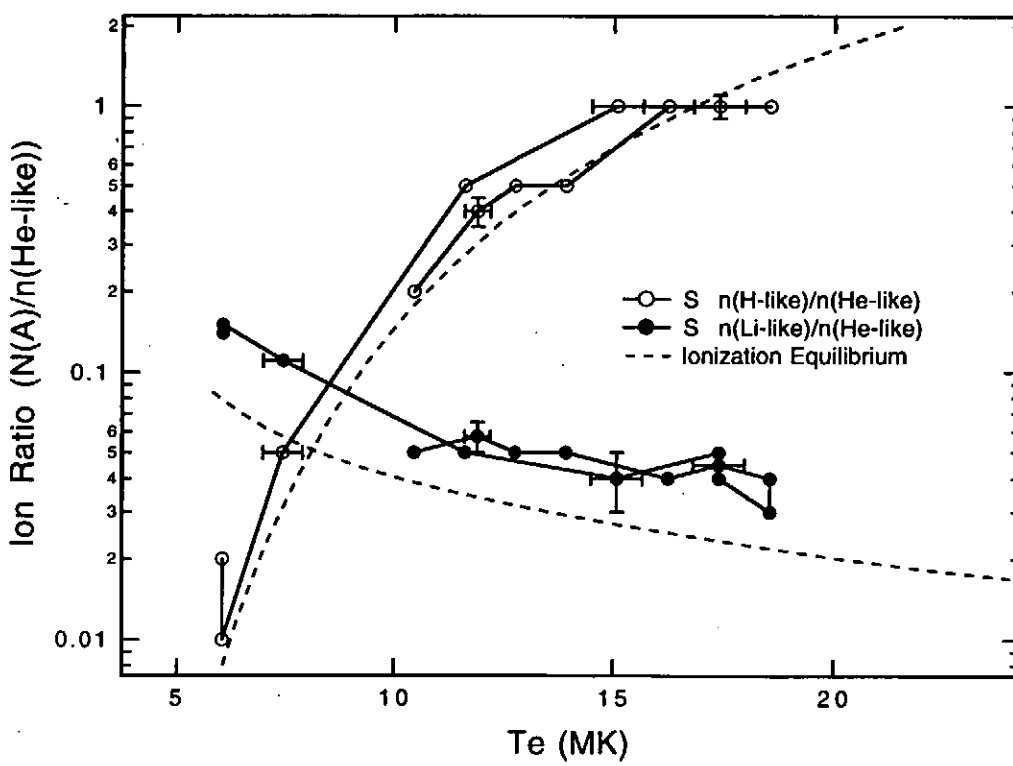


Fig.5 (b) The derived ion density ratios from the intensity ratios of Sion spectra

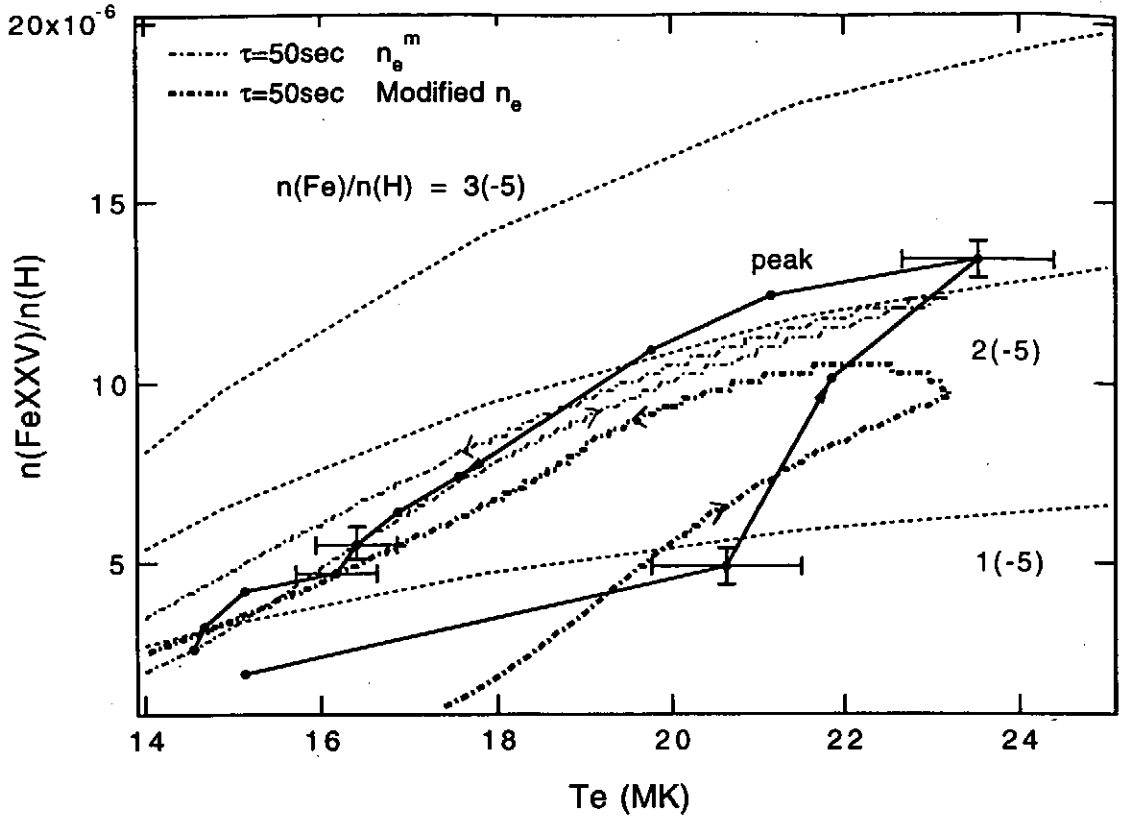


Fig.6 (a) The density ratios of He-like Fe ions to hydrogen

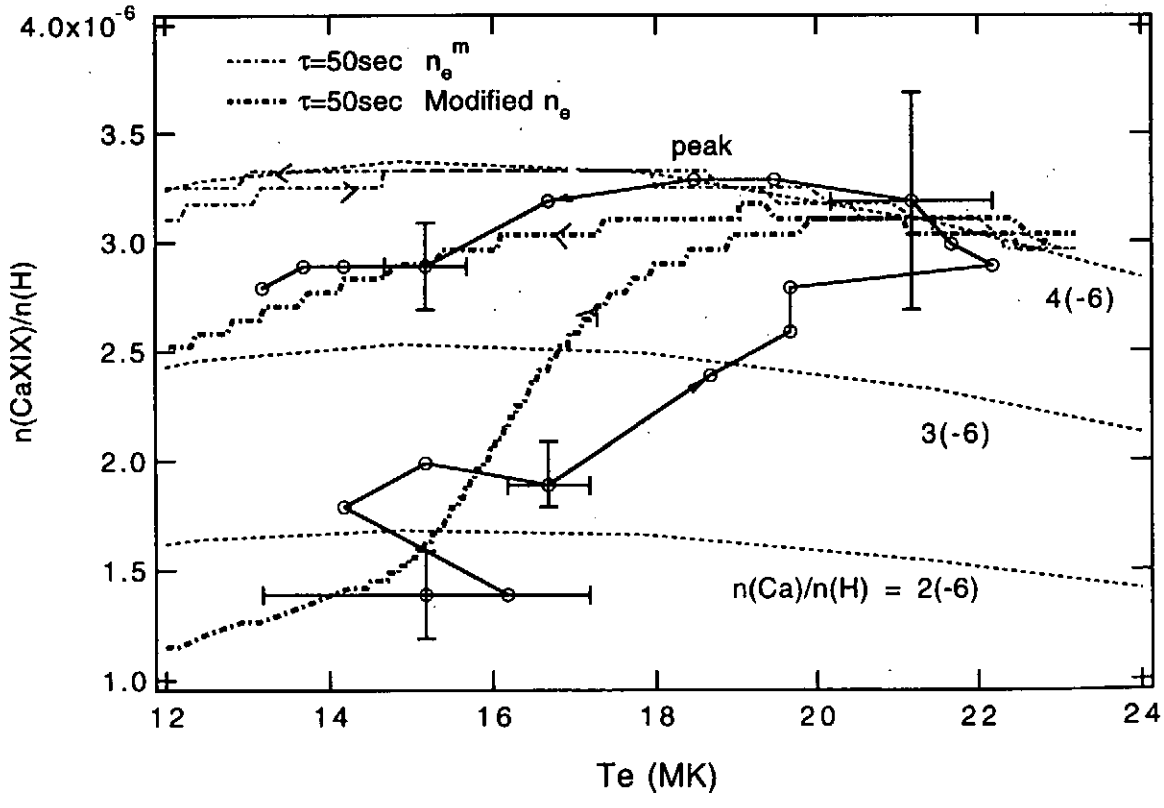


Fig.6 (b) The density ratios of He-like Ca ions to hydrogen

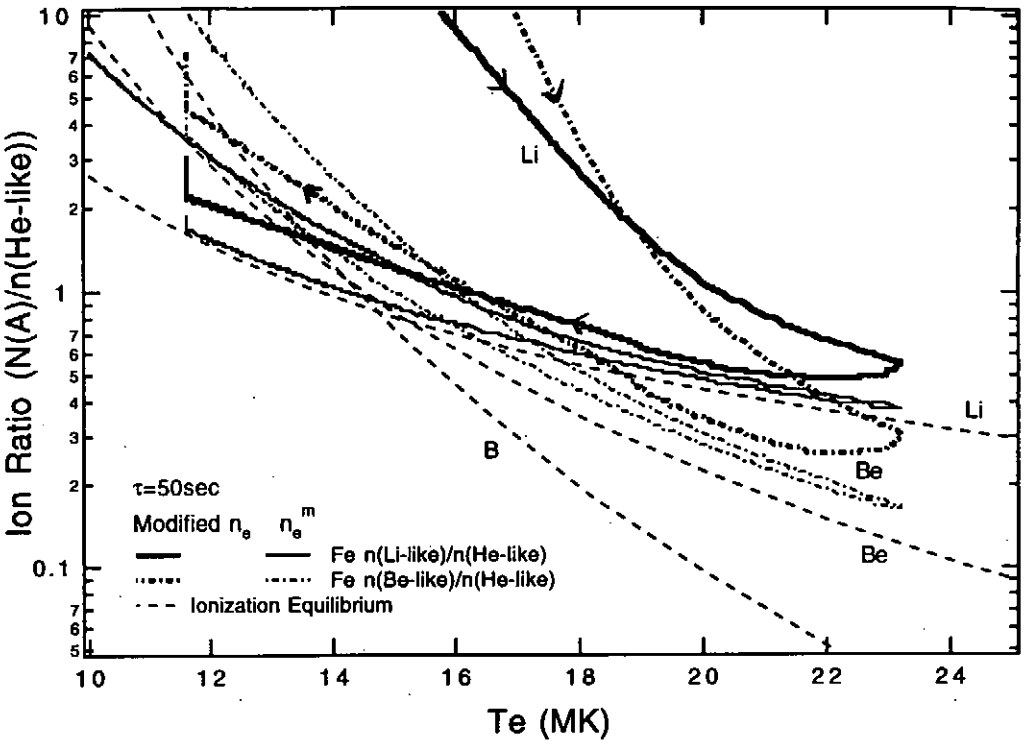


Fig.7 (a) The calculated ion density ratios of Fe ions as a function of electron temperature

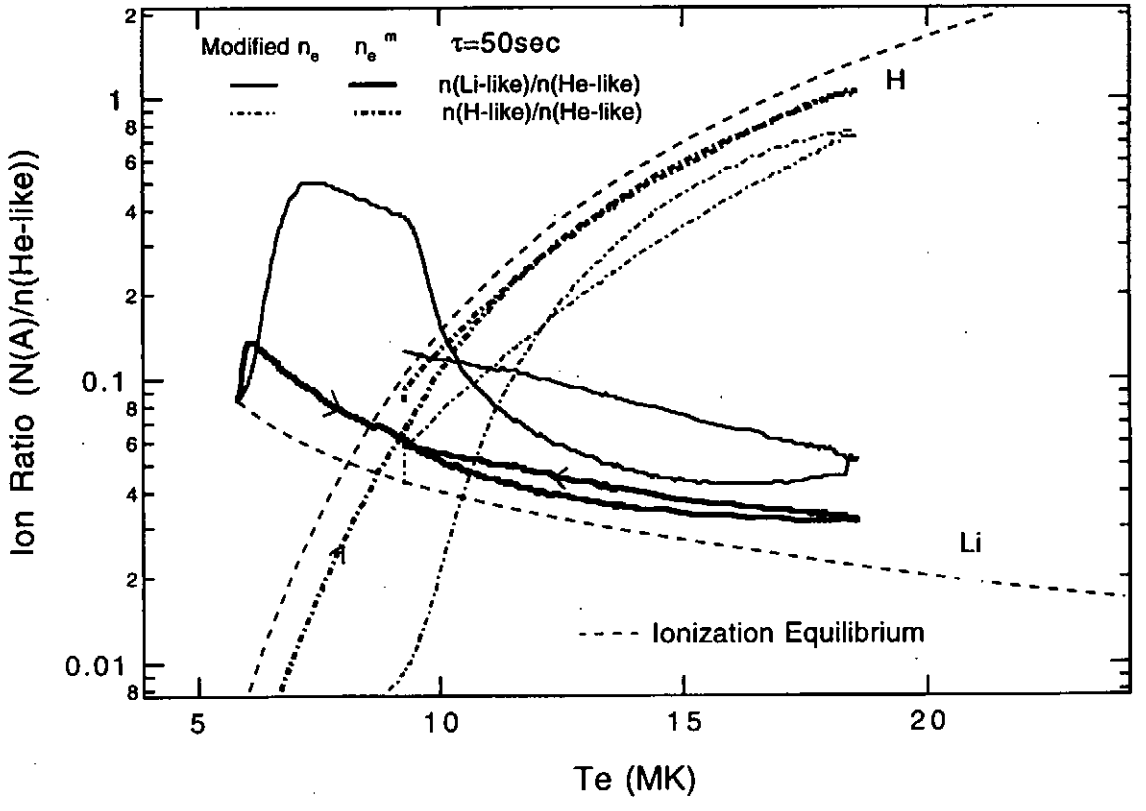


Fig.7 (b) The calculated ion density ratios of S ions as a function of electron temperature

# DETERMINATION OF THE DARK SPACE STRUCTURE IN FRONT OF THE SUBSTRATE IN A HE ECR PLASMA USING POLARIZED LASER-INDUCED FLUORESCENCE SPECTROSCOPY

T. ODA, K. TAKIYAMA and H. TOYOTA

*Department of Applied Physics and Chemistry, Faculty of Engineering, Hiroshima University,*

*1-4-1, Kagamiyama, Higashi-Hiroshima 739, JAPAN*

For detailed measurement of spatial distribution of metastable ($2^1S$) helium atoms in plasma flow from an ECR plasma source, influence of the applied magnetic field $\boldsymbol{B}$ was investigated on polarized laser-induced fluorescence (LIF) following a forbidden excitation ($2^1S - 4^1D$) by pulsed dye laser. Beat structure was found in temporal variation of an LIF polarized component perpendicular to $\boldsymbol{B}$ when the exciting laser was linearly polarized parallel to $\boldsymbol{B}$. It was found that the spatial distribution of $2^1S$ atoms decreased toward the downstream and markedly in interacting region in front of a substrate inserted in the plasma flow. Axial distribution of applied magnetic field strength in the plasma flow was also obtained from the observed LIF.

## 1 Introduction

Electron cyclotron resonance (ECR) plasmas are now widely utilized for processing plasmas.[1] The role of radicals in these plasmas has been well recognized, particularly in region in front of substrate, with which the plasma flow interacts, so that the plasma processes are dominantly controlled. Metastable atoms of rare gases often used as buffer gases in the processing plasmas also play the role of radicals.[2] Because of this, atom density measurement is required. Metastable atoms have been also utilized for plasma diagnostics. For instance, measurement of electric field distribution in glow discharges has been carried out using the laser-induced fluorescence (LIF) technique in which the forbidden excitation is made from $2^1S$ state.[3,4] To apply this technique to diagnostics in dark space in front of substrate in processing plasmas with applied magnetic field, it is important to know influence of the magnetic field on polarized LIF.[5] Measurement of axial magnetic field itself would be also desirable.

In a previous paper,[6] (hereafter called paper I) we reported measurements of axial distribution of He I metastable atom density ($n_{2S}$) along an ECR plasma flow by polarized laser-induced fluorescence (LIF) spectroscopy.[7] In this experiment, a new development was introduced to sufficiently reduce intense laser stray light, which involved observation of an LIF with different wavelength far from that of incident laser. This fluorescence was due to forbidden excitation by the electric quadrupole (QDP) transition. Our measurements showed that the He I metastable atom density was as high as $10^{11}$ cm$^{-3}$ near the outlet of the plasma flow, and gradually decreased toward the down stream. Influence of the applied magnetic

field, however, was not revealed on the polarized LIF from the plasma. Detailed distribution of $n_{2S}$ was also not measured in the interacting region in front of the substrate.

In the present paper, we describe an investigation of the influence of applied magnetic field on polarized LIF ($4^1D - 2^1P$) following the forbidden excitation due to QDP transition. The axial distribution of plasma parameters, electron density $n_e$ and temperature $T_e$ as well as the plasma potential $\phi$ were also measured by a probe. We determined axial distribution of applied magnetic field strength in the plasma flow from observed polarized LIF. Further detailed measurement of the metastable atom density distribution was made using our LIF technique in the interacting region on the substrate in the ECR plasma flow.

## 2 Experimental apparatus

The experimental apparatus and procedure are almost the same as in paper I. Figure 1 shows side view of the compact NTT-type ECR source[8] in a vacuum chamber with observation port and laser injection optical system. A disk substrate (24$\phi$ x 5 mm) is situated at 6.8 cm from the outlet of plasma source and is grounded (0 V). The ECR plasma is produced by a microwave of 2.45 GHz with a power of 260 W. The working gas is helium with the pressure of 2.2 x $10^{-2}$ Torr. Axial profiles of plasma parameters (electron density $n_e$, electron temperature $T_e$ and plasma potential $\phi$) were measured by a cylindrical probe.

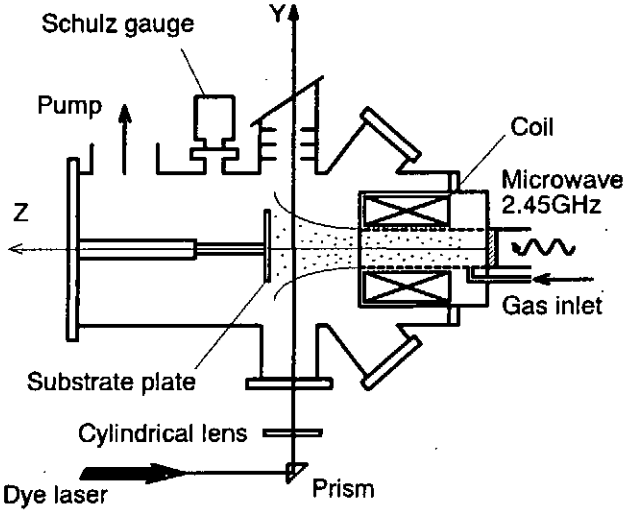


Fig. 1: Side view of experimental set up, including LIF observation geometry.

For the LIF observation, a YAG-laser-excited dye laser (pulse width of 3 ns, line width of 1 pm and repetition rate of 10 Hz) is introduced into the plasma flow along the $y$-axis. The polarization direction of the laser is chosen to be linearly parallel $e_z$ or perpendicular $e_x$ to the $z$-axis. Laser-induced fluorescence is observed along the $x$-axis perpendicular to both the $y$- and $z$-axes. The polarization components are separated using a sheet polarizer. A 25 cm

monochromator equipped with a photomultiplier tube is used to observe LIF. To obtain the absolute value $n_{2S}$ at $\Delta z$ = 17.6 mm from the substrate surface, metastable atoms ($2^1S$) are excited to the $3^1P$ level by the dye laser (501.6 nm) with linear polarization parallel to the $z$-axis, and the subsequent resonance fluorescence (RF) is observed. Collision-induced fluorescence (CIF : 667.8 nm) from $3^1P$ level to $3^1D$ level is also observed. Relative spatial distribution of $n_{2S}$ along the $z$-axis is measured by exciting $2^1S$ atoms to the $3^1D$ level due to QDP transition and by observing the subsequent LIF ($3^1D$ - $2^1P$ : 667.8 nm), whose intensity is proportional to $n_{2S}$, provided that the exciting laser is sufficiently weak and kept constant. This method has a great advantage to avoid the influence of laser stray light as shown in paper I. To reveal the influence of applied magnetic field on polarized LIF, the fluorescence ($4^1D$ - $2^1P$ : 492.2 nm) induced by exciting $2^1S$ atoms to the $4^1D$ level (397.2 nm) due to QDP transition is observed.

## 3 Experimental results and discussion

### *3.1 Profiles of plasma parameters*

Axial distributions along the $z$-axis of $n_e$, $T_e$ and $\phi$ obtained from probe measurements are depicted in Fig. 2, where $\Delta z$ indicates the distance from the substrate surface along the $z$-axis Both $n_e$ and $\phi$ decrease toward the substrate while $T_e$ keeps almost constant. These behaviors are quite similar to the previous experimental results. Moreover, detailed measurements made in this experiment show a larger decrease rate of $n_e$ and $\phi$ in the interacting region (dark space) of about 10mm width in front of the substrate plate. The decrease of $n_e$ is probably due to radial diffusion of electrons because the magnetic field diverges and decreases toward the down stream and also due to recombination loss.

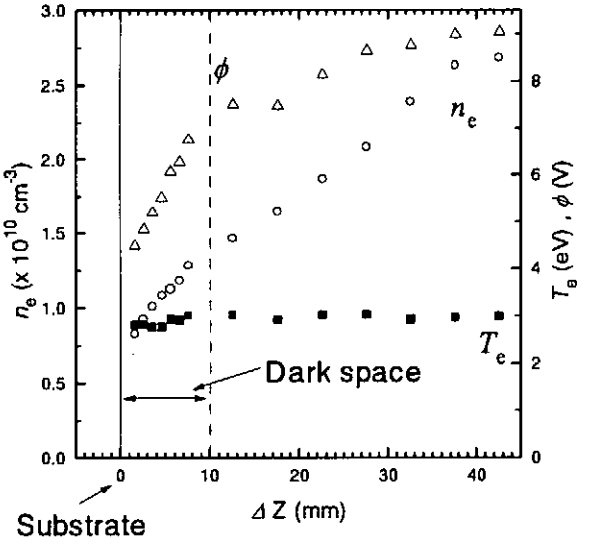


Fig. 2: Axial profiles of plasma potential $\phi$, electron density $n_e$, electron temperature $T_e$ along the plasma flow, where $\Delta z$ indicates the distance from the substrate surface.

*3.2 Influence of magnetic field on polarized LIF components*

The polarized LIF of 492.2 nm line induced by forbidden excitation due to QDP transition was observed at $\Delta$ z =17.6 mm. Figure 3 shows the results obtained with (a) $e_x \perp \boldsymbol{B}$ and (b) $e_z \,//\, \boldsymbol{B}$, where closed and open circles, $i_z$ and $i_y$ represent the component parallel to the $z$- and $y$-axes, respectively. In the case of $e_x \perp \boldsymbol{B}$ (Fig. 3(a)), $i_y$ is much stronger than $i_z$. This is because the alignment of atoms is produced by the laser excitation: only the excitation with $\Delta m_l = \pm 2$ from the $2^1$S level with $m_l=0$ due to QDP transition. Because the emitting atoms are quantized along the $z$-axis, only $i_y$ is observed along the $x$-axis. Very weak component $i_z$ appearing in a little bit later time is due to collisional transfer between the magnetic sub-levels in the $4^1$D level. In the present plasma, the gas pressure was rather low and the electron density is also low. Then the collisional transfer rate should be small. No magnetic effect was observed on this LIF up to under the present ECR source. In the case of $e_z \,//\, \boldsymbol{B}$ (Fig. 3(b)), both components rise up identically for about 5 ns from the beginning. That is, the LIF is unpolarized in the beginning. This is because the emitting atoms are quantized along the $x$-axis in this case due to the QDP transition, and the circularly polarized lights are emitted along the $x$-axis. In the later time, it should be noted that beat structure appears in the temporal development of $i_y$, while $i_z$ behaves in the quite similar way as the component $i_y$ shown in Fig. 3(a). The frequency of beat $f_H$ agrees exactly with twice the Lamor frequency ($\omega_L / 2\pi$),

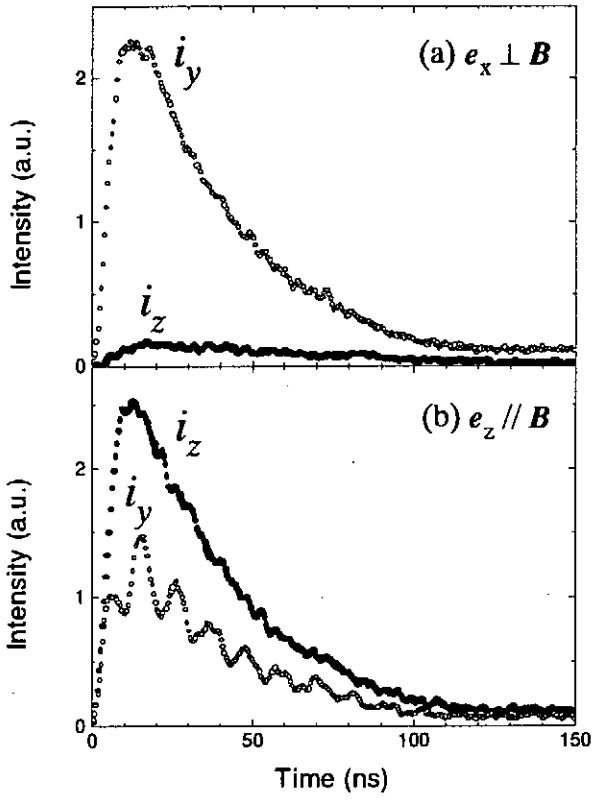


Fig. 3: Typical time variation of the polarization components of 492.2 nm line following the pulsed laser excitation (a) $e_x \perp \boldsymbol{B}$ and (b) $e_z // \boldsymbol{B}$.

$$f_H = 2\frac{\omega_L}{2\pi} . \qquad (1)$$

This beat is obviously originated from the Hanle effect because of the Lamor precession of the quantization axis of the emitting atoms. The decrease in intensity is also explained by the preceding.

The magnetic field strength can be obtained from the measured beat frequency $f_H$. Figure 4 shows the spatial distribution of applied magnetic field $\boldsymbol{B}$ along the $z$-axis obtained from eq. (1). The solid line shows the spatial distribution of magnetic field strength obtained from theoretical calculation using applied coil current of 15.8 A for the ECR source. The experimentally obtained magnetic field distribution decreases from 50 to 20 Gauss toward the downstream of plasma flow.

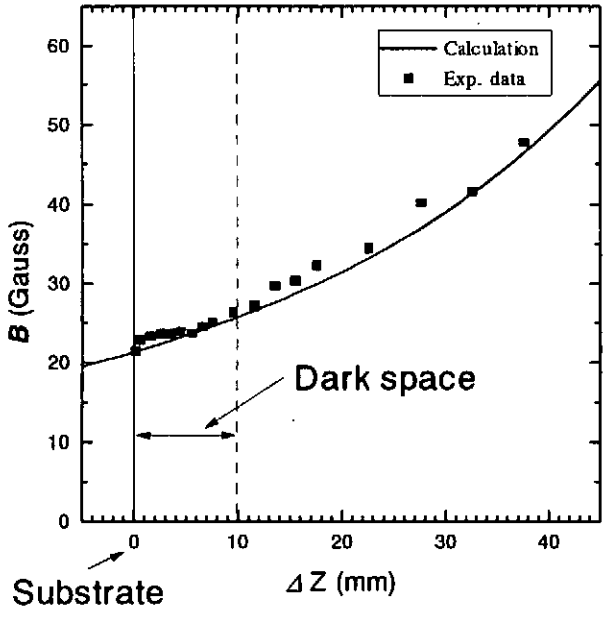


Fig. 4: Spatial distribution of applied magnetic field $\boldsymbol{B}$ along the z-axis.

*3.3 Distribution of the metastable atom density along the z-axis*

The absolute measurement of metastable atom density was carried out at $\Delta z$ = 17.6 mm where the resonant LIF (501.6 nm line) was observed as mentioned in section 2, using the same procedure described in paper I. We obtained $n_{2S}$ = 1.6 x $10^{11}$ $cm^{-3}$ at this point. The relative distribution of $n_{2S}$ along the $z$-axis was obtained from observation of the LIF (667.8 nm) associated with QDP excitation by the laser (504.2 nm). Figure 5 shows measured distributions of $n_{2S}$ along the $z$-axis. These value $n_{2S}$ also decrease toward the substrate. Moreover, detailed measurements made in this experiment show that a larger decrease of $n_{2S}$ takes place in the dark space of about 10 mm width in front of the substrate.

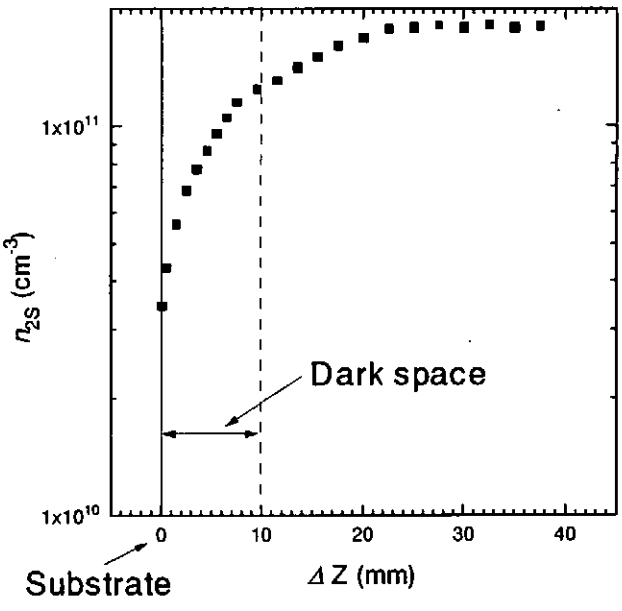


Fig. 5: Axial distribution of the metastable atom density $n_{2S}$.

Production mechanism of metastable atoms was already briefly discussed in paper I to be mainly due to the electron-impact excitation from the ground state ($1^1S$) to the $2^1S$ atoms because Doppler profile measurement of the 667.8 nm line showed the drift velocity of metastable atoms along the $z$-axis was less than the thermal velocity. The decrease of $n_{2S}$, however, could not be explained by the simple collisional-radiative processes. One of the possible processes is that $2^1S$ atoms are destroyed on the substrate surface. The larger decrease of $n_{2S}$ observed in front of the substrate may suggest this process.

## 4 Summary

Behavior of the polarized laser-induced fluorescence ($4^1D - 2^1P$) due to the electric quadrupole transition of helium atom was revealed in the applied magnetic field in an ECR plasma flow. When polarization direction of exciting laser was perpendicular to the magnetic field, the observed LIF showed strong spatial anisotropy. For another laser excitation with the polarization direction parallel to the field, the beat structure appeared on the observed LIF. This beat structure was caused by the Lamor precession of the quantization axis of emitting atoms (Hanle effect). Axial distribution of the magnetic field strength was obtained from the beat period. The LIF technique developed here is effective to measure *in-situ* magnetic field distribution in the processing plasmas.

Detailed spatial profile of $n_{2S}$ was measured in a plasma flow from ECR plasma source with high spatial resolution of 0.1 mm using our laser-induced fluorescence spectroscopy. In the dark space in front of substrate, $n_{2S}$ was found to sharply decrease toward the substrate. Production mechanism of metastable atoms was already briefly discussed in paper I to be mainly due to the electron-impact excitation from the ground state ($1^1S$) to the $2^1S$ atoms.

The decrease of $n_{2S}$, however, could not be explained by the simple collisional-radiative processes. One possible process for this decay is that $2^1S$ atoms are destroyed on the substrate surface. The larger decrease of $n_{2S}$ observed in front of the substrate may suggest this process.

**Acknowledgements**

This work was supported in part by a Grant-in-Aid for Scientific Research (C) from the Ministry of Education, Science, Sports and Culture, and by Electric Technology Research Foundation of Chugoku.

**References**

1 K. Ono, M. Tuda, K. Nishikawa, T. Oomori and K. Namba, Jpn. J. Appl. Phys. **33** (1994) 4424.
2 H. Yoshida, M. Ukai, H. Kawamura, N. Kouchi and Y. Hatano, J. Chem. Phys. **97** (1992) 3289.
3 K. Takiyama, H. Sakai, M. Yamasaki, T. Oda and K. Kawasaki, in Proc. 6th Inter. Sympo. *Laser-Aided Plasma Diagnostics*, Bar Harbor, Maine, 1993 edited by P. P. Woskov, pp.43
4 K. Takiyama and T. Oda, in Proc. 7th Inter. Sympo. *Laser-Aided Plasma Diagnostics*, Kyushu Univ., Fukuoka, Japan, 1995 edited by K. Muraoka, pp.227
5 K. Takiyama, T. Katsuta, M. Watanabe, S. Li, T. Oda, T. Ogawa and K. Mizuno, Rev. Sci. Instrum. **68** (1997) 1028
6 H. Toyota, M. Watanabe, K. Takiyama and T. Oda, Jpn. J. Appl. Phys. **36** (1997) 4670.
7 K. Takiyama, H. Sakai, M. Yamasaki and T. Oda, Jpn. J. Appl. Phys. **33** (1994) 5038.
8 S. Matsuo and M. Kiuchi, Jpn. J. Appl. Phys. **22** (1983) L210.

# Linear X-Ray Line Polarization Effects on Spectral Measurements Using an Electron Beam Ion Trap

Peter Beiersdorfer

*Department of Physics and Space Technology*
*Lawrence Livermore National Laboratory, Livermore, CA 94550, USA*

Line emission from an electron beam ion trap (EBIT) source is produced in the collision of trapped ions with a uni-directional electron beam and generally is linearly polarized. This polarization must be taken into account when using spectrocopic data to infer cross sections for electron-ion interaction processes. A good theoretical and experimental understanding of polarization effects is, therefore, paramount for accurate measurements. On the other hand, the source provides a unique environment for measuring the amount of linear polarization under very well controlled conditions. As a result, predictions of linear polarization caused by uni-directional electron impact can be tested. A review of polarization effects on spectral measurements employing an EBIT source is given. The technique for measurements of the linear line polarization using the two crystal technique is discussed, and new results for the polarized K-shell emission from heliumlike $Fe^{24+}$ for energies up to 120 keV are presented.

## 1. Introduction

The Electron Beam Ion Trap (EBIT) device utilizes a dense ($< 5 \times 10^{12}$ cm$^{-3}$) mono-energetic beam of electrons to produce and excite highly charged ions from virtually any element or isotope of choice. By analyzing the line radiation emitted in the interaction between the ions and the electron beam, cross sections can be determined for the particular electron-ion interaction process studied. For example, the device has been used to measure the electron-impact excitation cross sections of the K-shell transitions in heliumlike $Ti^{20+}$ through $Fe^{24+}$ [1,2], the resonance strengths of dielectronic recombination satellites [3], including those involving high-n spectator satellites [4,5], and the cross sections for electron-impact ionization of lithiumlike ions [6]. The device has also been used to measure indirect excitation processes such as innershell ionization and radiative cascades [7].

As was shown in Refs. [8] and [9], quasi-stationary ions colliding with unidirectional electrons emit line radiation that is generally both anisotropic and polarized. Therefore, the intensity of a specific line depends on the observation angle relative to the axis defined by the electron beam and on whether or not the emission is analyzed with a polarization-sensitive instrument. Polarization phenomena, thus, play an important role in EBIT measurements, and, if not taken properly into account, can lead to results that are wrong. This means that cross section measurements on an EBIT, even measurements of relative cross sections, require a good understanding of polarization effects.

While polarization effects complicate the analysis of spectral line formation processes in EBIT, these effects can be measured directly and the amount of linear polarization can be inferred. In fact, EBIT represents a unique spectroscopic facility for studying alignment processes in highly charged ions by directional electrons in a

controlled, well characterized laboratory environment.

Here, we review the measurements of linear polarization of x-ray lines that have been performed with the EBIT source, and we present the results of recent measurements that show that the EBIT technique can be used to measure the linear polarization not only at threshold, but also at energies ten to twenty times the threshold energy, or, in the case of the $Fe^{24+}$ K-shell lines at electron energies above 100 keV. Such high-energy measurements are of special importance for polarization spectroscopy. In many plasmas, polarized line emisstion is produced by a suprathermal tail in the electron distribution function with energies that are orders of magnitude larger than the bulk thermal energy. The testing of theoretical predictions of ion alignment away from the threshold energy for line excitation is therefore of critical importance for evaluating the predictive capabilities of theory.

## 2. Anisotropy of the Emitted Radiation

For the conditions given in an EBIT, we assume quasi-stationary ions colliding with electrons traveling along the z-direction, i.e., we assume cylindrical symmetry. This is a good assumption as long as the electron beam energy is large compared to the thermal energy of the electrons. (In the case where this assumption does not hold, see the contribution by Savin, Gu, and Beiersdorfer in these Proceedings). Using the formalism developed by Steffen and Alder [10], the two intensity components of linearly polarized line radiation with electric field vector parallel and perpendicular to the electron beam direction can then be described by

$$I_{\parallel}(\vartheta) = \frac{1}{8\pi} \sum_{\lambda=even} B_\lambda A_\lambda [P_\lambda(\vartheta) + \Gamma(\kappa) f_\lambda P_\lambda^2(\vartheta)] \langle I_{\parallel} \rangle \qquad (1)$$

and

$$I_{\perp}(\vartheta) = \frac{1}{8\pi} \sum_{\lambda=even} B_{\lambda} A_{\lambda} [P_{\lambda}(\vartheta) - \Gamma(\kappa) f_{\lambda} P_{\lambda}^{2}(\vartheta)] \langle I_{\perp} \rangle, \tag{2}$$

as discussed in more detail in Ref. [11]. Here, $B_{\lambda}$ is the orientation parameter; $A_{\lambda}$ is the angular distribution coefficient; $P_{\lambda}(\vartheta)$ and $P_{\lambda}^{2}(\vartheta)$ represent the Legendre and associated Legendre polynominal, respectively; $\langle I_{\parallel} \rangle$ and $\langle I_{\perp} \rangle$ are the $4\pi$-averaged intensity components. We assume that the emitted radiation is described by a single multipole operator where $\lambda$ represents the multipole order of the emitted radiation.

The parameters $B_{\lambda}$ are given by

$$B_{\lambda} = \sum_{m} (-1)^{J_i + m} [(2\lambda + 1)(2J_i + 1)]^{1/2} \begin{pmatrix} J_i & J_i & \lambda \\ -m & m & 0 \end{pmatrix} \sigma_m. \tag{3}$$

Here $J_i$ is the initial total angular momentum, $m$ is the magnetic quantum number, and $\sigma_m$ is the population density of each respective sublevel normalized such that $\Sigma_m \sigma_m = 1$. The large parentheses denote the Wigner 3-$j$ symbol. The angular distribution coefficient $A_{\lambda}$ is given by

$$A_{\lambda} = (-1)^{J_i + J_f - 1} [(2\lambda + 1)(2J_i + 1)]^{1/2} (2L + 1) \begin{pmatrix} L & L & \lambda \\ 1 & -1 & 0 \end{pmatrix} \begin{Bmatrix} L & L & \lambda \\ J_i & J_i & J_f \end{Bmatrix} \tag{4}$$

$L$ represents the order of pure $2^L$ multipole decays. The large braces denote the Wigner 6-$j$ symbol. The coefficient $f_{\lambda}$ is given by

$$f_{\lambda} = -\left[\frac{(\lambda - 2)!}{(\lambda + 2)!}\right]^{1/2} \frac{\begin{pmatrix} L & L & \lambda \\ 1 & 1 & -2 \end{pmatrix}}{\begin{pmatrix} L & L & \lambda \\ 1 & -1 & 0 \end{pmatrix}}. \tag{5}$$

The function $\Gamma(\kappa)$ determines the sign. For electric multipole transitions it equals $\Gamma(E) = 1$, for magnetic multipole transitions it equals $\Gamma(M) = -1$.

The intensity variation of the emitted radiation $I(\vartheta)$ is given by the sum of $I_{\|}(\vartheta)$ and $I_{\perp}(\vartheta)$:

$$I(\vartheta) = \frac{1}{4\pi} \sum_{\lambda=even} B_\lambda A_\lambda P_\lambda(\vartheta) \langle I_s \rangle. \tag{6}$$

Here, $\langle I_s \rangle$ is the $4\pi$-averaged line source intensity, i.e.,

$$\int I(\vartheta) d\Omega = \langle I_s \rangle. \tag{7}$$

Defining the linear polarization $P$ at an observation angle $\vartheta = 90^o$ relative to the z-axis as the fractional difference between the intensity of light with electric field vector parallel to the beam direction, $I_{\|}$, and the intensity of light with electric field vector perpendicular, $I_{\perp}$,

$$P = \frac{I_{\|}(90^o) - I_{\perp}(90^o)}{I_{\|}(90^o) + I_{\perp}(90^o)}, \tag{8}$$

and evaluating the coefficients in Eq. (6), we find the following expressions for the angular variation of the intensity of the emitted light. For an electric dipole (E1) transitions (with $L = 1$) we find

$$I(\vartheta) = \frac{3}{4\pi} \frac{1 - P\cos^2\vartheta}{3 - P} \langle I_s \rangle. \tag{9}$$

For a magnetic dipole (M1) transitions ($L = 1$) we find

$$I(\vartheta) = \frac{3}{4\pi} \frac{1 + P\cos^2\vartheta}{3 + P} \langle I_s \rangle. \tag{10}$$

Generally, the angular intensity variation of higher-order multipole transitions cannot be expressed as a simple expression of $P$. In the case of the $1s2p\ ^3P_2 \rightarrow 1s^2\ ^1S_0$ magnetic dipole quadrupole (M2) transition ($L = 2$) in heliumlike systems, one can show that $B_4(^3P_2) << B_2(^3P_2)$. For the case of heliumlike $Fe^{24+}$ it was shown in Ref. [11] that $B_4(^3P_2)/B_2(^3P_2) \approx 1.6 \times 10^{-3}$. Thus, this M2 transition behaves as a dipole transition. In particular, its angular intensity variation is given by

$$I(\vartheta) = \frac{3}{4\pi} \frac{1 - P\cos^2\vartheta}{3 - P} \langle I_s \rangle, \tag{11}$$

i.e., it is identical to that of E1 transitions.

The anisotropy in the line emission of linearly polarized lines can be illustrated by looking at the spectra predicted for the K-shell emission of heliumlike $Fe^{24+}$. At threshold of excitation and ignoring cascade effects, the polarizations of the four K-shell transitions in $Fe^{24+}$ have been predicted in Refs. [12] to be +0.584, −0.518, −0.196, and 0.0 for the transitions $1s2p\ ^1P_1 \rightarrow 1s^2\ ^1S_0$ (labeled $w$ in the notation of Ref. [14]), $1s2p\ ^3P_2 \rightarrow 1s^2\ ^1S_0$ (labeled $x$), $1s2p\ ^3P_1 \rightarrow 1s^2\ ^1S_0$ (labeled $y$), and $1s2s\ ^3S_1 \rightarrow 1s^2\ ^1S_0$ (labeled $z$), respectively. A comparison of the $4\pi$-average spectral emission with that observed at $\vartheta = 0°$ and $\vartheta = 90°$ is given in Fig. 1. Because the angular dependence of the emission is different for each line, there are dramatic differences in the spectral shape when looking at different observation angles relative to the electron beam direction. In fact, the ratio of the intensities of $w$ and $x$ changes by a factor of about three when the viewing angle is changed from $\vartheta = 0°$ to $\vartheta = 90°$.

A second example of the angular dpendence of the emitted line radiation is given in Fig. 2, where we show the predicted spectra of the K-shell satellites of $Fe^{24+}$ produced by the KLL dielectronic recombination resonances. These lines are all electric dipole transitions. Their polarizations have been given by Inal and Dubau [13], ranging from −0.75 to +0.60. Again, a dramatic difference can be seen when comparing the spectral emission at $\vartheta = 0°$ with that at $\vartheta = 90°$, or with the $4\pi$ averaged emission. From these examples it is very clear that it is imperative that the polarization of every line is known lest significant uncertainties in the line intensities are made.

The construction of the EBIT allows viewing of the ions in the trap via radial ports, i.e., in the plane perpendicular to the electron beam direction at $\vartheta = 90°$, as shown in Fig. 3. A direct view into the trap along the axis of the electron beam at $\vartheta = 90°$ is possible as well. The solid angle subtended by the latter line of sight is, however, very small because any axial spectrometer must be placed about 10 times

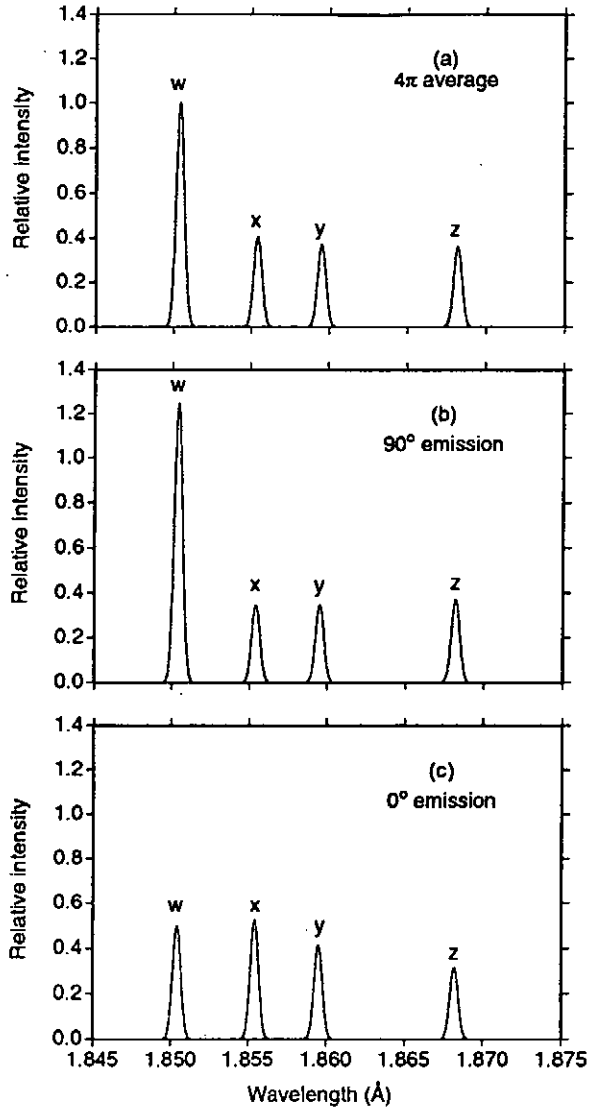


Figure 1: Predicted spectral line intensities of the resonance line $w$, the intercombination lines $x$ and $y$, and the forbidden line $z$ in heliumlike $Fe^{24+}$ excited by collisions with a 6850-eV electron beam: (a) emission averaged over a $4\pi$ solid angle; (b) emission observed at an angle $\vartheta = 90^{o}$, i.e., in the plane perpendicular to the electron beam direction; (c) emission observed at an angle $\vartheta = 0^{o}$, i.e., a line of sight along the electron beam direction.

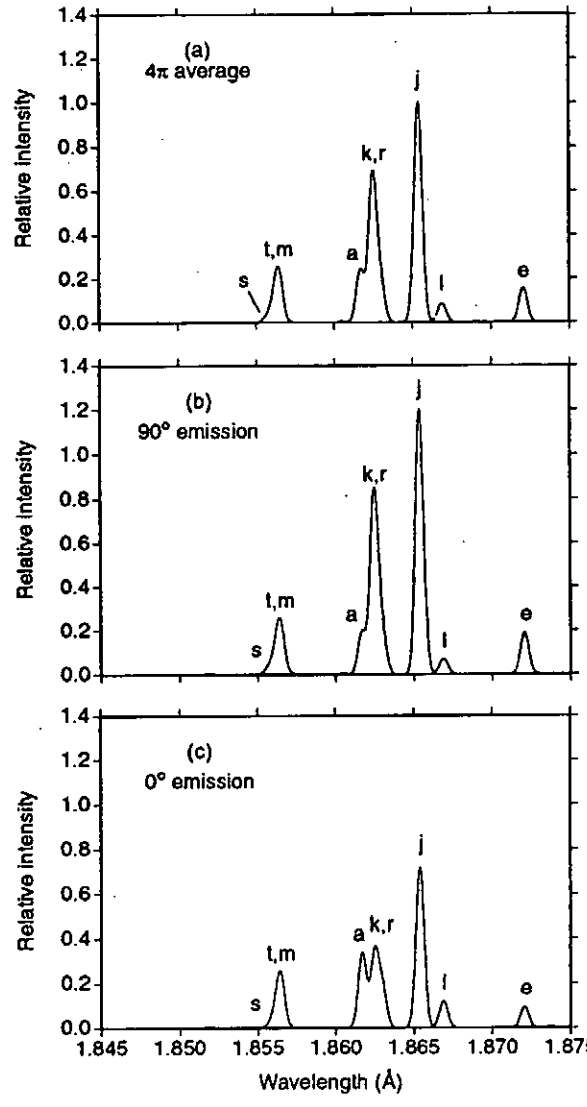


Figure 2: Predicted spectral line intensities of the $2 \rightarrow 1$ dielectronic satellite transitions of heliumlike $Fe^{24+}$ produced by KLL resonant electron capture: (a) emission averaged over a $4\pi$ solid angle; (b) emission observed at an angle $\vartheta = 90°$, i.e., in the plane perpendicular to the electron beam direction; (c) emission observed at an angle $\vartheta = 0°$, i.e., a line of sight along the electron beam direction. The transitions are labeled in standard notation (cf. Ref. [14]).

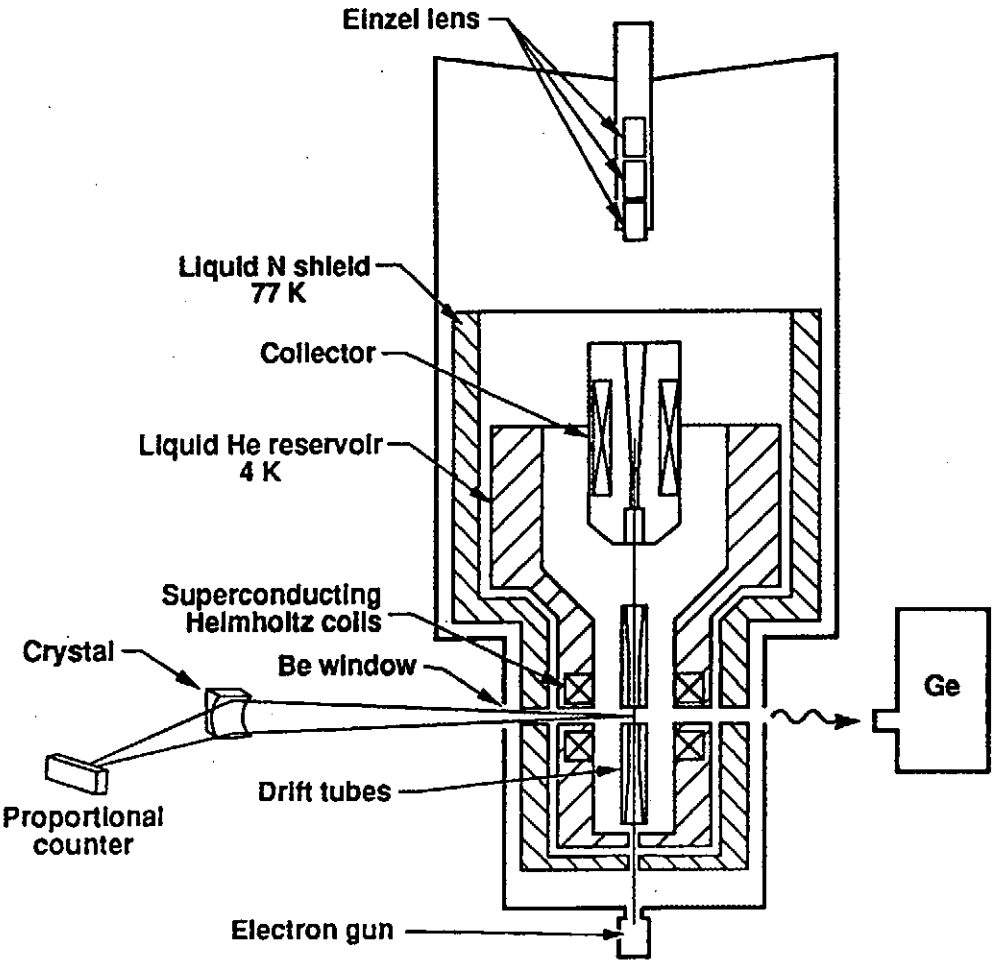


Figure 3: Schematic layout of the crystal-spectrometer on the LLNL EBIT facility. Ions are produced and trapped in a 2-cm long region between the superconducting Helmholtz coils. The ions are excited by an electron beam propagating between the electron gun and the collector. X rays are analyzed and dispersed with crystal spectrometers in the plane perpendicular to the direction of the electron beam.

further away from the trap than any radial spectrometer. As result, all line emission spectra from highly charged ions have so far been recorded at observation angles of $\vartheta = 90^o$.

## 3. Crystal-Spectrometer Measurements

The use of crystal spectrometers adds another dimension to the complexity of accurate interpretation of polarized x-ray line emission. The reflectivity of a given crystal depends on whether the electric field vector lies parallel or perpendicular to the diffraction plane. Moreover, the reflectivity for each polarization component depends on the Bragg angle and the type of crystal (for some crystal types on the individual specimen) used. The relative intensities of the observed spectral lines will thus depend on the type of crystal, the Bragg angle, and value of the linear polarization of each line.

The intensity of an x-ray line observed on EBIT with a crystal spectrometer at $90^o$ to the beam direction can be written as

$$I^{obs} = R_{||} I_{||} + R_{\perp} I_{\perp}. \tag{12}$$

Here, $R_{||}$ and $R_{\perp}$ are the integrated crystal reflectivities for x rays polarized parallel and perpendicular to the electron beam directions, i.e., perpendicular and parallel to the plane of dispersion, respectively.

The ratio $R = R_{\perp}/R_{||}$ depends strongly on the Bragg angle $\theta$, as illustrated in Fig. 4. For mosaic crystals the ratio varies as $\cos^2(2\theta)$; for perfect crystals it varies as $|\cos(2\theta)|$ [15]. The ratio for actual crystals lies in between the two extremes. Most crystals approach the values for perfect crystals although the value of $R$ is typically reduced by absorption. Calculations of integrated reflectivities of perfect crystals can be found, for example, in Ref. [16].

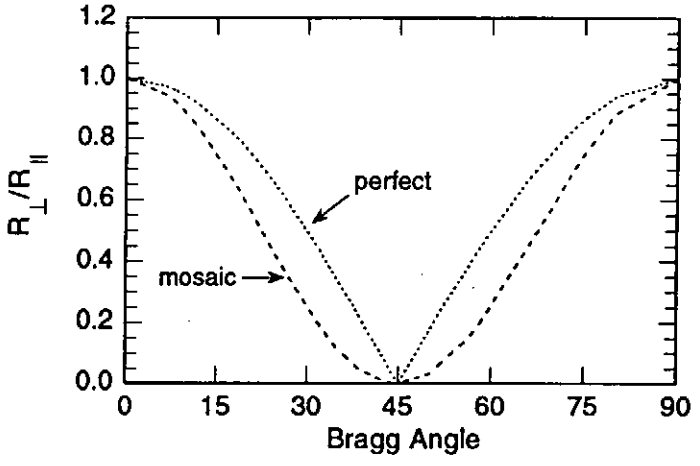


Figure 4: Variation of the relative crystal reflectivities $R_\perp/R_{||}$ for x rays polarized perpendicular and parallel to the electron beam direction. The dotted line represents the values for a mosaic crystal; the dashed line represents the values for an ideal crystal. At a Bragg angle of 45° the reflection of the perpendicular component vanishes for any type of crystal, $R_\perp/R_{||} = 0$.

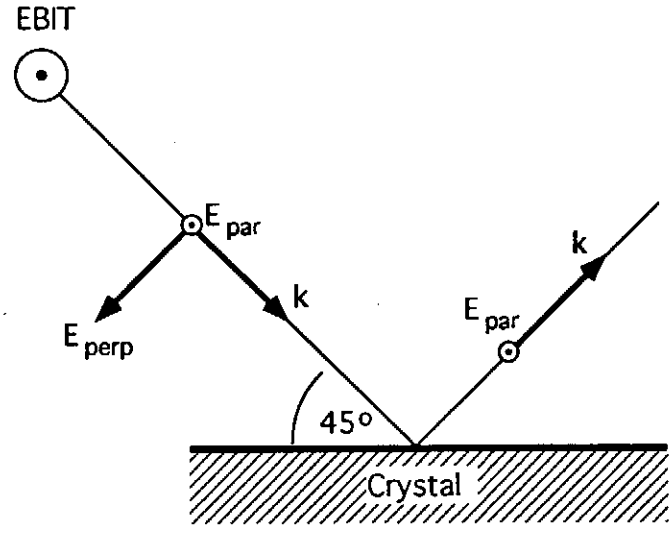


Figure 5: Schematic diagram of the reflection of linearly polarized x rays off a crystal surface at a Bragg angle of 45°. The electron beam is in the direction out of the page as indicated at the EBIT position. The plane of dispersion of the crystal is perpendicular to the beam direction. Only the parallel polarization state is reflected; the polarization state perpendicular to is completely absorbed by the crystal.

Because analyzing crystals reflect the two polarization components differently the intensity observed with crystal spectrometers differs from the emitted intensity. The effect is strongest at $\theta = 45^{\circ}$ where $I_{\perp}$ vanishes and only $I_{||}$ is observed, as illustrated in Fig. 5. Consequently, the intensity of negatively polarized lines, i.e., lines with $I_{\perp} > I_{||}$ are disproportionally reduced when observed near $\theta = 45^{\circ}$. Positively polarized lines appear enhanced. Near $\theta = 90^{\circ}$ or $0^{\circ}$, both polarization components are reflected nearly equally, and the observed spectra are the least altered by crystal effects.

For the spectrum of heliumlike iron, the polarization depedendence of the crystal

reflectivity means that line $w$ will be enhanced, while lines $y$ and especially $x$ are strongly reduced when observed near $\theta = 45^o$. This was indeed observed and reported in Ref. [17]. The two spectra of $Fe^{24+}$ simultaneously observed with two different crystals in Ref. [17] are shown in Fig. 6. The first spectrometer used a LiF(220) crystal with lattice spacing $2d = 2.848$ Å and observed the lines at a nominal Bragg angle of $41^o$. The second used a Si(220) crystal with lattice spacing $d = 3.840$ Å and observed the lines at a nominal Bragg angle of $29^o$. The relative reflectivities $R_\perp/R_\parallel = 0.48$ for Si(220) and $R_\perp/R_\parallel = 0.12$ for LiF(220) [16]. As expected from the difference in the relative crystal reflectivities, the relative intensities of the four heliumlike lines differ notably in the two spectra. The triplet lines are suppressed relative to the singlet line intensity in both spectra, but this suppression is much more pronounced in the spectrum obtained with the LiF(220) crystal. Predictions of the spectral line emission based on the values of the relative reflectivities are also shown in Fig. 6, and good agreement with the measurements is found. Again, it is clear from this discussion that it is imperative that the amount of linear polarization is known. Moreover, it is very important to account for the crystal spectrometer response to the polarized line emission.

## 4. Measurements of the Degree of Linear X-ray Line Polarization

While the dependence of the observed spectral line emission on the amount of polarization, the Bragg angle, and the type of crystal employed in the observation complicates the analysis of spectral data from an EBIT device, it also represents a unique opportunity. By making simultaneous measurements of x-ray line spectra with two spectrometers, such as those presented in Fig. 6, the degree of linear polarization

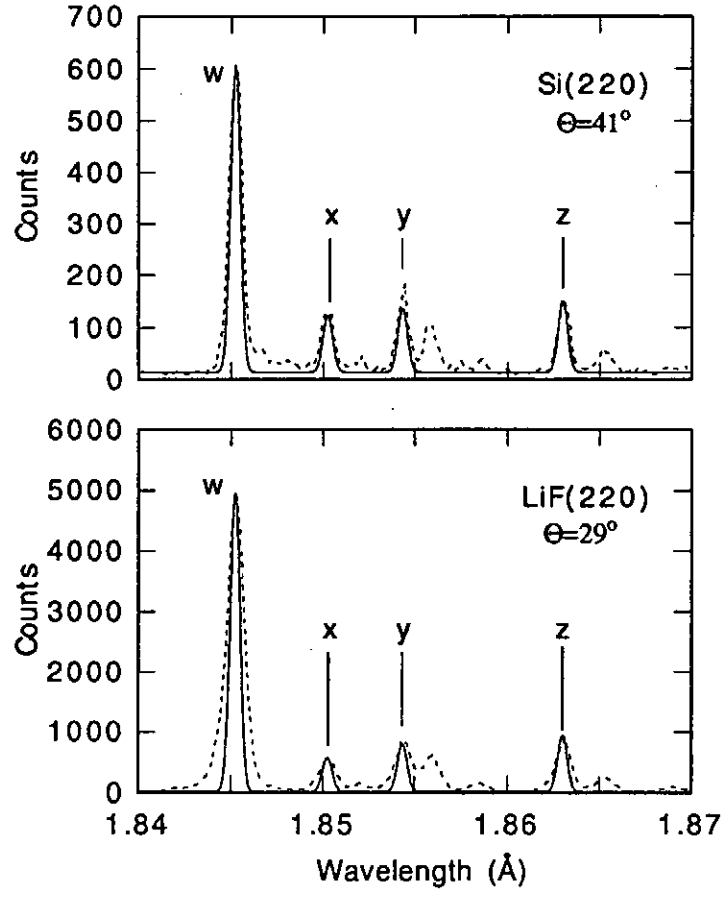


Figure 6: Crystal-spectrometer spectra of the four lines $w$, $x$, $y$, and $z$ in heliumlike $Fe^{24+}$ excited by direct electron-impact excitation by a 6850-eV electron beam (dashed lines). The top spectrum was obtained with a Si(220) crystal at a Bragg angle of about 41°; the bottow spectrum was obtained with a LiF(220) crystal at a Bragg angle of about 29°. Unlabled features are from lower charge states of iron. The predicted spectral intensities (solid lines), normalized to the intensity of line $w$, are superimposed for comparison.

of a given line can be determined provided the relative crystal reflectivities are known and the two spectra can be normalized to each other with the help of lines that have a known amount of linear polarization.

Making use of Eq. (12), the intensity ratio of two lines $a$ and $b$ observed with crystal $C1$ is given by

$$\frac{I^a}{I^b}|_{C1} = \frac{I^a_{||} + R_{C1} I^a_{\perp}}{I^b_{||} + R_{C1} I^b_{\perp}}. \tag{13}$$

Here, we assumed that $R = R_{\perp}/R_{||}$ is constant in the range of Bragg angles spanned by the two lines. Similarly, the ratio of the two lines observed with crystal $C2$ is

$$\frac{I^a}{I^b}|_{C2} = \frac{I^a_{||} + R_{C2} I^a_{\perp}}{I^b_{||} + R_{C2} I^b_{\perp}}. \tag{14}$$

Making use of Eq. (8) and combing Eqs. 13 and 14, we can express the polarization $P_a$ of line $a$ in terms of the polarization $P_b$ of line $b$:

$$P_a = \frac{\frac{I^a}{I^b}|_1 (1 + R_1 \frac{1-P_b}{1+P_b})(R_2 + 1) - \frac{I^a}{I^b}|_2 (1 + R_2 \frac{1-P_b}{1+P_b})(R_1 + 1)}{\frac{I^a}{I^b}|_1 (1 + R_1 \frac{1-P_b}{1+P_b})(R_2 - 1) - \frac{I^a}{I^b}|_2 (1 + R_2 \frac{1-P_b}{1+P_b})(R_1 - 1)} \tag{15}$$

From Eq. (15) it follows that the polarization of a given line can be determined by measuring the difference of its intensity when looked at with two spectrometers relative to that of the known line.

Because transitions from upper levels with total angular momentum $J$=1/2 are stricly unpolarized, they provide excellent reference lines for polarization measurements. This fact has been used by Savin *et al.*, as discussed in these proceedings. They measured the polarization of the $4p_{3/2} \rightarrow 2s_{1/2}$ transition in lithiumlike $Fe^{23+}$ by comparing it to the close by and unpolarized $4p_{1/2} \rightarrow 2s_{1/2}$ transition.

In the following, we are concerned about the polarization of the heliumlike K-hell transitions. No unpolarized line exists among the heliumlike transitions. However, near threshold for electron-impact excitation the polarization of the forbidden line $z$ is

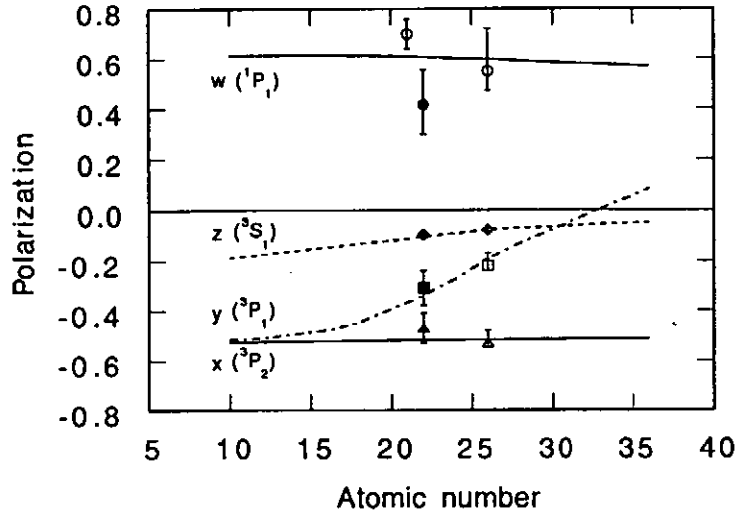


Figure 7: Predicted polarizations of the four $2 \rightarrow 1$ transitions $w$, $x$, $y$, and $z$ in the heliumlike ions $Ne^{8+}$ through $Kr^{34+}$. The predictions are for nuclei without a magnetic moment. The newly measured values for $Ti^{20+}$ from Ref. [18] are shown for comparison. Also shown are the measured values for $Fe^{24+}$ from Ref. [11] and the value for the resonance line in $Sc^{19+}$ from Ref. [19].

completely determined by that of line $x$ because of cascade contributions, as discussed in Ref. [11]. This linkage was shown to enable a determination of the polarization of all observed lines in the heliumlike K-shell spectrum in the absence of an unpolarized reference line [11].

The technique was originally applied to heliumlike $Fe^{24+}$ [11]. The results of this measurement are shown in Fig. 7. Recently, we have applied the technique to a measurement of the polarization of the K-shell transitions in heliumlike $Ti^{20+}$. The titanium ions were excited about 100 eV above the direct electron-impact excitation threshold and simultaneously observed with a Si(111) crytal at $\theta = 24.7°$ and a Si(220)

crytal at $\theta = 43.1^{o}$. The details of this measurement will be described elsewhere [18]. The results from this measurement are also given in Fig. 7. For comparison, the figure shows the polarization predictions for different heliumlike ions from relativistic distorted-wave calculations [11]. Very good agreement is found.

The figure also shows the measured value for line $w$ in heliumlike $Sc^{19+}$ measured by Henderson *et al.* [19]. This datum was obtained with a modified technique. Instead of using two crystals with different reflection properties, only one crystal was used but measurements were made in two planes of diffraction. The first was made in the same plane as described above; the second was made in the plane perpendicular to the first by rotating the entire spectrometer by $90^{o}$. The latter technique has also been applied to measurements of the linear polarization of $3s \rightarrow 2p$ transitions in neonlike $Ba^{46+}$ [20].

In order to test the predictions away from threshold measurements are currently in progress at the Livermore high-energy EBIT facility to determine the linear polarization of the heliumlike $Fe^{24+}$ lines at very high electron beam energy. These measurements employ two LiF crystals cut to the (220) and (200) planes. Results for the $w$ line obtained at beam energies as high as 120 keV are shown in Fig. 8. The results are compared to predictions and good agreement is found. The analysis of the remaining heliumlike lines is still in progress and will be published at a future date [21].

## 5. Conclusion

Because an EBIT uses a monoenergetic electron beam, polarization effects are maximized. This provides a unique opportunity to test the calculations of the linear polarization of the line emission from highly charged ions in a controlled laboratory

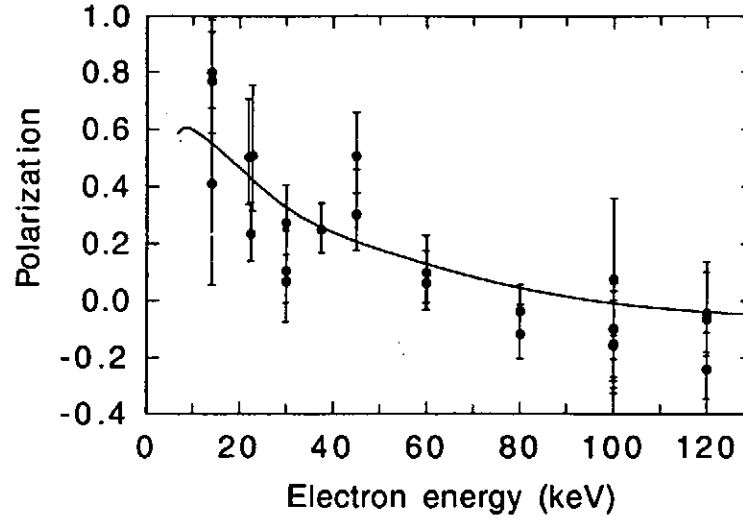


Figure 8: Measured polarization values of the resonance line $w$ heliumlike $Fe^{24+}$ for different electron beam energies from Ref. [21]. Predictions from Inal and Dubau from Ref. [12] are shown for comparison.

setting.

Depsite this great opportunity only a small number of such measurements have been performed to date. These include measurements of the 1–2 K-shell line emission from heliumlike $Sc^{19+}$ [19] and $Fe^{24+}$ [11] mentioned above, and measurements of the $3s \rightarrow 2p$ line emission in neonlike $Ba^{46+}$ [20]. These measurements were performed at or close to threshold for electron-impact excitation. As we have shown, new measurements have been undertaken at the Livermore EBITs to extend the polarization measurements to the K-shell transitions of $Ti^{20+}$ and to electron energies nearly twenty times above threshold in the case of $Fe^{24+}$. So far, very good agreement with relativistic distorted-wave calculations was found [12,22,23].

Polarization measurements with the Livermore EBIT have recently also been ex-

tended to cover dielectronic satellite emission of lithiumlike, berylliumlike, and boron-like iron [24,25], as discussed by Shlyaptseva *et al.* in these proceedings. These measurements test the accuracy of the calculations of alignment in resonant processes. Again, good agreement was found.

In addition, polarization measurements also have been concerned with L-shell transitions of $Fe^{23+}$, as discussed by Savin, Gu, and Beiersdorfer in these proceedings. These measurements were made at rather low beam energies ($\approx$ 2000 eV). At such low electron energies, the EBIT source no longer represents an ideal beam-ion collision experiment. The thermal electron motion perpendicular to the beam direction starts to play an important role and depolarization effects become relevant. However, as the contribution by Savin *et al.* shows, such depolarization effects are small compared to the accuracy limits of a given polarization measurement and to first approximation can be ignored or approximately accounted for. However, as the electron energy is yet smaller ($<$ 1000 eV), such effects may play a significant role.

Measurements of polarization are still only in their infancy and many classes of measurements have yet to be performed. For example, no measurements that include substantial cascade contributions have yet been made and compared with theory. The presence of a nuclear magnetic field was shown to have a strong effect on the observed linear polarization in heliumlike $Sc^{19+}$ [19]. But this has not been investigated in any other system. Aluminum would be a suitable candidate, since this element has been employed routinely in investigations of laser-produced plasmas.

Because of the growing importance of plasma polarization spectroscopy in the research of high-temperature plasmas, we expect that many more measurements of the linear polarization of x-ray lines (and of UV, and visible lines) will be undertaken with EBITs. Because only very little has been studied so far, the field represents a fertile ground for exciting new discoveries and the development of novel, polarization-

based spectral diagnostics.

## Acknowledgments

The author would like to G. Brown, V. Decaux, J. Lepson, S. Utter, and K. Widmann for their contributions to the measurements and analyses presented. This work was supported by the Department of Energy, Office of Basic Energy Science, Division of Chemical Science, and the National Aeronautics and Space Administration X-Ray Astronomy Research and Analysis Program under work order W-19127 and performed under the auspices of the Department of Energy by Lawrence Livermore National Laboratory under contract W-7405-ENG-48.

## References


[1] S. Chantrenne, P. Beiersdorfer, R. Cauble, and M. B. Schneider, Phys. Rev. Lett. **69**, 265 (1992).

[2] K. L. Wong, P. Beiersdorfer, K. J. Reed, and D. A. Vogel, Phys. Rev. A **51**, 1214 (1995).

[3] P. Beiersdorfer, T. W. Phillips, K. L. Wong, R. E. Marrs, and D. A. Vogel, Phys. Rev. A **46**, 3812 (1992).

[4] P. Beiersdorfer, M. B. Schneider, M. Bitter, and S. von Goeler, Rev. Sci. Instrum. **63**, 5029 (1992).

[5] A. J. Smith, P. Beiersdorfer, V. Decaux, K. Widmann, K. J. Reed, and M. H. Chen, Phys. Rev. A **54**, 462 (1996).

[6] K. Wong, P. Beiersdorfer, M. H. Chen, R. E. Marrs, K. J. Reed, J. H. Scofield, D. A. Vogel, and R. Zasadzinski, Phys. Rev. A **48**, 2850 (1993).

[7] P. Beiersdorfer, A. L. Osterheld, M. H. Chen, J. R. Henderson, D. A. Knapp, M. A. Levine, R. E. Marrs, K. J. Reed, M. B. Schneider, and D. A. Vogel, Phys. Rev. Lett. **65**, 1995 (1990).

[8] J. R. Oppenheimer, Z. Phys. **43**, 27 (1927).

[9] I. C. Percival and M. J. Seaton, Philos. Trans. R. Soc. London **A251**, 113 (1958).

[10] R. M. Steffen and K. Alder, in *The Electromagnetic Interaction in Nuclear Spectroscopy*, edited by W. D. Hamilton (North-Holland, New York, 1975), p. 505.

[11] P. Beiersdorfer, D. A. Vogel, K. J. Reed, V. Decaux, J. H. Scofield, K. Widmann, G. Hölzer, E. Förster, O. Wehrhan, D. W. Savin, and L. Schweikhard, Phys. Rev. A **53**, 3974 (1996).

[12] M. K. Inal and J. Dubau, J. Phys. B **20**, 4221 (1987).

[13] M. K. Inal and J. Dubau, J. Phys. B **22**, 3329 (1989).

[14] A. H. Gabriel, Mon. Not. R. Astron. Soc. **160**, 99 (1972).

[15] A. Burek, Space Sci. Instrum. **2**, 53 (1976).

[16] B. L. Henke, E. M. Gullikson, and J. C. Davis, At. Data Nucl. Data Tables **54**, 181 (1993).

[17] P. Beiersdorfer, J. Crespo López-Urrutia, V. Decaux, K. Widmann, and P. Neill, Rev. Sci. Instrum. **68**, 1073 (1997).

[18] P. Beiersdorfer, G. V. Brown, S. B. Utter, E. J. Clothiaux, and A. J. Smith, in preparation .

[19] J. R. Henderson, P. Beiersdorfer, C. L. Bennett, S. Chantrenne, D. A. Knapp, R. E. Marrs, M. B. Schneider, K. L. Wong, G. A. Doschek, J. F. Seely, C. M. Brown, R. E. LaVilla, J. Dubau, and M. A. Levine, Phys. Rev. Lett. **65**, 705 (1990).

[20] E. Takács, E. S. Meyer, J. D. Gillaspy, J. R. Roberts, C. T. Chandler, L. T. Hudson, R. D. Deslattes, C. M. Brown, J. M. Laming, J. Dubau, and M. K. Inal, Phys. Rev. A **54**, 1342 (1996).

[21] P. Beiersdorfer, J. K. Lepson, and K. Widmann, in preparation .

[22] H. L. Zhang, D. H. Sampson, and R. E. H. Clark, Phys. Rev. A **41**, 198 (1990).

[23] K. J. Reed and M. H. Chen, Phys. Rev. A **48**, 3644 (1993).

[24] A. S. Shlyaptseva, R. C. Mancini, P. Neill, and P. Beiersdorfer, Rev. Sci. Instrum. **68**, 1095 (1997).

[25] A. S. Shlyaptseva, R. C. Mancini, P. Neill, P. Beiersdorfer, J. Crespo López-Urrutia, and K. Widmann, Phys. Rev. A **57**, 888 (1998).

# The effects of electron spiraling on the anisotropy and polarization of photon emission from an electron beam ion trap

D. W. Savin[1], M. F. Gu[1], and P. Beiersdorfer[2]

[1]Columbia Astrophysics Laboratory and Department of Physics, Columbia University, New York, NY 10027

[2] Department of Physics and Space Technology, Lawrence Livermore National Laboratory, Livermore, CA 94550

**Abstract**

We present a theoretical formalism for calculating the anisotropy and polarization of photon emission due to a spiraling beam of electrons in an electron beam ion trap (EBIT). We present measurements of the polarization for the Fe XXIV $4p\ ^2P_{3/2} \rightarrow 2s\ ^2S_{1/2}$ X-ray transition due to electron impact excitation. We discuss these results, together with previously reported EBIT polarization measurements, in the light of electron spiraling. We find that spiraling effects cannot yet be discerned in these measurements. This is important for many EBIT measurements concerned with X-ray line intensity measurements. While the amount of spiraling is not accurately known, neglecting its effects introduces an error typically no larger than that given by counting statistics.

## 1 Introduction

A unidirectional beam of electrons colliding with atomic or ionic targets may produce anisotropically emitted, partially polarized line radiation [1, 2, 3]. The emitted intensity from the target system depends upon the angle of observation relative to the axis defined by the beam. The measured intensity depends upon the angle of observation and whether or not the instrument used to analyze the emission is polarization sensitive. In this paper we discuss anisotropy and polarization issues relating to electron-ion collision studies which use an electron beam ion trap (EBIT) and detect the resulting photon emission. In particular we focus on the effect on the observed polarization of electron motion perpendicular to the electron beam direction.

EBITs use a magnetically confined, directed beam of unpolarized electrons to produce and trap an ensemble of unpolarized ions [4, 5, 6]. The theoretical formulae for calculating polarization of photon emission from an EBIT has been presented by Beiersdorfer *et al.* [7] for a unidirectional beam. The electrons in an EBIT, however, are not truly unidirectional [7, 8, 9]. They possess a velocity component $\mathbf{v}_\perp$ which is perpendicular to the confining magnetic field $\mathbf{B}$. This produces spiraling along $\mathbf{B}$. The pitch angle $\theta$ is given by $\sin^2\theta = E_\perp/E$ where $E_\perp$ is the electron energy component due to $\mathbf{v}_\perp$ and $E$ is the total electron energy.

The average value of $E_\perp$ depends on the EBIT operating conditions, but we can estimate it for optimal operating conditions. The electron beam in an EBIT is formed in a region of low magnetic field strength. The $\mathbf{B}$ field in the trapping region is typically $\sim 3$ T. Using the principle of adiabatic invariants [10, 11] gives

$$E_\perp = E_{\perp c}\left(\frac{r_c}{r_b}\right)^2 = E_{\perp c}\left(\frac{B}{B_c}\right) \tag{1}$$

where $E_{\perp c}$ is the transverse energy of the electrons at the cathode, $r_c$ is the radius of the beam at the cathode, $r_b$ is the radius of the beam in the trapping region, and $B_c$ is the magnetic field strength at the cathode. $E_{\perp c}$ is roughly given by the cathode temperature $k_B T_c$ where $k_B$ is the Boltzmann constant and $T_c$ is the cathode temperature. For the Lawrence-Livermore EBIT, $r_c = 1.5$ mm, $r_b \sim 30$ $\mu$m and $k_B T_e \sim 0.1$ eV [4, 5, 7] which yields $E_\perp \sim 250$ eV. $E_\perp$ has also been estimated for the NIST EBIT [12] using two different techniques. The first technique used the electron cyclotron frequency as an upper limit on the rigid

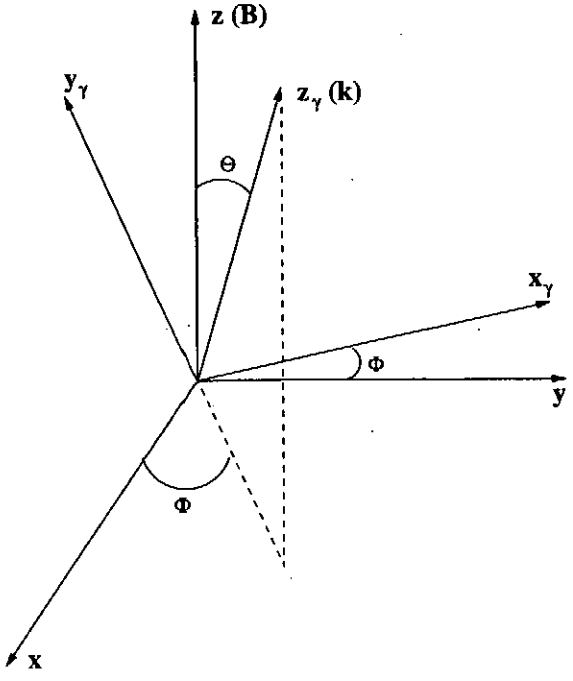


Figure 1: The relationship between the laboratory frame $S$ and the photon frame $S_\gamma$. The projection of the $z_\gamma$-axis onto the $xy$-plane is shown by the dashed lines. The $x_\gamma$-axis lies in the $xy$-plane.

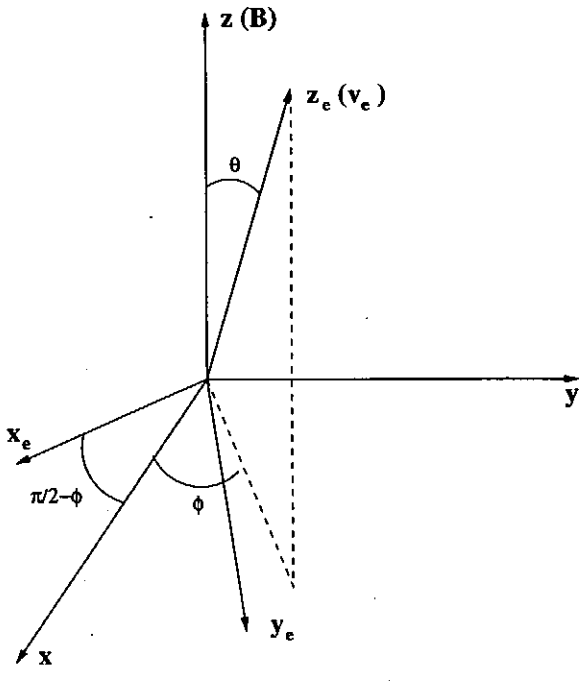


Figure 2: The relationship between the laboratory frame $S$ and the electron frame $S_e$. The projection of the $z_e$-axis onto the $xy$-plane is shown by the dashed lines. The $x_e$-axis lies in the $xy$-plane.

rotation of the beam, from which an estimate of $E_\perp \lesssim 700$ eV was derived [9]. The second technique involved a theoretical estimate of $B_c$. Takács *et al.* [9] derived a value of $B_c \sim 225$ $\mu$T. Their cathode temperature was $k_B T_c \sim 0.13$ eV and they find $E_\perp \sim 1700$ eV.

In this paper we investigate the effects of a non-vanishing value of $E_\perp$, *i.e.* of electron spiraling, on EBIT measurements. In Section 2 we use the theoretical formalism given by Stefan and Alder [13] to describe the photon emission from an EBIT taking spiraling into account. Section 3 discusses experiments to measure the polarization of the Fe XXIV $4p\ ^2P_{3/2} \rightarrow 2s\ ^2S_{1/2}$ transition produced by electron impact excitation (EIE). Section 4 discusses measurement uncertainties and presents our results. In Section 5 we discuss the results of our new polarization measurements as well as several previously reported EBIT polarization measurements [7, 8, 9] in the light of the effects of electron spiraling.

## 2 Theory

Here we develop theoretical expressions for the predicted angular distribution of photon emission from an EBIT. We are interested in collision processes which form an excited ion of initial total angular momentum $J_i$ which then radiatively decays to a final state of total angular momentum $J_f$. Our analysis follows the prescription of Steffen and Alder [13] and is valid for initial and final states of definite angular momentum.

We begin by defining three reference frames: the laboratory frame, the photon frame, and the electron frame. The relationship between the three is shown in Figures 1 and 2. In the laboratory frame $S$, $\mathbf{B}$ defines the $+z$-axis. In this frame, the directions of the electron velocity $\mathbf{v_e}$ and of the emitted photon $\mathbf{k}$ are given, respectively, by their polar angles $\theta$ and $\Theta$, and azimuthal angles $\phi$ and $\Phi$. The $+z$-axes of the photon frame $S_\gamma$ and the electron frame $S_e$ are determined by $\mathbf{k}$ and $\mathbf{v_e}$, respectively. The $+x$-axis of $S_\gamma$ is defined by $\mathbf{B} \times \mathbf{k}$. To bring $S$ to $S_\gamma$, a rotation $R(\Phi, \Theta, \pi/2)$ is performed, where $R(\alpha, \beta, \gamma)$ is the rotation operator expressed in Euler angles [14, 15]. We define the $+x$-axis of $S_e$ by $\mathbf{v_e} \times \mathbf{B}$. A rotation $R(-\pi/2, \theta, \pi - \phi)$

brings $S_e$ to $S$.

For radiative decays $i \rightarrow f$, the probability of detecting a photon emitted in the direction $\mathbf{k}$ using a detector with an efficiency matrix $\varepsilon$ is given by [13]

$$W(\mathbf{k},\varepsilon) = \sum_{\tau,\tau'} < \tau|\rho_0^0(J_f)|\tau' >< \tau'|\varepsilon|\tau > (2J_f+1)^{1/2} \tag{2}$$

where $< \tau|\rho_0^0(J_f)|\tau' >$ is the reduced matrix operator in the $S$ frame for a single photon process, $\rho_0^0(J_f)$ is a $2\times 2$ matrix, and $\tau$ and $\tau'$ label photon helicity states. A label of $\tau$ or $\tau' = +1(-1)$ corresponds to left(right) circularly polarized light [14]. Re-expressing $< \tau|\rho_0^0(J_f)|\tau' >$ in terms of the statistical tensor before photon emission, $\rho_q^\lambda(J_i)$, gives

$$\begin{aligned} < \tau|\rho_0^0(J_f)|\tau' > &= \frac{d\Omega}{8\pi} \sum_{LL'\lambda q} \frac{\begin{pmatrix} L & L' & \lambda \\ \tau & -\tau' & \mu \end{pmatrix}}{\begin{pmatrix} L & L' & \lambda \\ 1 & -1 & 0 \end{pmatrix}} \left(\frac{2J_i+1}{2J_f+1}\right)^{1/2} \rho_q^\lambda(J_i) \\ &\times[\gamma(EL)+\tau\gamma(ML)][\gamma^*(EL')+\tau'\gamma^*(ML')] \\ &\times F_\lambda(LL'J_fJ_i) D_{q\mu}^{(\lambda)*}(S\rightarrow S_\gamma) \Big/ \sum_{L\pi}|\gamma(\pi L)|^2. \end{aligned} \tag{3}$$

Here $L$ is the order of what Steffen and Alder call a pure $2^L$ multipole decay; the quantities in the large parenthesis denote Wigner 3-$j$ symbols; and $\gamma(\pi L)$ is the multipole transition amplitude with $\pi = E(M)$ for electric(magnetic) transitions. $F_\lambda(LL'J_fJ_i)$ is given by

$$F_\lambda(LL'J_fJ_i) = (-1)^{J_f+J_i-1}[(2\lambda+1)(2L+1)(2L'+1)(2J_i+1)]^{1/2} \begin{pmatrix} L & L' & \lambda \\ 1 & -1 & 0 \end{pmatrix} \begin{Bmatrix} L & L' & \lambda \\ J_i & J_i & J_f \end{Bmatrix} \tag{4}$$

where the quantity in the large braces denotes a Wigner 6-$j$ symbol. The properties and values of the 3-$j$ and 6-$j$ symbols are given by Cowan [16]. $D_{q\mu}^{(\lambda)*}(S\rightarrow S_\gamma) = D_{q\mu}^{(\lambda)*}(\Phi,\Theta,\pi/2)$ is the rotation matrix from $S$ to $S_\gamma$. The rotation matrices are described in detail in Refs. [14] and [15].

EBIT measurements commonly use detectors which are sensitive to linearly polarized radiation. For these detectors, the efficiency matrix in the representation of helicity states is given by [13]

$$\varepsilon = \frac{\mathcal{E}}{2} \begin{pmatrix} 1 & -Qe^{-i2\alpha} \\ -Qe^{i2\alpha} & 1 \end{pmatrix} \tag{5}$$

where $\mathcal{E}$ is the total efficiency of the detector; $\alpha$ is the angle between the polarization axis of the detector and the $x_\gamma$-axis; and $Q$ is the linear polarization efficiency. We define the efficiency for radiation polarized along the polarization axis of the detector as $\mathcal{E}_p = \frac{\mathcal{E}}{2}(1+Q)$ and perpendicular to the polarization axis as $\mathcal{E}_s = \frac{\mathcal{E}}{2}(1-Q)$. The efficiency matrix may now be written as

$$\varepsilon = \frac{1}{2} \begin{pmatrix} \mathcal{E}_s+\mathcal{E}_p & (\mathcal{E}_s-\mathcal{E}_p)e^{-i2\alpha} \\ (\mathcal{E}_s-\mathcal{E}_p)e^{i2\alpha} & \mathcal{E}_s+\mathcal{E}_p \end{pmatrix} \tag{6}$$

A straightforward manipulation of Equation 3 gives

$$< \tau|\rho_0^0(J_f)|\tau > = \frac{d\Omega}{8\pi} \left(\frac{2J_i+1}{2J_f+1}\right)^{1/2} \sum_{\lambda q} \tau^\lambda \rho_q^\lambda(J_i) A_\lambda^\pm D_{q0}^{(\lambda)*}(S\rightarrow S_\gamma) \tag{7}$$

$$< \tau|\rho_0^0(J_f)|-\tau > = \frac{d\Omega}{8\pi} \left(\frac{2J_i+1}{2J_f+1}\right)^{1/2} \sum_{\lambda q} \tau^\lambda \rho_q^\lambda(J_i) A_{\lambda,2}^\pm D_{q\mp 2}^{(\lambda)*}(S\rightarrow S_\gamma). \tag{8}$$

$A_\lambda^+$, $A_{\lambda,2}^+$, and $D_{q-2}^{(\lambda)*}$ ($A_\lambda^-$, $A_{\lambda,2}^-$, and $D_{q2}^{(\lambda)*}$) correspond to $\tau = +1(-1)$ and

$$A_\lambda^+ = \sum_{L\pi L'\pi'} F_\lambda(LL'J_fJ_i)\gamma(\pi L)\gamma^*(\pi' L') \Big/ \sum_{L\pi}|\gamma(\pi L)|^2 \tag{9}$$

$$A^{-}_{\lambda} = \sum_{L\pi L'\pi'} (-1)^{L+L'+\Lambda(\pi)+\Lambda(\pi')} F_\lambda(LL'J_fJ_i)\gamma(\pi L)\gamma^*(\pi' L') \Big/ \sum_{L\pi} |\gamma(\pi L)|^2 \tag{10}$$

$$A^{+}_{\lambda,2} = \sum_{L\pi L'\pi'} (-1)^{\Lambda(\pi')} \frac{\begin{pmatrix} L & L' & \lambda \\ 1 & 1 & -2 \end{pmatrix}}{\begin{pmatrix} L & L' & \lambda \\ 1 & -1 & 0 \end{pmatrix}} F_\lambda(LL'J_fJ_i)\gamma(\pi L)\gamma^*(\pi' L') \Big/ \sum_{L\pi} |\gamma(\pi L)|^2 \tag{11}$$

$$A^{-}_{\lambda,2} = \sum_{L\pi L'\pi'} (-1)^{L+L'+\Lambda(\pi)} \frac{\begin{pmatrix} L & L' & \lambda \\ 1 & 1 & -2 \end{pmatrix}}{\begin{pmatrix} L & L' & \lambda \\ 1 & -1 & 0 \end{pmatrix}} F_\lambda(LL'J_fJ_i)\gamma(\pi L)\gamma^*(\pi' L') \Big/ \sum_{L\pi} |\gamma(\pi L)|^2 \tag{12}$$

where $\Lambda(E) = 0$ and $\Lambda(M) = 1$. It can be shown that $A^{\pm *}_{\lambda} = A^{\pm}_{\lambda}$ and $A^{\pm *}_{\lambda,2} = (-1)^{\lambda} A^{\mp}_{\lambda,2}$, which ensures that $\rho^0_0(J_f)$ is hermitian. Symetry under time reversal implies the transition amplitudes $\gamma(\pi L)$ are all real or all pure imaginary [14]. So $A^{\pm}_{\lambda,2}$ is real and $A^{\pm}_{\lambda,2} = (-1)^{\lambda} A^{\mp}_{\lambda,2}$. The angular distribution factor can now be written

$$\begin{aligned} W(\Phi,\Theta,\alpha,\mathcal{E}_p,\mathcal{E}_s) &= \frac{d\Omega}{16\pi} \sum_{\lambda q} (2J_i+1)^{1/2} \rho^{\lambda}_q(J_i) \\ &\times \Bigg\{ (\mathcal{E}_p + \mathcal{E}_s)(A^{+}_{\lambda} + (-1)^{\lambda} A^{-}_{\lambda}) \left(\frac{4\pi}{2\lambda+1}\right)^{1/2} Y^*_{\lambda q}(\Theta,\Phi) \\ &-(\mathcal{E}_p - \mathcal{E}_s)\Big[ A^{+}_{\lambda,2} D^{(\lambda)*}_{q-2}(\Phi,\Theta,\pi/2+\alpha) \\ &+(-1)^{\lambda} A^{-}_{\lambda,2} D^{(\lambda)*}_{q2}(\Phi,\Theta,\pi/2+\alpha)\Big] \Bigg\}. \end{aligned} \tag{13}$$

Here we have used [15]

$$D^{(\lambda)*}_{q0}(\Phi,\Theta,\pi/2) = \left(\frac{4\pi}{2\lambda+1}\right)^{1/2} Y^*_{\lambda q}(\Theta,\Phi) \tag{14}$$

where $Y_{\lambda q}$ is the spherical harmonic and

$$D^{(\lambda)*}_{q\pm 2}(\Phi,\Theta,\pi/2+\alpha) = D^{(\lambda)*}_{q\pm 2}(\Phi,\Theta,\pi/2) e^{\pm i2\alpha}. \tag{15}$$

The radiating system is formed by an electron colliding with a quasistationary ion. In this, the $S_e$ frame, the system is axisymmetric along $\mathbf{v_e}$ and the initial statistical tensor $\rho'^{\lambda}_q$ is nonzero only for $q = 0$. The statistical tensors in $S$ and $S_e$ are related by the rotation

$$\begin{aligned} \rho^{\lambda}_q(J_i,\theta,\phi) &= \sum_{q'} \rho'^{\lambda}_{q'}(J_i) D^{(\lambda)*}_{q'q}(-\pi/2,\theta,\pi-\phi) \\ &= \rho'^{\lambda}_0(J_i) D^{(\lambda)*}_{0q}(-\pi/2,\theta,\pi-\phi) \end{aligned} \tag{16}$$

where

$$\rho'^{\lambda}_0(J_i) = \sum_m (-1)^{J_i+m} (2\lambda+1)^{1/2} \begin{pmatrix} J_i & J_i & \lambda \\ -m & m & 0 \end{pmatrix} g_m. \tag{17}$$

The factor $g_m$ represents the population density of the magnetic sublevel $m$. The $m$ values are quantized along $\mathbf{v_e}$. The density matrix $\rho'$ is normalized so that $\mathrm{Tr}\rho' = \sum_m g_m = 1$. It is convenient to introduce the orientation parameters which are defined as

$$B_\lambda(J_i) = (2J_i+1)^{1/2} \rho'^{\lambda}_0(J_i). \tag{18}$$

The density matrix is normalized so that $B_0$=1.

The electrons in an EBIT can be described by a pitch angle distribution $f(\cos\theta)$, which we normalize so that $\int_{-1}^{1} d(\cos\theta) f(\cos\theta) = 1$. The electrons travel along the $\sim 3$ T magnetic field lines in the trapping volume, spiraling incoherently with a cyclotron frequency of $\sim 5.3\times10^{11}$ revolutions $s^{-1}$. For kinetic energies $\lesssim 100$ keV, the electrons undergo $\gtrsim 25$ revolutions as they traverse the observed central 1 cm length of the trap. This large number of revolutions allows us to calculate the initial statistical tensor of the radiating system by averaging Equation 16 over $\theta$ and $\phi$. This gives

$$\begin{aligned}
\rho_q^{\lambda}(J_i) &= \int_{-1}^{1} d(\cos\theta) f(\cos\theta) \int_0^{2\pi} \frac{d\phi}{2\pi} \rho_q^{\lambda}(J_i,\theta,\phi) \\
&= \rho_0'^{\lambda}(J_i) \int_{-1}^{1} d(\cos\theta) f(\cos\theta) \int_0^{2\pi} \frac{d\phi}{2\pi} D_{0q}^{(\lambda)*}(-\pi/2,\theta,\pi-\phi) \\
&= \delta_{q0} g_\lambda \rho_q'^{\lambda}(J_i) \qquad (19)
\end{aligned}$$

where

$$g_\lambda = \int_{-1}^{1} d(\cos\theta) f(\cos\theta) P_\lambda(\cos\theta) \qquad (20)$$

and $P_\lambda(\cos\theta)$ is the Legendre polynomial. Using Equations 13, 18, and 19 yields the angular distribution factor for radiation produced by a spiraling beam of electrons,

$$\begin{aligned}
W(\Phi,\Theta,\alpha,\mathcal{E}_p,\mathcal{E}_s) &= \frac{d\Omega}{16\pi} \sum_\lambda g_\lambda B_\lambda \Big\{ (\mathcal{E}_p+\mathcal{E}_s)(A_\lambda^+ + (-1)^\lambda A_\lambda^-) P_\lambda(\cos\Theta) - (\mathcal{E}_p-\mathcal{E}_s) \\
&\quad \times \Big[ A_{\lambda,2}^+ D_{0-2}^{(\lambda)*}(\Phi,\Theta,\pi/2+\alpha) + (-1)^\lambda A_{\lambda,2}^- D_{02}^{(\lambda)*}(\Phi,\Theta,\pi/2+\alpha) \Big] \Big\}. \qquad (21)
\end{aligned}$$

Here we have used

$$\left(\frac{4\pi}{2\lambda+1}\right)^{1/2} Y_{\lambda 0}^*(\Theta,\Phi) = P_\lambda(\cos\Theta). \qquad (22)$$

Parity is typically a good quantum number for atomic states. When this is true, the multipole transition amplitudes $\gamma(\pi L)$ and $\gamma(\pi' L')$, which link the same initial and final states, vanish unless

$$\pi_i \pi_f = (-1)^{L+\Lambda(\pi)} = (-1)^{L'+\Lambda(\pi')} \qquad (23)$$

where $\pi_i$ and $\pi_f$ are the parities of the initial and final states [14]. This ensures that $(-1)^{L+L'+\Lambda(\pi)+\Lambda(\pi')} = 1$. We can now define the angular distribution coefficients $A_\lambda$ and $A_{\lambda,2}$ as

$$A_\lambda \equiv A_\lambda^+ = A_\lambda^- \qquad (24)$$

$$A_{\lambda,2} \equiv A_{\lambda,2}^+ = A_{\lambda,2}^-. \qquad (25)$$

Since $A_{\lambda,2} = (-1)^\lambda A_{\lambda,2}$, it vanishes for $\lambda = odd$. $A_\lambda$ is normalized so that $A_0 = 1$. The rotation matrix elements $D_{0\pm2}^{(\lambda)*}$ can be expressed [15, 17]

$$D_{0\pm2}^{(\lambda)*}(\Phi,\Theta,\pi/2+\alpha) = -\left(\frac{(\lambda-2)!}{(\lambda+2)!}\right)^{1/2} P_\lambda^{(2)}(\cos\Theta) e^{\mp i2\alpha} \qquad (26)$$

where $P_\lambda^{(2)}(\cos\Theta)$ is the associated Legendre polynomial. Using Equations 21, 24, 25, and 26 gives

$$\begin{aligned}
W(\Phi,\Theta,\alpha,\mathcal{E}_p,\mathcal{E}_s) &= \frac{d\Omega}{8\pi} \sum_{\lambda=even} g_\lambda B_\lambda \Bigg[ (\mathcal{E}_p+\mathcal{E}_s) A_\lambda P_\lambda(\cos\Theta) \\
&\quad + (\mathcal{E}_p-\mathcal{E}_s) A_{\lambda,2} \left(\frac{(\lambda-2)!}{(\lambda+2)!}\right)^{1/2} P_\lambda^{(2)}(\cos\Theta)\cos 2\alpha \Bigg]. \qquad (27)
\end{aligned}$$

The above derivation is valid for an admixture of multipole transitions. For atomic systems, the approximation of transitions as single multipole operators is accurate so long as $(\alpha Z_{eff})^2 \ll 1$, where $\alpha$ is the fine

structure constant and $Z_{eff}$ is the effective nuclear charge of the ion [18]. In this approximation, $L = L'$ and the angular distribution coefficients become

$$A_\lambda = F_\lambda(LLJ_fJ_i) \tag{28}$$

$$A_{\lambda,2} = (-1)^{\Lambda(\pi)} \frac{\begin{pmatrix} L & L & \lambda \\ 1 & 1 & -2 \end{pmatrix}}{\begin{pmatrix} L & L & \lambda \\ 1 & -1 & 0 \end{pmatrix}} A_\lambda. \tag{29}$$

The angular distribution factor can now be written

$$\begin{aligned} W(\Theta, \alpha, \mathcal{E}_p, \mathcal{E}_s) &= \frac{d\Omega}{8\pi} \sum_{\lambda=even} g_\lambda A_\lambda B_\lambda \Big[ (\mathcal{E}_p + \mathcal{E}_s) P_\lambda(\cos\Theta) \\ &\quad - (\mathcal{E}_p - \mathcal{E}_s) f_\lambda(L) P_\lambda^{(2)}(\cos\Theta) \cos 2\alpha \Big] \end{aligned} \tag{30}$$

where

$$f_\lambda(L) = -(-1)^{\Lambda(\pi)} \left( \frac{(\lambda-2)!}{(\lambda+2)!} \right)^{1/2} \frac{\begin{pmatrix} L & L & \lambda \\ 1 & 1 & -2 \end{pmatrix}}{\begin{pmatrix} L & L & \lambda \\ 1 & -1 & 0 \end{pmatrix}}. \tag{31}$$

Taking $\mathcal{E}_p(\mathcal{E}_s) = 1(0)$ and $\mathcal{E}_p(\mathcal{E}_s) = 0(1)$, the emitted angular distribution along the $p$ and $s$ axes of the detector, is given, respectively, by

$$W_{p(s)}(\Theta, \alpha) = \frac{d\Omega}{8\pi} \sum_{\lambda=even} g_\lambda A_\lambda B_\lambda \Big[ P_\lambda(\cos\Theta) \mp f_\lambda(L) P_\lambda^{(2)}(\cos\Theta) \cos 2\alpha \Big] \tag{32}$$

where the $-(+)$ corresponds to the $p(s)$ polarization component of the radiation. The polarization factor $P(\Theta, \alpha)$ can be defined

$$\begin{aligned} P(\Theta, \alpha) &= \frac{W_s(\Theta, \alpha) - W_p(\Theta, \alpha)}{W_s(\Theta, \alpha) + W_p(\Theta, \alpha)} \\ &= \cos 2\alpha \frac{\sum_{\lambda=even} f_\lambda(L) P_\lambda^{(2)}(\cos\Theta) g_\lambda B_\lambda A_\lambda}{\sum_{\lambda=even} P_\lambda(\cos\Theta) g_\lambda B_\lambda A_\lambda}. \end{aligned} \tag{33}$$

For a non-spiraling beam, $\Theta = \pi/2$, and $\alpha = 0$, this matches with the standard definition of the polarization factor [1, 2, 3]. Equation 30 can now be expressed in terms of $P(\Theta, \alpha)$ as

$$W(\Theta, \alpha, \mathcal{E}_p, \mathcal{E}_s) = \frac{d\Omega}{8\pi} \Big[ (\mathcal{E}_s + \mathcal{E}_p) + (\mathcal{E}_s - \mathcal{E}_p) P(\Theta, \alpha) \Big] \sum_{\lambda=even} P_\lambda(\cos\Theta) g_\lambda A_\lambda B_\lambda \tag{34}$$

For a polarization insensitive detector, $\mathcal{E}_p = \mathcal{E}_s = \mathcal{E}/2$, and

$$W(\Theta) = \frac{\mathcal{E} d\Omega}{4\pi} \sum_{\lambda=even} g_\lambda A_\lambda B_\lambda P_\lambda(\cos\Theta). \tag{35}$$

The vast majority of EBIT measurements involve the detection of dipole radiation ($L = 1$) using photon detectors placed so that $\Theta = \pi/2$ and $\alpha = 0$. For this situation

$$P = \frac{\mp 3 g_2 A_2 B_2}{2 - g_2 A_2 B_2}. \tag{36}$$

Here we have used

$$\begin{aligned} P_0(0) &= +1 \\ P_2(0) &= -\frac{1}{2} \\ P_2^{(2)}(0) &= +3 \\ f_2(1) &= \mp\frac{1}{2} \\ g_0 = A_0 = B_0 &= +1 \end{aligned}$$

where $-(+)$ corresponds to electric(magnetic) dipole radiation. We define $P = \mathcal{P}$ for situations where the pitch angle of the electrons $\theta = 0$, in which case $g_\lambda = 1$ and

$$\mathcal{P} = \frac{\mp 3 A_2 B_2}{2 - A_2 B_2}. \tag{37}$$

Re-writing equation 37 in terms of $A_2 B_2$ gives

$$A_2 B_2 = \frac{2\mathcal{P}}{\mathcal{P} \mp 3}. \tag{38}$$

$P$ can now expressed in terms of $\mathcal{P}$ as

$$P = \mathcal{P}\frac{3 g_2}{3 \mp (1 - g_2)\mathcal{P}}. \tag{39}$$

If the electrons have an arbitrary fixed pitch angle $\theta_0$, *i.e.* $f(\cos\theta) = \delta(\cos\theta - \cos\theta_0)$, then

$$\begin{aligned} g_2 &= -\frac{1}{2} + \frac{3}{2}\cos^2\theta_0 \\ &= 1 - \frac{3}{2}\epsilon \end{aligned} \tag{40}$$

where $\epsilon = \sin^2\theta_0 = E_\perp / E$. The polarization of photon emission from an EBIT is then given by

$$P = \mathcal{P}\frac{2 - 3\epsilon}{2 \mp \epsilon\mathcal{P}} \tag{41}$$

and the angular distribution factor by

$$W(\mathcal{E}_p, \mathcal{E}_s) = \frac{d\Omega}{8\pi}\left[(\mathcal{E}_s + \mathcal{E}_p) + (\mathcal{E}_s - \mathcal{E}_p)P\right]\frac{3}{3 \mp P}. \tag{42}$$

Thus we find for dipole radiation that if $f(\cos\theta) = \delta(\cos\theta - \cos\theta_0)$ accurately describes the electron pitch angle distribution, then the effect of electron spiraling on the anisotropy and polarization of the emitted radiation can be fully and easily accounted for using only the pitch angle $\theta_0$ and the polarization $\mathcal{P}$ for a non-spiraling electron beam.

The upper level in the $i \rightarrow f$ decay may sometimes be populated by cascades from a higher-lying excited level. The effect of cascades on the predicted emission is calculated through the use of the de-orientation factor as described by Stefan and Alder [13] and applied to atomic transitions by Beiersdorfer *et al.* [7]. This factor is unaffected by electron spiraling.

# 3 Experimental Technique

The electron density in the Lawrence-Livermore EBITs [4, 5, 19] can be varied between $\sim 10^{11} - 10^{13}$ cm$^{-3}$. The energy spread of the electron beam for typical operating parameters is $\Delta E \sim 50$ eV [5, 20]. For typical measurement energies $\Delta E/E << 1$ and the beam energy can be approximated as monoenergetic. In this approximation, the total line formation rate can be written

$$I = \sigma(E) v_e(E) \int n_e(\mathbf{r}) n_q(\mathbf{r}) d^3\mathbf{r} \tag{43}$$

where $\sigma$ is the total cross section for collisionally producing the line of interest and includes cascade contributions; $n_e(\mathbf{r})$ is the electron density at $\mathbf{r}$; $n_q(\mathbf{r})$ is the density at $\mathbf{r}$ of ions in charge state $q$ of the element of interest; and $\int d^3\mathbf{r}$ is over the volume of the trap. Excited ions are assumed to radiatively decay on a time scale significantly shorter than either the trapping time of the ions or the timescale over which the charge balance in the trap may change.

The diameter of the electron beam in EBIT is $\sim$ 60 $\mu$m [5]. The attractive potential of the electron beam and the applied magnetic field confine the ions in the radial direction. The temperature of the ions is $\sim$ 600 eV for operating parameters typically used for EBIT spectroscopy measurements [21, 22]. If the radiative lifetime of the excited ions is $\lesssim 10^{-9}$ s, then the excited ions will radiatively decay primarily within the confines of the electron beam. Photon emission from EBIT is thus similar to that from an entrance slit for a spectrometer.

We have used a flat crystal spectrometer (FCS) [23, 24], for the present measurements. Crystal spectrometers are polarization sensitive instruments. The reflectivity of a crystal is different for photons polarized perpendicular to the dispersion plane ($s$-polarized) and for photons polarized in the dispersion plane ($p$-polarized) [25, 26]. The dispersion plane of the FCS on EBIT is perpendicular to the magnetic field that confines the electrons (*i.e.*, $\Theta = \pi/2$ and $\alpha = 0$). The FCS views the central $\sim$ 1 cm length of the trap. Between EBIT and the FCS is a 4$\mu$m thick polypropelene window. X-rays are detected using a flowing gas proportional counter [27] with a 4$\mu$m thick polypropelene window. There is a continuous flow of 90% Ar and 10% $CH_4$ at a constant pressure of $\sim$ 1 atmosphere. A series of vertical apertures collimate the observed emission for a maximum divergence of $\lesssim$ 18 milliradians in the vertical dimension. In the horizontal dimension the angular width of the collected radiation overfills the angular acceptance angle of the crystals used.

The intensity of a dipole transition as measured using a crystal spectrometer can be calculated by multiplying Equations 42 and 43. $W$ is essentially constant over the solid angle collected by the crystal spectrometer (CS). So, setting $\mathcal{E}_p = TD\psi R_p$ and $\mathcal{E}_s = TD\psi R_s$, we have

$$I^{CS} = \frac{3TD\psi[(R_s + R_p) + (R_s - R_p)P]}{2(3 \mp P)} \left(\frac{I}{4\pi}\right) \tag{44}$$

where $T$ accounts for all window transmittances, $D$ is the detection efficiency of the proportional counter, $\psi$ is the effective vertical angle collected by the spectrometer, and $R_s$ and $R_p$ are the integrated reflectivities of the crystal for radiation polarized, respectively, perpendicular to and parallel to the dispersion plane. The solid angle $d\Omega$ is implicitly accounted for in the terms $\psi R_s$ and $\psi R_p$.

Polarization measurements of dipole transitions are carried out using a crystal spectrometer and simultaneously observing two lines, $a$ and $b$, with nearly identical Bragg angles. If the two line are emitted by the same charge state, then the measured line ratio will be independent of $\int n_e n_q d^3\mathbf{r}$. Assuming that $T$, $A$, $R_s$, and $R_p$ are essentially constant over the range of Bragg angles spanned by the two lines, then we may use Equations 43 and 44 to write

$$\frac{I_a^{CS}}{I_b^{CS}} = \frac{[1 + f + (1 - f)P_a]\sigma_a}{[1 + f + (1 - f)P_b]\sigma_b} \tag{45}$$

where $f = R_p/R_s$. Polarization factors are determined by observing the same pair of lines with two different crystals. Using Equation 45 for the two different crystals, 1 and 2, $P_a$ can be expressed in terms $P_b$ as

$$P_a = \frac{\left(\frac{I_a}{I_b}\right)_2 \left(f_1 + 1\right)\left(\frac{1-P_b}{1+P_b} f_2 + 1\right) - \left(\frac{I_a}{I_b}\right)_1 \left(f_2 + 1\right)\left(\frac{1-P_b}{1+P_b} f_1 + 1\right)}{\left(\frac{I_a}{I_b}\right)_2 \left(f_1 - 1\right)\left(\frac{1-P_b}{1+P_b} f_2 + 1\right) - \left(\frac{I_a}{I_b}\right)_1 \left(f_2 - 1\right)\left(\frac{1-P_b}{1+P_b} f_1 + 1\right)}. \tag{46}$$

where we have dropped the $CS$ superscript for convenience. Equation 46 simplifies somewhat if the $J_i = 1/2$ for line $b$. For this situation, $B_\lambda(1/2)$ is nonzero only for $\lambda \leq 1$ so that $P_b = 0$.

# 4 Measurement

Measurement of the Fe XXIV $4p\,^2P_{3/2} - 2s\,^2S_{1/2}$ polarization produced by EIE were carried out by measuring its intensity relative to that of the $4p\,^2P_{1/2} - 2s\,^2S_{1/2}$ transition using two different crystals. Since $J_i = 1/2$ for the $4p\,^2P_{1/2} - 2s\,^2S_{1/2}$ transition, the line is unpolarized and thus provides an ideal polarization reference.

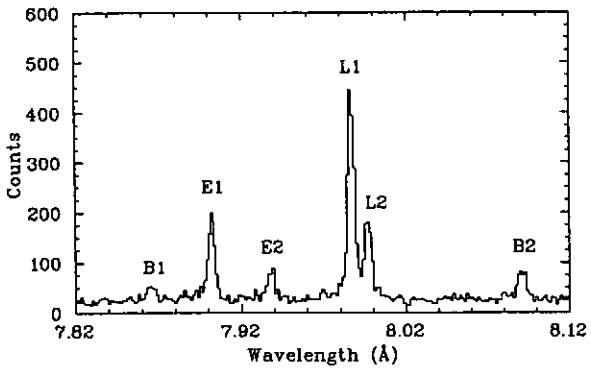


Figure 3: Iron spectrum recorded at an electron beam energy of 4.6 keV. The spectrum was collected over $\sim$ 26 hours using an ammonium dihydrogen phosphate (101) crystal in first order. Lines are labeled using the notation of Table 1.

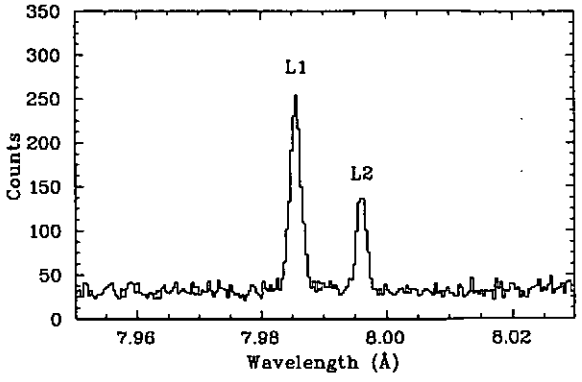


Figure 4: Iron spectrum recorded at an electron beam energy of 4.6 keV. The spectrum was collected over $\sim$ 27 hours using an $\alpha$-quartz $(10\bar{1}0)$ crystal in first order. Lines are labeled using the notation of Table 1.

| Label | Fe Ion | Transition | $\lambda$ (Å) |
|---|---|---|---|
| B1 | XXII | $2s^2 2p\ ^2P_{1/2} - 2s2p_{1/2}5p_{1/2,3/2}$ | 7.865 |
| E1 | XXIII | $2s2p\ ^1P_1 - 2s5d\ ^1D_2$ | 7.901 |
| E2 | XXIII | $2s2p\ ^1P_1 - 2s5s\ ^1S_0$ | 7.936 |
| L1 | XXIV | $2s\ ^2S_{1/2} - 4p\ ^2P_{3/2}$ | 7.986 |
| L2 | XXIV | $2s\ ^2S_{1/2} - 4p\ ^2P_{1/2}$ | 7.996 |
| B2 | XXII | $2s^2 2p\ ^2P_{1/2} - 2s^2 5d\ ^2D_{3/2}$ | 8.091 |

Table 1: Observed iron spectral lines. Line identifications and wavelengths come from Wargelin *et al.* [28]. The labeling convention is L for Li-like Fe XXIV, E for Be-like Fe XXIII, and B for B-like Fe XXII

Representative iron spectra collected for the present results are shown in Figures 3 and 4. Figure 3 was obtained using an ammonium dihydrogen phosphate [ADP (101)] crystal and Figure 4 using an $\alpha$-quartz $(10\bar{1}0)$ crytsal. All spectra were collected in first order. Line ratios were determined using the fitted integrated line intensities. Observed lines are listed in Table 1. Line identifications and wavelengths are from Wargelin *et al.* [28]. The spectra consist entirely of lines due to Fe XXII, XXIII, and XXIV. Spectra collected when no iron ions were in the trap were devoid of any discernable spectral lines. Contamination of the observed spectra from elements other than iron is thus believed to be insignificant.

Observed line intensities may be affected by recombination-cascade processes such as charge transfer (CT) with background gas molecules or radiative recombination (RR) with either beam electrons or low energy background electrons. The effects of CT and RR on Fe XXIV EIE produced $(3p\ ^2P_{3/2} - 2s\ ^2S_{1/2})/(3p\ ^2P_{1/2} - 2s\ ^2S_{1/2})$ and $(4p\ ^2P_{3/2,1/2} - 2s\ ^2S_{1/2})/(3p\ ^2P_{1/2} - 2s\ ^2S_{1/2})$ line ratio measurements was investigated by Savin *et al.* [29] and found to be insignificant. By inference, we assume that both CT and RR have an insignificant effect on the measured $(4p\ ^2P_{3/2} - 2s\ ^2S_{1/2})/(4p\ ^2P_{1/2} - 2s\ ^2S_{1/2})$ line ratios.

Measured line ratios were reproducible to within 5 to 7 percent. This is slightly greater than predicted by $1\sigma$ counting statistics and is attributed as to variations introduced when determining the background levels of the collected spectra. The resulting uncertainties in the measured polarization factors were determined by calculating the variance of Equation 46 [30].

The value used in Equation 46 for $f$ depends on the Bragg angle, $\theta_B$, of the observed line. The Bragg angle was calculated using the measured wavelengths of the Fe XXIV lines [28] and the measured $2d_\infty$ spacing for $\alpha$-quartz $(10\bar{1}0)$ [31, 32] and ADP (101) crystals [33, 34]. Uncertainties in the measured wavelengths and $2d_\infty$ spacings have an insignificant effect on the present results.

| Source | 2.5 keV | 4.6 keV |
|---|---|---|
| Line intensity measurements using: | | |
| $\alpha$-quartz($10\bar{1}0$) | 0.089 | 0.147 |
| ADP(101) | 0.094 | 0.101 |
| Theoretical $f$ values: | | |
| $\alpha$-quartz($10\bar{1}0$) | 0.008 | 0.050 |
| ADP(101) | 0.003 | 0.012 |
| Quadrature Sum | 0.130 | 0.186 |

Table 2: Summary of uncertainties for Fe XXIV $4p\ ^2P_{3/2} \rightarrow 2s\ ^2S_{1/2}$ polarization measurements. All uncertainties are quoted at a confidence level believed to be equivalent to a $1\sigma$ confidence level.

The values of $f$ used were determined from theoretical considerations and the reported measured properties of $\alpha$-quartz and ADP. For a perfect crystal with negligible absorption, $f = |\cos(2\theta_B)|$; but for a perfect crystal with with non-negligible absorption, $f$ may be significantly less. For a mosaic crystal $f = \cos^2(2\theta_B)$ [25, 26]. The properties of $\alpha$-quartz ($10\bar{1}0$) deviates from those of a perfect crystal at $\sim 8$ Å (roughly the wavelength of the Fe XXIV $4p - 2s$ lines) [35]. The value of $f_{quartz}$ at $\sim 8$ Å is bounded by the theoretical values of 0.764 for a perfect crystal and 0.584 for a mosaic crystal. ADP is a crystal with a significant amount of absorption [26]. The value of $f_{ADP}$ at $\sim 8$ Å is bounded by the theoretical values of 0.046 for a perfect crystal with absorption [26] and 0.016 for a mosaic crystal. We used the limits on the theoretical values of $f_{quartz}$ and $f_{ADP}$ to calculate average values which we then used in the Equation 46. Using the uncertainties in $f$ for the different crystals, we determined the resulting uncertainties in the measured polarization factors by calculating the variance of Equation 46.

Table 2 lists the uncertainties associated with the $4p\ ^2P_{3/2} - 2s\ ^2S_{1/2}$ polarization measurement. Uncertainties are quoted at a confidence level believed to be equivalent to a $1\sigma$ statistical confidence level. The uncertainties are treated as random sign errors and added in quadrature.

The measured polarization factors of Fe XXIV $4p\ ^2P_{3/2} \rightarrow 2s\ ^2S_{1/2}$ line emission produced by EIE at collision energies of 2.5 and 4.6 keV are shown in Figure 5. The error bars represent the estimated $1\sigma$ uncertainties.

# 5 Discussion

In order to estimate the effect of electron spiraling on the measured polarization of the Fe XXIV $4p\ ^2P_{3/2} \rightarrow 2s\ ^2S_{1/2}$ transition, we plot in Figure 5 the theoretical polarization factors as a function of collision energy for $E_\perp = 0$, 250, and 700 eV. We have assumed that $f(\cos\theta) = \delta(\cos\theta - \cos\theta_0)$. The collision energy was above the ionization potential for Fe XXIV [36] and cascades contributed to the observed $4p - 2s$ lines intensities. A relativistic distorted wave code was used to calculate the population of the magnetic sublevels $m$ due to electron impact excitation [37]. Radiative rates and cascades branching ratios were calculated using a multiconfiguration, relativisitic, parametric potential method in intermediate coupling [38]. Using these theoretical atomic data, a collisional-radiative model was constructed to determine the $g_m$ values for the initial statistical tensor $\rho_0^{\prime\lambda}$ (*cf.* Equation 17). Cascade contributions to the theoretical polarization were account for as described in Beiersdorfer *et al.* [7].

As can be seen in Figure 5, the present results are in reasonable agreement with theory. The agreement does not depend on whether or not spiraling has been taken into account. This is a result of three factors: the relatively small value of $E_\perp/E$ for the energies at which the measurement were carried out, the moderate polarization of the lines, and the large error bars.

Polarization measurements using the present technique involve subtraction (*cf.* Equation 46). To produce polarization measurements with small relative uncertainties requires that the uncertainties in the values being subtracted be extremely small. Meeting this requirement is often limited by counting statistics which only improve as the square root of the data acquisition time. One quickly runs into the limits of diminishing returns. This means that the effect of electron spiraling in many cases will not be significant. Uncertainties

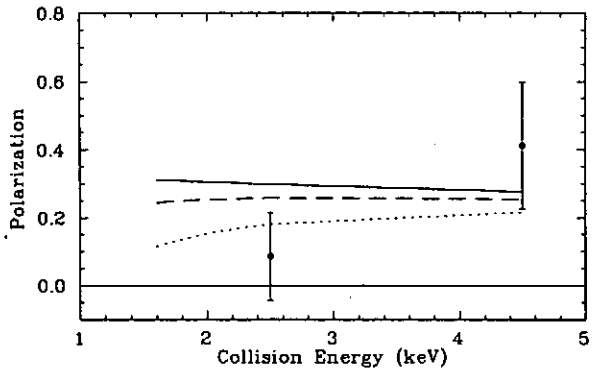


Figure 5: Measured and theoretical Fe XXIV $4p\ ^2P_{3/2} \rightarrow 2s\ ^2S_{1/2}$ polarization factor. The measured values are shown with their estimated $1\sigma$ uncertainties. The theoretical values are shown for $E_\perp = 0$ eV (solid line), 250 eV (dashed line), and 700 eV (dotted line).

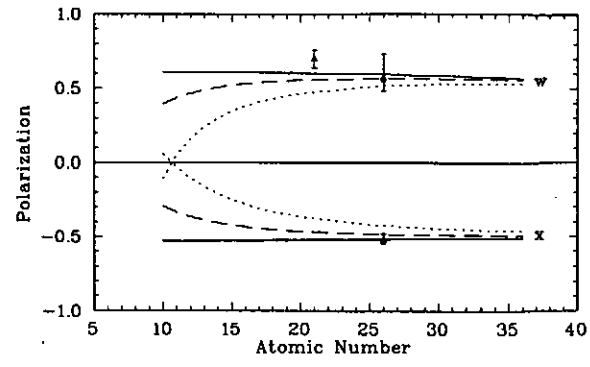


Figure 6: Measured and theoretical polarization factors for $1s2p\ ^1P_1 \rightarrow 1s^2\ ^1S_1$ ($w$) and $1s2p\ ^3P_2 \rightarrow 1s^2\ ^1S_1$ ($x$) line emission in heliumlike ions produced by electron impact excitation at threshold. The measured value for Sc XX (triangle) is from Henderson *et al.* [8] and for Fe XXV (circles) from Beiersdorfer *et al.* [7]. The $E_\perp = 0$ eV theoretical values are from Beiersdorfer *et al.* Also shown are the theoretical polarization factors for $E_\perp = 250$ eV (dashed line) and 700 eV (dotted line).

determined by statistics will typically be larger than the effect of spiraling. This was also noted in Refs. [7], [8] and [9] and now is confirmed by our rigorous analysis.

We have also reanalyzed the previous polarization measurements of transitions in heliumlike ions [7, 8] in light of our analysis of electron spiraling. The polarization factors for $1s2p\ ^1P_1 \rightarrow 1s^2\ ^1S_1$ ($w$) and $1s2p\ ^3P_2 \rightarrow 1s^2\ ^1S_1$ ($x$) line emission produced by electron impact excitation at threshold are $\gtrsim 0.6$ and $\lesssim -0.5$, respectively. Figure 6 shows the theoretical polarization factors of $w$ and $x$ as a function of atomic number $Z$ for $E_\perp = 0$, 250, and 700 eV. Note that as $Z$ increases, the threshold excitation energy increases, and $E_\perp/E$ decreases. In light of the $1\sigma$ error bars of the measurements, we note again that the effects of electron spiraling is unimportant in these measurements. However, the measured polarization factor of Fe XXV $x$ does strongly suggests that $E_\perp$ was significantly less than 700 eV for the Fe XXIV measurements.

Depolarization of the observed line emission can occur due to electron collision which redistribute the population of the $m$ levels of the excited state. We estimates these effects to be insignificant for the Sc XX, Fe XXIV, and Fe XXV results. If we assume the $m$-changing cross section is $\sim 10^{-16}$ cm$^2$ (a large overestimate for such highly charged ions), then the $m$-changing rate coefficient is $\sim 3 \times 10^{-7}$ cm$^3$ s$^{-1}$. For typical EBIT electron densities, this yields an $m$-changing rate of $\sim 4 \times 10^5$ s$^{-1}$ which is significantly smaller than the radiative rates for the transitions of interest. However, $m$-changing electron collisions may be important for forbidden transitions with radiative lifetimes of $\sim 1$ $\mu$s.

Polarization measurements have also been carried out for a magnetic quadrupole transition in neonlike barium at energies $\gtrsim 5.0$ keV [9]. The measured polarization ranged between $\sim -0.25$ and 0.05. We expect that electron spiraling probably has an insignificant effect on the measured polarization. The polarization factor is relatively small and the value of $E_\perp/E$ also relatively small.

# 6 Conclusions

We have presented a theoretical formalism for calculating the anisotropy and polarization of photon emission due to a spiraling beam of electrons in an EBIT. We have presented polarization measurements of the Fe XXIV $4p\ ^2P_{3/2} \rightarrow 2s\ ^2S_{1/2}$ transition due to EIE and discussed previously reported measurements in an attempt to determine the importance of electron spiraling. We showed that the effect of electron spiraling is

smaller or equal to the accuracy limits of the present measurements. Measurments at very low beam energy, where $E_\perp/E$ approaches unity, may show a strong effect provided statistical uncertainties are kept small. The insensitivity of most crystal spectrometer measurements to spiraling effects is the result of the fact that polarization is in general only a relatively small correction to the observed line intensities. The bulk of this correction can be carried out without knowledge of the exact value of $E_\perp$.

# 7 Acknowledgements

The authors wish to thank K. J. Reed for providing the Fe XXIV electron impact excitation cross sections to magnetic sublevels, D. A. Liedahl for providing the Fe XXIV radiative rates, J. Dubau, V. L. Jacobs, and R. E. Marrs for stimulating conversation, and P. A. D'Antonio, E. W. Magee, and D. H. Nelson for their expert technical support. Work performed at Lawrence Livermore National Laboratory was performed under the auspices of the US Department of Energy (contract W-7405-ENG-48). This program is supported by NASA High Energy Astrophysics X-Ray Astronomy Research and Analysis grant NAG5-5123 (Columbia University) and work order W-19127 (Lawrence Livermore).

# References

[1] I. C. Percival and M. J. Seaton, Phil. Trans. R. Soc. London Ser. A **251**, 113 (1958).

[2] U. Fano and J. H. Macek, Rev. Mod. Phys. **45**, 553 (1973).

[3] M. K. Inal and J. Dubau, J. Phys. B **20**, 4221 (1987).

[4] M. A. Levine, R. E. Marrs, J. R. Henderson, D. A. Knapp, and M. B. Schneider, Phys. Scr. **T22**, 157 (1988).

[5] M. A. Levine, R. E. Marrs, J. N. Bardsley, P. Beiersdorfer, C. L. Bennett, M. H. Chen, T. Cowan, D. Dietrich, J. R. Henderson, D. A. Knapp, A. Osterheld, B. M. Penetrante, M. B. Schneider, and J. H. Scofield, Nucl. Instrum. Methods **B43**, 431 (1989).

[6] R. E. Marrs, in *Experimental Methods in the Physical Sciences, Volume 29A, Atomic Molecular, and Optical Physics: Charged Particles*, eds. F. B. Dunning and R. G. Hulet (Academic Press, San Diego, 1995), 391.

[7] P. Beiersdorfer, D. A. Vogel, K. J. Reed, V. Decaux, J. H. Scofield, K. Widmann, G. Hölzer, E. Förster, O. Wehrhan, D. W. Savin, and L. Schweikhard, Phys. Rev. A **53**, 3974 (1996).

[8] J. R. Henderson, P. Beiersdorfer, C. L. Bennett, S. Chantrenne, D. A. Knapp, R. E. Marrs, M. B. Schneider, K. L. Wong, G. A. Doschek, J. F. Seely, C. M. Brown, R. E. LaVilla, J. Dubau, and M. A. Levine, Phys. Rev. Lett. **65**, 705 (1990)

[9] E. Takács, E. S. Meyer, J. D. Gillaspy, J. R. Roberts, C. T. Chantler, L. T. Hudson, R. D. Deslattes, C. M. Brown, J. M. Lamming, J. Dubau, and M. K. Inal, Phys. Rev. A **54** 1342 (1996)

[10] J. D. Jackson, *Classical Electrodynamics*, (John Wiley & Sons, New York, 1975), 588.

[11] S. Pastuszka, U. Schramm, M. Grieser, C. Broude, R. Grimm, D. Habs, J. Kenntner, H.J. Miesner, T. Schüßler, D. Schwalm, and A. Wolf, Nucl. Instrum. Methods **A369**, 11 (1996).

[12] J. D. Gillaspy, J. R. Roberts, C. M. Brown, and U. Feldman, in *VIth International Conference on the Physics of Highly Charged Ions*, eds. P. Richard, M. Stöckli, C. L. Cocke, and C. D. Lin, AIP Conference Proceedings No. 274 (American Institute of Physics, New York, 1993), 682.

[13] R. M. Steffen and K. Alder, in *The Electromagnetic Interaction in Nuclear Spectroscopy*, ed. W. D. Hamilton (North-Holland Publishing Company, Amsterdam, 1975), 505.

[14] K. Alder and R. M. Steffen, in *The Electromagnetic Interaction in Nuclear Spectroscopy*, ed. W. D. Hamilton (North-Holland Publishing Company, Amsterdam, 1975), 1.

[15] A. Bohr and B. R. Mottelson, *Nuclear Structure: Volume I*, (W. A. Benjamin, Inc., New York, 1969).

[16] R. D. Cowan, *The Theory of Atomic Structure and Spectra*, (University of California, Berkeley, 1981).

[17] A. R. Edmonds, *Angular Momentum in Quantum Mechanics*, (Princeton University Press, Princeton, 1960), pp. 23, 24 & 59.

[18] J. D. Jackson, *Classical Electrodynamics*, (John Wiley & Sons, New York, 1975), 760.

[19] R. E. Marrs, P. Beiersdorfer, S. R. Elliott, D. A. Knapp, and Th. Stoehlker, Phys. Scr. **T59**, 183 (1995).

[20] P. Beiersdorfer, T. W. Phillips, K. L. Wong, R. E. Marrs, and D. A. Vogel, Phys. Rev. A **46**, 3812 (1992).

[21] P. Beiersdorfer, V. Decaux, S. R. Elliot, K. Widmann, and K. Wong, Rev. Sci. Instrum. **66**, 303 (1995).

[22] P. Beiersdorfer, V. Decaux, and K. Widmann, Nucl. Instrum. Methods **B98**, 566 (1995).

[23] P. Beiersdorfer and B. J. Wargelin, Rev. Sci. Instrum. **65**, 13 (1994).

[24] P. Beiersdorfer, J. R. Crespo López-Urrutia, E. Förster, J. Mahiri, and K. Widmann, Rev. Sci. Instrum. **68**, 1077 (1997).

[25] A. H. Compton and S. K. Allison, *X-Rays in Theory and Experiment*, (D. Van Nostrand Company, Inc., New York, 1935), Chapter VI.

[26] B. L. Henke, E. M. Gullikson, and J. C. Davis, At. Data Nucl. Data Tables **54**, 181 (1993).

[27] C. J. Borkowski and M. K. Kopp, Rev. Sci. Instrum. **39**, 1515 (1968).

[28] B. J. Wargelin, P. Beiersdorfer, D. A. Liedahl, S. M. Kahn, and S. von Goeler, Astrophys. J. **496**, 1031 (1998).

[29] D. W. Savin, P. Beiersdorfer, J. Crespo López-Urrutia, V. Decaux, E. M. Gullikson, S. M. Kahn, D. A. Liedahl, K. J. Reed, and K. Widmann, Astrophys. J. **470**, L73 (1996).

[30] P. R. Bevington, *Data Reduction and Error Analysis for the Physical Sciences*, (McGraw-Hill, New York, 1969), 64.

[31] Ö Adell, G. Brogren, and L.-E. Haeggblom, Ark. Fys. **7**, 197 (1953).

[32] M. A. Blokhin, *X-Ray Spectroscopy*, (Hindustan Publishing Corporation, Delhi, 1962), 231.

[33] N. G. Alexandropoulos and G. C. Cohen, Appl. Spectrosc. **28**, 155 (1974).

[34] D. M. Barrus, R. L. Blake, H. Felthauser, E. E. Fenimore, and A. J. Burek, in *Low Energy X-ray Diagnostics–1981*, ed. D. T. Attwood and B. L. Henke, AIP Conference Proceedings No. 75, (American Institute of Physics: New York, 1981), 115.

[35] G. Brogren, Ark. Fys. **22**, 267 (1962).

[36] R. L. Kelly, J. Phys. Chem. Ref. Data **16**, Suppl. 1 (1987).

[37] H. L. Zhang, D. H. Sampson, and R. E. H. Clark, Phys. Rev. A **41**, 198 (1990).

[38] M. Klapisch, J. L. Schwob, B. S. Fraenkel, and J. Oreg, J. Opt. Soc. Am. **67**, 148 (1977).

# Experimental plans with Tokyo-EBIT

Hirofumi Watanabe
Kyoto University, Kyoto 606-8317, Japan
University of Electro-Communications, Chofu 182-8585, Japan

Shunsuke Ohtani
University of Electro-Communications, Chofu 182-8585, Japan
Cold Trapped Ions Project, ICORP, Japan Science and Technology Corporation (JST), Chofu 182-0024, Japan

Abstract
A new electron beam ion trap (Tokyo-EBIT) has been completed in Institute for Laser Science, University of Electro-Communications, Tokyo. The maximum parameters of the electron beam are designed to be 340 keV and 300 mA. The preliminary experiments have been performed in 1997. We report here the recent results and planned experiments such as electron-ion collision experiments, atomic structure measurements by X-ray and visible spectroscopy and ion-surface interaction experiments.

## §1. Introduction

The electron beam ion trap (EBIT) is a unique ion source which has been developed as a means of producing and trapping highly charged ions (HCIs) [1]. This device is based on the electron beam ion source (EBIS) concept [2], but with a shorter trap length to limit plasma instabilities [3]. We have recently constructed a new EBIT in the University of Electro-Communications, Tokyo, to study the physics of highly charged ions [4,5].

In this report, we introduce briefly the general feature of the Tokyo-EBIT, the recent results in preliminary experiments and the some research subjects planned.

## §2. Overview of the Tokyo-EBIT

The Tokyo-EBIT is shown schematically in figure 1. An electron beam emitted from an electron gun is accelerated, magnetically compressed and injected in a drift tube assembly. This assembly consists of the successive three cylindrical electrodes. In the central drift tube HCIs are produced by successive ionization by electron impact. The HCIs are also trapped, radially by the space charge potential produced by the electron beam, and axially by the positive potential applied to the end drift tubes to the central one. After passing through the drift tube region, the electron beam is collected by an electron collector at the decelerated energy. The maximum electron beam energy is designed to be 340 keV. To achieve this condition, the gun and the collector are floated to -300 kV, and the drift tube (trap) assembly is to +40 kV. Compression of the electron beam is made by the combination of electrostatic and magnetic field applied in

the region between the gun and the trap. The magnetic field is produced by a superconducting coil of Helmholz type. Eight observation ports are situated around the trap in the center of the Helmholz coil to facilitate spectroscopy, gas and probe injections.

Table 1 summarizes designed and presently achieved parameters of Tokyo-EBIT. The maximum energy is limited by the insulation voltage outside of the EBIT in air. We will use $SF_6$ gas at 2 atmospheres as the insulation gas when we will operate over 100 kV. The electron current of 250 mA has been achieved. This is not limited by the emissivity of the cathode itself, but by the stability of the electron beam at low energies (<100 keV). This value will be increased by increases of the electron beam energy. The magnetic field of 4.5 T has been already achieved.

## §3. On-going experiments (1997).

Figure 2 shows a typical X-ray spectrum observed with a Ge solid state detector. The electron energy and the current in this measurement were 75 keV and 150 mA, respectively. We can see several peaks from three dominant species of ions: krypton, barium and tungsten. Krypton gas was injected from outside of the EBIT through the gas-injection port, while barium and tungsten were evaporated from the cathode and ionized in the trap region. Radiative recombination (RR) lines to the $n$=1, $n$=2 and $n$=3 levels of barium and krypton ions are observed. From the identification of these peaks, we can confirm that H-like and bare krypton and barium ions have been produced in the trap. The small peaks observed at 83 and 94 keV are from RR into the highly charged tungsten ions.

A two dimensional X-ray spectrum obtained by use of multiparameter data acquisition system [6] is shown in figure 3. Krypton gas was also introduced in this case. The electron beam energy to produce initial charge state distribution was 17 keV, which is almost identical to the ionization energy of He-like krypton ions (16.8 keV) and is much larger than that of Li-like krypton ions (4 keV). Therefore, He-like krypton ions are considered to be predominant in the trap. X-ray signal are measured by the Ge detector while the electron beam energy are changed linearly from 17 keV to 7 keV and then from 7 keV to 17 keV. This scan was performed once per 100 ms and its width was 20 ms. In this figure the horizontal axis represents the X-ray energy and the vertical axis the electron beam energy. X-ray signals along a vertical line at around 13 keV of X-ray energy is due to X-ray emission from n=2-1 transitions and that at around 15 keV is from n=3-1 transitions. Diagonal lines are attributed to RR processes, since the X-ray energy of RR processes increases linearly with the electron energy. At the crossing of the vertical and diagonal lines, there are strong peaks. These are resonance processes due to dielectronic recombination (DR) of He-like krypton ions. Since cross sections of RR processes can be estimated theoretically, the resonance strengths for DR processes might be determined by normalization of the line intensity of DR to RR.

Two kinds of X-ray spectra measured with a flat LiF(200) crystal spectrometer

are shown in figure 4. A position sensitive proportional counter was used as a detector. We observed $n$=3-2 transitions in Ne-like barium and xenon ions. A 7.8 keV, 110 mA electron beam was used for each spectrum. At atomic number $Z$ around $Z$=55, with increase of $Z$, suitable representation of Ne-like atomic systems changes from $L$-$S$ coupling scheme to $j$-$j$ coupling. As shown by Kagawa *et al* [7], the order of level energies and the oscillator strengths for the respective transitions between these levels oscillate at around $Z$=55 due to mixing of the wave functions. Accordingly, systematic measurements of wavelengths and intensity ratios for these transitions are important to check the theoretical treatment of relativistic many body systems.

Typical charge spectra of extracted argon and krypton ions are shown in figure 5. Both spectra were observed by pulsed mode in which the potential of the central drift tube is set to the same potential as the upper drift tube to dump the trapped ions. The charge state distribution measured using pulsed mode reflects the charge balance in the trap. For argon ions, when a 27.6 keV, 115 mA electron beam was used, bare argon ions show the maximum peak in the spectrum. For krypton, with a 48.2 keV, 130 mA electron beam, B-like ions (31+) show the maximum. The number of the extracted ions is typically several thousand counts per pulse in pulsed mode, and about $10^4$ counts per second in continuous mode.

## §4. Planned experiments.

As already mentioned, the present value of the maximum electron beam energy is limited by the insulation voltage of the system in air. The insulation system with use of $SF_6$ gas has been completed recently and will make it possible to increase the beam energy. We will begin 300 keV operation in near future.

We are planning to perform electron-ion collision experiments. We will measure electron impact ionization cross section of H-like and He-like ions by observations of extracted ions, in addition to X-ray spectroscopic studies. DR experiments will be systematically performed not only by X-ray measurement, but also by ion extraction methods.

As for high resolution X-ray spectroscopy, the measurement of transition energies in Ne-like ions will be systematically continued for HCIs with atomic numbers around 55. In addition, we are planning to develop a high energy spectrometer of transmission type to study a few electrons very high $Z$ ions.

We intend to observe transitions in visible region. We are measuring the spectra for magnetic dipole transitions of $(3d^4)\ ^5D_3$-$^5D_2$ for Ti-like ions of $Z$=54-92. We have calculated wavelengths of these transitions, which are shown in figure 6. These wavelengths are obtained by the multi-configuration Dirac-Fock calculation (GRASP92 code) [8]. The wavelengths are anomalously stable with respect to $Z$. The measurements of wavelengths of these transitions give useful information for plasma diagnostics.

We are constructing an echelle type visible spectrometer with large spectral range and high resolution. This might be very useful to survey unknown spectra

such as transitions between fine structure levels or hyper fine structure levels. By laser induced fluorescence spectroscopy, we will make precise spectroscopic studies in visible region. We have prepared OPO laser system which is tunable in the whole visible range. An optical system for introduction of the laser into the trap region is under consideration.

With an improved extraction line system for HCIs, we are planning to perform various kinds of ion-surface collision experiments.

## References


[1] M. A. Levine, R. E. Marrs, J. R. Henderson, D. A. Knapp and M. B. Schneider: Phys. Scr. T **22** (1988) 157.

[2] E. D. Donets and V. P. Ovsyannikov: Sov. Phys. -JETP **53** (1981) 466.

[3] M. A. Levine, R. E. Marrs and R. W. Schmieder: Nucl. Instrum. Methods A **237** (1985) 429

[4] F. J. Currell, J. Asada, K. Ishii, A. Minoh, K. Motohashi, N. Nakamura, K. Nishizawa, S. Ohtani, K. Okazaki, M. Sakurai, H. Shiraishi, S. Tsurubuchi and H. Watanabe: J. Phys. Soc. Jpn **65** (1996) 3186.

[5] H. Watanabe, J. Asada, F. J. Currell, T. Fukami, T. Hirayama, K. Motohashi, N. Nakamura, E. Nojikawa, S. Ohtani, K. Okazaki, M. Sakurai, H. Shimizu, N. Tada and S. Tsurubuchi: J. Phys. Soc. Jpn **66** (1997) 3795.

[6] F. J. Currell, J. Asada, T. Fukami, T. Hirayama, N. Nakamura, K. Motohashi, E. Nojikawa, K. Okazaki, S. Ohtani, M. Sakurai, H. Shiraishi, S. Tsurubuchi and H. Watanabe: Phys. Scr. T **73** (1997) 371.

[7] T. Kagawa, Y. Honda and S. Kiyokawa: Phys. Rev. A **44** (1991) 7092.

[8] F. A. Parpia, C. F. Fischer and I. P. Grant: Comp. Phys. Commu. **94** (1996) 249.


## Figure captions

Figure 1. Schematic view of the Tokyo-EBIT

Figure 2. A typical X-ray spectrum taken with a Ge solid state detector.

Figure 3. A two dimensional X-ray spectrum for Kr ions.

Figure 4. X-ray spectra of $n$=3-2 transitions in Ne-like barium and xenon ions taken with a flat LiF(200) crystal spectrometer.

Figure 5. Charge spectra of extracted argon and krypton ions.

Figure 6. Wavelengths of magnetic dipole transition of $(3d^4)$ $^5D_3$-$^5D_2$ for Ti-like ions. These are obtained by the multi-configuration Dirac-Fock calculation by use of GRASP92 code.

Table 1 The operational parameters of the Tokyo EBIT.

| Parameter | Tokyo-EBIT (designed) | Tokyo-EBIT (achieved) |
|---|---|---|
| Beam Energy (keV) | 10-340 (in $SF_6$) | 2.5-80 (in air) |
| Beam Current (mA) | 0-300 | 0-250 |
| Magnetic field (T) | 0-4.5 | 0-4.5 |

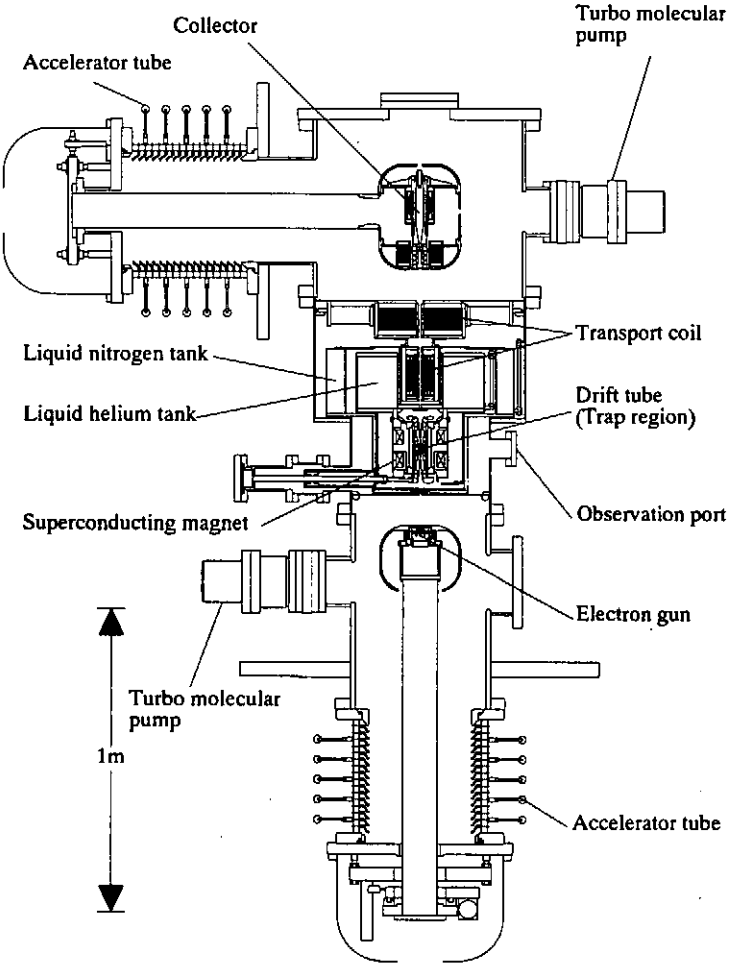
Collector
Turbo molecular pump
Accelerator tube
Transport coil
Liquid nitrogen tank
Liquid helium tank
Drift tube (Trap region)
Observation port
Superconducting magnet
Electron gun
Turbo molecular pump
1m
Accelerator tube

Fiugre 1

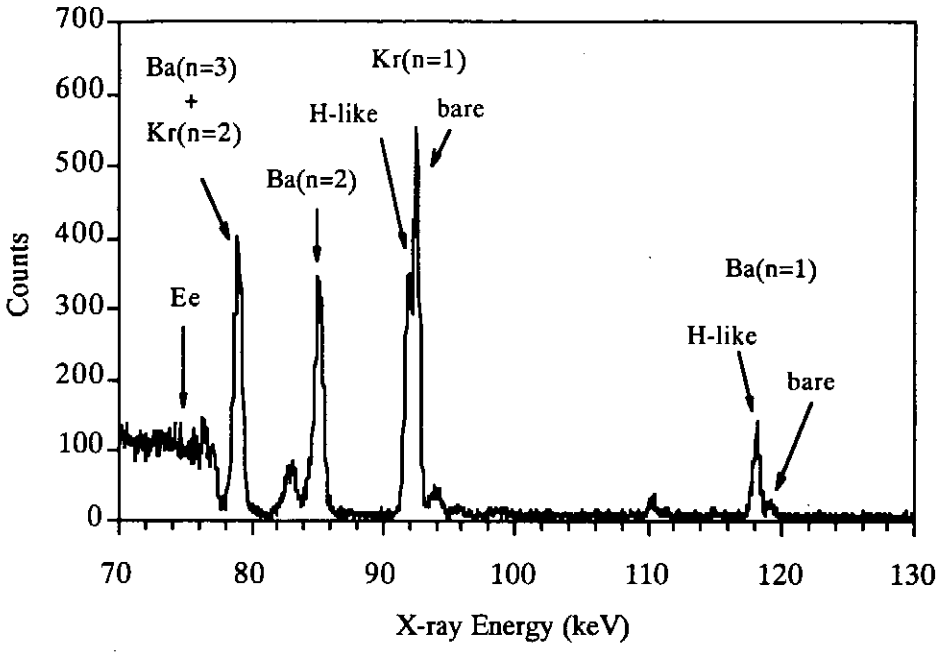


Figure 2

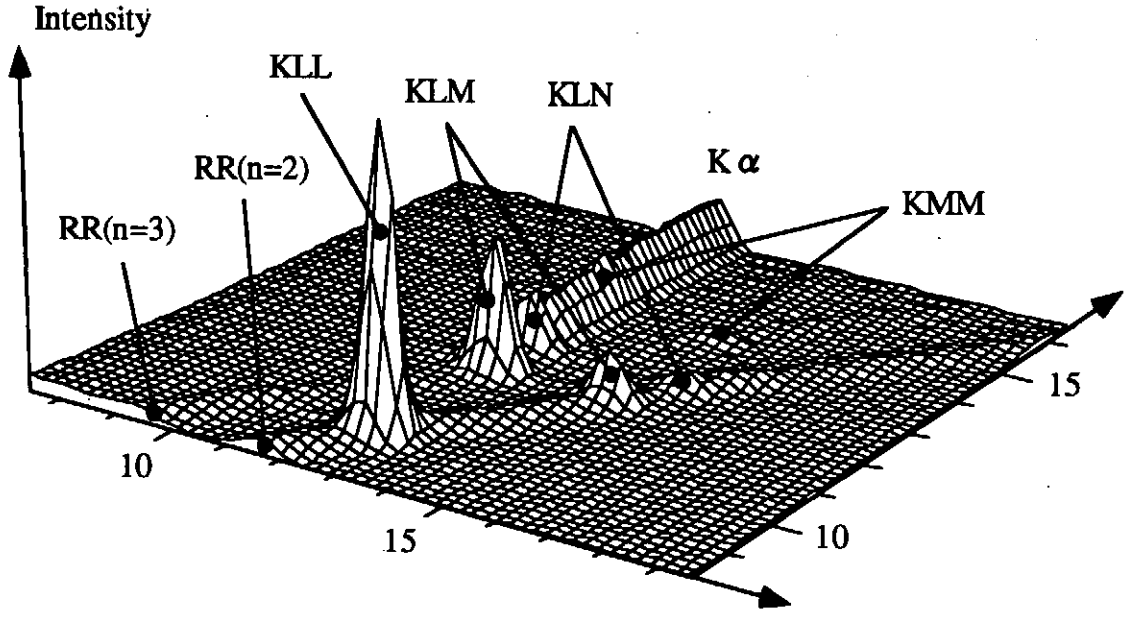


Figure 3

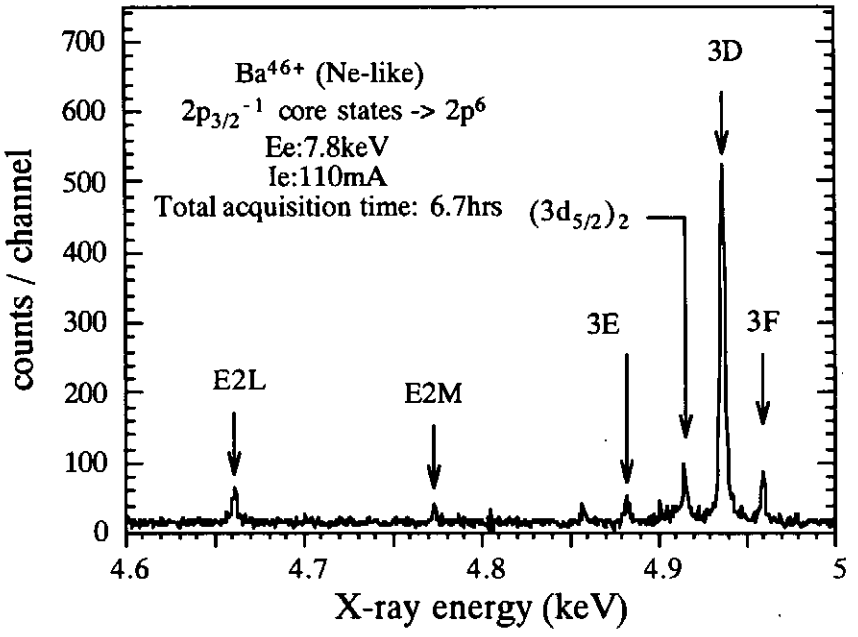
Ba46+ (Ne-like)
2p3/2-1 core states -> 2p6
Ee:7.8keV
Ie:110mA
Total acquisition time: 6.7hrs
(3d5/2)2
3D
3E
3F
E2L
E2M
counts / channel
X-ray energy (keV)

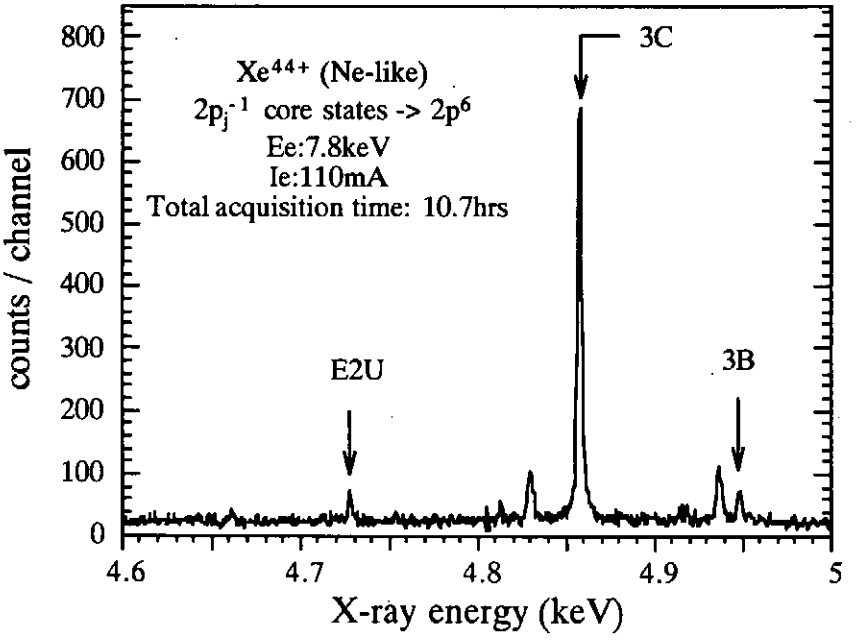
Xe44+ (Ne-like)
2pj-1 core states -> 2p6
Ee:7.8keV
Ie:110mA
Total acquisition time: 10.7hrs
3C
E2U
3B
counts / channel
X-ray energy (keV)

Figure 4

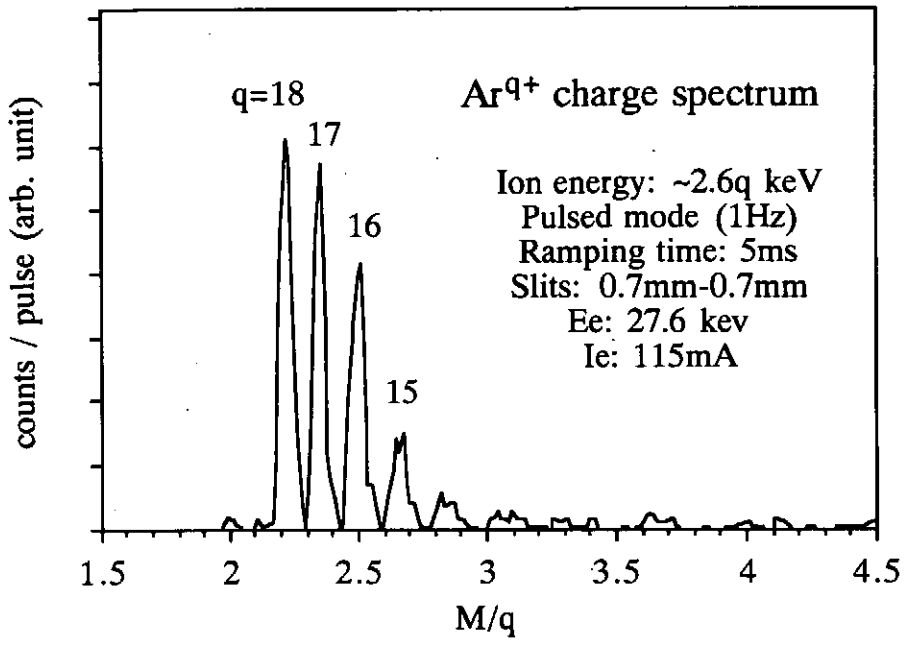
q=18
17
16
15
Ar^q+ charge spectrum
Ion energy: ~2.6q keV
Pulsed mode (1Hz)
Ramping time: 5ms
Slits: 0.7mm-0.7mm
Ee: 27.6 kev
Ie: 115mA
counts / pulse (arb. unit)
1.5
2
2.5
3
3.5
4
4.5
M/q

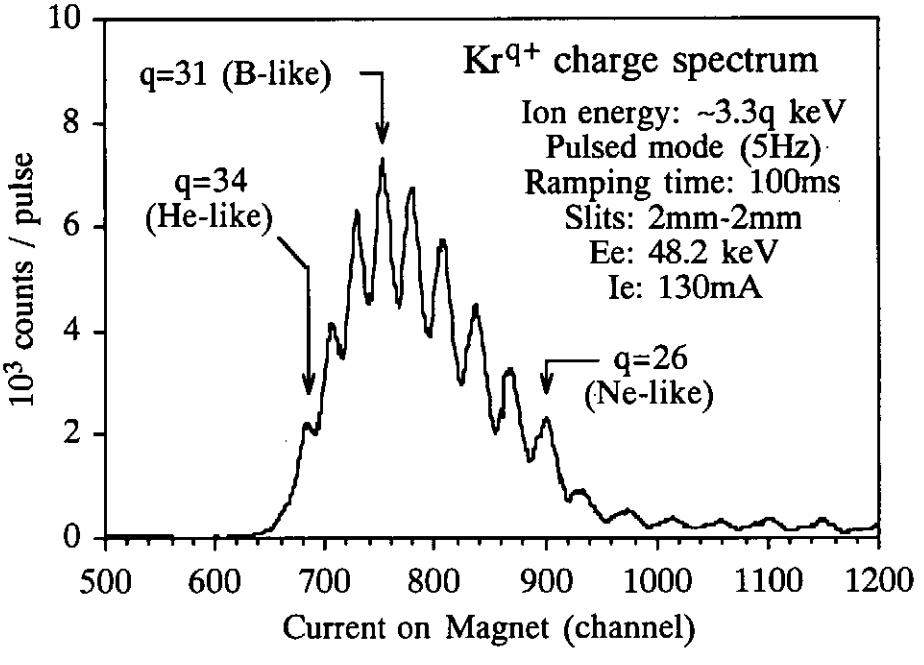
10
8
6
4
2
0
q=31 (B-like)
Kr^q+ charge spectrum
Ion energy: ~3.3q keV
Pulsed mode (5Hz)
Ramping time: 100ms
Slits: 2mm-2mm
Ee: 48.2 keV
Ie: 130mA
q=34
(He-like)
q=26
(Ne-like)
10^3 counts / pulse
500
600
700
800
900
1000
1100
1200
Current on Magnet (channel)

Figure 5

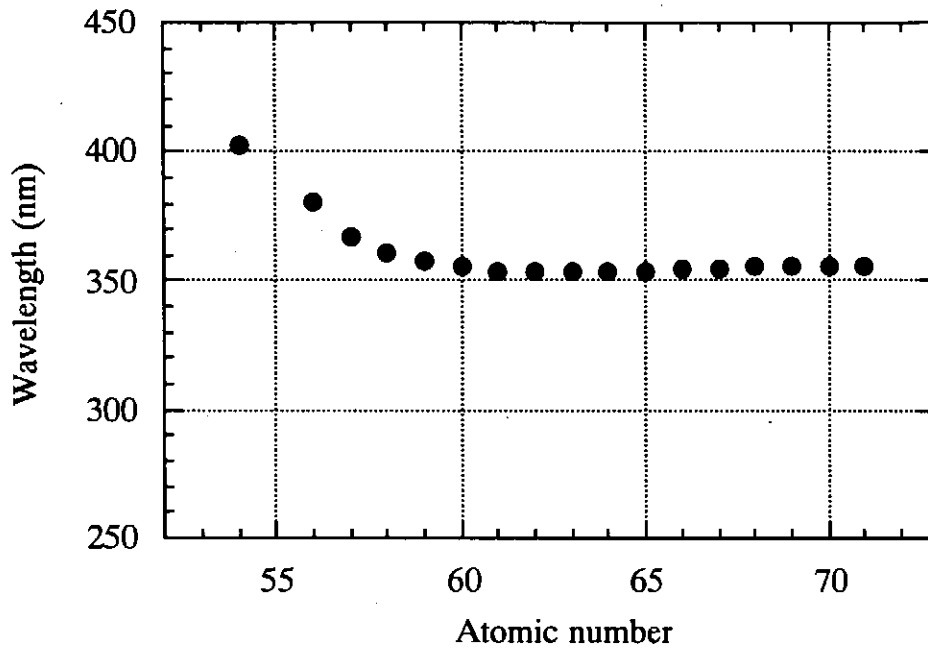


Figure 6

# POLARIZED PROFILES OF SPECTRAL LINES FROM PLASMAS: OVERVIEW OF THE THEORY AND OF DIAGNOSTIC APPLICATIONS

E. Oks

Physics Department, Auburn University, Auburn, AL 36849, USA

## 1. Introduction

Most of the papers on Plasma Polarization Spectroscopy discuss only the polarization of *absolute intensities* of spectral lines, i.e., intensities integrated over the wavelength or over the frequency. In distinction to that, this paper deals with the polarization of spectral line **profiles** (or **shapes**). In other words, we discuss here the polarization dependent on the wavelength (or on the frequency) scanned over the distribution of the *relative intensity* of the line. So we focus on the situations where the spectral line **broadening depends on the polarization**.

By the definition, spectral line profiles are normalized to unity. Therefore, profiles integrated over the wavelength (or over the frequency) do not depend on the polarization.

## 2. Profiles polarized due to anisotropic *quasistatic* fields

A textbook picture of the Stark effect for hydrogen lines in a static electric field **F** shows that they split up into $\sigma$- and $\pi$-components: $\sigma$-components, polarized in the plane perpendicular to **F**, are bunched primarily in the central region of the line, while $\pi$-components, polarized along **F**, are located primarily in the wings of the line. If the angular distribution of the static (or quasistatic) field is anisotropic, then the profiles of the same line observed in two orthogonal linear polarizations, $I_1(\Delta\omega)$ and $I_2(\Delta\omega)$, may differ from each other.

In 1973 Sholin and Oks [1] derived the expression for the axially-symmetrical distribution of a low-frequency plasma turbulence. (The latter term describes a number of electrostatic oscillations, such as ion-acoustic waves, Bernstein modes and others that could be responsible for the anomalous resistivity in plasmas.) Then they calculated analytically polarized profiles $I_1(\Delta\omega)$ and $I_2(\Delta\omega)$, as well as the Polarization Difference Profile (PDP) $D(\Delta\omega)=I_1(\Delta\omega)-I_2(\Delta\omega)$, and showed how to deduce from the PDP both the rms field strength and the anisotropy parameter.

This method for the plasma polarization diagnostics was then practically implemented in experiments by Babykin et al [2] at the machine called Dimpol. There a Penning discharge was used to generate the initial plasma in the magnetic mirror system. The subsequent application of an a.c. magnetic field of a large amplitude resulted in the development of the turbulent state in the current sheet separating the opposing magnetic fields. The plasma in the sheet was characterized by the electron density $N_e=1.2\times10^{13}$ $cm^{-3}$ and by the temperature $T \geq 10$ eV.

In one series of experiments, profiles of the hydrogen line $H_\alpha$ were observed in the r-direction with the linear polarizer oriented

in either the $\phi$- or z-directions of the cylindrical reference frame. The $\phi$-profiles were found to be significantly broader than the z-profiles. In another series of experiments, $H_\alpha$ profiles were observed in the z-direction with the polarizer oriented in either the $\phi$- or r-directions. No polarization difference was found in this series.

The analysis of the entire set of the experimental profiles led to the following conclusion. The turbulent electric fields in the current sheet were developed anisotropically: $F_\phi \approx F_r \approx 20$ kV/cm > $F_z \approx 8$ kV/cm. This kind of the angular distribution led to believe that the turbulent fields were associated with the Bernstein modes.

Later this diagnostic method was applied to a $\theta$-pinch by Volkov et al [3]. The electron density was $N_e \approx 5 \times 10^{14} cm^{-3}$, the ion temperature was $T_i \approx 30$ eV. Polarized profiles of the spectral line He II 4686 Å were observed. From the experimental PDP, the authors deduced parameters of the low-frequency turbulent field: $F_z \approx 30$ kV/cm, $F_\phi \approx 20$ kV/cm.

In the above experiments [2,3], the experimental profiles were practically symmetric with respect to the corresponding unperturbed wavelength $\lambda_0$ of the spectral line. However later, when this diagnostic method was applied to the plasma of solar flares, the observed PDP was found to be strongly asymmetric with respect to $\lambda_0$. The top of Fig. 1 shows the degree of linear polarization of the $H_\alpha$ profiles v. $\Delta\lambda = \lambda - \lambda_0$, observed by Babin and Koval [4]. In accordance to them, in 37% of solar flares that they analyzed, the observed linear polarization of the $H_\alpha$ profiles exceeded by 3-6 times the rms instrumental error.

The theoretical interpretation of the asymmetric PDP observed in [4] was given later by Gaisinsky and Oks [5]. They pointed out that for the case of the rms turbulent field $F \leq 3$ kV/cm, the fine structure of the $H_\alpha$ line is comparable with the Stark splitting by the turbulent field. With the allowance for the fine structure, the splitting becomes asymmetric, and so does the PDP (see the bottom of Fig. 1). They concluded that the best fit to the PDP observed in [4] corresponds to the rms turbulent field $F \approx 1$ kV/cm and the degree of anisotropy $F(\mathbf{e}_1)/F(\mathbf{e}_2) \approx 2$, where $\mathbf{e}_1$ and $\mathbf{e}_2$ are unit vectors corresponding to two orthogonal orientations of the polarizer used in [4].

## 3. Profiles polarized due to anisotropic *dynamic* fields

### 3.1. No coupling between the ion microfield and the dynamic field

1. In a single-mode field $\mathbf{E}(t) = \mathbf{E}_0 \cos\omega t$ or in a multi-mode field

$$\mathbf{E}(t) = \sum_{j=1}^{N} \mathbf{E}_j \cos(\omega t + \phi_j), \qquad (1)$$

each Stark component of a hydrogen or H-like line splits up into **satellites** at frequencies $\Delta\omega = p\omega$ corresponding to the wavelengths $\Delta\lambda = p\omega\lambda_0^2/(2\pi c)$, where $p = 0, \pm 1, \pm 2, \pm 3, \ldots$ . This has been shown

analytically by Blochinzew [6] for the single-mode field and by Lifshitz [7] for the multi-mode case. The final profile of the spectral line results from the superposition of satellite structures due to all Stark components of the line. In practice only the envelope of multiple satellites is frequently observed. The intensities of the satellites for various hydrogen and H-like lines as well as the halfwidths of the corresponding envelopes can be found in the book by Oks [8].

The first experiment on the polarization analysis of the Blochinzew's type satellites was conducted by Kamp and Himmel [9]. The satellites were induced by a linearly-polarized microwave field of the frequency $\nu$=34.8 GHz and of the fieldstrength $E_0 \geq 1$ kV/cm. Since the plasma electron density was $N_e \sim 5 \times 10^{12} cm^{-3}$, the typical ion microfield (the Holtsmark field) $F_H = 2.603 e N_i^{2/3} \leq 0.1$ kV/cm was much smaller than the microwave field. Therefore there was practically no coupling between these two types of field in distinction to experiments discussed in the next section. That was a necessary condition for Blochinzew's satellites to be observed.

Figure 2 shows the experimental profiles of the deuterium line $D_\beta$ from [9] with the polarizer parallel to the microwave field $\mathbf{E}_0$. The top profile, corresponding to the microwave field on, is more intensive in the wings than the bottom profile, recorded without the microwave field. Figure 3 shows a similar pair of experimental profiles from [9] with the polarizer perpendicular to $\mathbf{E}_0$. In the wings, the difference between the top and the bottom profiles in Fig. 3 is much less than in Fig. 2. The explanation is the following. The satellites polarized parallel to $\mathbf{E}_0$ are due to the $\pi$-components of the $D_\beta$ line, while the satellites polarized perpendicular to $\mathbf{E}_0$ are due to the $\sigma$-components. Since the Stark constant for the $\pi$-components is two times greater than for the $\sigma$-components, the intensity of the $\pi$-satellites in the conditions of the experiment [9] should be indeed significantly greater than the intensity of the $\sigma$-satellites.

2. *A polarization of line profiles in the x-ray region*, associated with the satellites of H-like lines caused by a dynamic field, was first observed only recently - in 1996 - by Clothiaux et al [10] (the results by this group were first reported by Oks in the invited review [11]). The experimental idea how to perform polarization measurements of x-ray line profiles is the following: if one observes a spectral line employing a crystal at the Bragg angle, and then observes the same line after rotating the crystal through 90°, the resulting spectra will correspond to two orthogonal linear polarizations. This can be achieved by using two spectrometers, so positioned with respect to each other that the plasma line source is in the plane of the spectrometer in one case and perpendicular to it in the other case (Fig. 4).

The experiments described in [10,11] were conducted at the advanced plasma radiation source PHOENIX. The PHOENIX is a powerful Z-pinch where the current reaches peak values of several mega-amperes during several tens of nanoseconds. Two high-resolution, x-ray crystal spectrometers were employed to record time-integrated profiles of the $L_\beta$ and $L_\gamma$ line of Al XIII observed in two orthogonal

linear polarizations: one polarization - parallel to the discharge current, another - perpendicular to it (Fig. 4). For the detailed lineshape analysis, the blue wing of the $L_\beta$ line and the red wing of the $L_\gamma$ line were used because they were free from blending lines.

For the experimental identification of the relevant line broadening mechanisms, the $L_\beta$ line is more appropriate than the $L_\gamma$ line. Indeed, the former does not have the central (unshifted) Stark component in distinction to the latter.

If the primary broadening mechanism would be the normal Stark broadening by ion and electron microfields, then the wings of the $L_\beta$ line should demonstrate a power law $I(\Delta\lambda) \propto (\Delta\lambda)^{-q}$, where $2 \leq q \leq 2.5$ . In this situation the experimental profiles plotted in Log-Log coordinates would be close to straight lines of slope q for the most part of the profile. However, this was not the case for our experimental profiles.

If the primary broadening mechanism would be the Doppler broadening, then the value of $\log[I(\Delta\lambda)/I(0)]$ should be proportional to $(\Delta\lambda)^2$. In this situation the plot of the experimental values of $\log[I(\Delta\lambda)/I(0)]$ vs. $(\Delta\lambda)^2$ would be close to the straight line. However, our experimental profiles did not straighten up in these coordinates either.

It turned out that our experimental profiles of the $L_\beta$ line become pretty close to straight lines being plotted as $\log[I(\Delta\lambda)/I(0)]$ vs. $(\Delta\lambda)$, as demonstrated in Fig. 5. This "log-quasilinear" shape of hydrogenic lines is well known for Balmer lines observed in solar flares where it is considered as the manifestation of non-thermal processes in the solar plasma and of turbulent electric fields that accompany those processes [12-14].

While a variety of turbulent electric fields had been spectroscopically diagnosed in plasmas of electron densities $N_e \leq 10^{20}cm^{-3}$, for a super high-density plasma of $N_e >> 10^{20}cm^{-3}$, expected at the final compression stage at PHOENIX, all the types of oscillatory electric fields, except those associated with the Langmuir waves at the plasma electron frequency $\omega_{pe}$, would be strongly damped due to a high collision frequency $\gamma_e$. Indeed, using the standard formulas of plasma physics [15], it is easy to estimate that, for those super high-density plasmas, out of all the types of waves only the Langmuir waves have the frequency significantly higher than the collisional damping rate $\gamma_e$.

It turned out that for a relatively broad range of parameters of the plasma and of the multi-mode field (1) at the frequency $\omega_{pe}$, the resulting theoretical profile demonstrates the log-quasilinear behavior. For example, Fig. 5 shows a typical experimental profile of the $L_\beta$ line plotted in Log I-vs.-$\Delta\lambda$ coordinates (dotted line) and a theoretical fit calculated as described above (solid line). The Doppler, opacity, and normal Stark effects are also incorporated in the calculations as secondary broadening mechanisms. It is seen that the theoretical profile broadened primarily by the turbulent field is indeed log-quasilinear and fits very well the experimental profile.

For the polarization analysis the $L_\gamma$ line is more appropriate

than the $L_\beta$ line, since the former is more sensitive to the electric fields than the latter. Figure 6 shows experimental profiles of the $L_\gamma$ line registered in two orthogonal linear polarizations (parallel and perpendicular to the discharge current). It demonstrates a significant polarization in the wings.

We have also used a flat-crystal spectrometer that registered unpolarized profiles of the $L_\gamma$, $L_\delta$, and $L_\varepsilon$ lines of Al XIII on one film in one shot. Our detailed analysis of all profiles of the $L_\beta$, $L_\gamma$, $L_\delta$, and $L_\varepsilon$ lines of Al XIII obtained during our experimental campaign at the PHOENIX, including the analysis of the anomalous intensity trend in the wings and the polarization analysis, has led to the following conclusions. The compressed PHOENIX plasma was characterized by the electron density $N_e \approx (1\text{-}3) \times 10^{21} cm^{-3}$ and by the rms nonthermal velocity of the macroscopic motion $v_{nt} = (4\text{-}8) \times 10^7 cm/s$. In this plasma there have developed highly suprathermal Langmuir waves of the electric field amplitude $E_0 \approx (3\text{-}6)$ GV/cm. Their angular distribution represents an ellipsoid, which is prolate along the discharge current, so that the ratio of its axes is approximately between 4:1 and 2:1. It is this anisotropy which is manifested via the significant polarization of the $L_\gamma$ line profiles. The shape of the angular distribution of the Langmuir waves is consistent with the mechanism of their generation by electron beams (run-away electrons) travelling parallel to the bulk plasma current.

3. *Satellites of non-hydrogen and non-H-like lines* (also known as *satellites of dipole-forbidden lines*), induced by a single-mode or a milti-mode oscillatory electric field, were first calculated theoretically by Baranger and Mozer [16] by the standard perturbation theory. A couple of such satellites nearest to the forbidden line were then first observed by Kunze and Griem [17] employing He lines. In the course of time, as experiments shifted to the higher amplitudes of the oscillatory field ($E_0 \geq 10$ kV/cm), multiple satellites were observed. For example, Fig. 7 shows multiple satellites of the line Li I 4603 Å observed by Rebhan [18] in a microwave field of the frequency $\nu$=9.5 GHz. The satellites appear symmetrically: - at even harmonics around the forbidden line and at odd harmonics around the allowed line. An analytical description of these kind of satellites at relatively high oscillatory fields, where the standard perturbation theory breaks down, was provided by Gavrilenko and Oks [19], who developed an adiabatic theory of the satellites.

The first polarization measurements of the satellites of dipole-forbidden lines were first conducted by Cooper and Ringler [20], who measured a polarization of He satellites. The first application of the polarization of He satellites for the experimental plasma diagnostics was done by Brizhinev et al [21].

Recently a new interesting theoretical result was obtained. As the oscillatory field increases further, the distribution of multiple satellites around a dipole-forbidden line becomes strongly asymmetric (in distinction to the lower field case [18]) and significantly polarized. An introductory discussion of this result, obtained analytically by Gavrilenko and Oks via the adiabatic theory of satellites, could be found in the Sect. 5.1.4 of the

Oks's book [8]. As a new example (not presented in [8]), Fig. 8 shows the spectrum of the forbidden line He I 5042 Å ($2^1S$-$3^1D$) under the field $\mathbf{E}_0\cos 2\pi\nu t$, where $\nu$=9.4 GHz, $E_0$=150 kV/cm. The top part corresponds to the polarization $\parallel\mathbf{E}_0$, the bottom part - to the polarization $\perp\mathbf{E}_0$. It is seen that the spectrum is indeed strongly asymmetric with respect to the field-perturbed position of the forbidden line (marked as 0) and significantly polarized.

The distribution of multiple satellites around the corresponding allowed line also becomes significantly polarized at high fields. However, in distinction to the forbidden line, the satellite distribution around the allowed line remains symmetric. This can be seen in Fig. 9, that shows, as an example, the spectrum of the allowed line He I 5016 Å ($2^1S$-$3^1P$) under the field $\mathbf{E}_0\cos 2\pi\nu t$, where $\nu$=9.4 GHz, $E_0$=150 kV/cm. The top part corresponds to the polarization $\parallel\mathbf{E}_0$, the bottom part - to the polarization $\perp\mathbf{E}_0$.

It should be emphasized, that for the He lines originating from the higher upper level of n=4, such as He I 4471 Å ($2^3P$-$4^3D$) and He I 4922 Å ($2^1P$-$4^1D$), it would suffice to have a field of $E_0\approx$25 kV/cm (at the same $\nu$=9.4 GHz) to observe this new effect. This new polarization effect should be of a great interest for future experiments.

### 3.2. Coupling between the ion microfield and the dynamic field

The results presented above, where the dynamic field had no coupling with the ion microfield, are valid only for relatively low density plasmas or relatively high dynamic fields, so that the typical (Holtsmark) ion field satisfies the inequality

$$F_H << \min(E_0, \omega) \qquad (2)$$

(here the atomic units are used: $\hbar$=e=$m_e$=1). Otherwise, the coupling becomes effective.

Details on variety of theoretical and experimental works concerning the coupling of these two fields can be found in the Oks's book [8]. Here we would like to focus only at two such effects that are especially important for the Plasma Polarization Spectroscopy.

1. Under the condition

$$F_H \sim \omega \geq E_0, \qquad (3)$$

radiators such as hydrogen atoms and H-like ions, provide a resonant coupling between the ion microfield and the dynamic field. The resonant coupling results in appearance of **local dips or depressions** in the hydrogen and H-like line profiles at frequencies $\Delta\omega$ corresponding to some rational multiples of the dynamic field frequency. These dips or depressions were observed in a large number of experiments conducted by variety of experimental groups in different countries for a broad range (over five orders of magnitude) of plasma densities (see, e.g., the references from Sects. 4.2.5, 7.4 of the Oks's book [8]).

In fact, the study of this phenomenon developed into a new area

of plasma spectroscopy - the intra-Stark spectroscopy - named so due to its limited analogy with the intra-Doppler spectroscopy in nonlinear optics. This new area has unique diagnostic applications.

A polarization analysis of such dips in experimental line profiles was first conducted by Zhuzhunashvili and Oks [22] at the same machine Dimpol as was used in the experiment [2] described above. Fig. 10 shows the experimental profiles of the $H_\alpha$ line from [22] observed in the z-direction with the polarizer in either the r-direction (Fig. 10a) or in the $\phi$-direction (Fig. 10b); the reference frame is cylindrical. The vertical lines mark the theoretically expected positions of dips/depressions.

The comparison of the widths of the same dip in two polarizations yielded the following. For the dips in the profiles of $\pi$-components: $(\Delta\lambda_{1/2})_{r\pi} > (\Delta\lambda_{1/2})_{\phi\pi}$. For the dips in the profiles of $\sigma$-components: $(\Delta\lambda_{1/2})_{r\sigma} < (\Delta\lambda_{1/2})_{\phi\sigma}$. This means that the rms value of the dynamic field in the $\phi$-direction was greater than in the r-direction.

In this experiment, the dips were also seen in the $H_\alpha$ line profiles observed in the r-direction with the polarizer in either the z- or $\phi$-directions. However, in these profiles there was practically no difference between the widths of the same dip in the two polarization.

The analysis of the entire set of the experimental profiles resulted in the following conclusions. In the plasma of the current sheet of the electron density $N_e \approx 3.4 \times 10^{13} cm^{-3}$, suprathermal Langmuir oscillations were developed primarily in the $z\phi$-plane (the plane spanned on the directions of the current and the magnetic field). This anisotropic dynamic field was characterized by the following rms amplitudes in three directions: $E_z \approx E_\phi \approx 3$ kV/cm $> E_r \approx 1$ kV/cm.

In the future experiments, a similar technique could be applied for the polarization analysis of dips in the profiles of H-like spectral lines of multicharged ions emitted from **laser produced plasmas.**

2. Under the condition

$$\omega >> E_0 \sim F_H, \tag{4}$$

radiators such as hydrogen atoms and H-like ions, provide a nonresonant coupling between the ion microfield and the dynamic field. The gist of the nonresonant coupling is as follows. A linearly polarized dynamic field "dresses" the states of the radiator and effectively modifies those component of the dipole moment of the radiator that are perpendicular to the dynamic field:

$$(d_\perp)_{eff} = d_\perp J_0(3nE_0/2Z\omega). \tag{5}$$

Here $J_0(x)$ is the Bessel function, n is the principal quantum number, Z is the nuclear charge of the radiator. As a result, the action of a quasistatic field **F** (e.g., the ion microfield) on the radiator can be suppressed - at least, partially. Indeed, $|J_0(x)| < 1$ at $x > 0$. Moreover, $J_0(x)$ is the oscillatory function; so if its argument corresponds to a zero of the Bessel function, the

suppression should be the most effective.

The effect of the nonresonant coupling of the two fields on the shape and polarization of spectral line profiles was first observed by Gavrilenko et al [23]. In this experiment, a peripheral plasma of the large tokamak T-10 was studied. The discharge current was J=180 kA, the toroidal magnetic field was $B_0$=1.65 T, the electron density at the edge was $N_e=2.5\times10^{13}cm^{-3}$. Profiles of the Balmer lines of deuterium $D_\alpha$, $D_\beta$, $D_\gamma$ were observed along the central chord in the equatorial plane of the tokamak in two polarizations: $\parallel \mathbf{B}_0$ and $\perp \mathbf{B}_0$.

The most prominent feature was the central minimum in the $D_\alpha$ profile polarized $\parallel \mathbf{B}_0$ (Fig. 11). In the same polarization, the central minimum was also observed in the $D_\gamma$ profile, but not in the $D_\beta$ profile (Fig. 12). This experimental result was totally counter-intuitive. Indeed, the $D_\alpha$ and $D_\gamma$ lines have intensive central (unshifted) Stark components, while the $D_\beta$ does not. Therefore, in experiments without polarizers, usually it is the $D_\beta$ line that exhibits the central minimum, while the $D_\alpha$ and $D_\gamma$ lines do not. With the allowance for the polarizer $\parallel \mathbf{B}_0$, all three lines should exhibit the central minimum (since the $D_\alpha$ and $D_\gamma$ line "lose" their central components in this polarization), contrary to this experiment [23].

A comprehensive analysis of all the data gathered in that experiment demonstrated that a consistent interpretation of the experimental results can be made only with the allowance for the nonresonant coupling of two electric fields: a dynamic one at the electron cyclotron frequency and a quasistatic (lower-frequency) turbulent field. Specifically, the interpretation employed the selective nature of the effect with respect to n. Indeed, Eq. (4) shows that the effective dipole matrix element depends on n, so that the dynamic field suppresses the quasistatic splitting of the lines $D_\alpha$, $D_\beta$, $D_\gamma$ in different ways. In the conditions of the experiment [23], the argument of the Bessel function in (4) for n=4 was close to the first zero of the Bessel function, so that the quasistatic splitting of the $D_\beta$ line was almost completely suppressed. For n=3 and n=5, the absolute value of the Bessel function was of the order of unity, so that for the $D_\alpha$ and $D_\gamma$ lines the suppression of the quasistatic splitting was much less significant than for the $D_\beta$ line.

## 4. Profiles polarized due to anisotropic *impact* broadening

### 4.1. Anisotropy of the impact width of hydrogen and H-like lines due to the coupling of the electron impacts and quasistatic fields

Recently a **Generalized Theory (GT)** of Stark broadening of hydrogen and H-like lines was developed by Ispolatov and Oks [24] and Oks et al [25]. The GT takes into account one of the components of the electron microfield **exactly** - on the equal footing with the quasistatic field. The analytical results of the GT represent a significant improvement over the standard theory that treated all three components of the electron microfield by the perturbation theory. Particularly, for neutral hydrogen, the GT is **convergent**, while the standard theory was intrinsically divergent at small impact parameters. The primary result of the GT is a coupling of

the electron impacts and the quasistatic fields.

The application of the GT to the Plasma Polarization Spectroscopy becomes important in the case of anisotropic quasistatic fields (associated with an anisotropically-developed low-frequency plasma turbulence). For hydrogen and H-like lines such as $H_\alpha$, $L_\alpha$, whose width is controlled primarily by the electron impact broadening of the central (unshifted) Stark component, the GT predicts a significant difference of the linewidths observed in two linear polarizations due to the coupling of the electron impacts and the quasistatic fields. This new polarization effect should be of a great interest for future experiments.

4.2. Polarization diagnostics of edge plasmas of tokamaks based on a novel spectroscopic effect

Last year Derevianko and Oks [26] had shown that the polarization analysis of the $L_\alpha$ profiles emitted by a neutral hydrogen or deuterium **beam** allows to measure both the magnetic pitch angle $\gamma_p$ and the effective charge $Z_{eff}$ simultaneously. From the spectroscopic point of view, that work constituted an application of the GT to the ion impact broadening. We had actually demonstrated in [26] that the impact width $\Delta\omega_{imp}$ of the central component of the $L_\alpha$ line, emitted by the atoms of the beam, becomes highly anisotropic:

$$\Delta\omega_{imp} \propto \sin^2\theta, \qquad (6)$$

where $\theta$ is the angle between the beam velocity $\mathbf{v}$ and the total magnetic field $\mathbf{B}=\mathbf{B}_T+\mathbf{B}_p$. This is yet another proposal for future experiments.

4.3. Polarization caused by an electron oscillatory shift in plasmas interacting with a laser radiation

The gist of this effect, described in Sect. 5.4 of the Oks's book [8] is the following. In the standard theory of the electron impact broadening, the nonzero effects of a width and a shift of spectral lines arise only in the second order of the Dyson expansion of the time evolution operator - the first order terms cancel after the averaging over the isotropic Maxwell distribution of electron velocities. However, in plasmas interacting with a laser field $\mathbf{E}_0\cos\omega t$, the electron velocity distribution acquires anisotropic corrections. Therefore, even in the first order of the Dyson expansion, a nonzero effect appears: a shift $d_e$ of spectral line components that we had named **Electron Oscillatory Shift (EOS).** The dominant contribution to the EOS comes from the quadrupole interaction of a radiator with perturbing electrons:

$$d_e \propto \langle Q_{zz} \rangle, \qquad (7)$$

where $\langle Q_{zz} \rangle$ is the zz-component of the quadrupole moment tensor (the axis $Oz \| \mathbf{E}_0$).

The most remarkable feature of the EOS is its **linear dependence on the laser field** at relatively small fields. Therefore the EOS

leads in the competition with other shifts, including the ion quadrupole shift and the shift due to the direct action of the laser field on radiators (the latter is quadratic with respect to $E_0$).

The EOS is **anisotropic**: the EOS of the entire spectral line (averaged over all components) depends on the direction of the observation:

$$\langle d_e^{\parallel E} \rangle = -2\langle d_e^{\perp E} \rangle. \qquad (8)$$

Therefore, the EOS also depends on the polarization:

$$\langle d_e^{\pi} \rangle = -\langle d_e^{\sigma} \rangle. \qquad (9)$$

In other words, the same spectral line observed in two linear polarizations should be shifted in the opposite directions in the spectrum.

The conditions for the experimental observation of the polarization-dependent EOS should be the most favorable for Li-like ions. This is the last proposal for future experiments made in this review.

## 5. Summary of proposals for future experiments on the polarization analysis of spectral line **profiles**

1. **Dips** in the profiles of H-like spectral lines of multicharged ions emitted from **laser produced plasmas.**
2. **Strongly-asymmetrical multi-satellite** profiles of He or Li dipole-forbidden lines in an **intense microwave** field.
3. **Anisotropic impact width** of the lines, such as $H_\alpha$, $L_\alpha$, due to the **coupling** of the electron impacts and (anisotropic) quasistatic fields.
4. **Anisotropic impact width** of the $L_\alpha$ profiles emitted by a neutral hydrogen or deuterium **beam in a tokamak**.
5. **Anisotropic Electron Oscillatory Shift** of Li-like lines emitted by **laser produced plasmas**.

## References


1. G.V. Sholin and E. Oks, Sov. Phys. Doklady **18**, 254 (1973).
2. M.V. Babykin, A.I. Zhuzhunashvili, E. Oks, V.V. Shapkin, and G.V. Sholin, Sov. Phys. JETP **38**, 86 (1974).
3. Ya.F. Volkov, V.G. Djatlov, and N.I. Mitina, Sov. Phys. Tech. Phys. **44**, 1448 (1974).
4. A.N. Babin and A.N. Koval, Bull. Crimean Astrophys. Obs. **66**, 89 (1983).
5. I. Gaisinsky and E. Oks, in "Solar Maximum Analysis" (Utrecht, VNU Science Press) 1987, p. 237.
6. D.I. Blochinzew, Phys. Z. Sow. Union **4**, 501 (1933).
7. E.V. Lifshitz, Sov. Phys. JETP **26**, 570 (1968).
8. E. Oks, *Plasma Spectroscopy: The Influence of Microwave and Laser Fields*, Springer Series on Atoms and Plasmas, Vol. 9 (Springer, New York, 1995).
9. A. Kamp and G. Himmel, Appl. Phys. B **47**, 177 (1988).
10. E.J. Clothiaux, E. Oks, J. Weinheimer, V. Svidzinski, and A. Schulz, J. Quant. Spectr. Rad. Transfer **58**, 531 (1977).
11. E. Oks, in "Spectral Line Shapes", v. 9, 13th Int. Conf., Firenze, Italy, 1996 (AIP Press, New York) 1997, p. 3.
12. Z. Svestka, Adv. Astron. Astrophys. **3**, 119 (1965).
13. E. Oks, Sov. Astron. Lett. **4**, 223 (1978).
14. A.N. Koval and E. Oks, Bull. Crimean Astrophys. Obs. **67**, 90 (1983).
15. NRL Plasma Formulary, NRL Publication 177-4405, Washington, DC, 1990.
16. M. Baranger and B. Mozer, Phys. Rev. **123**, 25 (1961).
17. H.-J. Kunze and H. Griem, Phys. Rev. Lett. **21**, 1048 (1968).
18. U. Rebhan, J. Phys. B **19**, 3487 (1986).
19. V.P. Gavrilenko and E. Oks, Sov. Phys. Tech. Phys. **9**, 111 (1983).
20. W.S. Cooper and H. Ringler, Phys. Rev. **179**, 226 (1969).
21. M.P. Brizhinev, V.P. Gavrilenko, S.V. Egorov, B.G. Yeryomin, A.V. Kostrov, E.A. Oks, and Yu.M. Shagiev, Sov. Phys. JETP **58**, 517 (1983).
22. A.I. Zhuzhunashvili and E. Oks, Sov. Phys. JETP **46**, 1122 (1977).
23. V.P. Gavrilenko, E. Oks, and V.A. Rantsev-Kartinov, JETP Letters **44**, 404 (1986).
24. Ya. Ispolatov and E. Oks, J. Quant. Spectr. Rad. Transfer **51**, 129 (1994).
25. E. Oks, A. Derevianko, and Ya. Ispolatov, J. Quant. Spectr. Rad. Transfer **54**, 307 (1995).
26. A. Derevianko and E. Oks, Rev. Sci. Instr. **68**, 998 (1997).

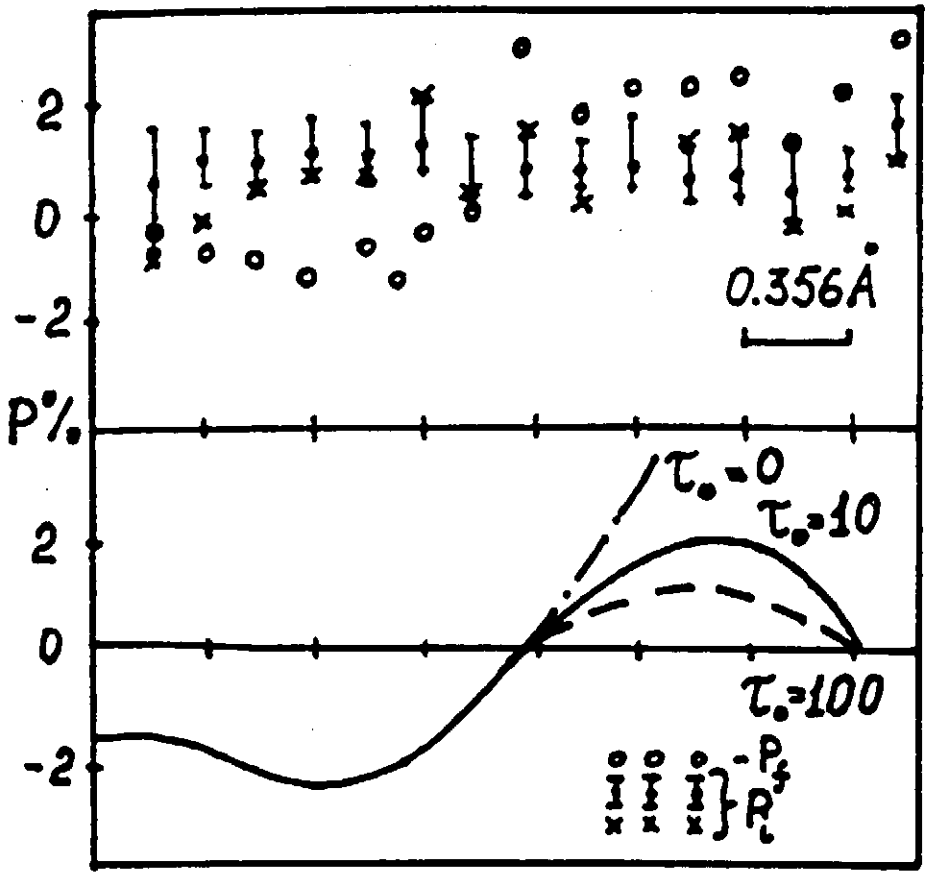


Fig. 1. Degree of linear polarization of the $H_\alpha$ profiles v. $\Delta\lambda=\lambda-\lambda_0$, observed by Babin and Koval [4] in the solar flare of 10.01.78 (the top part), compared to the theoretical calculations by Gaisinsky and Oks [5] (the bottom part). The observed polarization should be understood as the difference between the "raw" polarization of the flare (circles) and the instrumental polarization (dots, crosses).

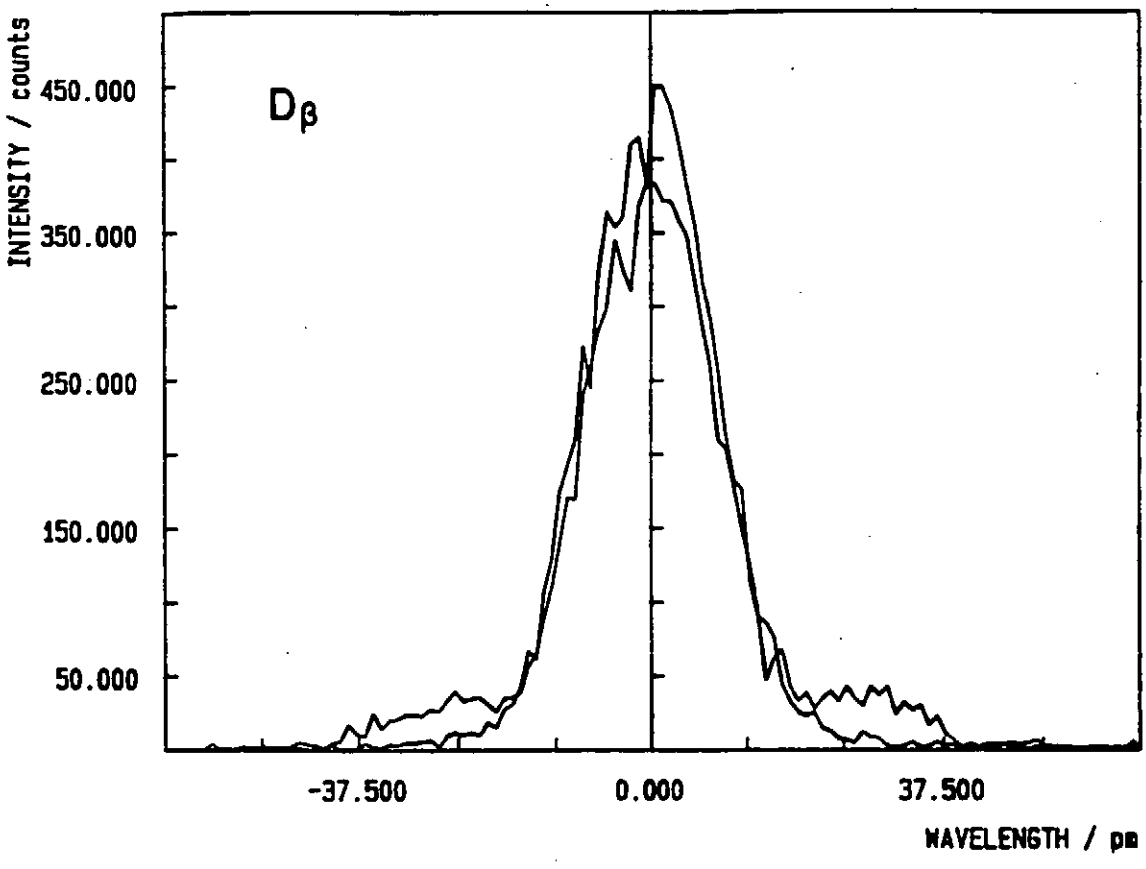


Fig. 2. Experimental profiles of the deuterium line $D_\beta$ from [9] with the polarizer parallel to the microwave field $\mathbf{E}_0$. The top profile, corresponding to the microwave field on, is more intensive in the wings than the bottom profile, recorded without the microwave field.

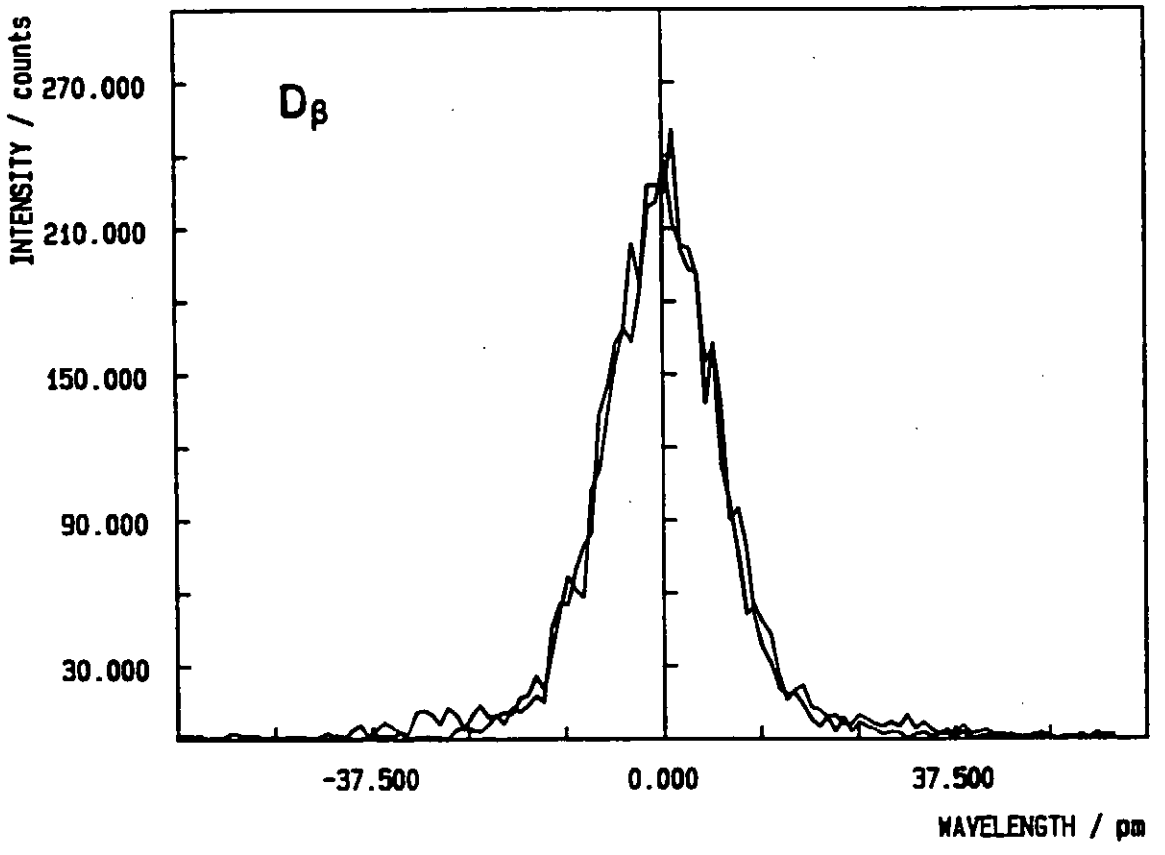


Fig. 3. A pair of experimental profiles from [9], analogous to those in Fig. 2, but with the polarizer perpendicular to $\mathbf{E}_0$.

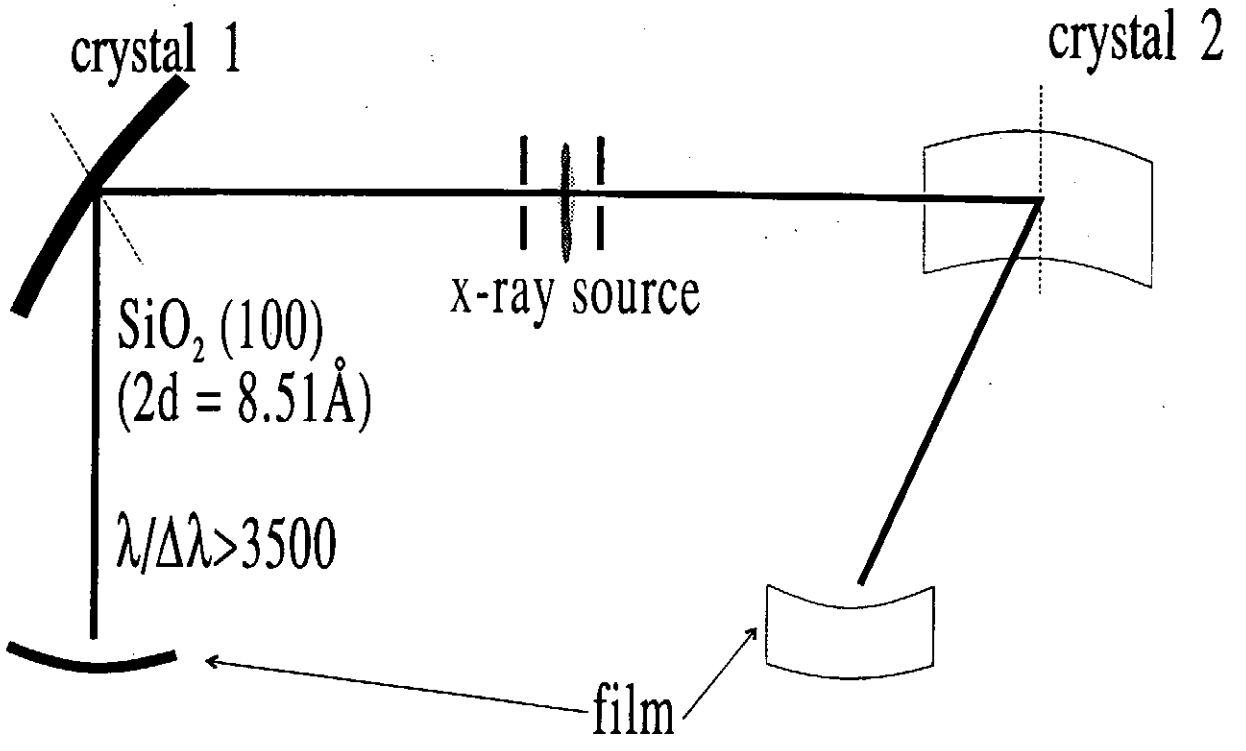


Fig. 4. Scheme for experimental analysis of a linear polarization of x-ray line profiles.

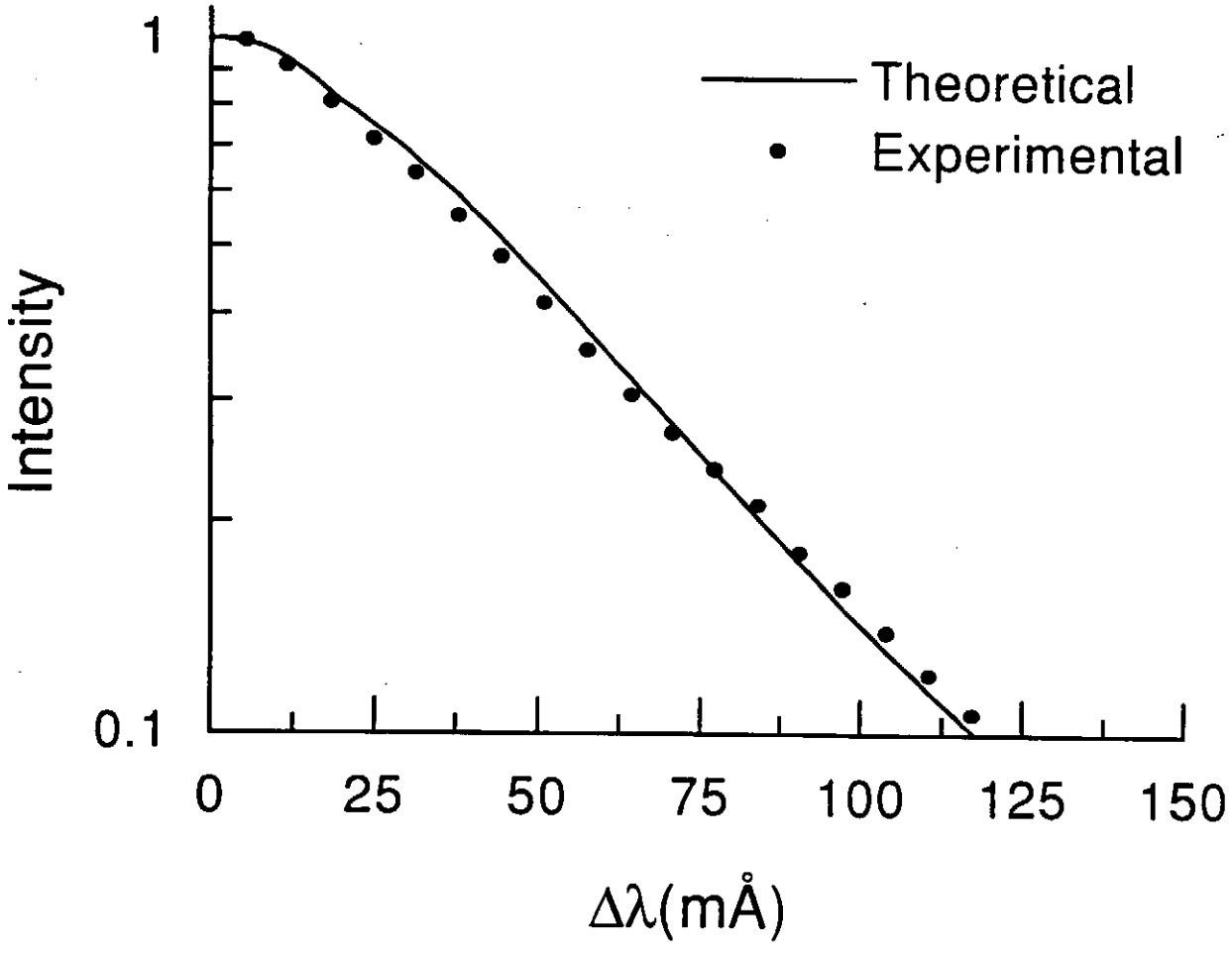


Fig. 5. Typical experimental profile of the Al XIII $L_\beta$ line plotted as Log I-vs.-$\Delta\lambda$ (dots). The theoretical curve includes the action of an electric field $\mathbf{E}(t)=\sum_k \mathbf{E}_k \cos(\omega_{pe}t+\phi_k)$ as the primary broadening mechanism and the Doppler, opacity, and normal Stark effects as the secondary broadening mechanisms.

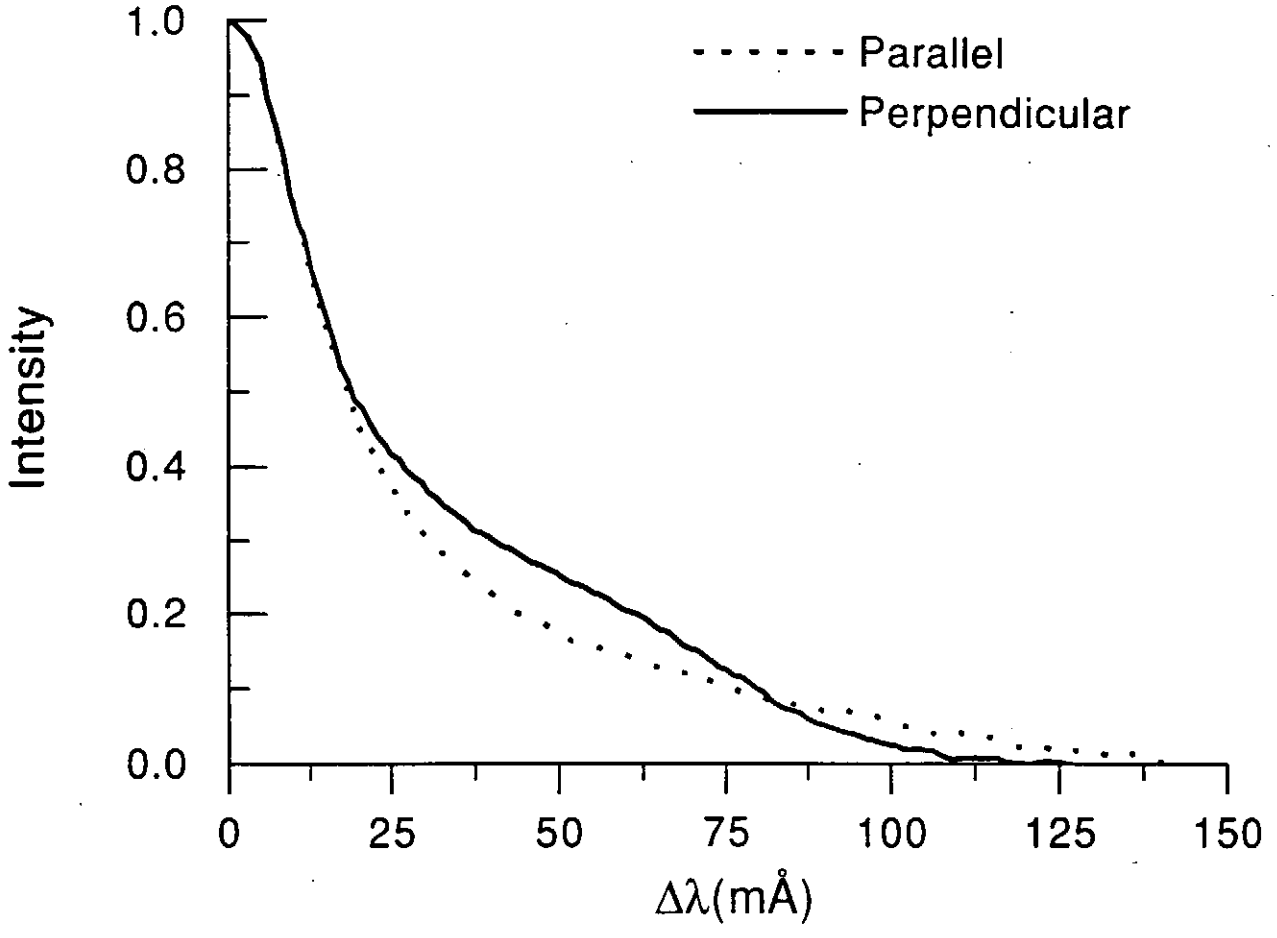


Fig. 6. Experimental profiles of the Al XIII $L_\gamma$ line (5.739 Å) recorded in two linear polarizations: parallel to the discharge current (line with dots) and perpendicular to the discharge current (line with squares).

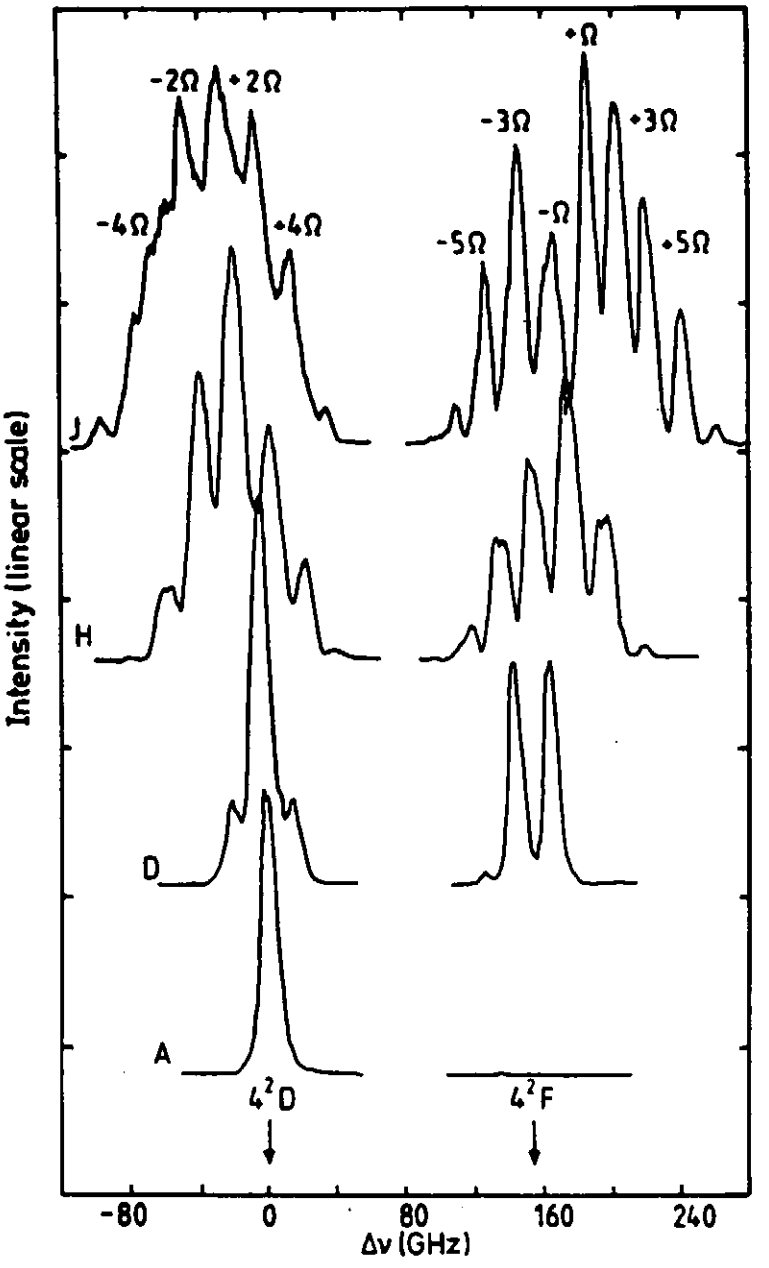


**Fig. 7.** Satellites of $2^2P-4^2D$ and $2^2P-4^2F$ transitions of Li I at a microwave frequency of 9.5 GHz and different microwave amplitudes: *A* – 0 kV/cm, *D* – 2.5 kV/cm, *H* – 8.2 kV/cm, *J* – 11.5 kV/cm. From [18]

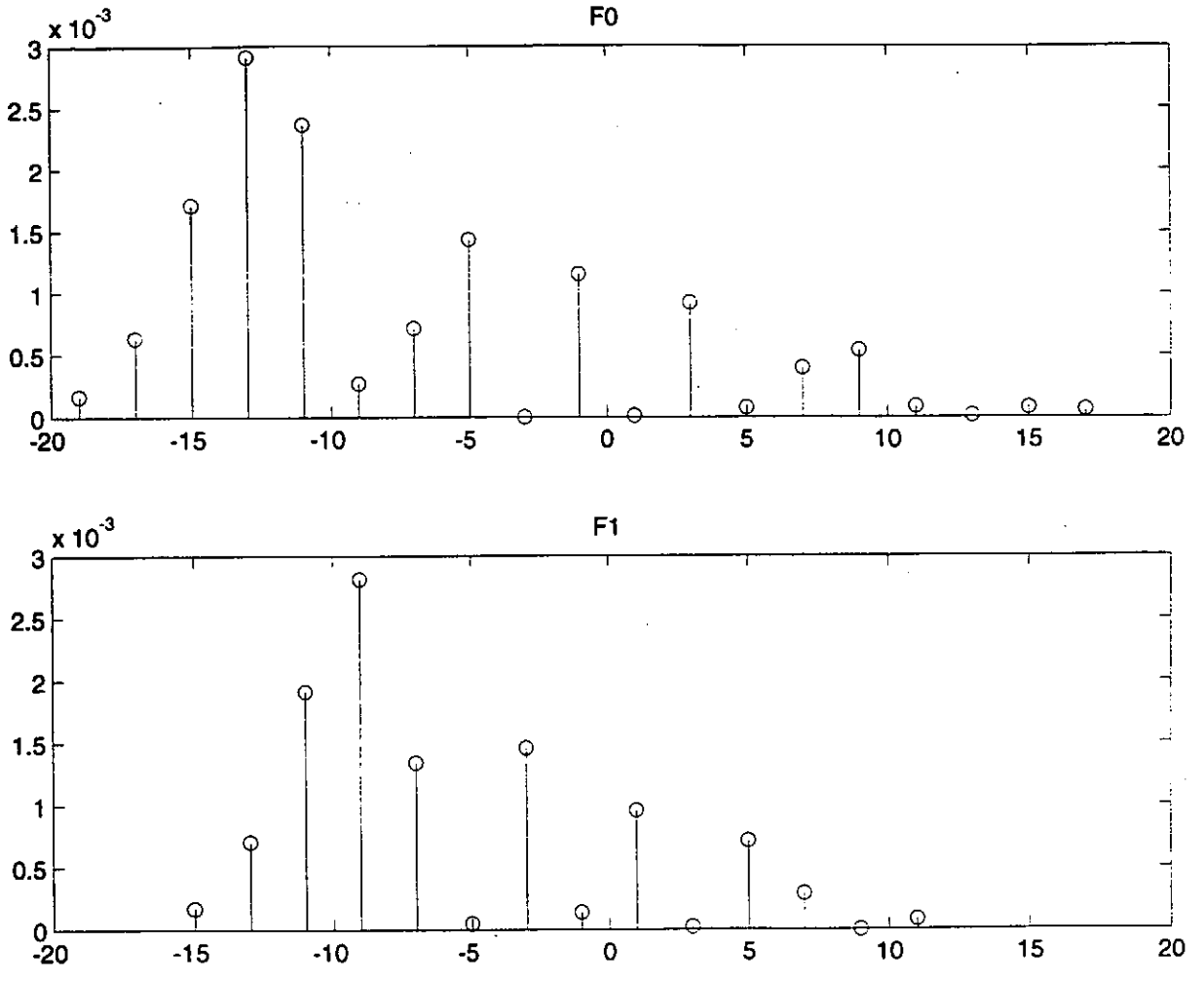


Fig. 8. Spectrum of the forbidden line He I 5042 Å ($2^1S$-$3^1D$) under the field $\mathbf{E}_0\cos 2\pi\nu t$, where $\nu$=9.4 GHz, $E_0$=150 kV/cm. The top part corresponds to the polarization $\parallel \mathbf{E}_0$, the bottom part - to the polarization $\perp \mathbf{E}_0$.

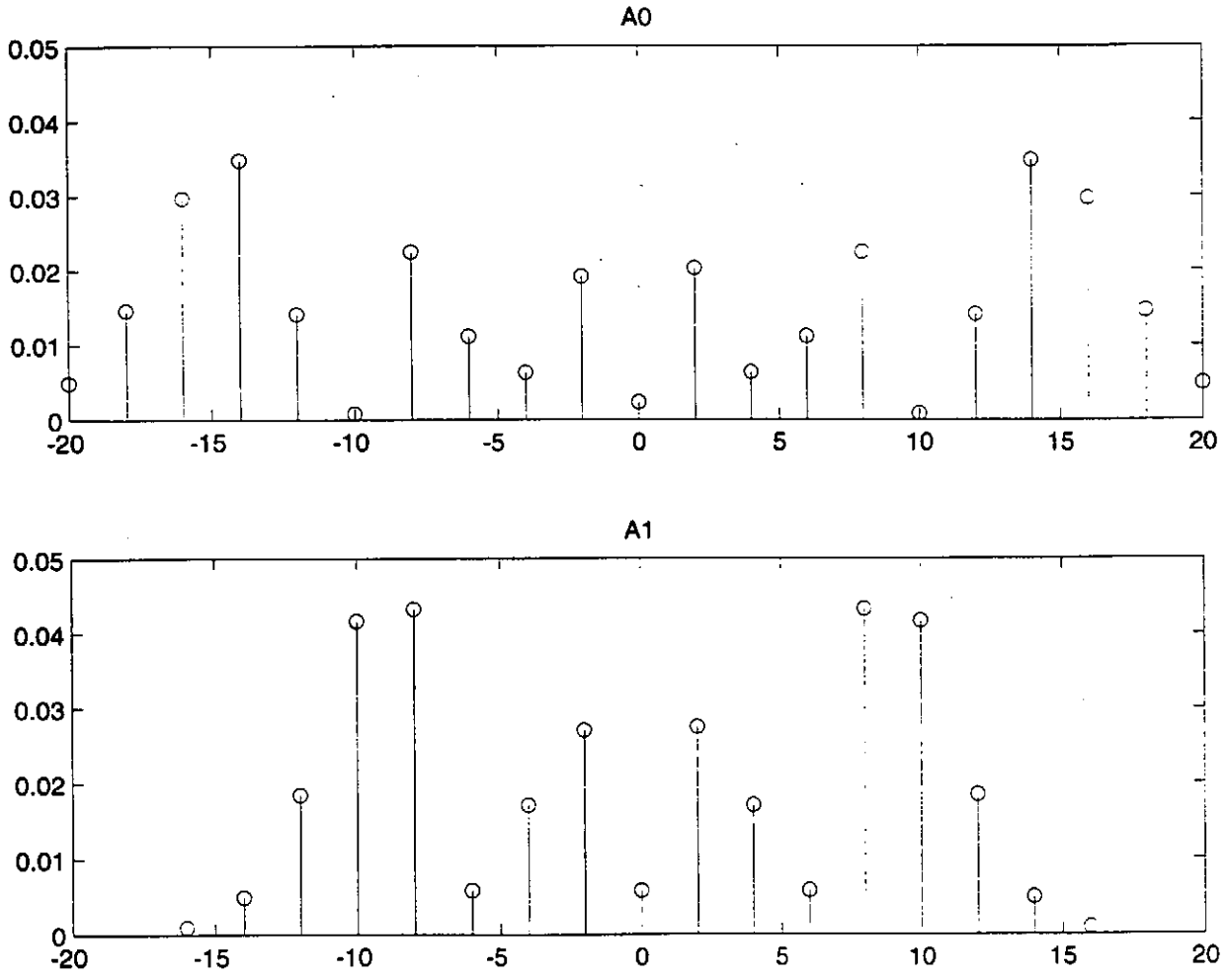


Fig. 9. Spectrum of the allowed line He I 5016 Å ($2^1S$-$3^1P$) under the field $\mathbf{E}_0\cos 2\pi\nu t$, where $\nu$=9.4 GHz, $E_0$=150 kV/cm. The top part corresponds to the polarization $\parallel \mathbf{E}_0$, the bottom part - to the polarization $\perp \mathbf{E}_0$.

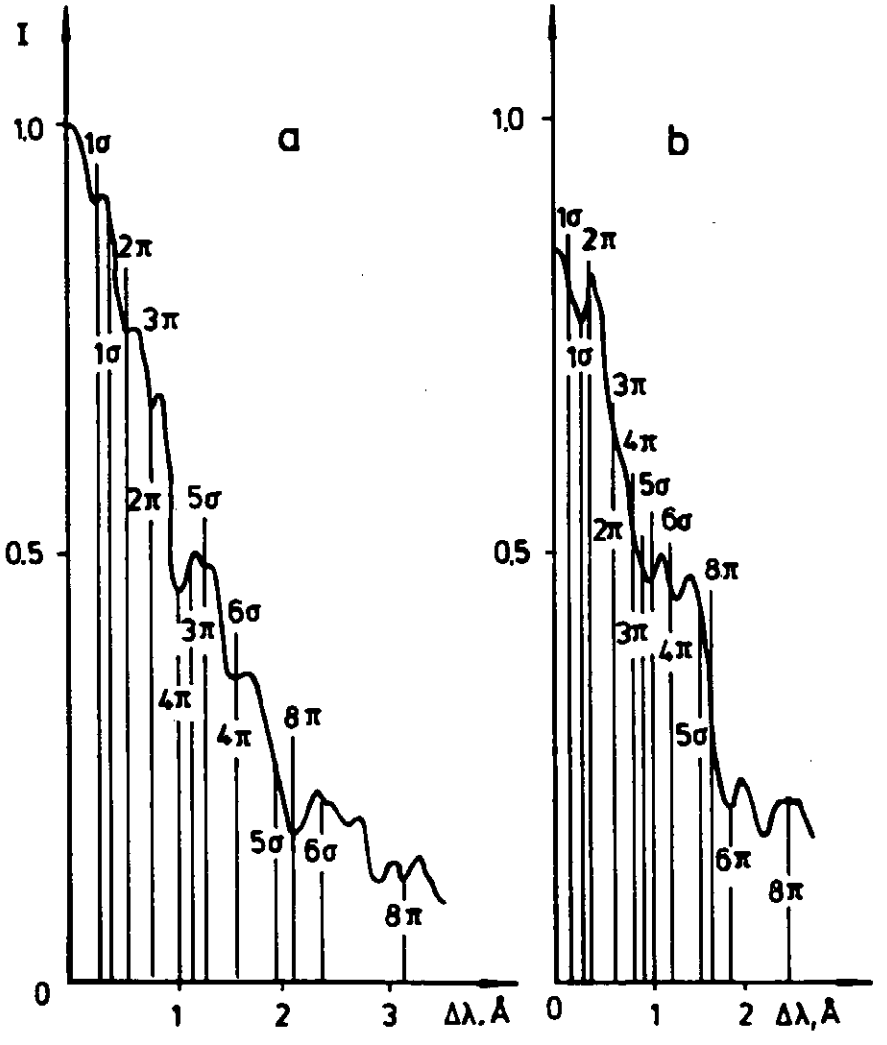


Fig. 10. Experimental profiles of the $H_\alpha$ line from [22] observed in the z-direction with the polarizer in either the r-direction (Fig. 10a) or in the $\phi$-direction (Fig. 10b); the reference frame is cylindrical. The vertical lines mark the theoretically expected positions of dips/depressions.

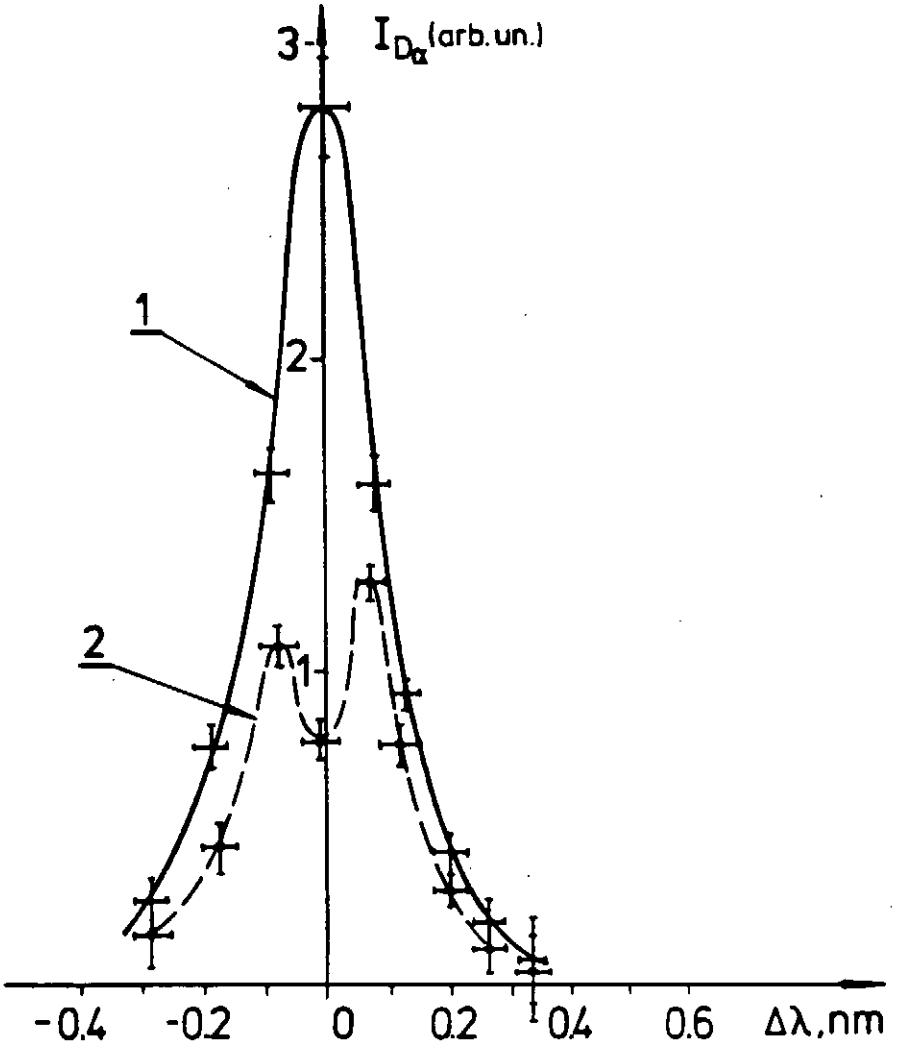


Fig. 11. Profiles of the deuterium line $D_\alpha$ observed along the central chord in the equatorial plane of the tokamak T-10 in two polarizations [23]: $\parallel \mathbf{B}_0$ (dashed line) and $\perp \mathbf{B}_0$ (solid line).

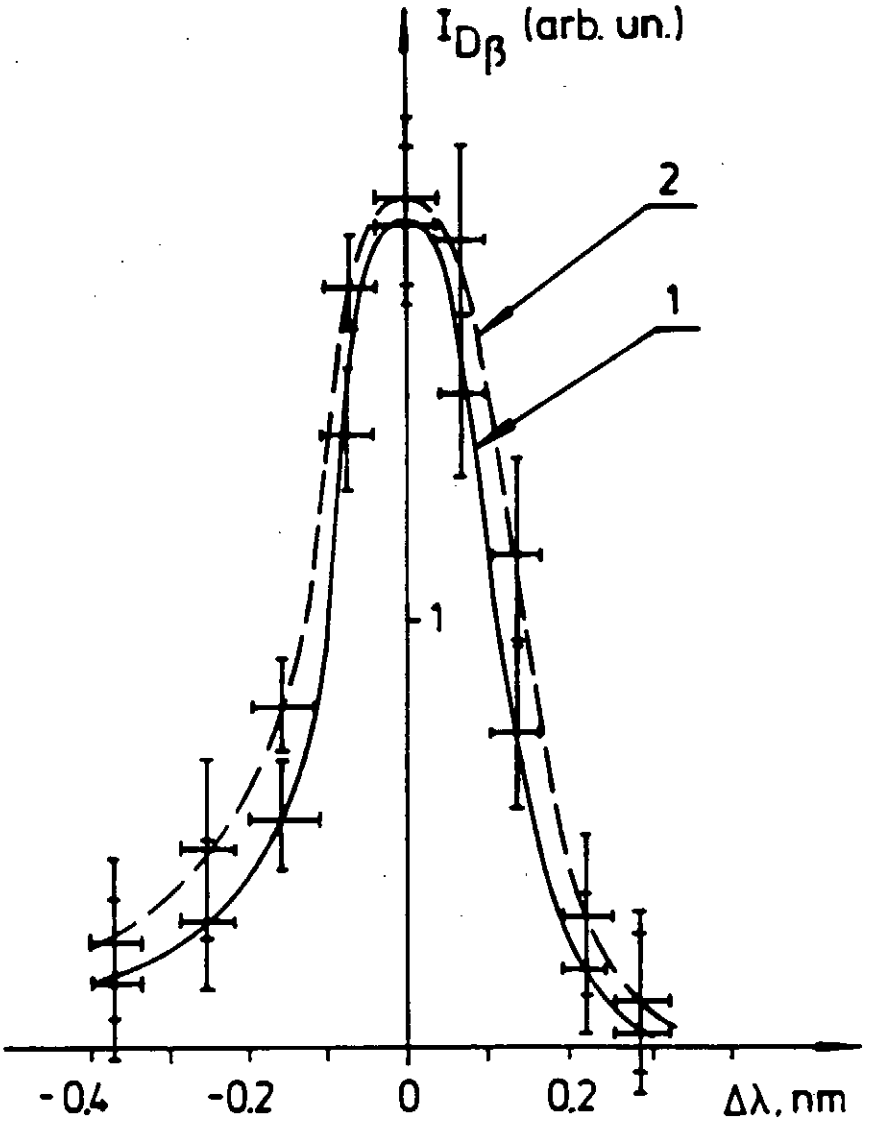


Fig. 12. Profiles of the deuterium line $D_\beta$ observed along the central chord in the equatorial plane of the tokamak T-10 in two polarizations [23]: $\parallel \mathbf{B}_0$ (dashed line) and $\perp \mathbf{B}_0$ (solid line).

# IMPACT POLARIZATION AND ALIGNMENT CREATION PARAMETERS VIA STEPWISE EXCITATION PROCESSES

G. Csanak[(1)], D. C. Cartwright[(1)], S. A. Kazantsev[(2)], and I. Bray[(3)]

(1) Los Alamos National Laboratory, Los Alamos, NM 87545, USA

(2) Institute of Physics, St. Petersburg State University, 7/9 Universitetskaya nab.

199034 St. Petersburg, RUSSIA*

and DASOP Observatoire de Paris, Meudon

Jules Janssen 92195 FRANCE

(3) Electronic Structure of Materials Centre, The Flinders University of South Australia

G.P.O. Box 2100, Adelaide 5001, AUSTRALIA

PACS Number: 34.80 Dp

* Permanent address

**Abstract**

We report here results from first order many body theory, distorted wave approximation, and converged close coupling calculations for polarization fractions and alignment creation parameters in the case of $2\,^1S \rightarrow n\,^1P(n = 3-5)$, $2\,^3S \rightarrow n\,^1P(n = 2-5)$, $2\,^1S \rightarrow n\,^1D(n = 3-5)$, $2\,^3S \rightarrow n\,^1D(n = 3-5)$, $2\,^3S \rightarrow n\,^3D(n = 3-5)$, and $2\,^1S \rightarrow n\,^3D(n = 3-5)$ excitations in helium for electron impact energies from threshold to several hundred eV.

## 1. Introduction

An anisotropic velocity distribution function of fast charged particles in a plasma results in polarized radiation being emitted by the plasma. The anisotropic distribution of the charged particle velocities creates alignment in an ensemble of atoms, ions, and molecules via impact excitation [1]. This mechanism, called self-alignment, occurs in dilute ionized media such as a low pressure gas-discharge plasma, the outer ionosphere of the Earth, and the upper layer of the solar chromosphere [2]. The new possibilities of spectropolarimetry as a plasma diagnostic tool are based on the fact that the polarization of an ensemble of atomic systems (atoms, ions) and the polarization characteristics of the plasma emission are determined, essentially by the quadrupole moment of the relative velocity distribution of colliding species within the plasma [1]. Therefore the measurement of the degree of polarization of the plasma emission will provide information about the structural parameters of ionized media and about the energy transport within it.

According to the way it is implemented, passive and active spectropolarimetric techniques can be specified. Passive spectropolarimetric techniques, based on the polarization analysis of a plasma emission, have been effectively used in the past for sensing the structural parameters of discharge sources, including the drift velocity

of ions, and energy transport into the chromospheric location of solar flares [2].

The fundamental atomic collisional process for active spectropolarimetric observation of hot plasmas is charge exchange. Theoretical problems of spectropolarimetry under charge exchange have been resolved with the help of the pseudolevel technique [3].

A study of the polarization effects in dense ionized media could expand considerably the spheres of applications of polarization spectroscopy mainly to applied physics, including surface processes and material destruction.

The development of practical applications of plasmas in materials-etching and -deposition, laser physics, and plasma chemistry increased interest in different stepwise excitation processes via metastable and highly populated low-lying atomic states. Under certain plasma conditions metastable and low-lying atomic (ionic) states will play a role in temporary energy storage, facilitating the process of collisional excitation and ionization.

The stepwise self-alignment process of the $J = 1$ states of noble gases created by resonance light reabsorption has been studied in the past experimentally and theoretically in the positive column plasma of d.c. and high frequency discharges in noble gases for pressures of more than 0.5 Torr [4]. It was found that initial excitation from the ground state populates levels of $^1S$ symmetry and the reabsorption on $J = 0 - J = 1$ transitions of the anisotropic resonance radiation propagating inside the plasma creates aligned $J = 1$ states. In the range of pressures 0.1–0.5 Torr this photoabsorption self-alignment process is in competition with the direct electron impact alignment and for lower pressures only direct impact self-alignment from the ground state occurred. For dense ionized media ($n > 10^{15}$ cm$^{-3}$), however the stepwise impact processes will play a significant role in the kinetics of self-alignment in the plasma [4]. It is expected therefore, that the alignment creation, destruction and stepwise self-alignment impact processes

with participation of metastable atoms and electrons will be required to model the alignment dynamics in plasmas at intermediate and high pressures.

## 2. Theoretical Foundation

### 2.1 General Background

In this work we shall consider the stepwise electron impact excitation of helium by a monoenergetic and unidirectional electron beam and the creation of alignment and polarized radiation via the stepwise excitation process. Some of the motivation for our work is depicted in Figs. 1 and 2. We report here theoretical results for polarization fractions and alignment creation parameters for the excitation from the $2\ ^1S$, and $2\ ^3S$ states of helium (and we compare them with results for the excitation out of the $1^1S$ state) computed by first order many body theory (FOMBT) and by the distorted wave approximation (DWA) [5, 6, 7], and by the converged close coupling (CCC) method [8, 9].

In the past the polarization-fraction calculations for monoenergetic and unidirectional electron beams (see e.g., Ref. 10 for a review) were based on the theories of Oppenheimer [11], Penney [12], and Percival and Seaton [13]. The calculations based on the works of Oppenheimer and Penney envisioned a stationary state in which the electron beam excited a given atomic state which emits radiation and the excitation and radiative decay are in a stationary equilibrium. Percival and Seaton [13] envisioned that radiation originates from the combined system of atom and electron. From the point of view of physical interpretation for the emitted radiation one can look at the theories of Oppenheimer [11] and Penney [12] as the description of a two-step process: alignment creation by electronic excitation and alignment destruction by dipole radiation, the two processes being in equilibrium under stationary conditions. In the more general and comprehensive theory of Percival and Seaton [13], the excitation and radiative processes are intertwined.

It can be shown however (see, e.g., Ref. 14, Sec. 5.5, and Ref. 15) that the same result is obtained by envisioning either a two-step process (the same as before) or a three-step process: electron impact excitation followed by a relaxation of the atomic excited states due to fine and/or hyperfine structure effects and followed by radiative decay. We shall show later that in some of our cases this three-step process description is relevant. In order to characterize the first process Kazantsev and coworkers [2, 4] introduced a quantity called alignment creation cross section which will be referred to here as *alignment creation parameter* [16]. This parameter, along with the integrated electron impact cross section, will play a significant role in calculating the polarization characteristics of radiating atoms (ions) excited by anisotropic electron beams.

In order to elucidate the physical meaning of the *alignment creation parameter* we shall consider the two-level scheme (essentially a modern formulation of the theory of Oppenheimer) discussed in Ref. 2. They denote the statistical operator [17] associated with a level of energy $E$ and angular momentum $J$ ($J$ can refer to the total angular momentum of the atom or for $LS$ coupled systems to the pair of quantum numbers of total orbital angular momentum, $L$, and total spin, $S$) by $\hat{\rho}_J$. which is related by the formula,

$$\hat{\rho}_J = \sum_{M,M'} \left| E, J, M \right\rangle \rho^{E,J}_{M,M'} \left\langle E, J, M' \right| \tag{1}$$

to the density matrix $\rho^{E,J}_{M,M'}$ associated with level $E, J$, where $\langle E, J, M|$ refers to the state vector of the $M$ magnetic sublevel of level: $E, J$ and which is normalized to the total population of the level $E, J$ (i.e., $tr\hat{\rho}_J$ is equal to the population of that level). The two-level scheme uses the following approximate equation for the temporal evolution of $\hat{\rho}_J$ [2].

$$\frac{d\hat{\rho}_J}{dt} = -\bar{\Gamma}\hat{\rho}_J + \hat{F}_J \tag{2}$$

where $\tilde{\Gamma}$ is called the relaxation operator and $\hat{F}_J$ is referred to as the excitation operator [18]. The $\hat{\rho}_J$ and $\hat{F}_J$ operators can be expanded in terms of the irreducible tensor-operators [19]:

$$\hat{T}_q^{(k)} = \sum_{M,M'} (-1)^{J-M} C \begin{matrix} J & J & k \\ M' & -M & q \end{matrix} |E,J,M\rangle\langle E,J,M'| \tag{3}$$

in the form:

$$\hat{\rho}_J = \sum_{k,q} \rho_q^{(k)}(J)\hat{T}_q^{(k)} \tag{4a}$$

$$\hat{F}_J = \sum_{k,q} F_q^{(k)}(J)\hat{T}_q^{(k)} \,. \tag{4b}$$

For $LS$-coupled systems the density matrix factorizes in orbital space and in spin space, and one can assume isotropy in spin-space and then in Eqs. (3), (4a,b) $J$ should be interpreted as $L$, the total *orbital* angular momentum, and $\hat{\rho}_J$ as the reduced density matrix in "orbital angular momentum space." In the following equations also in case of an $LS$-coupled system, $J$ refers to $L$.

In our simple two-level scheme we can assume that the excitation occurs via electron impact and the relaxation via radiation. Under these conditions Eq. (2) can be written in the form (Ref. 2, p. 25),

$$\frac{d\rho_q^{(k)}}{dt} = -\Gamma_k \rho_q^{(k)} + F_q^{(k)} \tag{5}$$

where $\Gamma_k$ is the relaxation constant of the polarization moment of rank $k$. For stationary conditions $\left(\dot{\rho}_q^{(k)} = 0\right)$ we obtain:

$$\rho_q^{(k)} = F_q^{(k)}/\Gamma_k \,. \tag{6}$$

In the case of an excitation by a *monoenergetic electron beam* propagating along the direction $\mathbf{n}$, if the axis of quantization (i.e., the z-axis) is taken along $\mathbf{n}$, then due to cylindrical symmetry along $\mathbf{n}$ only the longitudinal components (i.e., the

$q = 0$ components) of the excitation tensor will be different from zero, and for these components we can write:

$$F_k(v) \equiv F_0^{(k)}(J) = v\sigma^{(k)}(v) \tag{7}$$

with

$$\sigma^{(k)}(v) = (2k+1)^{1/2} \sum_M (-1)^{J-M} \begin{pmatrix} J & J & k \\ M & -M & 0 \end{pmatrix} \sigma_M(v) \tag{8}$$

where $\sigma_M(v)$ is the integral magnetic sublevel excitation cross section of level $M$ with incident electron velocity $v$ while $\sigma^{(0)}(v) = (2J+1)^{-1/2}\sigma(v)$ where $\sigma(v)$ is the magnetic sublevel summed excitation cross section and the $(\ldots)$ is a $3j$ coefficient. We shall refer to $\sigma^{(2)}(v)$ as the *alignment creation parameter*, which can also be given in the form [20]:

$$\sigma^{(2)}(v) = \sqrt{5}\left[(2J+3)(2J+1)(J+1)J(2J-1)\right]^{-1/2} * \sum_M \left[3M^2 - J(J+1)\right]\sigma_M(v)\,. \tag{9}$$

The $\sigma^{(k)}(v)$ parameters are the special cases of the integrated state multiples of Bartschat and coworkers [21, 22] that are defined for an unpolarized incident electron beam as,

$$\langle \mathcal{T}(J)_{kq} \rangle = (2k+1)^{1/2} \sum_M (-1)^{J-M} \begin{pmatrix} J & J & k \\ M & -M & q \end{pmatrix} \sigma_m(v)\,. \tag{10}$$

Thus we have,

$$\sigma^{(k)}(v) = \langle \mathcal{T}(J)_{k0} \rangle\,. \tag{11}$$

In order to characterize the physical state of alignment of the atom, we introduce here the normalized alignment parameter via the expression

$$\tilde{\sigma}^{(2)}(v) = \sigma^{(2)}(v)/\sigma\,. \tag{12}$$

It can be shown that within the validity of the theories of Oppenheimer and Penney (and for a monoenergetic unidirectional electron beam) the polarization

characteristics of the emitted radiation are related to the $\rho_q^{(k)}(k = 0, 1, 2)$ parameters (see Ref. 2, pp. 16–24). In the case of electron impact excitation by a *monoenergetic directed electron beam* the radiation will be linearly polarized and the associated Stokes parameters can be obtained from $\rho_0^{(0)}$ and ${}^{\hat{n}}\rho_0^{(2)}$ (see Ref. 2, p. 27). From the Stokes parameter expressions the following formula is obtained for the polarization fraction:

$$P = \left(\frac{3}{2}\right)^{3/2} \begin{Bmatrix} 1 & 1 & 2 \\ J & J & J_1 \end{Bmatrix} {}^{\hat{n}}\rho_0^{(2)} \left[\frac{(-1)^{J+J_1}}{\sqrt{2J+1}}\rho_0^{(0)} - \frac{3}{2\sqrt{6}} \begin{Bmatrix} 1 & 1 & 2 \\ J & J & J_1 \end{Bmatrix} {}^{\hat{n}}\rho_0^{(2)}\right]^{-1} \tag{13}$$

where $\rho_0^{(0)}$ and ${}^{\hat{n}}\rho_0^{(2)}$ are calculated in the coordinate system whose z-axis is along the direction of the exciting electron beam and $J_1$ refers to the total angular momentum of the final level to which the system decays via dipole radiation. Equation (12) shows how the alignment of the excited state, ${}^{\hat{n}}\rho_0^{(2)}$, created in the electron impact excitation process, is related to the polarization fraction in the case when the two-step description is valid.

From Eqs. (6), (7), and (13) it immediately follows that the polarization fraction, $P$, will be proportional to the *alignment creation parameter*, $\sigma^{(2)}(v)$, in these cases.

As mentioned earlier, in a plasma an anisotropic electron distribution will lead via atomic excitation to the emission of polarized light. If the electron distribution function is given by $f(\mathbf{v})$ [23], one can expand $f(\mathbf{v})$ in terms of spherical harmonics $C_q^{(k)}(\mathbf{n})(\mathbf{n} = \mathbf{v}/v,\ v = |\mathbf{v}|)$ in the form

$$f(\mathbf{v}) = \sum_{k=0}^{\infty} \sum_{q=-k}^{k} C_q^{(k)}(\mathbf{n}) f_q^{(k)}(v) \tag{14}$$

where

$$f_q^{(k)} = \frac{2k+1}{4\pi} \int d\mathbf{n} C_q^{(k)*}(\mathbf{n}) f(\mathbf{v}) \tag{15}$$

where $f(\mathbf{v})$ in normalized as

$$\int d\mathbf{v} f(\mathbf{v}) = N_e \tag{16}$$

with $N_e$ being the electron density in the plasma. In Eq. (14) $f_0^{(0)}(v)$ describes the isotropic part of the velocity distribution function while $f_q^{(2)}(v)(q = 0, \pm 1, \pm 2)$ characterizes the quadrupole tensor of the free-electron distribution. Under these conditions it can be shown (see Ref. 2, p. 34) that the Stokes parameters describing the polarization characteristics of the emitted radiation originating from an atomic level can be expressed in terms of the integrals (Ref. 2, p. 34),

$$I_q^{(k)} = \int_0^\infty v^3 f_q^{(k)}(v)\sigma^{(k)}(v)\, dv \qquad (-k \leq q \leq k)$$

with $k = 0$ and 2 as well as of other constants (including $\Gamma_0$ and $\Gamma_2$). Thus along with the electron distribution function, the $\sigma^{(0)}(v)$ and $\sigma^{(2)}(v)$ parameters determine the polarization characteristics of the emitted radiation. In the formulas for the Stokes parameters referred to above (the equations given on p. 34 of Ref. 2, the $I_q^{(2)}$ (with $q = \pm 2$) integral appears in the numerator and the combination of $I_0^{(0)}$ and $I_0^{(2)}$ integrals in the denominator, i.e., the $I_q^{(2)}$ integrals are *normalized* by a term which contains $I_0^{(0)}$, i.e., an integral of the integrated cross section.

### 2.2 Application to Selected Transitions in Helium

The application of the formalism given by Eqs. (1–13) to the case of the excitation of the $He\ n\,^3P$ and $n\,^3D$ states by monoenergetic and unidirectional electron beams however is not valid, and the more general three-step process description is needed. This is due to the fact that while the electron impact excitation process (and thus the alignment creation in the excited state) can be well described within the $LM_LSM_S$ coupling formalism, following the excitation but before the radiative decay, relaxation occurs to fine-structure levels which influences the polarization characteristics of the emitted radiation. The importance of the fine-structure relaxation is due to the fact that for the $n\,^3P$ and $n\,^3D$ levels in general the fine-structure splitting is larger than the natural line-width and therefore fine-structure relaxation occurs before radiative decay. In the case of the $2\,^3P$ level of

He the fine-structure splittings are more than $10^3$ times larger than the natural line-width. In the case of the $3\,^3P$ level, the smaller splitting is about 10 times, the larger is about 100 times larger than the natural width. Thus our conditions are fulfilled. In the case of the $4\,^3P$ level, the smaller splitting is practically nonexistent (i.e., equal to zero) and the larger splitting is about 100 times larger than the natural line-width. In the case of the $3\,^3D$ level, one of the splittings is of the same order as the natural line-width while the other one is about 30 times larger. For the $4\,^3D$ level, the appropriate ratios are about 1.5 and 15. Thus in most cases our assumption is either completely or partially satisfied. In the latter cases the error introduced into the result due to the assumption with respect to the ratio of the widths is much smaller than that introduced by other means (e.g., by the collisional model).

For helium one can use the $LM_LSM_S$ coupling scheme for the description of the electron impact process and interpret $J$ in Eq. (6) as $L$, i.e., as the total *orbital* angular momentum of the atom. In this coupling scheme the excitation is incoherent in the $M_L$ and $M_S$ magnetic sublevel quantum numbers (see, e.g., Ref. 15, p. 241). Then we obtain from Eq. (6),

$$\text{for } L = 1\,,$$
$$\sigma^{(2)}(v) = \sqrt{\frac{2}{3}}\,(\sigma_1(v) - \sigma_0(v)) \tag{17a}$$

$$\text{and for } L = 2\,,$$
$$\sigma^{(2)}(v) = -\sqrt{\frac{2}{7}}\,(\sigma_0(v) + \sigma_1(v) - 2\sigma_2(v))\ , \tag{17b}$$

where $\sigma_{M_L} = \sigma_{M_L}(v)$ refers to the electron impact excitation cross section of the magnetic sublevel $M_L$. If we denote by $\sigma(LM_LSM_S)$ the electron impact excitation cross section of the $LM_LSM_S$ state then $\sigma_{M_L}$ is defined as

$$\sigma_{M_L} = \sum_{M_S} \sigma(LM_LSM_S) \,. \tag{18}$$

We note here that in the case of excitation out of the $2\,^3S$ level a spin-sublevel averaging is included into the definition of $\sigma(LM_LSM_S)$.

It was pointed out by Percival and Seaton [13] that in the case of an $LS$-coupled system $\sigma_{M_L}$ and $\sigma(LM_LSM_S)$ are related by the formula

$$\sigma(LM_LSM_S) = (2S+1)^{-1}\sigma_{M_L} \,. \tag{19}$$

The formulas for the polarization fractions can be obtained from Percival and Seaton [13] as,

for $L = 1$ and $S = 0$ (i.e., for $^1P$ excitation)

$$P = \frac{\sigma_0 - \sigma_1}{\sigma_0 + \sigma_1} \tag{20a}$$ for $^1P - {}^1S$ optical transition

for $L = 2$ and $S = 0$ (i.e., for $^1D$ excitation)

$$P = 3\frac{\sigma_0 + \sigma_1 - 2\sigma_2}{5\sigma_0 + 9\sigma_1 + 6\sigma_2} \tag{20b}$$ for $^1D \rightarrow {}^1P$ optical transition

$$P = 3\frac{\sigma_0 + \sigma_1 - 2\sigma_2}{15\sigma_0 + 29\sigma_1 + 26\sigma_2} \tag{20c}$$ for $^1D \rightarrow {}^1F$ optical transition.

Following the electron impact excitation, which was described in the $LM_LSM_S$ coupling scheme, in the case of $n\,^3P$ and $n\,^3D$ level excitations one must consider spin-orbit relaxation before the radiative decay takes place. The spin-orbit relaxation was discussed by Blum [14] and by Bartschat and Csanak [15]. In the

case of an $LS_1 \rightarrow L_2S_2$ transition Blum [14] obtained the following formula for the polarization fraction after the fine-structure relaxation has been taken into account:

$$P = \frac{(-1)^{L+L_2} \begin{Bmatrix} 1 & 1 & 2 \\ L & L & 2 \end{Bmatrix} G(L)_2 \left(\frac{3}{2}\right)^{1/2} \langle T(L)^+_{20} \rangle}{\frac{1}{\gamma}\frac{2}{3(2L+1)^{1/2}} \langle T(L)_{00} \rangle + (-1)^{L+L_2} \begin{Bmatrix} 1 & 1 & 2 \\ L & L & L_2 \end{Bmatrix} G(L)_2 \frac{1}{6^{1/2}} \langle T(L)^+_{20} \rangle} \tag{21}$$

where $\gamma$ is the decay constant of the $LS_1$ level and $G(L)_k$ is given as

$$G(L)_k = \frac{1}{\gamma}\frac{1}{2S_1+1}\sum_{J_1}(2J_1+1)^2 \begin{Bmatrix} L & J_1 & S_1 \\ J_1 & L & k \end{Bmatrix}^2 . \tag{22}$$

For a $^3P \rightarrow {}^3S$ transition we have $L = 1$, $S_1 = 1$, $L_2 = 0$, $S_2 = 1$, and we obtain

$$G(1)_2 = \frac{5}{18} \cdot \frac{1}{\gamma} . \tag{23}$$

Using this result along with the

$$\langle T(1)^+_{00} \rangle = \frac{1}{\sqrt{3}} [2\sigma_1 + \sigma_0] \tag{24a}$$

$$\langle T(1)^+_{20} \rangle = \frac{2}{\sqrt{6}} [\sigma_1 + \sigma_0] \tag{24b}$$

expressions in Eq. (19), we obtain for the polarization fraction:

$$P = \frac{15(\sigma_0 - \sigma_1)}{67\sigma_1 + 41\sigma_0} . \tag{20d}$$

We obtain similarly

$$P = \frac{3(\sigma_0 - \sigma_1)}{73\sigma_0 + 143\sigma_1} \tag{20e}$$ for $^3P \rightarrow {}^3D$ optical transition

and for $L = 2$ and $S = 1$ (i.e., for $^3D$ excitation)

$$P = 213\frac{\sigma_0 + \sigma_1 - 2\sigma_2}{671\sigma_0 + 1271\sigma_1 + 1058\sigma_2} \tag{20f}$$ for $^3D \rightarrow {}^3P$ optical transition

$$P = 213\frac{\sigma_0 + \sigma_1 - 2\sigma_2}{2171\sigma_0 + 4271\sigma_1 + 4058\sigma_2} \tag{20g}$$ for $^3D \rightarrow {}^3F$ optical transition

These latter formulas are identical to those given by Percival and Seaton [13].

We note here that Eqs. (20d, e, f, g) can be obtained directly via the $LSJM$ coupling scheme if one assumes incoherent excitation of the $JM$ sublevels and sums over the intensities following the original scheme of Penney [12]. However this procedure falsifies the physics (as was shown by Percival and Seaton [13] and recently by Bartschat and Csanak [15]), since the initial (electron impact) excitation creates an incoherent state in the $LM_LSM_S$ coupling scheme but not in the $LSJM$ coupling scheme. (See the discussion of Bartschat and Csanak [15] on pp. 241–2.) It is only after the spin-orbit relaxation process is taken into account and if the fine-structure splitting is much larger than the natural line-width of the level, that the result is obtained which appears to suggest that the initial (electron impact) excitation was incoherent in the $LSJM$ coupling scheme. (See the discussion of Blum [14] of this subject on p. 139.) So the picture we have presented above not only describes the physics properly but it is also more general since it is applicable in those cases also when the spin-orbit coupling energy is comparable to the natural line-width.

We note here that the above discussion shows that small interactions influence the polarization fraction in the case of radiation being emitted by a metastable level. It is quite conceivable that in case the radiating system (atom or ion) is situated in a plasma the interaction with the plasma-environment will also influence the polarization characteristics of the emitted radiation. The possible depolarization of the emitted radiation due to heavy-particle collisions have been investigated in the past (see, e.g., Rebane and Rebane [24], Rebane [25, 26]). The investigation of plasma-effects due to electronic collisions is for future work.

## 3. Numerical Results and Discussion

Our results are presented in Figs. 3–9. In Fig. 3 we show our DWA and CCC results for the normalized alignment parameter in the case of $2\,^3S \rightarrow 2\,^3P$, $2\,^3S \rightarrow 3\,^3P$, and $2\,^3S \rightarrow 3\,^3D$ excitations and compare them with the multi-channel eikonal (MCE) theory results of Mansky and Flannery [27]. The DWA shows qualitative, in some cases quantitative, agreement with the CCC results while the MCE results strongly differ from those of DWA and CCC. This figure shows that low-energy electrons ($E < 10$ eV) can create considerable alignment ($|\tilde{\sigma}_2| \sim 0.2 - 0.5$), and in the case of $2\,^3S \rightarrow 3\,^3D$ excitation medium energy electrons (15 eV $\leq E \leq$ 200 eV) can also create considerable alignment ($\tilde{\sigma}_2 \sim 0.25$). Figures 4–5 show our results for the alignment creation parameter, and Fig. 4 shows our results for the polarization fraction, $P$. Figure 4 shows that the absolute values of the alignment creation parameter for the $2\,^1S \rightarrow n\,^1P(n = 2\text{–}5)$ transitions for most energies are about 1 or 2 orders of magnitude higher than the same quantities for the $1\,^1S \rightarrow n\,^1P(n = 2\text{–}5)$ transitions. The alignment creation parameter for the $2\,^1S \rightarrow 2\,^1P$ transition is about an order of magnitude larger than those for the $2\,^1S \rightarrow n\,^1P(n = 3, 4, 5)$ transitions. The alignment creation parameter for the $2\,^3S \rightarrow n\,^1P(n = 2\text{–}5)$ transitions decreases rapidly with increasing energy most probably due to the exchange nature of this excitation process. Figure 5 shows that alignment creation in an $2\,^1S \rightarrow n\,^1D(n = 3, 4, 5)$ transition is about $10^3$–$10^4$ times larger than those for the $1\,^1S \rightarrow n\,^1D(n = 3\text{–}5)$ excitation processes. The alignment creation parameters for the $2\,^1S \rightarrow n\,^1D(n = 3\text{–}5)$ processes also decrease rapidly with increasing energy. Similar conclusions hold for excitations to the $n\,^3D(n = 3\text{–}5)$ levels, as can be seen from Fig. 6.

Figures 7 and 8 show our DWA results for the alignment creation parameter, integral cross section, for the normalized alignment creation parameter, and for the polarization fraction in the case of the $2\,^3S \rightarrow 2\,^3P$, $2\,^1S \rightarrow 2\,^3P$, and $1\,^1S \rightarrow 2\,^3P$

excitations.

Figure 9 shows $P$ for $2\,^1S \rightarrow n\,^1P(n = 3,4,5)$ and $1\,^1S \rightarrow n\,^1P(n = 2,3)$ excitations (upper panel) and for $2\,^3S \rightarrow n\,^1P(n = 2\text{–}5)$ excitations compared with those for $1\,^1S \rightarrow n\,^1P(n = 2,3)$ excitations (lower panel). It can be seen immediately that in general the absolute magnitude of $P$ for the $2\,^1S \rightarrow n\,^1P(n = 3,4,5)$ transitions is smaller than those for the $1\,^1S \rightarrow n\,^1P(n = 2,3)$ transitions. This is due to the fact that while the alignment creation parameter is larger for the $2\,^1S \rightarrow n\,^1P(n = 3,4,5)$ excitations than those for the $1\,^1S \rightarrow n\,^1P(n = 2,3)$ excitations, the cross sections, i.e., the denominator in the formula for $P$, is also larger giving a ratio which is slightly smaller. The same holds for the $2\,^3S \rightarrow n\,^1P(n = 2\text{–}5)$ excitation processes also except for very small incident electron energies: In their respective thresholds the $P$-values are approximately equal. This seems to indicate that in highly anisotropic and quasi-monoenergetic plasmas the metastable states (due to their usually low population density) will not play a significant role in influencing the polarization characteristics of the emitted radiation. On the other hand in plasmas that are only weakly anisotropic and with substantial anisotropy for low-energy electrons, the metastable states will be populated and they can be easily excited by low-energy electrons, therefore in such cases metastable states will play a significant role in determining the polarization characteristics of the emitted radiation. Only numerical results with given $f^{(0)}(v)$ and $f^{(2)}(v)$ distribution functions can give quantitative answers. This will be the subject of future work.

## Acknowledgments

Two of the authors (G. C. and D. C. C.) want to acknowledge the financial support of the U.S. DOE. The authors want to thank Professor Klaus Bartschat for valuable help in clarifying certain scientific issues and Dr. David Kilcrease for

reading and criticizing the manuscript.

## References


1. Kazantsev, S. A., *JETP Letters* **37**, 159 (1983).
2. Kazantsev, S. A. and Hénoux, J.-C., *Polarization Spectroscopy of Ionized Gases* (Dodrecht: Kluwer 1995).
3. Kazantsev, S. A. and Petrashen, A., *Optics and Spectroscopy* **77**, 807 (1994).
4. Kazantsev, S. A., Polynovskaa, N. Ya., Pyatnitskii, L. N., and Edelman, S. A., *Sov. Phys. Usp.* **31**, 785 (1988).
5. Csanak, G., Cartwright, D. C., and da Paixão, F. J., *Phys. Rev. A* **48**, 2811 (1993).
6. Cartwright, D. C. and Csanak, G., *Phys. Rev. A* **51**, 454 (1995).
7. Cartwright, D. C. and Csanak, G., *Phys. Rev. A* **55**, 1962 (1997).
8. Bray, I., *Phys. Rev. A* **49**, 1066 (1994).
9. Fursa, D. V. and Bray, I., *Phys. Rev. A* **52**, 1279 (1995).
10. Moiseiwitsch, B. L. and Smith, S. J., *Revs. of Modern Physics* **40**, 238 (1968).
11. Oppenheimer, J. R., *Z. Phys.* **43**, 27 (1927).
12. Penney, W. G., *Proc. Natl. Acad. Sci.* **18**, 231 (1932).
13. Percival, I. C. and Seaton, M. J., *Phil. Trans. Roy. Soc. A* **251**, 113 (1958).
14. Blum, K., *Density Matrix Theory and Applications* (New York: Plenum 1981).
15. Bartschat, K. and Csanak, G., *Comments At. Mol. Phys.* **32**, 233 (1996).
16. Since this quantity can take negative values the present authors feel that to call it a 'cross section' is somewhat misleading though indicative that it has area dimension. Essentially the same parameter was called *alignment parameter* by Blum (Ref. 14, p. 115).
17. For the concept of statistical operator (or density operator) see e.g., Ref 14, Chps. 1 and 2.

18. For a general background for Eq. (2) see e.g., A. Corney, *Atomic and Laser Spectroscopy* (Oxford:Clarendon, 1977), pp. 492–502.
19. For the definition of irreducible tensor operators and expansion of operators in terms of them see e.g., Ref. 14, Chapter 4
20. This definition is essentially identical to the definition of the *alignment parameter* by Blum (Ref. 14, Eq. (4.6.11)).
21. Bartschat, K., Blum, K., Hanne, G. F., and Kessler, J., *J. Phys. B: At. Mol. Phys.* **14**, 3761 (1981).
22. Bartschat, K. and Blum, K., *Z. Phys. A* **304**, 85 (1982).
23. We use here the treatment and notation of Ref. 2, Sect. 1.2.3.
24. Rebane, V. N. and Rebane, T. K., *Optics and Spectroscopy* **20**, 101 (1966).
25. Rebane, V. N., *Optics and Spectroscopy* **21**, 229 (1966).
26. Rebane, V. N., *Optics and Spectroscopy* **24**, 163 (1968).
27. Mansky, E. J. and Flannery, M. R., *J. Phys. B: At. Mol. Opt. Phys.* **25**. 1591 (1992).

## Figure Captions

**Figure 1**

Schematic representation for one-step and two-step process of alignment-creation and emission of polarized radiation and the various regions of electron distribution that are "probed."

**Figure 2**

One-step and two-step excitation processes in helium. The lower panel shows that excitation cross sections out of metastable states are much larger than those from the ground state. On the lower right panel **n** refers to the ground state He atom density.

**Figure 3**

Comparison of theoretical results for the normalized alignment parameter obtained from converged close coupling (CCC) calculations, from distorted wave approximation (DWA) calculations, and from multi-channel eikonal (MCE) theory (Mansky and Flannery [27]) in the case of $2\,^3S \rightarrow 2\,^3P$ excitation (left panel), $2\,^3S \rightarrow 3\,^3P$ excitation (middle panel), and $2\,^3S \rightarrow 3\,^3D$ excitation (right panel).

**Figure 4**

Alignment creation parameters obtained from DWA calculations for electron impact excitations to final $n\,^1P(n = 2\text{–}5)$ levels from (a) the $2\,^1S$ level, left panel, (b) the $2\,^3S$ level, middle panel, and (c) the $1\,^1S$ level, right panel.

**Figure 5**

Same as Fig. 3 except for $n\,^1D(n = 3\text{–}5)$ final levels.

**Figure 6**

Same as Fig. 3 except for $n\,^3D(n = 3\text{–}5)$ final levels.

**Figure 7**

Alignment creation parameters and integral cross sections (lower panels), normalized alignment parameters and polarization fractions from DWA calculation for the (a) $2\,^3S \rightarrow 2\,^3P$ excitation (left panels), (b) $2\,^1S \rightarrow 2\,^3P$ excitation (middle panel), (c) $1\,^1S \rightarrow 2\,^3P$ excitation (right panels).

**Figure 8**

Same as Fig. 7 except for (a) $2\,^3S \rightarrow 3\,^3D$ excitation (left panels), (b) $2\,^1S \rightarrow 3\,^3D$ excitation (middle panels), (c) $1\,^1S \rightarrow 3\,^3D$ excitation (right panels).

**Figure 9**

Polarization fractions for (a) $2\,^1S \rightarrow n\,^1P$ excitations: upper panel and for (b) $2\,^3S \rightarrow n\,^1P$ excitations: lower panel. In both cases results are also shown for $1\,^1S \rightarrow n\,^1P(n = 2, 3)$ excitations also.

# Metastable States May Provide Additional Information about $N_e(E)$

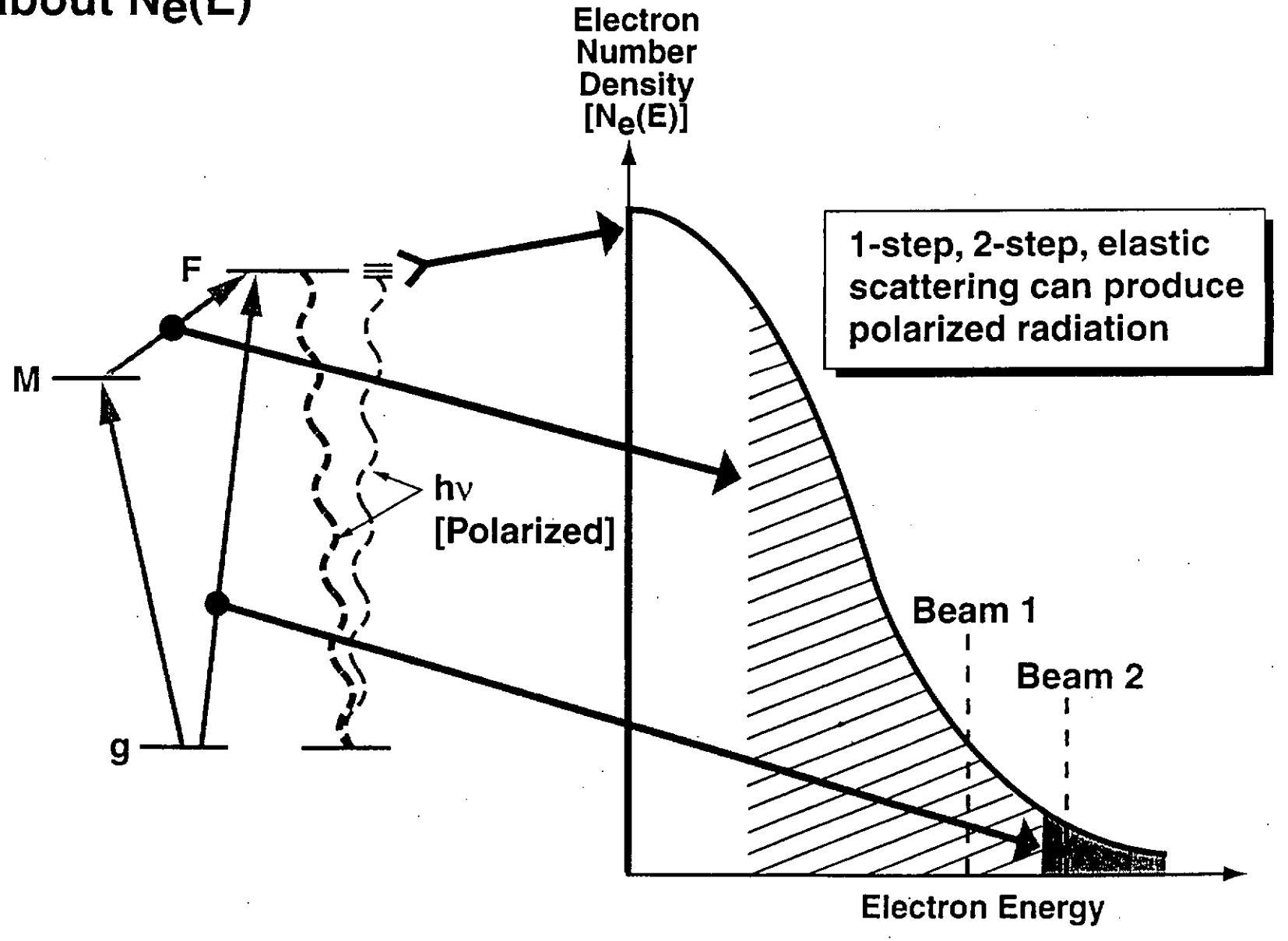

# Atomic Structure Can Lead to High Excited State Densities

## [Most atoms except "one-electron" systems are candidates]

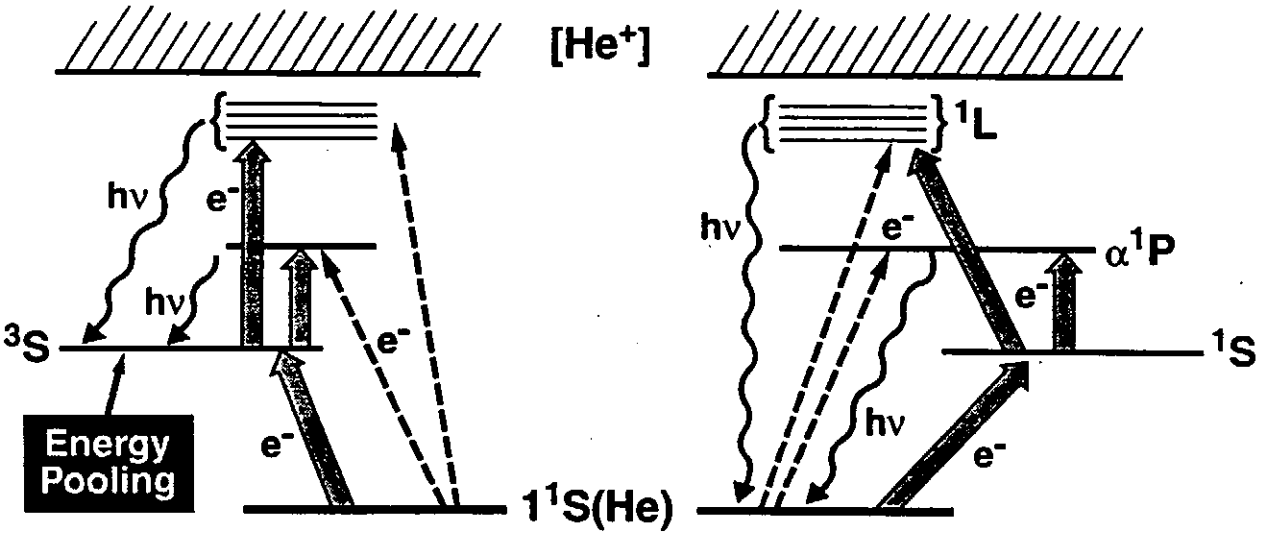


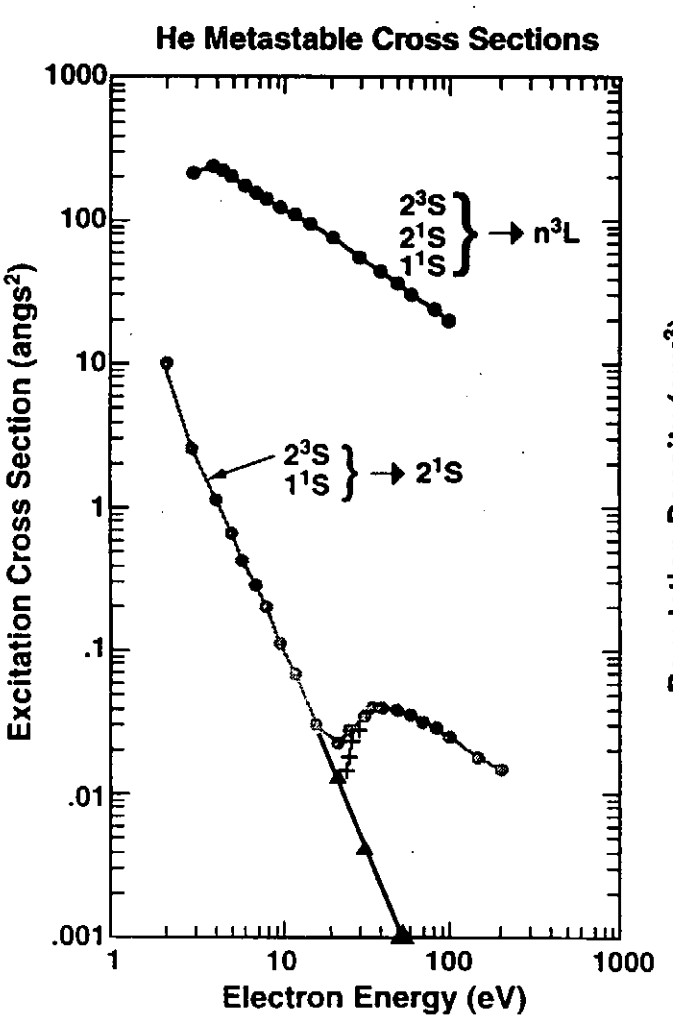


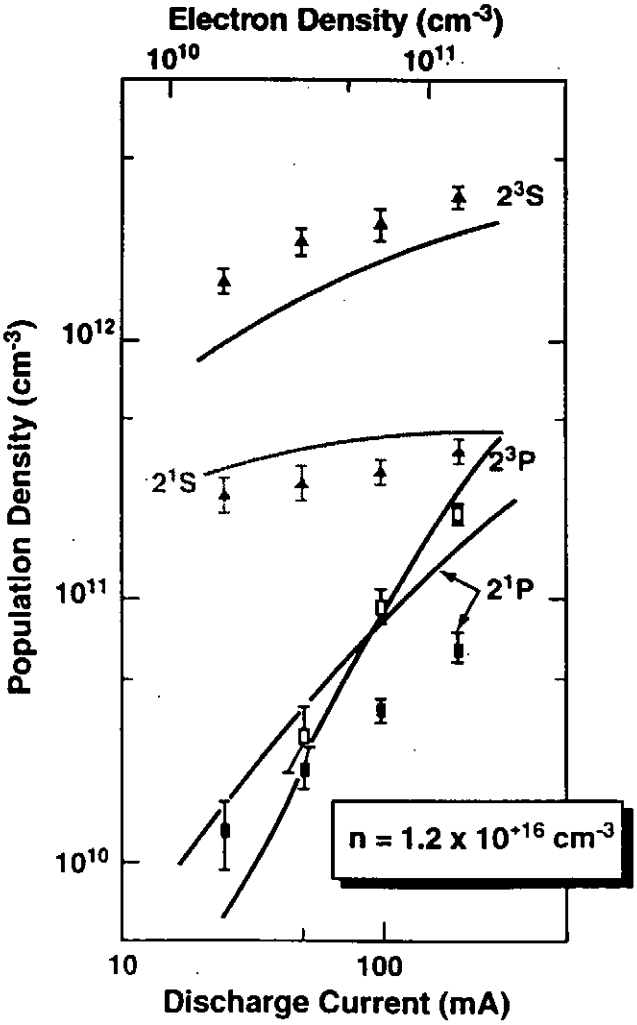


T. Fujimoto, JQSRT 21, 439 (1979)

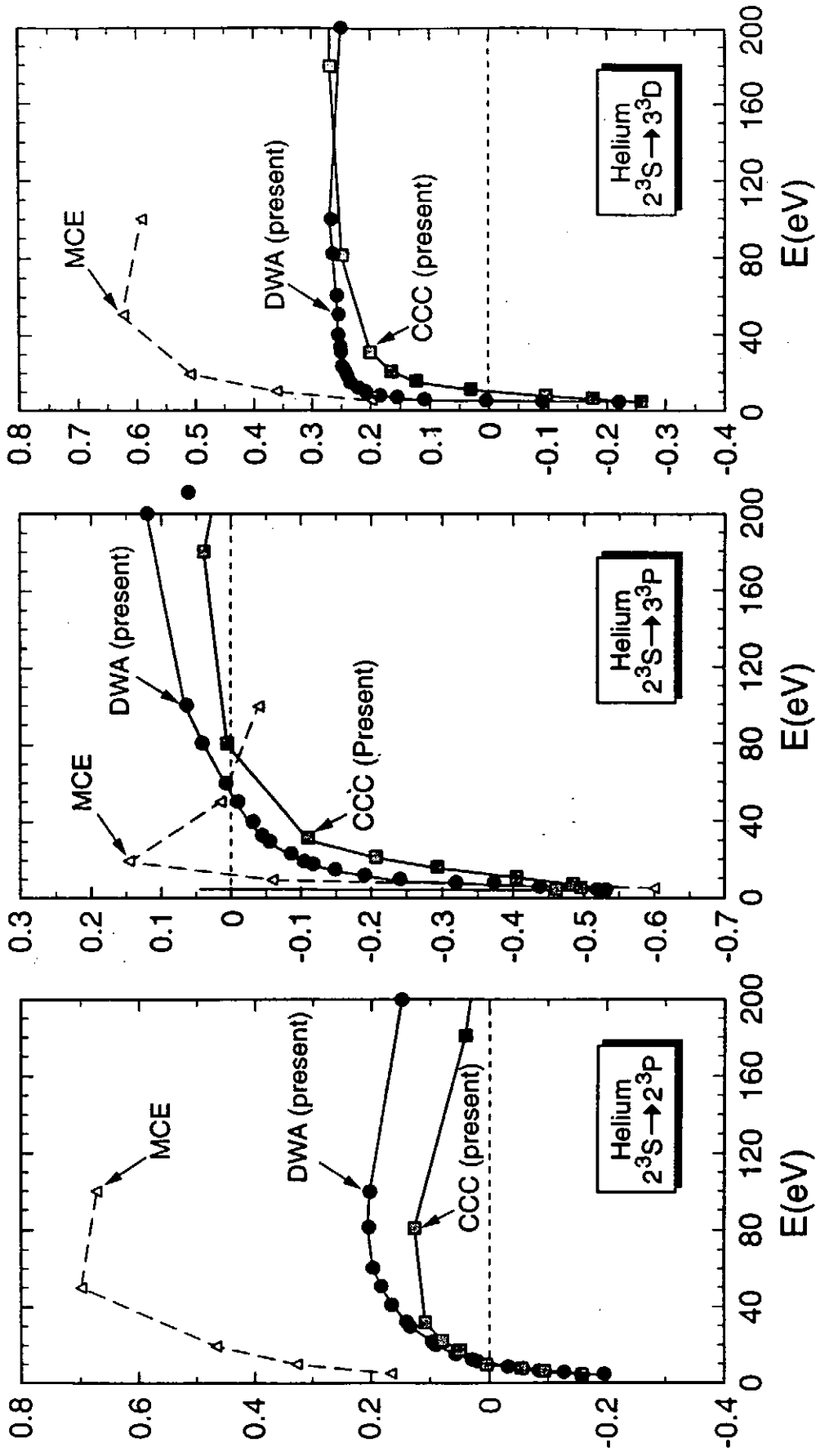
Normalized Alignment Parameter
E(eV)
Helium
$2^3S \rightarrow 2^3P$
MCE
DWA (present)
CCC (present)
Helium
$2^3S \rightarrow 3^3P$
CCC (Present)
Helium
$2^3S \rightarrow 3^3D$

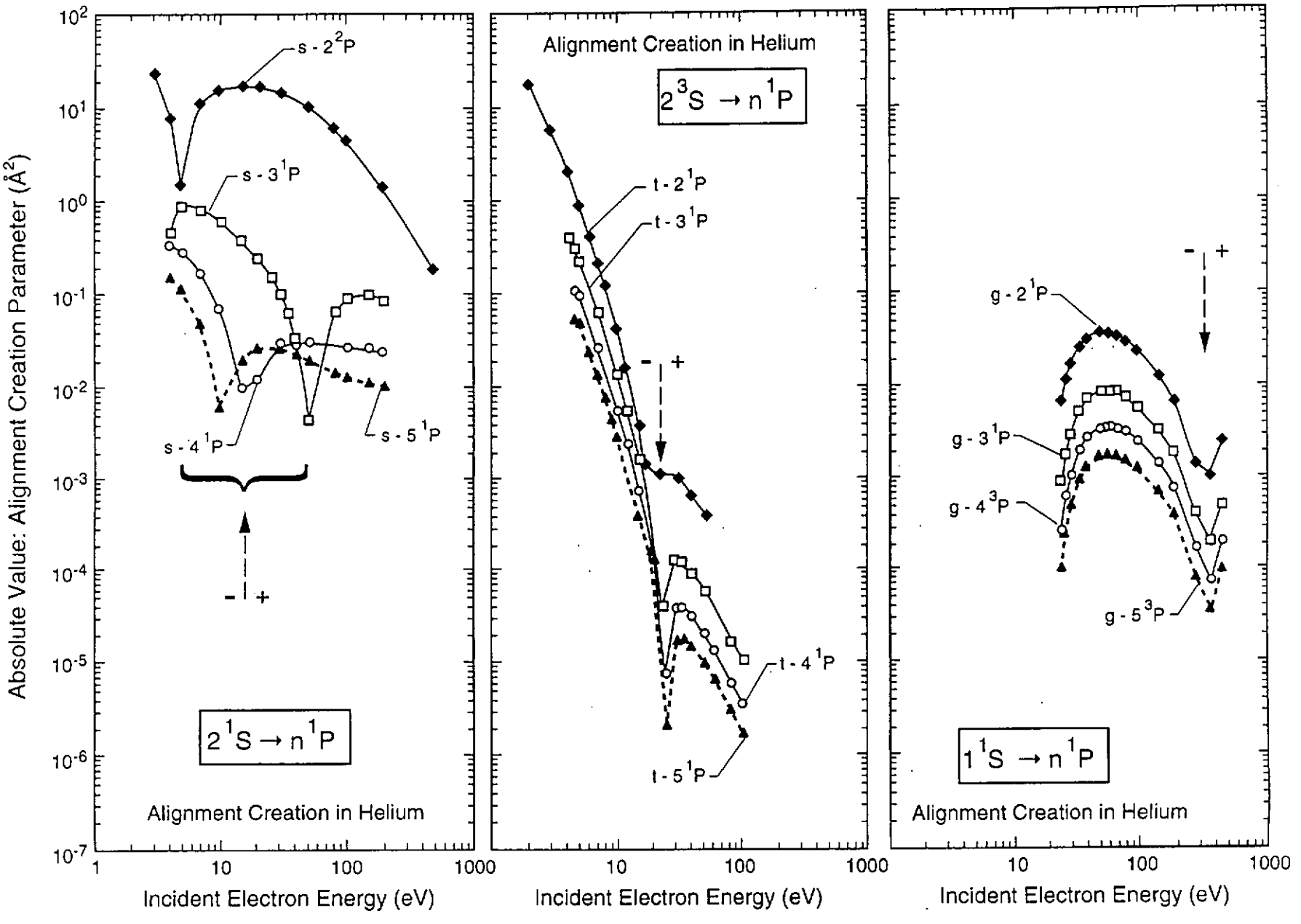
Absolute Value: Alignment Creation Parameter (Å²)
Incident Electron Energy (eV)
s - 2¹P
s - 3¹P
s - 4¹P
s - 5¹P
2¹S → n¹P
Alignment Creation in Helium
Alignment Creation in Helium
2³S → n¹P
t - 2¹P
t - 3¹P
t - 4¹P
t - 5¹P
Alignment Creation in Helium
g - 2¹P
g - 3¹P
g - 4³P
g - 5³P
1¹S → n¹P

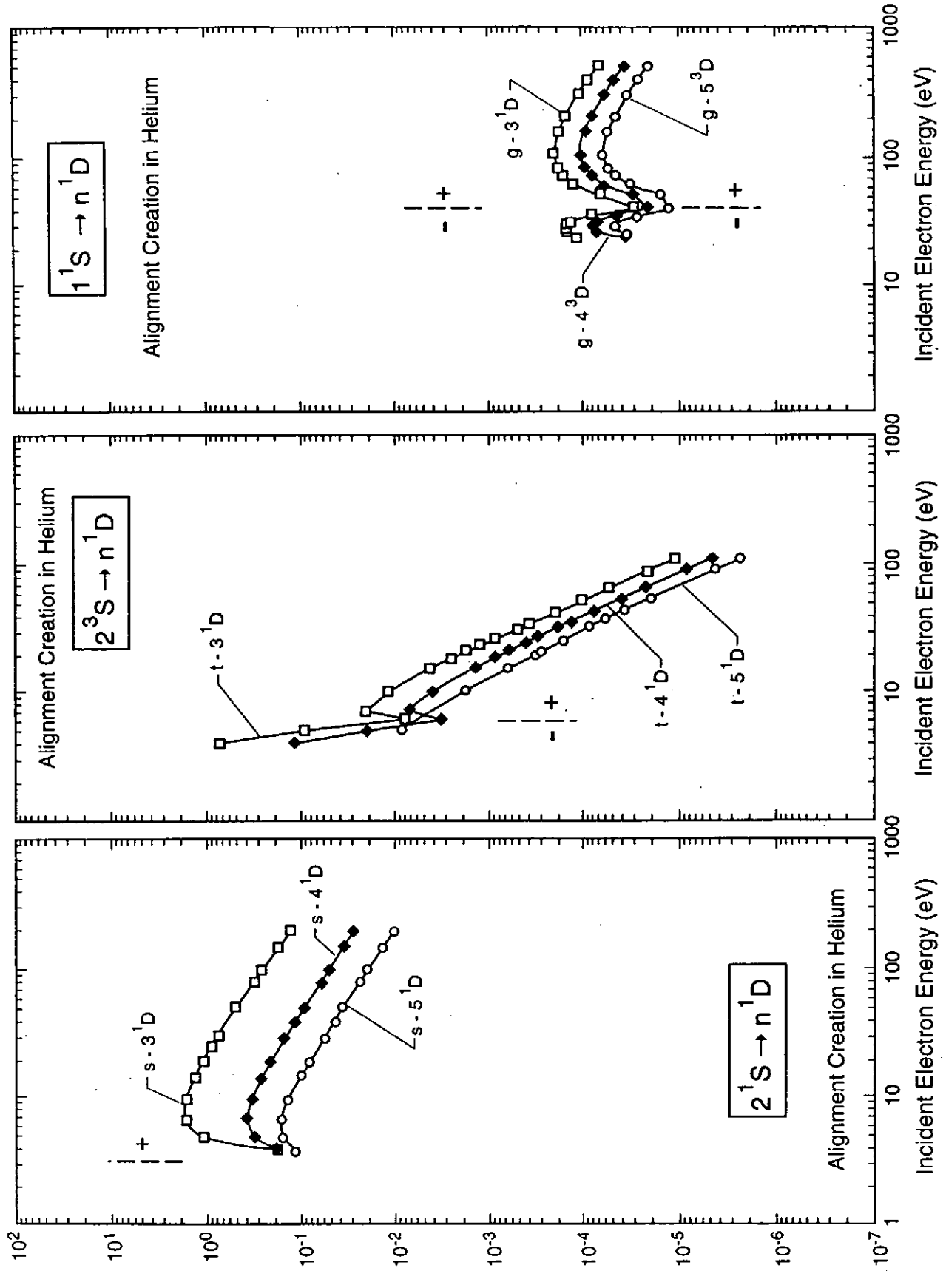
Absolute Value: Alignment Creation Parameter (Å²)
Alignment Creation in Helium
2 ¹S → n ¹D
s - 3 ¹D
s - 4 ¹D
s - 5 ¹D
Incident Electron Energy (eV)
Alignment Creation in Helium
2 ³S → n ¹D
t - 3 ¹D
t - 4 ¹D
t - 5 ¹D
Incident Electron Energy (eV)
Alignment Creation in Helium
1 ¹S → n ¹D
g - 3 ¹D
g - 4 ³D
g - 5 ³D
Incident Electron Energy (eV)

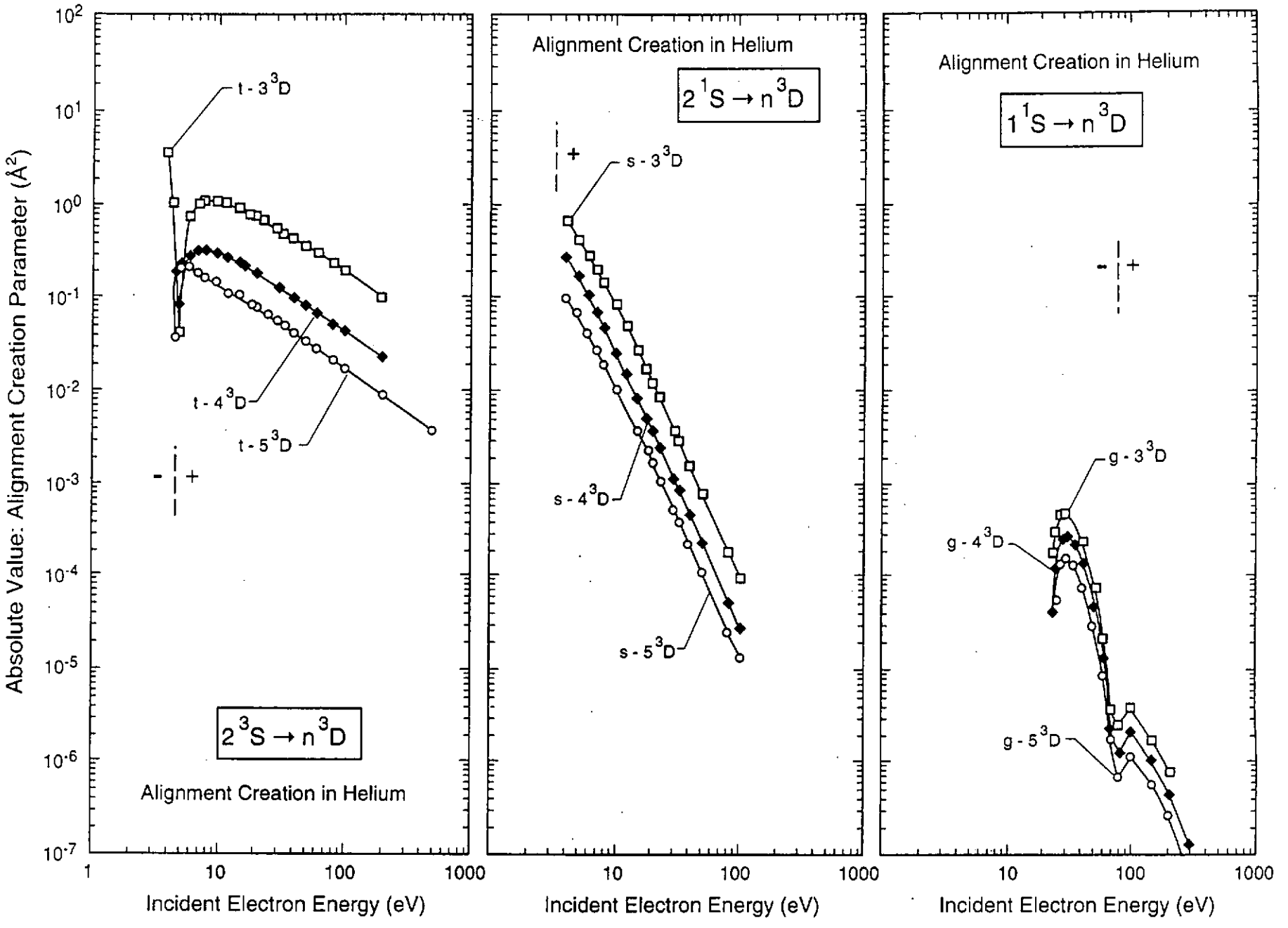
Absolute Value: Alignment Creation Parameter (Å²)
Incident Electron Energy (eV)
Incident Electron Energy (eV)
Incident Electron Energy (eV)
t - 3³D
t - 4³D
t - 5³D
2³S → n³D
Alignment Creation in Helium
Alignment Creation in Helium
2¹S → n³D
s - 3³D
s - 4³D
s - 5³D
Alignment Creation in Helium
1¹S → n³D
g - 3³D
g - 4³D
g - 5³D

# Alignment and Polarization in Helium

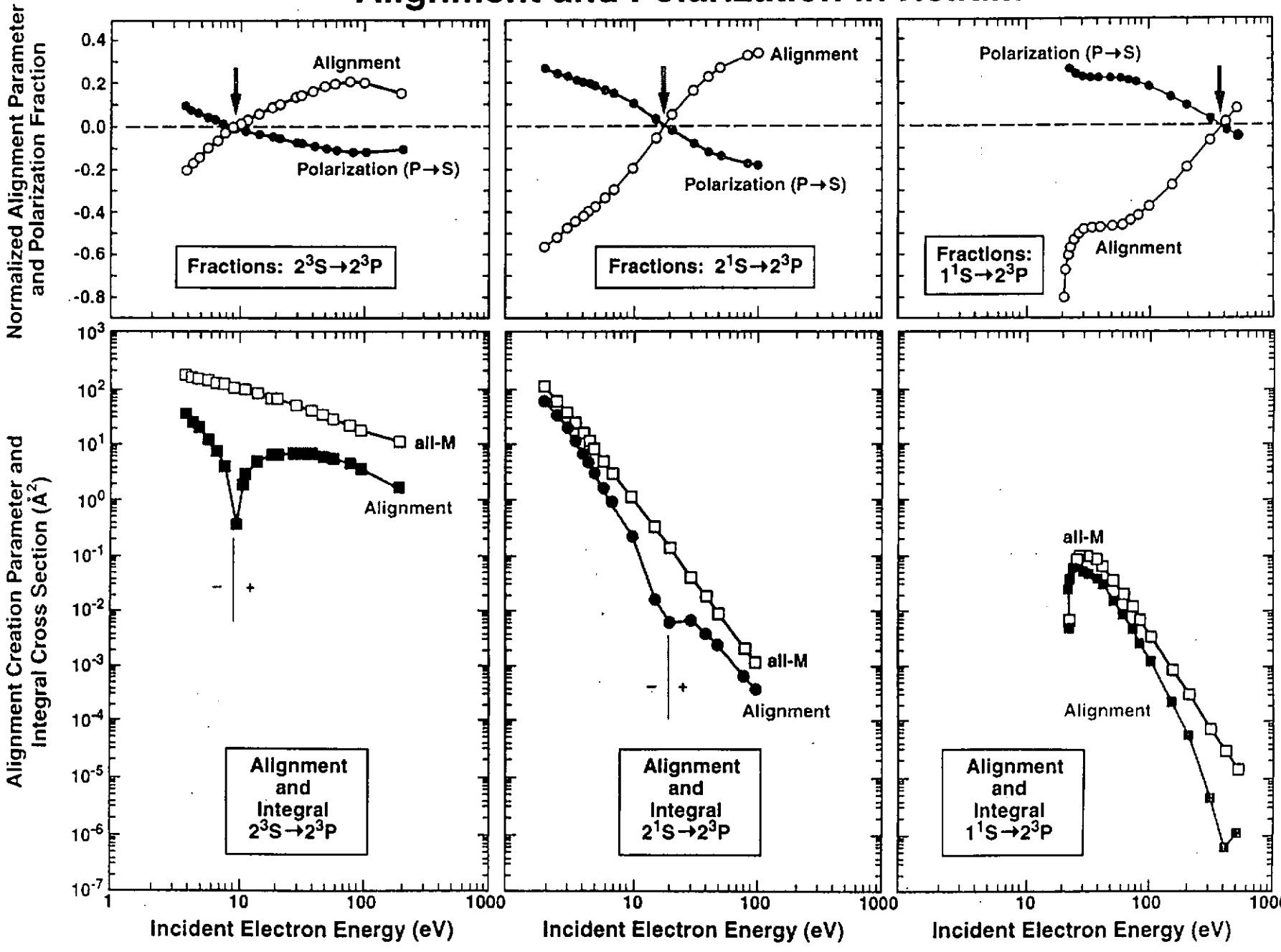

# Alignment and Polarization in Helium

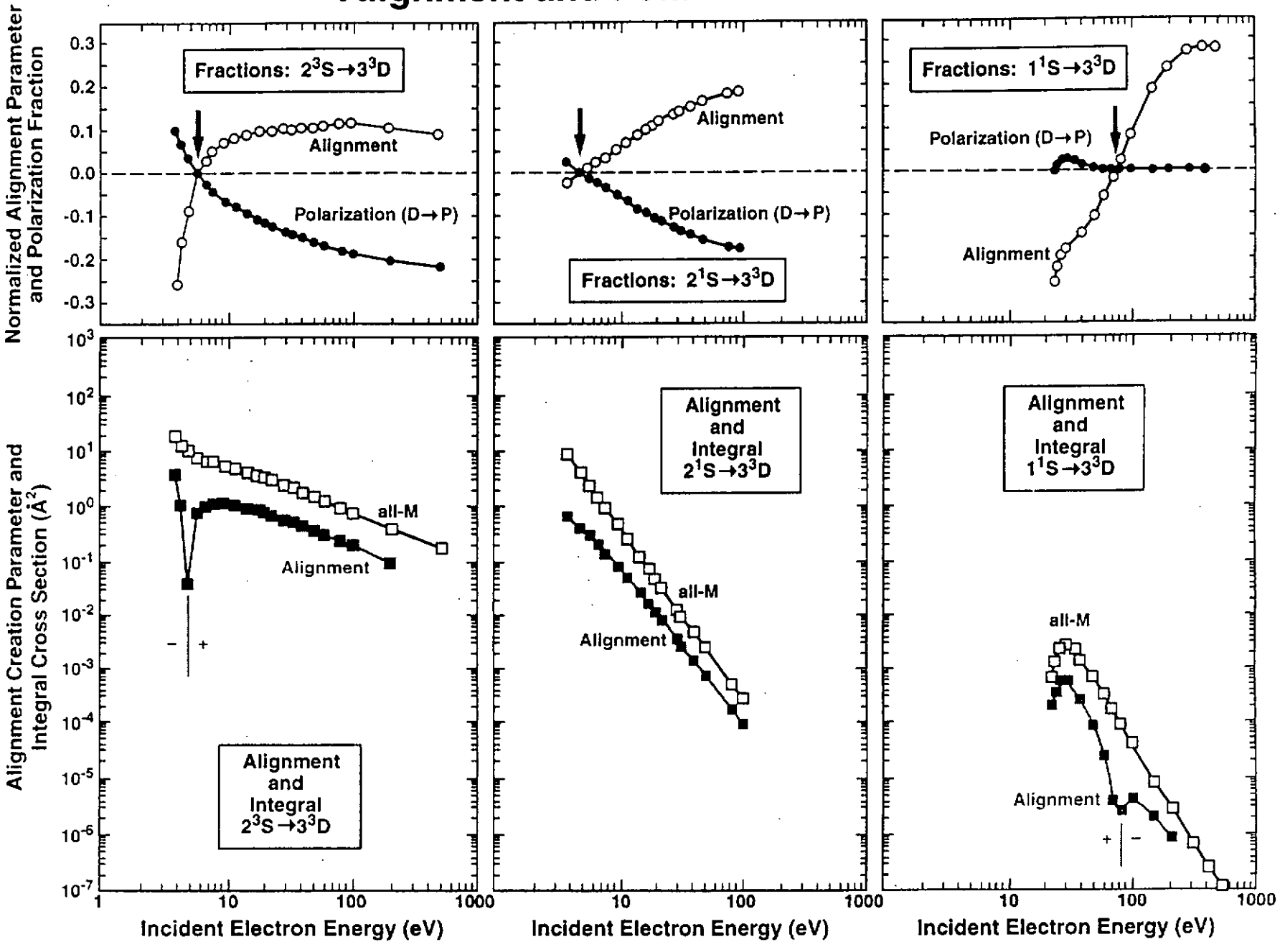

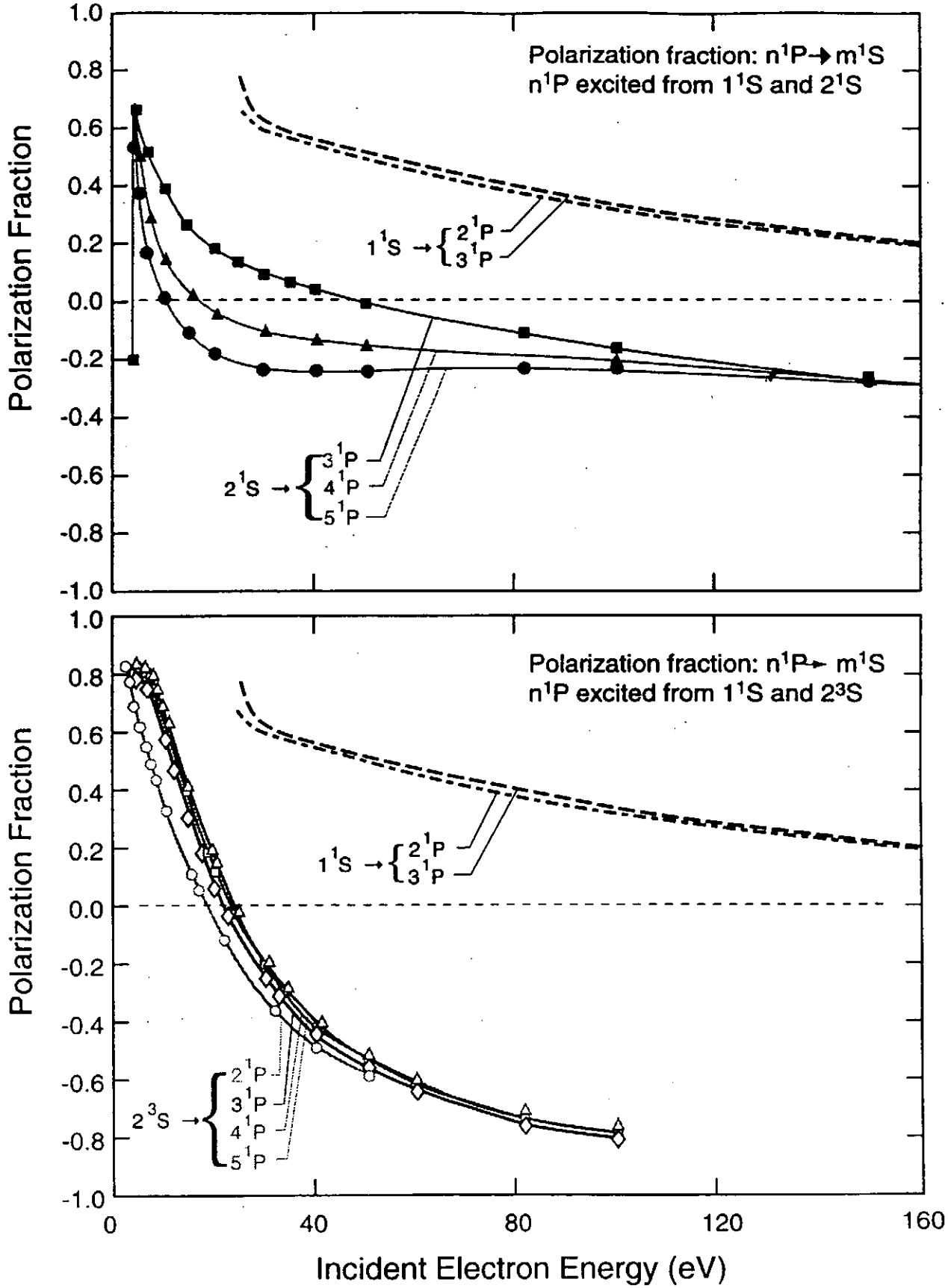
Polarization fraction: n¹P→m¹S
n¹P excited from 1¹S and 2¹S
1¹S → 2¹P, 3¹P
2¹S → 3¹P, 4¹P, 5¹P
Polarization Fraction
1.0
0.8
0.6
0.4
0.2
0.0
-0.2
-0.4
-0.6
-0.8
-1.0
Polarization fraction: n¹P→m¹S
n¹P excited from 1¹S and 2³S
1¹S → 2¹P, 3¹P
2³S → 2¹P, 3¹P, 4¹P, 5¹P
0
40
80
120
160
Incident Electron Energy (eV)

# Theoretical Predictions for the Polarization of the J=0-1 Neonlike Germanium X-Ray Laser Line in the Presence of a Directed Beam of Hot Electrons

M. K. Inal
Institut de Physique, Université A. Belkaid, BP 119
13000 Tlemcen, Algeria

J. Dubau and M. Cornille
UPR-176 CNRS, DARC, Observatoire de Paris
92190 Meudon Cedex, France

**Abstract**

The polarization of the neonlike germanium $J = 0 - 1$ laser line, which would arise from the existence of a directed beam of hot electrons in the amplifying plasma, is theoretically investigated. The relative populations of the magnetic sublevels in the lower $J$=1 laser level have been determined by allowing for the processes of direct excitation from the $2p^6$ ground level and collisional de-excitation from the upper $J$=0 laser level. Elastic collisions leading to transitions between the $M_J = 0$ and $M_J = 1$ sublevels within the lower level of the lasing line have also been taken into account. The required elastic and inelastic collision strengths for transitions between magnetic sublevels have been computed in a semi-relativistic distorted-wave approximation, for incident electron energies up to 15 keV. Our calculations predict a rather low degree of polarization for the $J$=0 – 1 line, although the elastic collisions are found to play a negligibly small role in the redistribution of magnetic sublevel populations.

## 1. Introduction

Amplification properties of soft-x-ray $(1s^22s^22p^5)3p \rightarrow (...)3s$ lasing lines in high density plasmas containing Ne-like ions collisionally excited by electrons have been studied intensively both theoretically [1] and experimentally [2]. While predicted to have the highest gain, the $(...)3p\ ^1S_0 \rightarrow (...)3s\ ^3P_1$ (so called $J = 0 - 1$ line) was not significantly amplified in the first x-ray laser experiments [3] because of refraction resulting from the large electron density gradients. This line is pumped almost totally by the strong monopole collisional excitation from the $1s^22s^22p^6$ ground level. Its gain has been demonstrated to be the largest for most Ne-like ions at early times, and quickly becomes weaker than those of the two main $J = 2 - 1$ lines [4]. Important improvements in the performance of the $J = 0 - 1$ laser beam have been achieved by the use of prepulse [5] and multiple pulse [6] techniques which allow to create a larger and more uniform density plasma.

In a recent x-ray laser experiment involving germanium plasma created by two 0.1 ns pulses [7], the $J = 0 - 1$ line at 19.6 nm was found to be appreciably polarized along the target surface, with a degree of polarization of -0.53. Kawachi et al. [7] attributed the observed

polarization to the difference in the gains between the "$\pi$" (parallel) and "$\sigma$" (perpendicular) components, arising from a nonuniform distribution of population densities among the magnetic sublevels $M_J = 0$ and $|M_J| = 1$ of the lower $J$=1 level. A ratio of about 3.5 between the populations of the $M_J = 0$ and $|M_J| = 1$ sublevels was required to explain the measured polarization degree. This selective $M_J$ sublevel population was interpreted by the authors as due to the effect of anisotropy in the radiation trapping of photons of the 0.98 nm 3s $^3P_1 \rightarrow$ $2p^6\ ^1S_0$ resonance line, in an expanding plasma which has a velocity gradient in the direction perpendicular to the target surface. In a very recent work [8], it has been shown that the effects of radiation trapping are quite negligible, and cannot explain the experimental result reported in ref. [7]. For the two main $J = 2 - 1$ lasing lines, which appear at 23.2 and 23.6 nm in $Ge^{22+}$, no polarization was observed [9].

The purpose of the present work is to investigate theoretically the polarization of the $J = 0 - 1$ $Ge^{22+}$ lasing line that would result from the presence of a directed beam of hot electrons in the amplifying plasma. As it is well known, electron-ion collisional processes involving incident electrons with an anisotropic velocity distribution leads in general to preferential population of particular magnetic sublevels within an ionic level $J > 1/2$ [10]. Hot electrons with a highly anisotropic angular distribution could be generated in plasmas produced by irradiation of solid targets with high-intensity short- and ultrashort-duration (ps down to tens of fs) laser pulses [11]. Polarization of x-ray emission from this kind of plasmas was observed [12], and the measured polarization of the 1s2p $^1P_1$-$1s^2$ $^1S_0$ resonance line of He-like aluminum ions provided a very useful tool for probing the strong anisotropy of the electron angular distribution due to nonlocal heat transport.

## 2. Inelastic and elastic collision rates

The $J = 0$ upper level (denoted $u$ level) of the lasing line is populated almost entirely by direct collisional excitation from the $2p^6\ ^1S_0$ ground level ($g$ level) and depopulated primarily through the spontaneous radiative decay and collisional de-excitation to the $J = 1$ lasing line lower level ($l$ level) as well as the collisional excitation to the more highly excited level (...) 3d $^1P_1$. For the $l$ level, three populating processes have been taken into consideration in the present study, namely the collisional excitation from the $g$ level and the spontaneous radiative decay and collisional deexcitation from the $u$ level. The depopulation of the $l$ level has been assumed to occur by means of a strong spontaneous radiative transition to $g$ and a collisional excitation to $u$. Also taken into account are the transitions between magnetic sublevels of $l$ level caused by elastic electron-ion collisions. We will be concerned here with the plasma period when the $J = 0$ - 1 lasing line is unsaturated, so that stimulated emission can be ignored in the population equations. We have chosen a bi-Maxwellian electron distribution for the free electrons, i.e.

$$F(E,\theta) = (1-f)\frac{2}{\sqrt{\pi}(kT_1)^{3/2}}E^{1/2}e^{(-\frac{E}{kT_1})}\phi_1(\theta) + f\frac{2}{\sqrt{\pi}(kT_2)^{3/2}}E^{1/2}e^{(-\frac{E}{kT_2})}\phi_2(\theta) \qquad (1)$$

where $f$ and $T_2$ are, respectively, the hot electron fraction and the hot temperature. The temperature $T_1$ is a few hundred eV whereas $T_2$ lies in the multi-keV range. $\phi_1(\theta)$ is an isotropic

angular distribution and $\phi_2(\theta)$ is a beam-like angular distribution along the quantization axis $z$, corresponding to the direction of the "pump" laser (normal to the target surface). The excitation rate coefficient $C$ for each collisional transition can be determined from the combination $(1-f)\,C^{(1)}(T_1)+f\,C^{(2)}(T_2)$ of two Maxwellian-averaged rate coefficients. The elastic and inelastic collision strengths needed in evaluating the $C^{(i)}$ coefficients have been computed over a wide energy range in the distorted-wave approximation using the basic codes DISWA [13] and JAJOM [14]. For the dipole excitations $g \rightarrow l, M_J$ and $u \rightarrow l, M_J$ and de-excitations $l, M_J \rightarrow u$ at relatively large impact-electron energies, the Coulomb-Bethe method was also employed to calculate the important contribution from higher partial waves. In Tables I*a* and I*b* are given the calculated rate coefficients for collisional transitions caused by the two groups of electrons, over the temperature ranges 200-500 eV and 2-8 keV, respectively. The rate coefficients for the transitions between $M_J = 0$ and 1 magnetic sublevels induced by elastic collisions with the isotropic cold electrons are also presented in Table I*a*. Note that the rate coefficient for $l \rightarrow u$ has not been included in Table I*a* since it can be obtained from $C_d\,(u \rightarrow l)$ by using the principle of detailed balance. It can first be seen that the elastic collision rate coefficients are very small comparatively to $C_d\,(u \rightarrow l)$ and $C_e\,(l \rightarrow u)$. Therefore the effect of elastic collisions in the redistribution of populations among the magnetic sublevels of the lower laser level can be neglected. It can also be seen from Table I*b* that for the directive electrons the excitation process from $g$ level populates preferentially the $l, M_J = 0$ sublevel while the collisional de-excitation from $u$ level favours the $|MJ| = 1$ sublevels. Our calculations predict that at, for example, an (electron-beam) impact energy of 250 Ry relative to the ground level, the cross-section ratios $\sigma_0/\sigma_1$ between the $M_J = 0$ and 1 sublevels are about 4.5 and 0.53, respectively, for excitation from $g$ and deexcitation from $u$. It is worth mentioning that for the third process involved in the population of $l$ level, i.e. the spontaneous radiative decay from $u$ level, there is no selection with respect to the $l$ magnetic sublevels.

### 3. Magnetic sublevel populations

The populations of the upper level and lower magnetic sublevels involved in the $Ge^{22+}$ $J = 0 - 1$ lasing line were determined using the collisional rate coefficients listed in Tables I*a* and I*b* and the radiative transition probabilities computed with the SUPERSTRUCTURE code [15] and reported in Ref.[16]. The total electron density was fixed at $5\text{x}10^{20}$ cm$^{-3}$ and the fraction of hot electrons was taken to be $f$ =0.05 and $f$ =0.1. Results of our calculations are presented in Table II for five selected values of the two electron temperatures $T_1$ and $T_2$. It appears that the largest ratio of the $M_J$ =0 to $M_J$ =1 populations occurs at low temperatures $T_1$ =200 - 300 eV. The $M_J$ =0 sublevel is only slightly overpopulated with respect to $M_J$ =1 when $T_1$ is greater than about 400 eV. Our calculations indicate that at, for example, $T_1$ =400 eV, $T_2$ =5 keV and $f$ =0.05 about 75% of the population of the whole $l$ level comes from collisional de-excitation from $u$ level and 17% from excitation from $g$ level. It should be mentioned that, in contrast to the excitation process from the $2p^6$ level, the hot electrons are much less efficient in the collisional de-excitation of the $u$ level because of the large difference between threshold energies for $n$ =2 - 3 and $n$ =3 - 3 transitions. This results in a weak preferential population

of $l, M_J = 1$ sublevel by the collisional de-excitation process from $u$. For $f > 0.05$, the $g \rightarrow l$ excitation is due dominantly to hot electrons.

## Conclusion

An analysis of the population processes of the sublevels of the lasing line $J = 0 - 1$ was presented. It was assumed the plasma to be in a steady state, the electron temperature and density corresponding to realistic values. The results show a very small possibility to have a strong polarization of the lasing line due to anisotropic electron excitation, except if the free electron are strongly anisotropic. One must not forget that a laser-produced plasma is far to be in a steady state situation, in particular when the X-ray lasing process starts. The atomic data presented here have therefore to be used in a time dependent collisional-radiative model. When the plasma parameters temporal gradients are large, the very different life times of the lower and upper level of the lasing line will become important.

## Acknowledgements

One of us (MKI) gratefully acknowledges financial support of CNRS, France, during his three month stay in Meudon Observatory. He also would like to thank the Organizing Committee of ICPP 1996, Nagoya, Japan, for financial support allowing him to participate in the Conference during which the present work was initiated.

## References

[1] P.B. Holden, S.B. Healy, M.T.M. Lightbody, G.J. Pert, J.A. Plowes, A.E. Kingston, E. Robertson, C.L.S. Lewis, and D. Neely, *J. Phys. B* **27**, 341 (1994).

[2] M. Murai, H. Shiraga, G. Yuan, H. Daido, H. Azuma, E. Miura, R. Kodama, M. Takagi, T. Kanabe, H. Takabe, Y. Kato, D. Neely, D.M. O'Neil, C.L.S. Lewis, and A. Djaoui, *J. Opt. Soc. Am. B* **11**, 2287 (1994).

[3] T.N. Lee, E.A. McLean, and R.C. Elton, *Phys. Rev. Lett.* **59**, 1185 (1987).

[4] D.M. O'Neil, C.L.S. Lewis, D. Neely, J. Uhomoibhi, M.H. Key, A.G. MacPhee, G.J. Tallents, S.A. Ramsden, A. Rogoyski, E.A. McLean, and G.J. Pert, *Opt. Commun.* **75**, 406 (1990).

[5] J. Nilsen and J.C. Moreno, *Opt. Lett.* **19**, 1137 (1994).

[6] H. Daido, R. Kodama, K. Murai, G. Yuan, M. Takagi, Y. Kato, I.W. Choi, and C.H. Nam, *Opt. Lett.* **20**, 61 (1995).

[7] T. Kawachi, K. Murai, G. Yuan, S. Ninomiya, R. Kodama, H. Daido, Y. Kato, and T. Fujimoto, *Phys. Rev. Lett.* **75**, 3826 (1995).

[8] D. Benredjem, A. Sureau, B. Rus, and C. M"ller, *Phys. Rev.* **A 56**, 5152, (1997).

[9] B. Rus, C.L.S. Lewis, G.F. Cairns, P. Dhez, P. Jaegle, M.H. Key, D. Neely, A.G. MacPhee, S.A. Ramsden, C.G. Smith, and A. Sureau, *Phys. Rev. A 51*, 2316 (1995).

[10] M.K. Inal and J. Dubau, *J. Phys. B* **20**, 4221 (1987).

[11] J.C. Kieffer, J.P. Matte, H. Pepin, M. Chaker, Y. Beaudoin, T.W. Johnston, C.Y. Chien, S. Coe, G. Mourou, and J. Dubau, *Phys. Rev. Lett.* **68,** 480 (1992).

[12] J.C. Kieffer, J.P. Matte, M. Chaker, Y. Beaudoin, C.Y. Chien, S. Coe, G. Mourou, J. Dubau, and M.K. Inal, *Phys. Rev.* **E 48**, 4648 (1993).

[13] W. Eissner and M.J. Seaton, *J. Phys. B* **5**, 2187 (1972).

[14] H.E. Saraph, *Comput. Phys. Commun.* **15**, 247 (1978).

[15] W. Eissner, M. Jones, and H. Nussbaumer, *Comput. Phys. Commun.* **8**, 270 (1974).

[16] M. Cornille, J. Dubau, and S. Jacquemot, *At. Data Nucl. Data Tables* **58**, 1 (1994).

**Table Ia.** Excitation and de-excitation rate coefficients (in units of $10^{-11}$ cm$^3$/s) for level-to-level collisional transitions ($g \rightarrow u$, $g \rightarrow l$, $u \rightarrow l$ and $u \rightarrow 3d^1P_1$) and for elastic rate coefficients for the transitions between $M_J$ =0 and $M_J$ =1 sublevels within the $l$ level, due to the isotropic and cold electron component of temperature $T_1$.

The subscripts $e$, $d$ and $el$ refer to excitation, de-excitation and elastic collisions, respectively.

| | $T_1$ (keV) | | | |
|---|---|---|---|---|
| | 0.2 | 0.3 | 0.4 | 0.5 |
| $C_e(g \rightarrow u)$ | 1.60(-2) | 1.24(-1) | 3.31(-1) | 5.84(-1) |
| $C_e(g \rightarrow l)$ | 3.36(-4) | 2.43(-3) | 6.38(-3) | 1.13(-2) |
| $C_d(u \rightarrow l)$ | 5.82(1) | 4.93(1) | 4.41(1) | 4.06(1) |
| $C_e(u \rightarrow 3d^1P_1)$ | 2.07(2) | 1.92(2) | 1.79(2) | 1.69(2) |
| $C_{el}^{(1)}(l0 \leftrightarrow l1)$ | 9.99(-1) | 7.73(-1) | 6.07(-1) | 5.14(-1) |

**Table Ib.** Rate coefficients (in units of $10^{-11}$ cm$^3$/s) for all considered collisional transitions, due to the directive and hot electron component of temperature $T_2$. The subscripts $e$ and $d$ refer to excitation and de-excitation, respectively. The results for elastic collisions are not shown because they are negligibly small.

| | $T_2$ (keV) | | | |
|---|---|---|---|---|
| | 2.0 | 3.0 | 5.0 | 8.0 |
| $C_e(g \rightarrow u)$ | 2.36 | 2.46 | 2.33 | 2.06 |
| $C_e^{(2)}(g \rightarrow l0)$ | 1.24(-1) | 1.49(-1) | 1.66(-1) | 1.67(-1) |
| $C_e^{(2)}(g \rightarrow l1)$ | 3.39(-2) | 4.48(-2) | 5.83(-2) | 7.13(-2) |
| $C_d^{(2)}(u \rightarrow l0)$ | 1.87(1) | 1.46(1) | 1.03(1) | 7.13 |
| $C_d^{(2)}(u \rightarrow l1)$ | 2.86(1) | 2.56(1) | 2.15(1) | 1.69(1) |
| $C_e^{(2)}(l0 \rightarrow u)$ | 1.93(1) | 1.51(1) | 1.07(1) | 7.40 |
| $C_e^{(2)}(l1 \rightarrow u)$ | 2.72(1) | 2.46(1) | 2.12(1) | 1.72(1) |
| $C_e(u \rightarrow 3d^1P_1)$ | 1.11(2) | 9.72(1) | 7.96(1) | 6.44(1) |

**Table II.** Populations of the upper level $u$ and of the lower magnetic sublevels $l$, $M_J = 0, 1$ of the $Ge^{22+}$ $J$ =0 - 1 lasing line, relative to the ground level $g$ population, for various values of the electron temperatures ($T_1$, $T_2$). These results were obtained for an electron density $5.10^{20}$ $cm^{-3}$ and for hot electron fractions $f = 0.1$ (upper entries) and 0.05 (lower entries). The ratio between the populations of the $l, M_J = 0$ and 1 magnetic sublevels is also shown.

| | $(T_1, T_2)$ (keV) | | | | |
|---|---|---|---|---|---|
| | (0.2,3.0) | (0.3,5.0) | (0.4,5.0) | (0.4,8.0) | (0.5,8.0) |
| $N_u/N_g$ | 9.91(-4) | 1.45(-3) | 2.48(-3) | 2.30(-3) | 3.54(-3) |
| | 5.16(-4) | 9.62(-4) | 1.97(-3) | 1.86(-3) | 3.10(-3) |
| $N_{l0}/N_g$ | 9.19(-5) | 1.11(-4) | 1.52(-4) | 1.43(-4) | 1.88(-4) |
| | 4.74(-5) | 6.80(-5) | 1.10(-4) | 1.04(-4) | 1.51(-4) |
| $N_{l1}/N_g$ | 6.73(-5) | 8.70(-5) | 1.30(-4) | 1.23(-4) | 1.71(-4) |
| | 3.45(-5) | 5.52(-5) | 9.82(-5) | 9.40(-5) | 1.43(-4) |
| $N_{l0}/N_{l1}$ | 1.36 | 1.28 | 1.17 | 1.16 | 1.10 |
| | 1.37 | 1.23 | 1.12 | 1.11 | 1.06 |

# Polarization-Dependent Spectra of X-ray Dielectronic Satellite Lines of Be- and B-like Fe

A.S. Shlyaptseva and R.C. Mancini

*Department of Physics*

*University of Nevada, Reno, NV 89557-0058*

## Abstract

We have studied the polarization properties of dielectronic satellite lines in Be- and B-like Fe ions excited through resonant electron capture by an electron beam. Using the photon density matrix formalism, we have calculated the degree of polarization and polarization-dependent spectra of dielectronic satellite lines, i.e., the spectral intensity distribution of lines associated with two polarization states, parallel and perpendicular to the electron beam. We discuss the dependence of such polarization-dependent spectra on the energy of the electron beam. These results are relevant to diagnostic applications of X-ray line polarization spectroscopy.

## I. INTRODUCTION

X-ray line spectroscopy has proved to be a very useful diagnostic tool to infer ionization balance, temperature and density in plasmas. Most of these diagnostics have been based on studies of line intensities, distributions and line shapes. However, for the case of non-equilibrium, anisotropic plasmas, it is the study of polarization of X-ray lines that can be useful to investigate properties of the electron distribution function. In this connection, X-ray line polarization spectroscopy can play an important role in bridging the gap between electron kinetic simulations and experiments. To our knowledge, the first theoretical inves-

tigations of polarization of X-ray line radiation applied to the diagnosis of high-temperature plasmas were done by Haug [1,2] for the case of solar plasmas. In his work, the degree of polarization of resonance lines in H- and He-like Fe ions excited by an electron beam was calculated using the results for polarization of electric dipole transitions in neutral atoms excited by electron impact from Ref. [3]. Few theoretical and experimental studies have been done on X-ray line polarization. In theoretical studies, two basic excitation mechanisms have been considered: electron impact excitation and dielectronic recombination. Theoretical calculations of the polarization of radiation by electron-impact excitation have been made for H-, He- and Li-like ions in the non-relativistic [4–8] and relativistic approximations [9,10]. Polarization of dielectronic satellite lines has been considered for H-, He- and Li-like ions in the non-relativistic [6,7,11] and relativistic approximations [12]. Also, polarization of dielectronic satellite lines of B-like ions has been computed in the non-relativistic approximation [13]. In laboratory plasmas, the polarization of X-ray line emission of multiply-charged Fe ions in plasmas produced by pulsed, high-current z-pinch discharges has been detected and associated with the presence of suprathermal electrons along the discharge axis [14]. More recently, observations of polarization of X-ray lines excited by electron impact were made in laser-produced plasmas for He-like Al ions by Kieffer et al. [15,16], at the Livermore Electron Beam Ion Trap (EBIT) for He-like Sc ions by Henderson et al. [17], for He- and Li-like Fe ions by Beiersdorfer et al. [18,19], for Be- and B-like Fe ions by Shlyaptseva et al. [20–22] and at the National Institute of Standards and Technology EBIT for Ne-like Ba ions by Takács et al. [23]. It should be emphasized that the measurements performed at EBIT can be used to make careful comparisons and testing of new theoretical calculations.

In this paper, we study polarization-dependent spectra of dielectronic satellite lines of Be- and B-like Fe. Our goal is to develop the capability of being able to calculate polarization-dependent spectra for the general case in which lines overlap and blend to form composite spectral features. Here, we illustrate this idea for the case of dielectronic satellite spectra in low-density plasmas. Theoretical results of the polarization properties of dielectronic satellite spectral features are discussed in detail.

## II. THEORETICAL APPROACH

### A. Formalism

A detailed discussion of the theoretical formalism we used is presented in Ref. [21]. Briefly, the degree of polarization of line transitions excited by an electron beam observed in a direction perpendicular to the electron beam is defined as:

$$P_0 = \frac{I_{\parallel} - I_{\perp}}{I_{\parallel} + I_{\perp}} \tag{1}$$

where $I_{\parallel}, I_{\perp}$ are the intensities associated with electric vectors polarized parallel and perpendicular to the electron beam, respectively. The intensities of dielectronic satellite lines associated with different polarization states have the following form:

$$I_{\parallel}(s) = \frac{3}{2} Q_d(s) \exp(-((E_b - E_a(s))/\Delta E)^2) \frac{1 + P_0}{3 - P_0} \tag{2}$$

$$I_{\perp}(s) = \frac{3}{2} Q_d(s) \exp(-((E_b - E_a(s))/\Delta E)^2) \frac{1 - P_0}{3 - P_0} \tag{3}$$

here $Q_d(s)$ is the intensity factor, and $E_a(s)$ is the autoionization energy of dielectronic satellite emission. We characterize the beam of electrons with a Gaussian distribution function centered at the beam energy $E_b$ and with a width $\Delta E$. Thus to calculate the intensity of a dielectronic satellite line $s$ associated with parallel and perpendicular polarization states, we need to know the atomic characteristics, $Q_d(s)$ and $E_a(s)$, and the degree of polarization of each satellite line $P_0(s)$.

In order to describe the polarization properties of dielectronic satellite line emission we use photon density matrix formalism. We consider the representation of the total momentum of the system. The initial state is characterized by the index $i$, target ion in the initial state (before recombination) and an incident electron. The autoionization state is characterized by the index $a$, target ion in the autoionization state. The final state is characterized by the index $f$, target ion in the final state (after recombination and emission of the photon) and emitted photon. The quantization axis z is taken along the direction of the electron beam.

For low electron-density beams, we can assume that the autoionizing states in the Be-like ions are populated by electron capture only from the ground state $1s^2 2s\ ^2S_{1/2}$ of the Li-like ions, and in the B-like ions by electron capture only from the ground state $1s^2 2s^2\ ^1S_0$ of the Be-like ions.

It can be shown that the elements of photon density matrix are connected to the degree of polarization (see Eqs.21-29 of [21]), and that a convenient expression for the maximum degree of polarization is given in the following simple form (see Eq.(30) in [21]):

$$P_0(s) = -\frac{3}{2\sqrt{10}\,\frac{B_0(s)}{B_2(s)} - 1} \tag{4}$$

here $B_L(s)$ is the so-called polarization moment of the ion:

$$B_L(s) = (-1)^{1-J_f-S_a}(2L+1)\begin{pmatrix} l & L & l \\ 0 & 0 & 0 \end{pmatrix}\begin{Bmatrix} L_a & L & L_a \\ J_a & S_a & J_a \end{Bmatrix}\begin{Bmatrix} J_a & L & J_a \\ j_{ph} & J_f & j_{ph} \end{Bmatrix} \tag{5}$$

where ( ) are the $3-j$ symbols, and { } are the $6-j$ symbols. In our case, $L$ can be equal to 0 or 2. If $B_2(s) = 0$, then the line has a zero degree of polarization. For non-zero $B_2(s)$, the degree of polarization $P(s)$ is nonzero and has a maximum for $\theta = 90°$. The results of the calculation of $P_0(s)$ are presented in the next Section.

### B. Atomic and Polarization characteristics

In Table 1 the atomic characteristics, namely wavelengths $\lambda$, radiative transition probabilities $A_r$, intensity factors $Q_d$, and autoionization energies $E_a$, used to calculate polarization-dependent spectra of Be- and B-like Fe dielectronic satellite line spectra are listed. Also displayed in Table 1 is the degree of polarization of each dielectronic satellite line $P_0(s)$, which has been computed using the formalism discussed in the previous section. Atomic data have been calculated using the 1/Z perturbation theory and approximation for atomic structure calculations implemented in the MZ code [24,25]; autoionization energies $E_a$ have been determined using the data from [26]. Fig. 1 shows that to produce Be-like Fe dielectronic satellite lines the energy of the beam has to be in the range from 4.665 $keV$ to

4.775 $keV$, and to produce B-like Fe the energy of the beam has to be in the range from 4.753 $keV$ to 4.809 $keV$. There are 16 Be-like lines combined into 7 peaks (1-7) and 7 B-like lines combined into 3 peaks (8-10) listed in Table 1, which correspond to spectral features that can be identified in the experimental spectra. For comparison, the lines in Table 1 are also labeled according to the notation of [27] where they were discussed in terms of their contribution to Tokamak spectra. Peaks 5, 7, and 10 are formed by a single line. All other peaks consist of more than one line. Relativistic effects are important for Fe ion, and intercombination Be-like lines 2, 10, 16 and B-like line 23 can be observed. In general, the lines contributing to the same peak have different magnitudes and signs of the degree of polarization $P_0$. According to Eq. (1), if the sign of $P_0$ is positive, the line is predominantly polarized parallel to the electron beam axis, and if the sign of $P_0$ is negative, the line is predominantly polarized perpendicular to the electron beam axis. Since we are assuming that electron capture originates only from the ground levels, then in the pure $LS$ coupling scheme autoionization levels associated with the configurations $1s2s2p^2$, $1s2s^22p^2$, and terms $S$ and $D$ can be populated, i.e.,

$$1s^22s\,^2S_{1/2} + \kappa s \rightarrow 1s2s2p^2;\ \ 1s^22s^2\,^1S_0 + \kappa s \rightarrow 1s2s^22p^2\ \ (s-channel) \qquad (6)$$

$$1s^22s\,^2S_{1/2} + \kappa d \rightarrow 1s2s2p^2;\ \ 1s^22s^2\,^1S_0 + \kappa d \rightarrow 1s2s^22p^2\ \ (d-channel) \qquad (7)$$

First we consider Be-like transitions (lines 1-16). The corresponding transitions arising from $S$ or $D$ levels (Eqs.(6-7)) are lines 2, 3, 4, 5, 6, 8, 11, 12, 13, and 15 in Table 1. All lines arising from terms populated via s-channel are unpolarized. Hence, lines 3, 4 and 5 are unpolarized. The polarization of lines 2, 6, 8, 11, 12, 13 and 15 was calculated according to Eqs.(4,5). All other lines, i.e., 1, 7, 9, 10, 14, and 16, occur from levels associated with $P$ terms, which, due to relativistic effects, are produced by mixing with $S$ and $D$ terms having the same $J_a$. There are two different $^3P$ terms corresponding to different intermediate momentum coupling. The terms $^3_1P$ and $^3_2P$ denote the intermediate momentum coupling $2p^2(^3P)2s(^2P)1s\ ^3P$ and $2p^2(^3P)2s(^4P)1s\ ^3P$, respectively. The mixing of terms $S$, $D$, and $P$ within a complex described by the same parity and the same $J_a$ increases with Z and

becomes significant for the case of Fe (Z=26). For example, for the level $^3_2P$, the largest mixing coefficients are 0.7 ($^3_2P$), 0.67 ($^3S$) and 0.17 ($^3_1P$) (for $J_a = 1$) and 0.78 ($^3_2P$), -0.6 ($^1D$) and 0.12 ($^3D$ (for $J_a = 2$). To calculate the polarization of lines arising from $P$ terms, we selected the main term ($S$ or $D$) depending on which makes the largest contribution to the level. This main term is then used to calculate the polarization of lines arising from $P$ levels according to Eqs.(4,5). The largest neglected contribution to the polarization of the line due to this procedure is less than 2%. The detailed description of this procedure is presented in [21].

Next, we consider B-like transitions (lines 17-23). The corresponding transitions arising from $S$ or $D$ levels (Eqs.(6-7)) are lines 17, 19, 21, and 22 in Table 1. The polarization of lines 19, 21, and 22 was calculated according to Eqs. (4,5). All other lines, i.e., 18, 20, and 23, occur from levels associated with $P$ terms, which, due to relativistic effects, are produced by mixing with $S$ and $D$ terms having the same $J_a$. All lines arising from levels with $J_a = 1/2$ are unpolarized. Thus, lines 17 and 20 are unpolarized. Lines arising from levels with $J_a \neq 1/2$ may show polarization. For $J_a = 3/2$, the levels $^2P$, $^2D$, and $^4P$ are mixed. For $J_a = 5/2$, the levels $^2D$ and $^4P$ are mixed. For $J_a = 3/2$ and 5/2, the main term is $^2D$. Moreover, the levels with $J_a = 1/2$ can be prepared only through s-channel, while the levels with $J_a = 3/2$ and 5/2 can be prepared only through d-channel. This differs from the case of Be-like ions, where we have two and even three $S$ or $D$ terms contributing in each of the $P$ terms, which can be excited through both channels. Following the same procedure as for Be-like ions, line 18 has the same polarization as line 22, and line 23 has the same polarization as line 21. The values of the degree of polarization calculated here in LS approximation agree well with the values of degree of polarization calculated in j-j coupling in non-relativistic approximation elsewhere [13].

### C. Polarization-dependent spectra

Theoretical results for polarization-dependent spectra of dielectronic satellite lines in Be- and B-like Fe ions are presented in Figs. 2 (a, b, c, and d), and Figs. 3 (a, b, and c), respectively. In Figs. 2 (a, b, c, and d), Be-like spectra are displayed for four different energies of the electron beam: a) $E_b = 4.717\ keV$, b) $E_b = 4.734\ keV$, c) $E_b = 4.762\ keV$, and c) $E_b = 4.775\ keV$, respectively. In Figs. 3 (a, b, c, and d), B-like spectra are displayed for four different energies of the electron beam: a) $E_b = 4.770\ keV$, b) $E_b = 4.790\ keV$, c) $E_b = 4.810\ keV$, and c) $E_b = 4.830\ keV$, respectively. These energies are in the range of the relevant autoionization energies for each ion listed in Table 1. The distribution of energies in the electron beam was modeled with a Gaussian function of 47 $eV$ of FWHM, and we used Voigt lineshapes of Voigt parameter $a = 0.7$ and FWHM$= 0.5m\mathring{A}$. The spectra displayed in Figs. 2, 3 illustrate the main properties of the theoretical results: (1) the dependence of the spectra on the electron beam energy $E_b$, and (2) the polarization properties of the spectra. As the value of the electron beam energy $E_b$ increases, different electron capture resonances are excited, and the spectrum changes significantly.

First we discuss the Be-like spectra (see Figs. 2 (a, b, c, and d)). As $E_b$ increases, peaks 1 and 2 are the first ones to "turn-on", then 3, 4, 5 and 6, and finally 7 follows. For $E_b = 4.775$ $keV$ (the highest value for Be-like lines here) peaks 1 and 2 begin to "turn-off". Peak 4 consists of a single, polarized line (line 10) which is an intercombination line and due to relativistic effects is very pronounced in the Fe spectrum. Another strong intercombination line (line 2) is also prominent at high values of $E_b$ but it blends with unpolarized line 3 to form peak 6. In general, lines with different degrees of polarization blend to give rise to peaks and the polarization properties of these spectral features can be traced back to those of their constituent lines.

Next, we consider B-like spectra (see Figs. 3 (a, b, c, and d)). For $E_b = 4.770\ keV$ (the lowest value for B-like spectra here), two peaks, 8 and 9, are intense. The intensity of peak 8 is a little larger than the intensity of peak 9, and for this value of $E_b$, both

peaks are predominantly positively polarized (i.e., parallel to the electron beam). As $E_b$ increases, the relative intensities of these two peaks change. Now, peak 9 becomes more intense than peak 8. Moreover, peak 10 "turns on", which consists from one unpolarized line (line 17), and thus is unpolarized for all energies $E_b$. Peak 9 continues to show the same positive polarization, but peak 8 starts to show negative polarization on its shortwavelength side. This is caused by the contribution of negatively polarized line 18 into peak 8. As the energy of the beam continues to increase, the shape of the peak 8 changes, as the relative contribution of the line 18 becomes more important. For $E_b = 4.830\ keV$ (the highest value for B-like spectra considered here), peak 8 has become predominantly negatively polarized, while peak 9 continues to be positively polarized, and peak 10 is unpolarized.

Three traces are shown in Figs. 2, 3 which represent the intensity distributions associated with the parallel polarization state, perpendicular polarization state, and their sum, i.e. the total intensity at 90°, calculated according to Eqs. (2, 3). This way of presenting the results clearly shows the relative contributions of parallel and perpendicular polarization states to the total intensity distribution, and it highlights those peaks (i.e. spectral features) which have significant polarization. The larger the difference between the intensity distributions associated with parallel and perpendicular polarization states, the larger the polarization of the peak.

These theoretical results have been compared with experiments performed at the LLNL EBIT where dielectronic satellite line emission from Fe ions produced at different energies of the electron beam was simultaneously recorded with two crystal spectrometers with different polarization sensitivities [20–22]. Specifically, we compared polarization-dependent spectra of Be-like Fe [20,21] and B-like Fe [22]. The agreement between theoretical and experimental spectra is overall very good. It extends from a good reproduction of the energy dependence of line emission, line position, and relative line intensities to the polarization-induced differences between the spectra from the two crystal spectrometers.

## III. SUMMARY AND CONCLUSIONS

We have studied theoretically the polarization properties of dielectronic satellite lines of Be- and B-like Fe ions excited by an electron beam. Using the photon density matrix formalism, we have calculated the degree of polarization of each dielectronic satellite line. Specifically, from a total of twenty three lines we found that six of them were unpolarized, while the other ones had different degrees of polarization either predominantly parallel or perpendicular to the electron beam axis. Based on the calculated atomic and polarization characteristics of satellite lines and on the assumption of a Gaussian distribution function for the electron beam, we have computed the line intensity distributions associated with two polarization states, parallel and perpendicular to the electron beam. With these spectral distributions we have modeled the complex dielectronic satellite line spectra of Be- and B-like Fe ions excited by an electron beam. These theoretical spectra have also been successfully compared with experimental measurements performed at the LLNL EBIT using two crystal spectrometers with different polarization sensitivity [20–22]. Polarization markers have been identified, which can be used to infer the presence of electron beams in low-density plasmas. These fundamental studies are important for the development of new X-ray line polarization diagnostics for plasmas.

# REFERENCES


[1] E. Haug, Solar Physics **61**, 129 (1979).

[2] E. Haug, Solar Physics **71**, 77 (1981).

[3] I. Percival and M.J. Seaton, Phil. Trans. Soc. London A **251**, 113 (1958).

[4] M.K. Inal and J. Dubau, J. Phys. B **20**, 4221 (1987).

[5] A.S. Shlyaptseva, A.M. Urnov and A.V. Vinogradov, *P.N. Lebedev Physical Institute Report* 194 (1981).

[6] A.V. Vinogradov, A.M. Urnov and A.S. Shlyaptseva, in *Atomic and Ionic Spectra and Elementary Processes in Plasmas, P. N. Lebedev Physics Inst. Proc., Academy of Sciences of Russia*, Ed. I.I. Sobelman (Nova Science, Commack, NY) **192**, 92 (1992).

[7] Y. Itikawa, R. Srivastava and K. Sakimoto, Phys. Rev. A **44**, 7195 (1984).

[8] M.K. Inal and J. Dubau, Phys. Rev. A **47**, 4794 (1993).

[9] H.L. Zhang, D.H. Sampson and R.D. Clark, Phys. Rev. A **41**, 198 (1990).

[10] K.J. Reed and M.H. Chen, Phys. Rev. A **48**, 3644 (1993).

[11] M.K. Inal and J. Dubau, J. Phys. B **22**, 329 (1989).

[12] M.H. Chen and J.H. Scofield, Phys. Rev. A **52**, 2057 (1995).

[13] A.S. Shlyaptseva, I.E. Golovkin and U.I. Safronova, J. Quant. Spectrosc. Radiat. Transfer **56**, 157 (1996).

[14] V.A. Veretennikov, A.E. Gurei, A.N, Dolgov, V.V. Korneev and O.G. Semenov, JETP Lett. **47**, 35 (1988).

[15] J.C. Kieffer, J.P. Matte, H. Pepin, M. Chaker, Y. Beaudoin, C.Y. Chien, S. Coe, G. Mourou and J. Dubau, Phys. Rev. Lett. **68**, 480 (1992).

[16] J.C. Kieffer, J.P. Matte, M. Chaker, Y. Beaudoin, C.Y. Chien, S. Coe, G. Mourou, J. Dubau and M.K. Inal, Phys. Rev. E **48**, 4648 (1993).

[17] J.R. Henderson, P. Beiersdorfer, C.L. Bennet, S. Chantrenne, D.A. Knapp, R.E. Marrs, M.B. Schneider, K.L. Wong, G.A. Doschek, J.F. Seely, C.M. Brown, R.E. LaVilla, J. Dubau and M.A. Levine, Phys. Rev. E **65**, 705 (1990).

[18] P. Beiersdorfer, D.A. Vogel, K.J. Reed, V. Decaux, J.H. Scofield, K. Widmann, G. Hölzer, E. Förster, O. Wehrhan, D.W. Savin and L. Schweikhard, Phys. Rev. A **53**, 3974 (1996).

[19] P. Beiersdorfer, J. Crespo López-Urrutia, V. Decaux, K. Widmann and P. Neill, Rev. Sci. Instrum. **68**, 1073 (1997).

[20] A.S. Shlyaptseva, R.C. Mancini, P. Neill and P. Beiersdorfer, Rev. Sci. Instrum. **68**, 1095 (1997).

[21] A.S. Shlyaptseva, R.C. Mancini, P. Neill, P. Beiersdorfer, J. Crespo López-Urrutia, and K. Widmann, Phys. Rev. A **57**, 888 (1998).

[22] A.S. Shlyaptseva, R.C. Mancini, P. Neill, P. Beiersdorfer, Phys. Rev. A (submitted for publication).

[23] E. Takács, E.C. Meyer, J.D. Gillaspy, J.R. Roberts, C.T. Chantler, L.T. Hundson, R.D. Deslattes, C.M. Brown, J.M. Laming, J. Dubau, M.K. Inal, Phys. Rev. A **54**, 1342 (1996).

[24] V.L. Vainshtein, U.I. Safronova, At. Data and Nucl. Data Tables **21**, 49 (1978).

[25] U.I. Safronova, Phys. Scr. **T26**, 59 (1989).

[26] U.I. Safronova and A.S. Shlyaptseva, Phys. Scr. **54**, 254 (1996).

[27] P. Beiersdorfer, T.W. Phillips, V.L. Jacobs, K.W. Hill, M. Bitter, S. Von Goeler and S.M. Kahn, Ap. J. **409**, 846 (1992).

## TABLES

TABLE I. Atomic and polarization characteristics for dielectronic satellite transitions $1s2s2p^2 \rightarrow 1s^22s2p$ of Be-like Fe and $1s2s^22p^2 \rightarrow 1s^22s^22p$ of B-like Fe.

| Ion | Peak | Line | Ref.[27] | Transition | $J_a - J_f$ | $\lambda(\AA)$ | $A_r(s^{-1})$ | $Q_d(s^{-1})$ | $E_a(eV)$ | $P_0$ |
|---|---|---|---|---|---|---|---|---|---|---|
| *Be* | 5 | 1 | *E*1 | $^3_2P - {}^3P$ | 1-2 | 1.8668 | 2.22[+14] | 6.84[+13] | 4751.6 | 0 |
| *Be* | 6 | 2 | *E*2 | $^1D - {}^3P$ | 2-2 | 1.8679 | 1.41[+14] | 7.00[+13] | 4747.6 | -1 |
| *Be* | | 3 | | $^3S - {}^3P$ | 1-1 | 1.8683 | 8.75[+13] | 3.23[+13] | 4735.0 | 0 |
| *Be* | 7 | 4 | *E*4 | $^1S - {}^1P$ | 0-1 | 1.8697 | 2.30[+14] | 3.52[+13] | 4775.3 | 0 |
| *Be* | | 5 | *E*5 | $^3S - {}^3P$ | 1-2 | 1.8715 | 3.71[+13] | 1.37[+13] | 4735.0 | 0 |
| *Be* | | 6 | *E*6 | $^3D - {}^3P$ | 1-1 | 1.8725 | 2.41[+14] | 1.75[+14] | 4719.9 | -3/7 |
| *Be* | 1 | 7 | *E*7 | $^3_1P - {}^3P$ | 1-0 | 1.8728 | 3.77[+14] | 1.17[+14] | 4715.2 | 3/5 |
| *Be* | | 8 | *E*8 | $^3D - {}^3P$ | 2-1 | 1.8735 | 3.17[+14] | 4.80[+14] | 4716.5 | 1/3 |
| *Be* | | 9 | *E*9 | $^3_1P - {}^3P$ | 2-2 | 1.8738 | 4.30[+14] | 1.54[+14] | 4726.8 | -3/5 |
| *Be* | 4 | 10 | *E*10 | $^3_2P - {}^1P$ | 2-1 | 1.8747 | 8.40[+13] | 8.20[+13] | 4756.3 | 3/5 |
| *Be* | | 11 | *E*11 | $^3D - {}^3P$ | 1-2 | 1.8757 | 8.05[+13] | 5.82[+13] | 4719.9 | 3/41 |
| *Be* | 2 | 12 | *E*12 | $^3D - {}^3P$ | 3-2 | 1.8758 | 2.30[+14] | 6.62[+14] | 4719.6 | 18/41 |
| *Be* | | 13 | *E*13 | $^3D - {}^3P$ | 2-2 | 1.8767 | 8.17[+12] | 1.24[+13] | 4716.5 | -3/7 |
| *Be* | 3 | 14 | *E*14 | $^3_1P - {}^3P$ | 1-2 | 1.8771 | 1.00[+14] | 3.11[+13] | 4715.2 | 3/41 |
| *Be* | | 15 | *E*15 | $^1D - {}^1P$ | 2-1 | 1.8781 | 1.45[+14] | 1.48[+14] | 4747.6 | 3/5 |
| *Be* | | 16 | *E*17 | $^5P - {}^3P$ | 3-2 | 1.8874 | 1.01[+13] | 2.92[+13] | 4679.1 | 18/41 |
| *B* | 10 | 17 | *B*2 | $^2S - {}^2P$ | 1/2-3/2 | 1.8795 | 2.88[+14] | 5.68[+13] | 4809.1 | 0 |
| *B* | | 18 | *B*3 | $^2P - {}^2P$ | 3/2-3/2 | 1.8814 | 5.77[+14] | 1.21[+14] | 4802.5 | -3/4 |
| *B* | 8 | 19 | *B*5 | $^2D - {}^2P$ | 3/2-1/2 | 1.8821 | 3.07[+14] | 2.51[+14] | 4785.4 | 3/5 |
| *B* | | 20 | *B*4 | $^2P - {}^2P$ | 1/2-1/2 | 1.8822 | 5.20[+14] | 9.03[+12] | 4785.1 | 0 |
| *B* | 9 | 21 | *B*6 | $^2D - {}^2P$ | 5/2-3/2 | 1.8849 | 2.05[+14] | 3.34[+14] | 4790.4 | 1/2 |
| *B* | | 22 | *B*8 | $^2D - {}^2P$ | 3/2-3/2 | 1.8863 | 3.80[+13] | 3.12[+13] | 4785.4 | -3/4 |
| *B* | | 23 | *B*9 | $^4P - {}^2P$ | 5/2-3/2 | 1.8916 | 2.89[+13] | 1.31[+13] | 4766.9 | 1/2 |

## FIGURES

FIG. 1. Schematic energy level diagram of the relevant Fe ionization stages. Energy levels are measured with respect to the He-like Fe ground state. Each box represents groups of energy levels associated with a given configuration; energy bounds for the box are indicated. Also shown are the ranges of energies for resonant electron capture from the ground states of He-, Li-, and Be-like Fe.

FIG. 2. Theoretical polarization-dependent spectrum of Be-like Fe calculated for four different energies of the electron beam: a) $E_b = 4.717keV$, b) $E_b = 4.734keV$, c) $E_b = 4.762keV$, b) $E_b = 4.775keV$. (– –): intensity associated with parallel polarization state, (···): intensity associated with perpendicular polarization state, (—): total intensity. Be-like spectral features are labeled according to the peak labeling of Table 1.

FIG. 3. Theoretical polarization-dependent spectrum of B-like Fe calculated for four different energies of the electron beam: a) $E_b = 4.770keV$, b) $E_b = 4.790keV$, c) $E_b = 4.810keV$, d) $E_b = 4.830keV$. (– –): intensity associated with parallel polarization state, (···): intensity associated with perpendicular polarization state, (—): total intensity. B-like spectral features are labeled according to the peak labeling of Table 1.

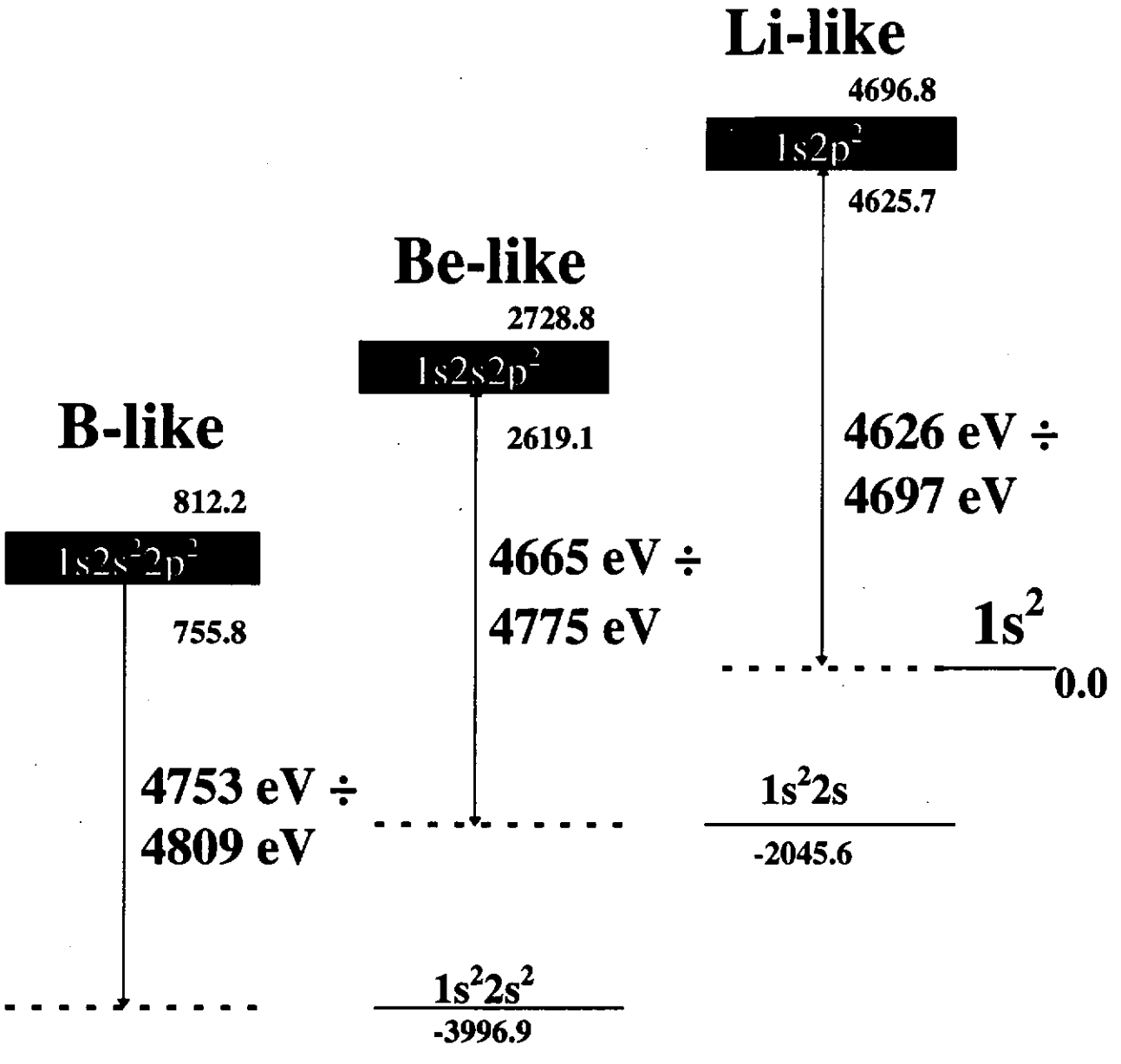
Li-like
4696.8
1s2p²
4625.7
Be-like
2728.8
1s2s2p²
2619.1
B-like
812.2
1s2s²2p²
755.8
4626 eV ÷
4697 eV
4665 eV ÷
4775 eV
1s²
0.0
4753 eV ÷
4809 eV
1s²2s
-2045.6
1s²2s²
-3996.9

**Fig. 1**

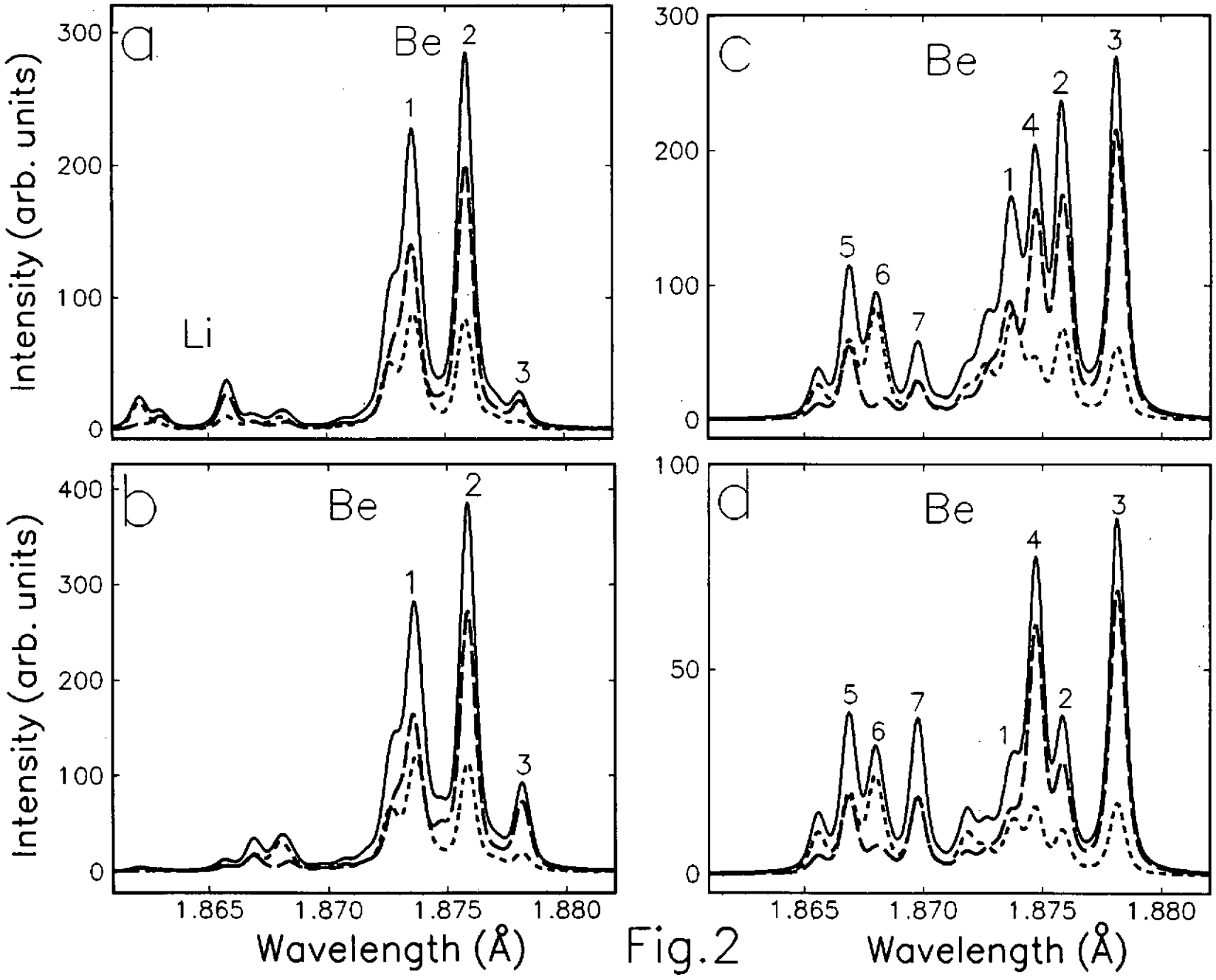
a
Be
Li
1
2
3
b
Be
1
2
3
c
Be
1
2
3
4
5
6
7
d
Be
1
2
3
4
5
6
7
Intensity (arb. units)
Intensity (arb. units)
Wavelength (Å)
Wavelength (Å)
1.865
1.870
1.875
1.880

Fig.2

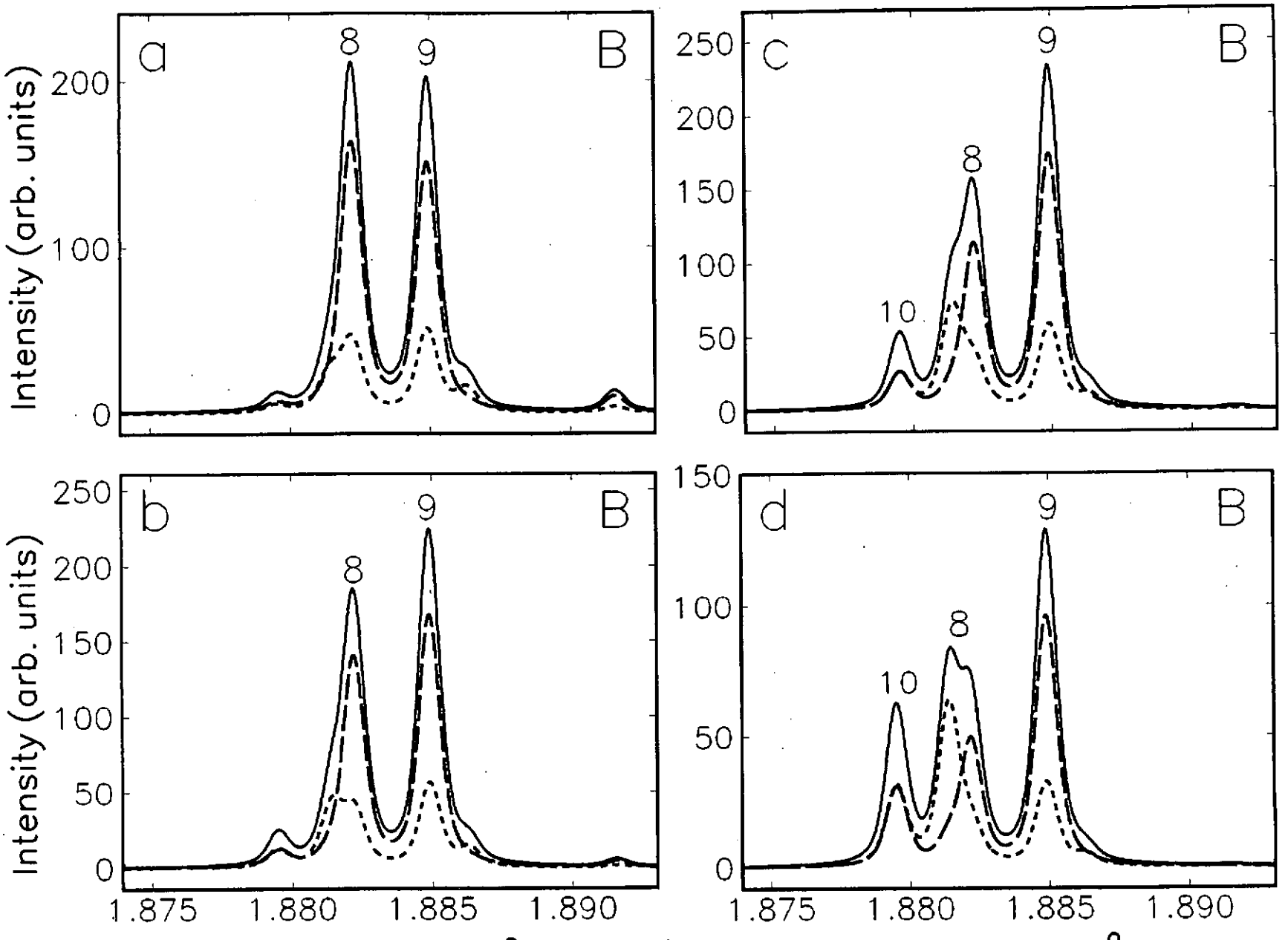
a
B
8
9
c
B
10
8
9
b
B
8
9
d
B
10
8
9
Intensity (arb. units)
Intensity (arb. units)
0
50
100
150
200
250
1.875
1.880
1.885
1.890
Wavelength (Å)
Wavelength (Å)

Fig.3

# Density-Matrix Description of Polarized Atomic Radiative Emission in Electric and Magnetic Fields

V. L. Jacobs

Institute for Plasma Research,

University of Maryland,

College Park, MD 20742-3511

and

Complex Systems Theory Branch, Code 6693,

Condensed Matter and Radiation Sciences Division,

Naval Research Laboratory,

Washington, D. C. 20375-5345 (Permanent Address)

A. B. Filuk (Deceased)

Ion Beam Generation Department, Organization 9533, MS 1186,

Sandia National Laboratories,

P. O. Box 5800, Albuquerque, New Mexico 87185-1186

(For Submission to the Proceedings of the Japan-U. S. Workshop and International Seminar on Plasma Polarization Spectroscopy, 26-28 January, 1998, Kyoto, Japan)

February, 1998

# ABSTRACT

A density-matrix description has been developed for the investigation of the angular distribution and polarization of radiative emission during single-photon atomic transitions in the presence of a general arrangement of static (or quasi-static) electric and magnetic fields. Particular emphasis has been given to the influence of directed collisional excitations, which may be produced by an anisotropic incident-electron velocity distribution. We have allowed for the possibility of the coherent excitation of the nearly degenerate field-dependent atomic substates. Coherent excitations may be produced by non-parallel electric and magnetic fields. Our main result is a general expression for the matrix elements of the photon-polarization density operator. This expression provides a unified framework for the analysis of the total intensity, angular distribution, and polarization of the Stark-Zeeman spectral patterns. For the observation of radiative emission in the direction of the magnetic field, the detection of linearly polarized emissions, in addition to the usual circularly polarized radiations, can reveal the presence of a perpendicular electric field or a coherent excitation mechanism.

# I. INTRODUCTION

Polarized radiative emission can occur as a result of a nonuniform (or nonstatistical) distribution of the population densities of the excited atoms (or ions) among the degenerate (or nearly degenerate) angular-momentum magnetic sublevels. A nonuniform distribution of population densities among the magnetic sublevels can be produced by, for example, directed electron or ion beam excitation, laser photon excitation, or the action of perturbing electric or magnetic fields. The measurement and analysis of the polarization of the atomic radiative emission can provide information on the nature of the excitation mechanisms and the strength of the electric or magnetic fields.

We have been concerned with applications of the density-matrix description of polarized atomic radiative emission to spectroscopic observations in electric and magnetic fields. Particular interest has been directed at radiative emission in the intense crossed electric and magnetic fields generated by the applied-B ion diodes of the Particle Beam Fusion Accelerators PBFA II and SABRE at Sandia National Laboratories (Bailey et al., 1995; Filuk et al., 1996). Our theoretical investigation has also been motivated by magnetic field measurements in tokamak plasmas, allowing for the Zeeman and the motional-Stark effects (Huang, Wróblewski, Finkenthal, and Moos, 1989; Ida et al., 1998). Electric and magnetic fields may also play an important role in the production of polarized radiative emission by the anisotropic electron velocity distributions in the Electron Beam Ion Trap (EBIT) devices at the Lawrence Livermore National Laboratory (Beiersdorfer et al., 1996) and at the National Institute of Standards and Technology (Takács et al., 1996). Finally, magnetic fields are now believed to influence the electric-field induced enhancement of

dielectronic recombination radiation that is observed in electron-ion beam interactions (Savin et al., 1996; Bartsch et al., 1997). In our analysis of polarized atomic radiative emission, we shall allow for a general set of steady-state excitation processes in the presence of an arbitrary arrangement of static (or quasi-static) electric and magnetic fields.

The geometry for spectroscopic observations in crossed electric and magnetic fields is illustrated in Fig. 1. We will be concerned with applications for which the total magnetic field acting on the radiating atomic system is the sum of an external (applied) magnetic field and an internal (dynamical) magnetic field. Examples of the dynamical magnetic field include the nearly parallel magnetic field that is due to electron diamagnetic compression of flux in the anode-cathode region of an applied-B ion diode (PBFA II) and the perpendicular poloidal magnetic field in a tokamak plasma. The viewing angle $\theta$ is taken to be parallel to the applied magnetic field in PBFA II and perpendicular to the known toroidal magnetic field in the case of a tokamak plasma.

Our theoretical description of polarized atomic radiative emission has been developed within the framework of the density-matrix approach. The theory of polarized radiative emission following directed-electron collisional excitation of an atomic system (in the absence of electric and magnetic fields) was first presented by Oppenheimer (1927) and subsequently refined by Percival and Seaton (1958). A density-matrix approach has been presented by Inal and Dubau (1987, 1989). A density-matrix description for dielectronic recombination radiation has been developed by Shlyaptseva, Urnov, and Vinogradov (1981, 1992). We have employed the formalism advanced in our density-matrix description of the angular distribution and polarization in single- and multi-photon ionization processes (Jacobs, 1972; 1973), as well as the formulation presented by Inal and Dubau (1987, 1989). The density-matrix approach can provide a fundamental description of the coherent excitation of the atomic states.

# II. DENSITY-MATRIX DESCRIPTION

In our description of polarized atomic radiative emission in electric and magnetic fields, we have employed the density matrix formalism. The density-matrix formalism has been discussed by Fano (1957), Jacobs (1972, 1773), Blum (1996), and by Kazantsev and J.-C. Hénoux (1995). We have assumed that the total Hamiltonian, describing the many-electron atomic system in the presence of an arbitrary arrangement of static (or quasi-static) electric and magnetic fields, has been diagonalized in a basis set consisting of discrete and continuum field-free eigenstates. The atomic excitation and spontaneous radiative emission processes are treated as independent events. The initial excited state is represented by a density matrix, whose diagonal elements give the familiar population densities and whose non-diagonal elements correspond to the coherences (Blum, 1996). A brief account of our description of polarized radiative emission has been published (Jacobs and Filuk, 1995).

The steady-state (frequency-integrated) intensity, angular distribution, and polarization of the radiation that is emitted in the transition $\gamma_i \rightarrow \gamma_f$ can be determined from the photon-polarization density operator. In the lowest-order of perturbation theory for the electromagnetic interaction V, the matrix elements of the photon-polarization density operator are given by

$$\left\langle \lambda \left| \rho^R \right| \lambda' \right\rangle = \sum_{f,i,i'} \left\langle \gamma_f, \vec{k}\lambda \left| V \right| \gamma_i, 0 \right\rangle \left\langle \gamma_i \left| \rho^A \right| \gamma_{i'} \right\rangle \left\langle \gamma_{i'}, 0 \left| V \right| \gamma_f, \vec{k}\lambda' \right\rangle. \qquad (1)$$

The photon helicity quantum numbers may have the numerical values $\lambda$, $\lambda' = \pm 1$, corresponding the right and left circular polarization along the direction of observation. The sums over f, i, and i' include the quantum numbers specifying degenerate or nearly degenerate sublevels of the field-dependent final and initial states in the radiative transition $\gamma_i \rightarrow \gamma_f$. These restricted sums are indicated by the prime above the summation symbol in Eq. (1). $\rho^A$ is the density operator representing the field-dependent atomic states. In order to determine the precise spectral distribution of the possibly overlapping Stark and Zeeman components, it is necessary to employ our more detailed (higher-order) density-matrix formulation, incorporating the individual line shifts and widths (Jacobs, Cooper, and Haan, 1994).

Since polarization is intimately related to angular momentum, it is advantageous to employ the angular-momentum representation for the atomic states and the multipole expansion for the quantized radiation field. We will assume that the field-dependent atomic eigenstates can be expanded in a basis set of field-free bound and continuum eigenstates:

$$|\gamma_i\rangle = \sum_{\Delta_i J_i M_i} |\Delta_i J_i M_i\rangle\langle\Delta_i J_i M_i|\gamma_i\rangle. \qquad (2)$$

Here $J_i$ is the total electronic angular momentum, $M_i$ is the component along a suitably chosen atomic quantization axis, and $\Delta_i$ denotes the set of remaining quantum numbers. Hyperfine structure will be ignored in our analysis.

In order to relate the photon polarization, which is defined with respect to the direction of observation, to the atomic quantization axis, it is necessary to expand the radiative-transition matrix elements in terms of the matrix elements of the electric and magnetic multipole operators:

$$\left\langle \Delta_f J_f M_f , \vec{k}\lambda | V | \Delta_i J_i M_i , 0 \right\rangle = \sum_j \sum_m \left( \frac{2j+1}{4\pi} \right)^{1/2} A(j) D^{(j)}_{\lambda m}(\hat{k}) \times (-1)^m \left\langle \Delta_f J_f M_f | Q^{(j)}_{-m} | \Delta_i J_i M_i \right\rangle . \quad (3)$$

Here $Q^{(j)}_m$ is the irreducible spherical-tensor form of the multipole-moment operator, and $D^{(j)}_{\lambda m}(\hat{k})$ designates the Wigner rotation-matrix element $D^{(j)}_{\lambda m}(\phi,\theta,0)$. The multiplying factor A(j) depends on the particular type of multipole radiation. The matrix elements of the multipole-moment operator can be evaluated in the angular-momentum representation, in terms of Wigner 3-j symbols and reduced matrix elements, using the Wigner-Eckart theorem:

$$\left\langle \Delta_f J_f M_f | Q^{(j)}_m | \Delta_i J_i M_i \right\rangle = (-1)^{J_f - M_f} \begin{pmatrix} J_f & j & J_i \\ -M_f & m & M_i \end{pmatrix} \times \left\langle \Delta_f J_f \| Q^{(j)} \| \Delta_i J_i \right\rangle . \quad (4)$$

In order to take into account both the electric and the magnetic multipole contributions associated with a given value of j, $Q^{(j)}_m$ should be defined to include the contributions associated with all permissible values of the photon parity.

Our general expression for the photon-polarization density matrix is obtained in the following form (Jacobs and Filuk, 1995):

$$
\begin{aligned}
\langle\lambda|\rho^{R}|\lambda'\rangle \;=\; & \sum_{i,i',f}{}' \langle\gamma_i|\rho^{A}|\gamma_{i'}\rangle \\
& \times \sum_{\Delta_f J_f M_f} \sum_{\Delta_f' J_f' M_f'} \langle\gamma_f|\Delta_f J_f M_f\rangle\langle\gamma_f|\Delta_f' J_f' M_f'\rangle^{*} \\
& \times \sum_{\Delta_i J_i M_i} \sum_{\Delta_i' J_i' M_i'} \langle\Delta_i J_i M_i|\gamma_i\rangle\langle\Delta_i' J_i' M_i'|\gamma_{i'}\rangle^{*} \\
& \times \sum_{j,m} \sum_{j',m'} \sum_{J,M,M'} \left(\Delta_f J_f \| Q^{(j)} \| \Delta_i J_i\right)\left(\Delta_f' J_f' \| Q^{(j')} \| \Delta_i' J_i'\right)^{*} \\
& \times \left(\frac{1}{4\pi}\right)(2j+1)^{1/2}(2j'+1)^{1/2}(2J+1)\,A(j)\,A(j')^{*} \\
& \times (-1)^{J_f+J_f'-M_f-M_f'-m-m'+\lambda'-m'+2j-2j'-M-M'} \\
& \times \begin{pmatrix} J_f & j & J_i \\ -M_f & -m & M_i \end{pmatrix}\begin{pmatrix} J_f' & j' & J_i' \\ -M_f' & -m' & M_i' \end{pmatrix} \\
& \times \begin{pmatrix} j & j' & J \\ \lambda & -\lambda' & -M \end{pmatrix}\begin{pmatrix} j & j' & J \\ m & -m' & -M \end{pmatrix} D^{(J)}{}_{MM'}\left(\hat{k}\right).
\end{aligned}
\tag{5}
$$

The prime above the summation symbol is used to indicate that the summations over f, i, and i' are to be taken over quantum numbers specifying degenerate or nearly degenerate field-dependent sublevels, as in Eq. (1). We emphasize that this expression can be employed for an arbitrary arrangement of electric and magnetic fields and for a general set of steady-state excitation processes. If we neglect field-induced mixing of the atomic eigenstates as well as the non-diagonal elements of the initial-state atomic density matrix, our general expression for the photon-polarization density matrix can be reduced to the result obtained by Inal and Dubau (1987), who investigated the directed electron excitation of polarized atomic radiative emission in the absence of electric and magnetic fields.

The photon-polarization density operator is most generally expressed by means of Eq. (5), as a function of the angles of photon emission. This density operator may be presented as an expansion in terms of the irreducible spherical-tensor operators $T^{(J)}{}_{M}(j,j')$ (Fano and Racah, 1959; Happer, 1972; Omont, 1977; Baylis, 1979):

$$\rho^R = \sum_{j,j'} \sum_{J,M,M'} \rho^R(j,j';J,M')T^{(J)}_M(j,j')D^{(J)}_{MM'}(\hat{k}). \qquad (6)$$

The coefficients $\rho^R(j,j';J,M')$ are referred to as the irreducible spherical-tensor components. The irreducible spherical-tensor representation of the photon density operator is advantageous, because only a very few electromagnetic multipoles are normally involved in an atomic radiative-emission process. In contrast, the irreducible spherical-tensor representation of the field-dependent atomic density operator, which may be expressed in the form

$$\rho^A = \sum_{\Delta_i \Delta_i'} \sum_{J_i J_i'} \sum_{K,N} \rho^A(\Delta_i \Delta_i' J_i J_i';K,N)T^{(K)}_N(J_i J_i'), \qquad (7)$$

involves two expansions over the entire basis set of unperturbed atomic eigenstates. Consequently, the irreducible spherical-tensor representation of the atomic density operator could be advantageous for weak fields or for parallel electric and magnetic fields. For atomic systems with axially symmetry, in which case N = 0, it is useful to introduce a representation of the atomic density operator in terms of components describing orientation (corresponding to odd values of K) and alignment (corresponding to even values of K). An atomic kinetics formalism based on this representation has been described by Csanak (1998) and by Fujimoto and Kawachi (1995).

The conventional representation of the photon-polarization density operator is based on the Stokes parameters. This representation can be expressed as follows (Blum, 1996):

$$\rho^R = \left(\frac{I}{2}\right)\begin{pmatrix} 1+\eta_2 & -\eta_3 + i\eta_1 \\ -\eta_3 - i\eta_1 & 1-\eta_2 \end{pmatrix}. \tag{8}$$

The total intensity I of the emitted radiation is expressed by the normalization condition on $\rho^R$. The parameters $\eta_1$ and $\eta_3$ specify linear polarization, while $\eta_2$ represents circular polarization.

## III. POLARIZATION OF RADIATIVE EMISSION ALONG THE MAGNETIC-FIELD DIRECTION

Due to the limited line-of-sight access to the anode-cathode region of the applied-B ion diode, the spectroscopic measurements on PBFA II have been carried out by viewing the radiative emissions in the direction of the vacuum magnetic field. The spectroscopic measurements in tokamak plasmas have been carried out by detecting the polarized emissions in a direction that is perpendicular to the known toroidal magnetic field, and therefore parallel to the poloidal magnetic field of interest. We are particularly interested in an investigation of the circular-polarization parameter $\eta_2$, which may be expressed in terms of the diagonal elements of the photon-polarization density operator as follows:

$$\eta_2 = \frac{I_+ - I_-}{I_+ + I_-} = \frac{\langle 1|\rho^R|1\rangle - \langle -1|\rho^R|-1\rangle}{\langle 1|\rho^R|1\rangle + \langle -1|\rho^R|-1\rangle}. \tag{9}$$

Here $I_+$ and $I_-$ are the intensities of the right and left circularly polarized radiative emissions. The linear-polarization parameters may be expressed in terms of the non-diagonal elements of the photon-polarization density operator.

We will now consider the case where only a single multipole component of the electromagnetic field is dominant in the determination of the radiative-transition probability, and we will ignore the interference between different multipole components. For the case of spectroscopic measurements in the magnetic-field direction, which corresponds to $\theta = 0$, the general result for the photon-polarization density matrix, which is given by Eq. (5), can be substantially simplified. It is advantageous to take the atomic quantization axis to be along the direction of the magnetic field. From a consideration of the angular-momentum-algebra selection rules, which are associated with the Wigner 3-j symbols, we find the following result: in the absence of a perpendicular electric field and a coherent excitation process, only the circularly-polarized radiative emissions will be observable in the direction of the magnetic field. The observation of linearly-polarized radiative emissions in the magnetic-field direction could reveal the presence of a perpendicular electric field or a coherent excitation process.

In the absence of a perpendicular electric field and a coherent excitation process, the Z-components of the total angular momenta are good quantum numbers and the initial-state atomic density matrix may be assumed to be diagonal. We now consider the weak-field limit and the case where the initial magnetic sublevels are uniformly populated, which can occur in the absence of a directed excitation process. Equal intensities of left- and right-circularly polarized radiative emissions should then be observable in the magnetic-field direction (Cowan, 1981). The individual spectral components may be symmetrically shifted by the Zeeman effect. An example of a weak-field Zeeman spectral pattern, describing a $^3P_2 \rightarrow {}^3P_1$ magnetic-dipole emission, is illustrated in Fig. 2. The presence of Doppler

broadening, together with other broadening mechanisms, usually results in the observation of two blended spectral features, corresponding to the unresolved components for each of the two circular polarizations. More complex spectral patterns can be produced in the presence of crossed electric and magnetic fields.

The observable Zeeman spectral patterns may be conveniently analyzed in terms of the intensity-weighted average of the shifts for the unresolved right- or left-circularly polarized components, as described by Feldman, Seely, Sheeley, Suckewer, and Title (1984) and by Jacobs and Seely (1987). It may be worthwhile to extend this average-shift analysis for the observation of polarized radiative emission in the presence of a perpendicular electric field.

# IV. SUMMARY AND CONCLUSIONS

A very general density-matrix description has been under development for the investigation of the total intensity, angular distribution, and the polarization of atomic radiative emissions in an arbitrary arrangement of static (or quasi-static) electric and magnetic fields. A general set of steady-state excitation processes may be taken into account. From this analysis, we conclude that the observation of linearly-polarized emissions in the direction of the magnetic field could indicate the presence of a perpendicular electric field or the importance of a coherent excitation process. For specific applications of our density-matrix description to spectroscopic observations in the crossed electric and magnetic fields of PBFA II and of tokamak plasmas, it will be necessary to obtain the energy level splittings and eigenstate transformations either by perturbation theory or by means of a direct diagonalization of the total Hamiltonian in a field-free basis

set. It will also be necessary to calculate the steady-state atomic-level population densities, allowing for the effects of directed excitation processes, and to investigate the influence of static atomic-state coherences. For a complete description of the spectral observations, it will be necessary to provide a self-consistent treatment of the atomic-state kinetics and the spectral-line shapes, taking into account the influence of collisional and radiative relaxation processes in the presence of electric and magnetic fields.

## ACKNOWLEDGMENTS

Helpful discussions with J. E. Bailey and E. J. McGuire are gratefully acknowledged. This work has been supported by the U. S. Department of Energy, under contract DE-AI02-93-ER54198 to the Naval Research Laboratory and contract DE-AC04-76-DP00789 to Sandia National Laboratories, and by the Office of Naval Research. V. L. Jacobs wishes to express appreciation to the Institute for Plasma Research, at the University of Maryland, for their hospitality during the one-year visiting-faculty appointment and to the Naval Research Laboratory, for the opportunity provided by the Advanced Graduate Research (Sabbatical) program.

# REFERENCES


J. E. Bailey, A. B. Filuk, A. L. Carlson, D. J. Johnson, P. Lake, E. J. Mc Guire,T. A. Mehlhorn, T. D. Pointon, T. J. Renk, W. A. Stygar, and Y. Maron, Phys. Rev. Letters **74,** 1171 (1995).

T. Bartsch et al., Phys. Rev. Letters **79**, 2233 (1997).

W. E. Baylis, in *Progress in Atomic Spectroscopy*, edited by W. Hanle and H. Kleinpoppen (Plenum, New York, 1979).

P. Beiersdorfer, et al., Phys. Rev. A **53**, 3974 (1996).

K. Blum, *Density Matrix Theory and Applications* , Second Edition, (Plenum, New York, 1996).

R. D. Cowan, *The Theory of Atomic Structure and Spectra* , (University of California Press, Berkeley, 1981).

G. Csanak, This Proceedings (1998).

U. Fano, Rev. Mod. Phys. **29**, 74 (1957).

U. Fano and G. Racah, *Irreducible Tensorial Sets,* (Academic Press, New York, 1959).

U. Feldman, J. F. Seely, N. R. Sheeley, Jr., S. Suckewer, and A. M. Title, J. Appl. Phys. **56**, 2512 (1984).

A. B. Filuk, J. E. Bailey, A. L. Carlson, D. J. Johnson, P. Lake, T. A. Mehlhorn, L. P. Mix, T J. Renk, W. A. Stygar, and Y. Maron, Phys. Rev. Letters **77**, 3557 (1996).

T. Fujimoto and T. Kawachi, in *Atomic Processes in Plasmas*, 9'th APS Topical Conference, edited by W. R, Rowan, AIP Conference Proceedings 322, (AIP, New York, 1995).

W. Happer, Rev. Mod. Phys. **44**, 169 (1972).

L. K. Huang, D. Wróblewski, M. Finkenthal, and H. W. Moos, Phys. Rev. A **40**, 5224 (1989).

K. Ida et al., This Proceedings (1998).

M. K. Inal and J. Dubau, J. Phys. B **20**, 4221 (1987).

M. K. Inal and J. Dubau, J. Phys. B **22**, 3329 (1989).

V. L. Jacobs, J. Phys. B **5**, 2257 (1972).

V. L. Jacobs, J. Phys. B **6**, 1461 (1973).

V. L. Jacobs, J. Cooper, and S. L. Haan, Phys. Rev. A **50**, 3005 (1994).

V. L. Jacobs and A. B. Filuk, Lasers and Particle Beams **13**, 303 (1995).

V. L. Jacobs and J. F. Seely, Phys. Rev. A **36**, 3267 (1987).

S. A. Kazantsev and J.-C. Hénoux, *Polarization Spectroscopy of Ionized Gases*, (Kluwer, Dordrecht, 1995).

A. Omont, Progress in Quantum Electronics **5**, 69 (1977).

J. R. Oppenheimer, Z. Phys. **43**, 27 (1927).

I. C. Percival and M. J. Seaton, Phil. Trans. R. Soc. A **251**, 113 (1958).

D. W. Savin, L. D. Gardner, D. B. Reisenfeld, A. R. Young, and J. L. Kohl, Phys. Rev. A **53**, 280 (1996).

A. S. Shlyaptseva, A. M. Urnov, and A. V. Vinogradov, P. N. Lebedev Physical Institute of the U. S. S. R. Academy of Sciences Report No. **194**, 1981.

E. Takács, et al., Phys. Rev. A **54**, 1342 (1996).

A. V. Vinogradov, A. M. Urnov, and A. S. Shlyaptseva, in *Atomic and Ionic Spectra and Elementary Processes in Plasmas*, Proceedings of the P. N. Lebedev Physics Institute, Academy of Sciences of Russia, Vol. **912**, Edited by I. I. Sobelman (Nova Science Publishers, Commack, New York, 1992), 93.

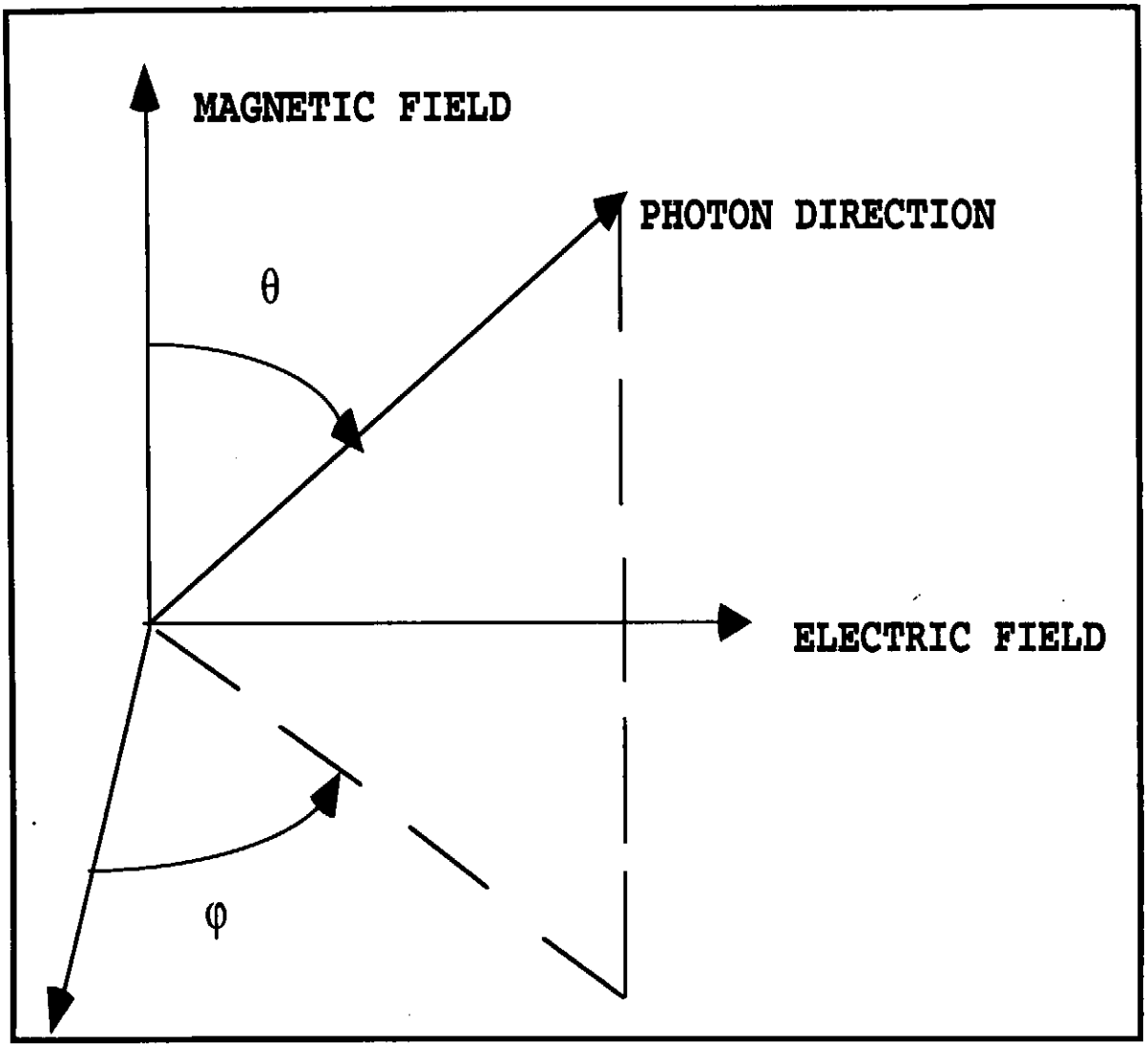


Fig. 1. Viewing angles for spectroscopic observations of polarized atomic radiative emission in perpendicular (crossed) electric and magnetic fields.

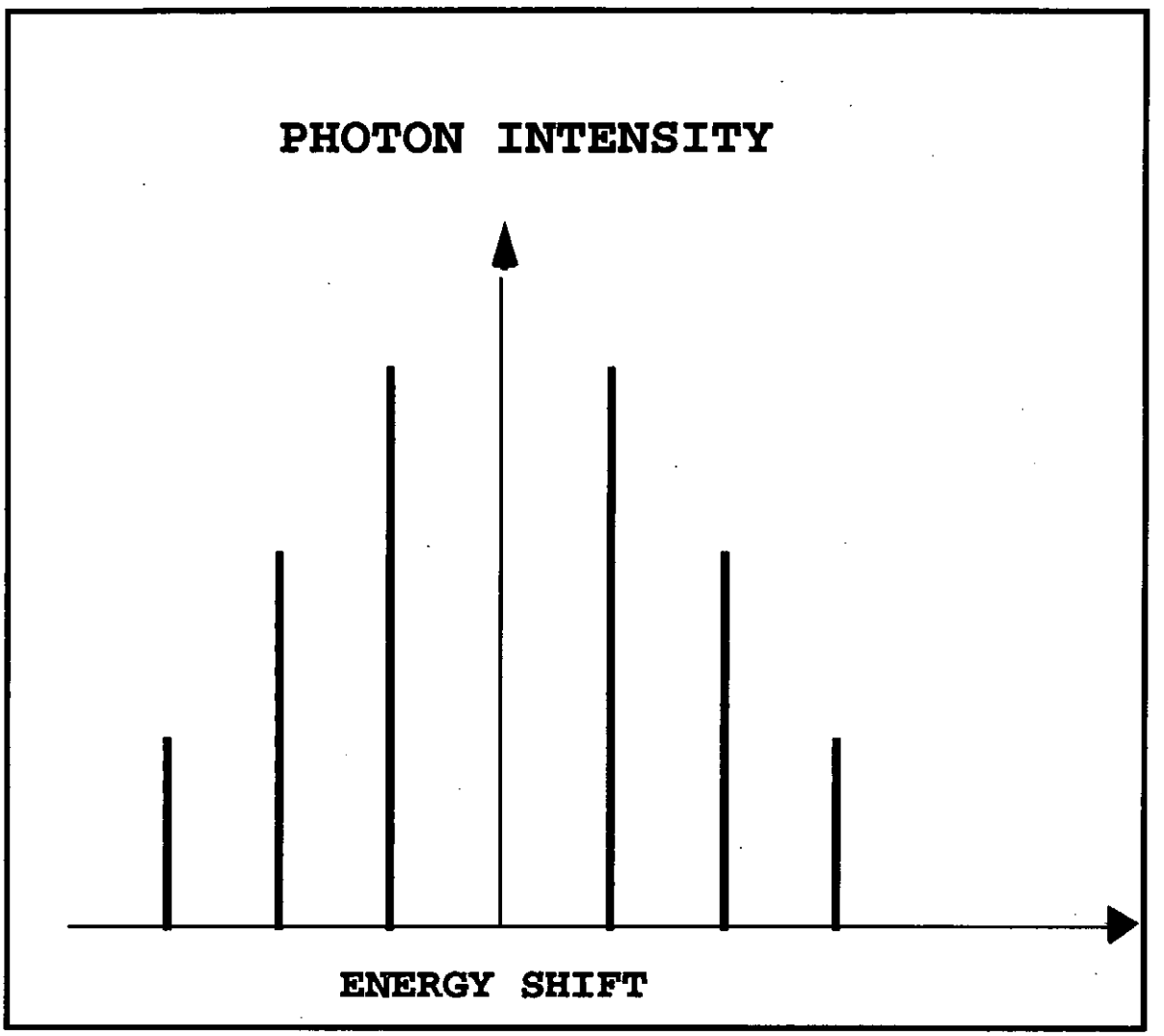


Fig. 2. A weak-field Zeeman pattern describing a $^3P_2 \rightarrow {}^3P_1$ magnetic-dipole emission. The symmetrically-shifted right- and left circularly polarized emissions are observed in the magnetic-field direction, in the absence of electric fields and for uniformly populated magnetic sublevels.

# Recombination of electrons with an anisotropic velocity distribution: Continuation of recombination cotinuum to series lines

Takashi Fujimoto and Takashi Imaida
*Department of Engineering Physics and Mechanics, Graduate School of Engineering*
*Kyoto Univerisity, Kyoto 606-8501*

For ions in recombination with electrons with directional motion, the recombination continuum to a $J = 0$ state is $\pi$ polarized, and this polarization characteristic should continue across the ionization threshold down to the series lines. A Monte Carlo calculation has been performed for electron collisions on a classical atom in excited states. No evidence is found to support the above conclusion.

## Introduction

Yoneda *et al.* [1] report a polarization measurement of a fluorine plasma produced by short pulse laser irradiation. A salient feature in their result is that the series lines of the heliumlike ion spectra show a typical pattern of a recombining plasma. The presence of the recombination continuum continuing from the series lines is in accordance with this observation. Another point to be noted is that, according to their assumption that the hydrogenlike Lyman lines are unpolarized, the recombination continuum is polarized with

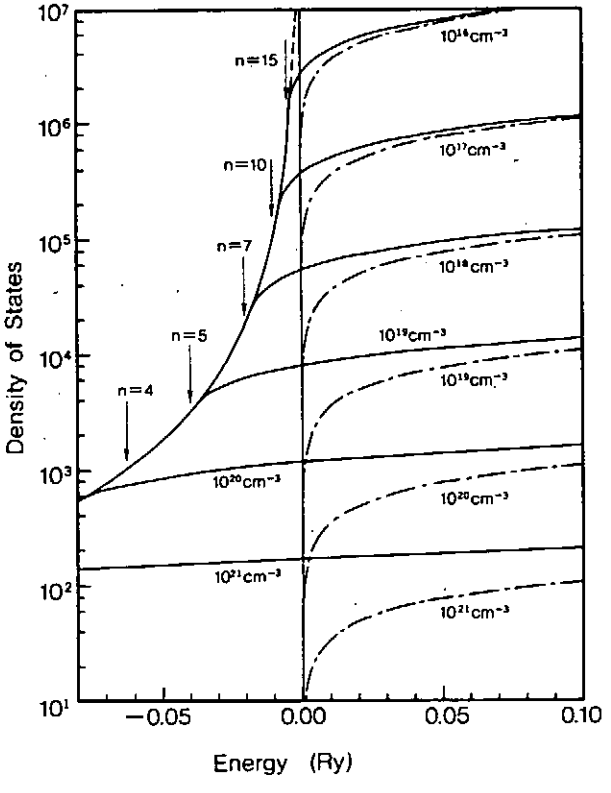


Fig. 1
Density of states of a hydrogen atom in plasma. [2]

the polarization degree of 15 - 25 %. When we look at the spectra carefully, we recognize that the characteristics of the recombination continuum, *i.e.*, the intensity per unit energy interval and the polarization degree, continue smoothly across the ionization limit down to the higher members of the series lines.

In this report we discuss the continuation from the recombination continuum to the series lines, first for plasmas with electrons having the Maxwellian velocity distribution and second for a plasma with an anisotropic distribution.

**Maxwellian velocity distribution**

The solid line in Fig. 1 shows the density of states (number of states per unit energy interval) of a hydrogen atom embedded in a plasma of finite electron density.[2] The density continues smoothly from the discrete states having negative energies to the continuum states with positive energies. We take a group of atoms in a plasma with a certain electron density, and we *fill* the state density with electrons with the Boltzmann distribution. Then, we will have a Boltzmann distribution of populations for the discrete states, a Maxwellian distribution for the continuum states, and the Saha-Boltzmann relationship between the discrete and conitnuum states (with a modification due to the finite density effect). This group of atoms emits radiation with a characteristic spectrum. An

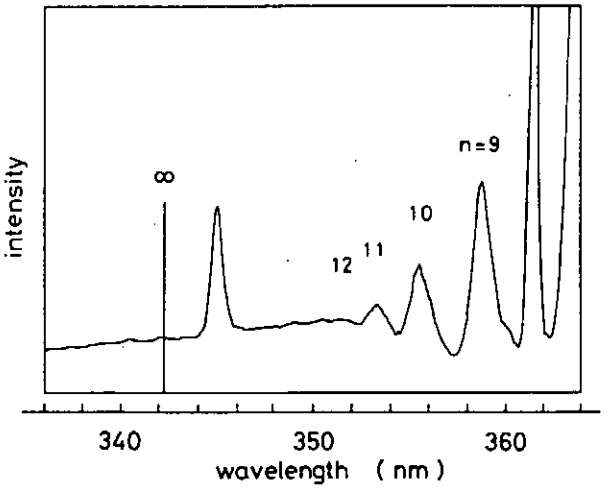


Fig. 2. Series lines and recombination continuum from a helium afterglow plasma.[3]

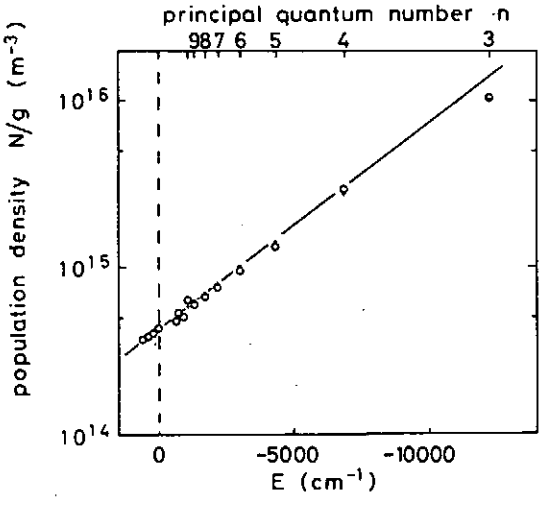


Fig. 3. The Boltzmann plot of the populations in discrete and continuum states.[3]

example of this kind of spectra is shown in Fig. 2;[3] this is for neutral helium in an afterglow of a pulsed discharge. The continuation property of intensities is clearly seen. Figure 3 shows a Boltzmann plot of the populations in the discrete states and in the *continuum states.* It may be understood that the straight line shows the Boltzmann distribution of the electrons with which we filled the state density as mentioned above. These spectral lines and continuum are, of course, unpolarized.

**Anisotropic velocity distribution**

As an extreme case of anisotropic velocity distributions of electrons, we take a group of electrons travelling only in the $z$-direction; the direction may be positive or negative and there may be a distribution of speeds: *i.e.*, the one dimensional distribution. We remember the wavefunction of atoms, hydrogen for example, in quantum mechanics. A wavefunction consists of the radial function and the angular function, and the latter is given by a spherical harmonics. It is noted that the latter is common for the discrete states and the continuum states. Our electrons having the directional velocities are interpreted as $m_l$=0 electrons, where $m_l$ stands for the projection of the orbital angular momentum $l$ of this electron with respect of the proton onto the quantization axis, *i.e.*, $z$-axis.

We now consider radiative recombination of these electrons into the ground state. For the purpose of simplicity we neglect the presence of the electron spin: the total angular momentum $J$ is equal to the orbital angular momentum. This is equivalent to consider transitions to the heliumlike ground state having $J = 0$.

Figure 4 shows the Kastler diagram for a transition from the $J = 1$ level to the $J = 0$ level. The transition without a change in the angular momentum emits the $\pi$ polarized

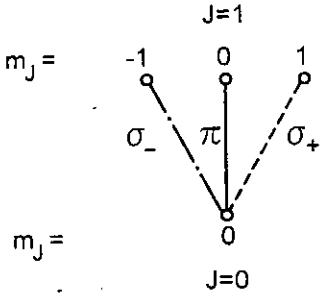


Fig. 4. The Kastler diagram for transition $J = 1 \rightarrow J = 0$.

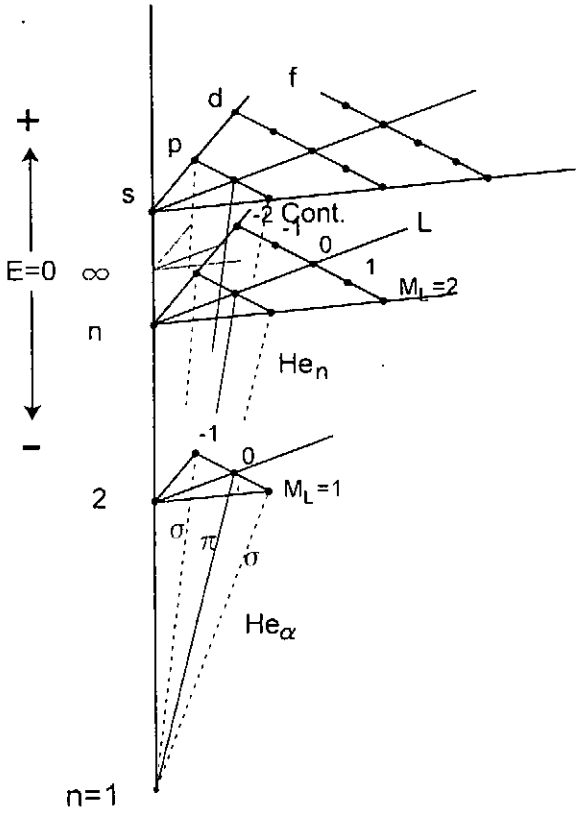


Fig. 5
Kastler diagram for the resonance-series lines and recombination continuum.

light and the transitions with a change by a unit angular momentum emit the $\sigma$ polarized light. Figure 5 shows *a three dimensional Kastler diagram* for the series lines and the recombination continuum. It is obvious that the recombination continuum for our electrons is $\pi$ polarized. From the continuation of various properties across the ionization limit, we may expect that this polarization property continues down to the higher members of the

resonance series lines. This expectation may be supported by the fact that the *shape* of the radial wavefunction of the discrete states gradually changes with $n$, the principal quantum number of the level, and it continues to the continuum Coulomb wavefunction. If we assume this, we come to the conclusion that, for high-lying excited state, only the $m_l$=0 magnetic sublevels should be populated, while other sublevels are unpopulated under our anisotropic condition.

**Population mechanism of the rydberg levels**

We return to the plasma with the Mawell distribution electrons. We are considering the recombining plasma. Figure 6 shows the schematic picture of the flows of electrons in

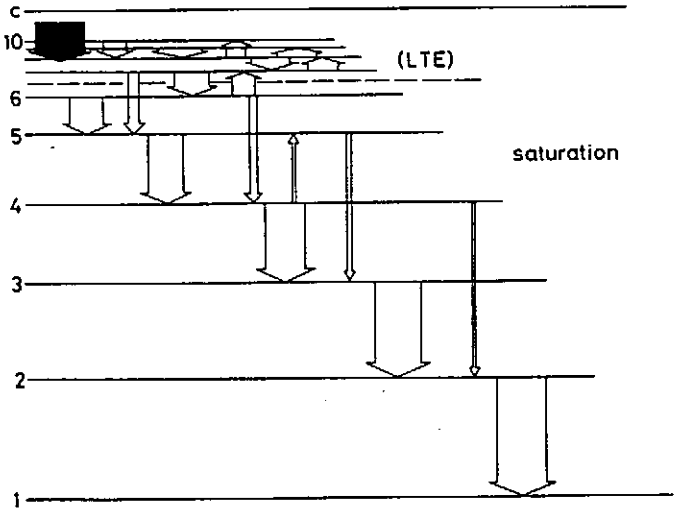


Fig. 6
Dominant flows of electrons in the energy level diagram of hydrogen in recombining plasma.[4]

the energy level diagram of hydrogen atoms in the plasma. For high-lying levels the population is controlled by the collisional transitions, deexcitation and excitation, between the adjacent levels. It should be noted that three-body recombination to and ionization from an excited level, which connect *directrly* this level with the conninuum electrons, never play any important role. These processes ensure the Saha-Boltzmann populations of these levels *as a whole*.

The above observation suggests that, in our anisotropic case, the population distribution in the plane of the three dimensional Kastler diagram is determined by electron collisions, and the directional collisions would lead to the peaked distribution on the $m_l$=0 line.

**Monte Carlo calcuation**

In order to examine whether the above conclusion is correct or not, we perform a Monte Carlo calculation of the electron collisions with excited atoms in the classical picture. Our objective is two-fold: 1. To see whether, by the directionl collisions, there is any tendency for the populations to move to the central line on a plane for rydberg states in Fig. 5. 2. Ionization may take place in some cases of collisions. When we reverse the direction

of time, this process is three-body recombination. Thus, from the examination of the ionizing collision process, we may be able to obtain some idea concerning the three-body recombination of the electrons having an anisotropic velocity distribution.

We take as an example a hydrogen atom with $n$ = 10, and shoot this atom with an electron with the speed of 0.2 au from the minus $z$-direction. This situation corresponds to the collision system with the excess energy of 0.41 eV. We follow the trajectories of both the electrons with time, where the proton is fixed at the origin. Since we treat the system classically, the angular momentum of the atomic orbit is expressed by the Bohr-Sommerfeld azimuthal quantum number $k$ in place of $l$. We perform a calculation for various impact

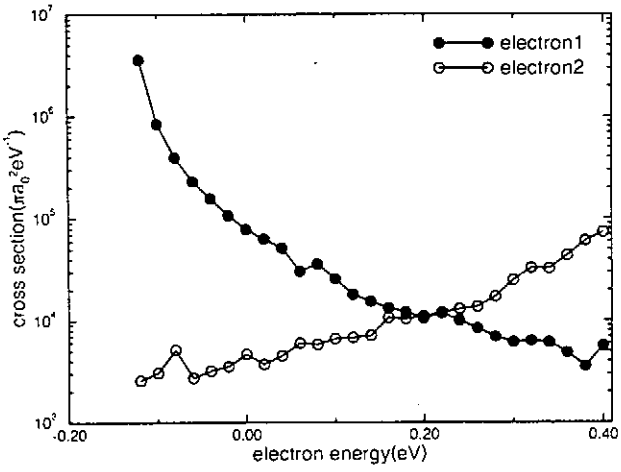


Fig. 7
The final energy of electron 1 which was the atomic electron in excited state before collision.

parameters and various relative phases of the electrons over $10^5$ times. Figure 7 shows the excitation and ionization cross section per unit energy interval for the initial atom state with $k$ = 6 and $m_l$ = 3. The negative energy part shows excitation, and the positive part ionization. It is seen that the cross section per energy interval continues smoothly from

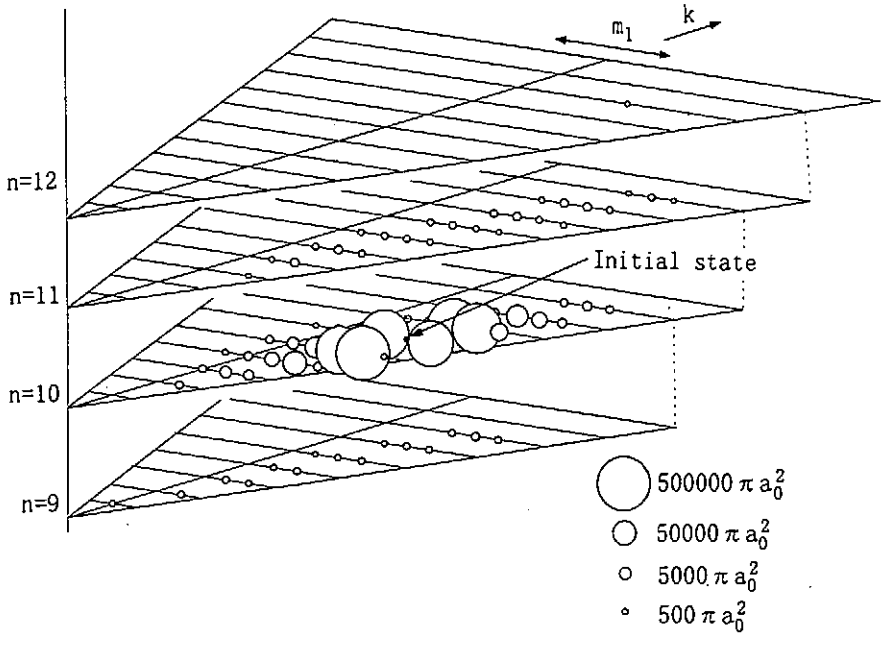


Fig. 8. The final state distribution by directional collisions.

excitation to ionization. It is noted that the conventional ionization cross section corresponds to the integration of the *cross section* for electron 1 over the positive energies.

Figure 8 shows the cross section for inelastice and elastic collisions, here we have *quantized* the classical final states into the states having the integer quantum numbers. The cross section value is expressed with the volume of the sphere placed on each point. No tendency is seen for the populations to move towards the central region.

Figure 9 shows the distribution of the relative angle of the directions of the two electrons in the case of ionization. If there were no angular correlation, the curve should be on the dotted line. In this figure the angular distribution for the case of excess energy of 0.06 eV is also shown. It may be noted that two electrons travelling in the same direction

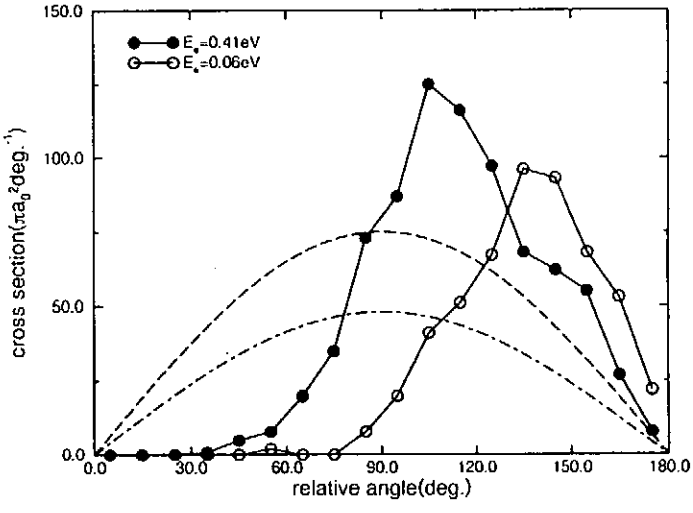


Fig. 9
Relative angle of outgoing electrons after ionizing collisions.

cannot make three-body recombination.

It may be noted that our present assumption of a classical orbit for the atomic electron is a rather poor approximation to the real quantum wavefunction. If we perform more realistic calculation the above conclusions may be modified to a certain extent.

**References**

[1] H. Yoneda, N. Hasegawa, S. Kawana and K. Ueda, Phys. Rev. E **56,** 988 (1997).
[2] I. Shimamura and T. Fujimoto, Phys. Rev. A **42**, 2346 (1990).
[3] A. Hirabayashi, Y. Nambu, M. Hauo and T. Fujimoto, Phys. Rev. A **37,** 77 (1988).
[4] T. Fujimoto, J. Phys. Soc. Japan **49**, 1569 (1980).

**Interpretation of line polarization measurements of a vacuum spark plasma.**

F. Walden, A. Urnov*, and H.-J.Kunze

Ruhr-Universitaet Bochum, 44780 Bochum, Germany *P.N.Lebedev Physical Institute of the Russian Academy of Sciences, 53 Leninski prospect, 117924 Moscow, Russia

**Abstract.**

Polarization measurements on AlXII ion lines emitted from micropinches in vacuum spark plasmas were carried out for the first time with the help of a double intensity ratio technique. A value of 0.12 was obtained for the polarization degree of the resonance line. The interpretation of the experimental data was made using a model which includes anisotropic non-thermal electrons. Parameters of the energy spectrum and of the anisotropy of the electrons as well as a relative density of non-thermal electrons of about 1% were obtained. The results show that X-ray line polarization spectroscopy is a powerful method for studying non-Maxwellian phenomena in hot dense plasmas.

## I. INTRODUCTION

During the last decade X-ray line polarization spectroscopy (XRLPS) became a subject of growing interest of both experimentalists and theoreticians [1,2]. Aside from a fundamental importance such investigations have been appreciated from the point of view of spectroscopic diagnostics. Measurements of the polarization state of X-ray line emission provide important information in addition to that which is usually derived from the spectra of hot plasmas: they make it possible to study the role of an anisotropic non-Maxwellian part of the distribution function in that range of the electron velocities which is relevant to the formation of the spectra . Up to now two successful polarization experiments have been carried out on hot high-density plasmas: on a Z-pinch [3] and on a laser-produced plasma [4] which demonstrated the potentials of the XRLPS methods. The present paper reports the results of polarization measurements of the AlXII resonance line emitted from micropinches in a vacuum spark plasma and their interpretation by means of an anisotropic non-thermal electron model consistent with the spectral data. Micropinches produced in vacuum spark discharges represent point sources of extraordinary brightness and thus offer unique possibilities for spectroscopic studies of highly charged ions as well as for applications. A knowledge on non-Maxwellian phenomena in these plasmas is important for the understanding of the energy transport and of the dynamics of the plasmas.

## II. POLARIZATION MEASUREMENTS

### 1. Experimental technique

The polarization degree P defined as the ratio of flux intensity of polarized photons ($I_p$) to the total intensity (I) is usually expressed through the Stokes parameters $\eta_i$ ($i = 1, 2, 3$). Lines emitted from an axially symmetric aligned atomic system characterized by unit vector $\mathbf{n}$ are linearly polarized with $\eta_1 = \eta_2 = 0$ and $\eta_3$ defined with respect to the axis chosen in $(\mathbf{k}, \mathbf{n})$-plane perpendicular

to the photon wave vector **k** through itensities of photons polarized parallel and perpendicular to this axis [5]. The degree of polarization P is equal to $|\eta_3|$. The parameter $\eta_3$ is a function of the angle $\theta = (\mathbf{k}, \mathbf{n})$ characterizing the direction of the line emission with respect to the axis **n**. For $\theta = 90^0$ its sign indicates the orientation of the electric vector **E** parallel (+) or perpendicular (-) to **n**.

The Stokes parameter $\eta_3(90^0)$ - its sign and an absolute value $P_0 = |\ \eta_3\ |$ , depends on the type of transition and on the polarization momenta of the M-states determined by the electron DF and by characteristics of elementary processes in the plasma. Measurements of this parameter for spectral lines provide a diagnostic tool for a quantitative analysis of the departure of the electron distribution function from a Maxwellian one.

In the present work a technique was used [6] which is based on measuring a double line intensity ratio defined as:

$$(a/b, \varphi) = \frac{i(a/b,\varphi)}{i(a/b,0)}; \qquad i(a/b, \varphi) = \frac{I(a.\varphi)}{I(b,\varphi)}; \qquad = (P_0(a), P_0(b), \varphi) \qquad (1)$$

where $i(a/b, \varphi)$, $i(a/b, 0)$are the intensity ratios for lines a and b in two spectra obtained by Bragg crystals with two orientations of the incidence planes with the angle $\varphi$ between them. Changing by means of rotation of the crystal around the line of sight the dependence of on $\varphi$ can be measured. The ratio of polarization degrees $P_0(a)/P_0(b)$ could be then obtained with the help of a fitting procedure. The value thus obtained depends on the parameters of the non-thermal electrons within the suggested model for the emitting plasma.

**2. Set-up description**

The vacuum spark discharge has been described in Ref.[7]. Two crystal spectrographs in Johann geometry were employed; one system was stationary, the plane of incidence of the second one was rotated around the line of observation. For the present studies ADP crystals were installed which had a 2d-spacing of 10.648 Angstrom. The spectra were recorded on film Kodak DEF 392.

## III. INTERPRETATION OF THE RESULTS

**1.Formulation of the model**

Our model for the plasma source assumes axial symmetry of the electron distribution function in the direction of a unit vector **n**, chosen along the Z-axis of quantization. Emitting ions shall be in a quasi-steady-state condition and are to be excited by collisions with unpolarized electrons characterized by a distribution function $f(\mathbf{v}; T)$ of the form:

$$f(\mathbf{v}; T) = (1 - n_{nt}) f_{th}(\varepsilon; T) + n_{nt} f_{nt}(\varepsilon, \alpha) \qquad (2)$$

where the first term $f_{th}(\varepsilon; T)$ refers to the thermal (Maxwellian) part and the second one, $f_{nt}(\varepsilon, \alpha)$ describes a non-thermal anisotropic distribution characterized by a pitch angle $\alpha$ and normalized as follows:

$$f_{nt}(\varepsilon; \alpha) = f_{nt}(\varepsilon) f(\varepsilon, \alpha); \quad \int_0^\infty f_{nt}(\varepsilon) d\varepsilon = 1; \quad 2\pi \int_{-1}^{1} f(\varepsilon, \alpha) d\cos\alpha = 1; \int_0^\infty f_{th}(\varepsilon; T) d\varepsilon = 1 \quad (3)$$

and the factor $n_{nt}$ :

$$n_{nt} = N_{nt}/N_e; \quad N_e = N_{th} + N_{nt} \tag{4}$$

is the relative density of nonthermal electrons ($n_{nt} \ll 1$).

In our model calculations the distribution function of the non-thermal electrons as proposed by Haug [8] is used:

$$f(\varepsilon, \alpha) = \frac{a+1}{2\pi}(\cos\alpha)^a \theta(\pi/2 - \alpha); \qquad a = \varepsilon/\varepsilon_0 \tag{5}$$

where $\varepsilon_0$ is the parameter characterizing the degree of anisotropy at different energies and $\theta(x)$ is the Heaviside step-function. The degree of anisotropy could be also characterized by the averaged with (5) pitch angle $\alpha_0 = \alpha_0(a)$.

The degree of polarization $\overline{P}_0$ at the angle $\theta$ =90$^0$ for lines excited by anisotropic electron beams is expressed as shown in [9] through the cross-sections for excitation of the $M_J$ -states averaged over the distribution function (1) with $n_{nt}$=1. For the resonance (w) and intercombination (y) lines of [He] ions it is given by

$$\overline{P}_0 = \lambda \frac{\langle v\sigma_0(\varepsilon,\alpha)\rangle - \langle v\sigma_1(\varepsilon,\alpha)\rangle}{\langle v\sigma_0(\varepsilon,\alpha)\rangle + \langle v\sigma_1(\varepsilon,\alpha)\rangle}; \qquad \lambda = sign\ \overline{\eta_3}(90^0) \tag{6}$$

where $\sigma_i(\varepsilon, \alpha)$ are the excitation cross-sections for $M_J$ -states relative to the quantization axis rotated on the angle $\varphi$ against the vector **n**. Using the general transformation properties for the cross-sections due to rotation of quantization axis $\overline{P}_0$ can be expressed through the degree of polarization of a unidirectional beam $\widetilde{P}_0$ as follows:

$$\overline{P}_0 = \frac{3\widetilde{P}_0}{3 - \widetilde{P}_0(1-\beta)} \tag{7}$$

where the parameter $\beta$ is defined as

$$\beta = \frac{\int v[\sigma_0(\varepsilon) - \sigma_1(\varepsilon)] f_{nt}(\varepsilon) \frac{a}{a+1} d\varepsilon}{\int v[\sigma_0(\varepsilon) - \sigma_1(\varepsilon)] f_{nt}(\varepsilon) d\varepsilon} \tag{8}$$

For a plasma the cross-sections have to be averaged over the distribution function (2) including the Maxwellian part, and other processes of the population of M-states aditional to direct electron impact excitation should be taken into account. Assuming that this population has isotropic character the polarization of lines under study is related to the value from (6) by means of

$$P_0 = \frac{3\overline{P}_0 g}{3 - (1-g)\overline{P}_0}; \qquad g = \frac{\langle v\sigma\rangle_{nt}}{tot} \tag{9}$$

Here $\langle v\sigma\rangle_{nt}$ is the rate of excitation by nonthermal electrons summed over all M-states and $_{tot}$ is the total rate of excitation of the J-level.

As is seen from eqs (6)-(9) there are two factors $\beta$ and g that lead to a decreasing of the $\overline{P}_0$ value. The first one is connected with the width of anisotropic function characterized by $a$ or the averaged pitch angle $\alpha_0$ and the second depends on the relative contribution of non-thermal electrons to the total population of J-level.

**2. Polarization calculations.**

To perform the calculations of the line polarization degree excited by a unidirectional electron beam as well as the parameter $\beta$, the excitation cross-sections for the M-components were obtained in the Coulomb- Born-Exchange approximation with the help of the ATOM code (see [9]). The results of calculations of $P_0$ for a monoenergetic beam agree to within 5% with those obtained in Ref.[4]

employing the distorted wave approximation. For calculations of the g-factor the collisional-radiative model described in [10] was used. In addition to direct electron impact excitation, cascades from excited states, recombination including dielectronic one, resonance scattering contribution, and ionization processes leading to the formation of the w- and y-line were taken into account.

For Al ions with a nuclear spin I=5/2 the depolarization effect of hyperfine interaction should be accounted for. As was shown in the paper [4] this effect considerably decreases (more than 5 times) the polarization of the y-line but having practically no influence on the w-line. An additional reduction of the polarization degree of the intercombination line is caused by a pumping from the metastable triplet states with the principle quantum number n=2 due to electron-ion inelastic collisions in a plasma with high electron density. This excitation is caused by the bulk of the isotropic Maxwellian electrons and totally suppresses the polarization of y-line.

**3. Self-consistent model**

Fitting of the angular dependence of the measured double intensity ratio by means of eq. (1) provides the determination of the polarization degree for the w-line. Thus for the averaged over 5 micropinches the value of $P_0 = 0.12$ was obtained. To derive the parameters of the distribution function of the anisotropic electrons a detailed self-consistent analysis of the spectra has to be carried out.

We consider in addition to the reference w and y lines also the groups of their [Li] ion satellites identified in the spectra: j+k, q+r, a+d+c, and those radiated from 1s2p3l states. We will denote them through j,q,a, and 3l, respectively. First we consider changes in their intensities relative to intensities of lines recorded with the fixed reference spectrograph: 3l/j, q/j, q/a, j/y, and y/w. All these ratios show variations which could be naturally connected with changes of plasma parameters. The most noticeable change (up to 2 times) is developed for 3l/j ratio while the others vary to within 20% of the averaged values. Another remarkable fact is that these variations are correlated with each other - an increase in one ratio is connected with an increase in all others. It is also important to emphasize that neither the averaged values of aforementioned ratios (which are equal to 0.7, 0.73, 0.9, 0.26, 0,38, respectively) nor can their variations be described by quasi-steady-state or transient (ionizing) thermal models usually used in the analysis of spectra..

The 3l/j ratio sensitive only to the electron temperature indicates values of T of about 1.5-2 times larger than those provided by the j/y ratio (about 600eV) even if accounting for possible reduction of the y-line due to the high density effect. To explain the y/w ratio one needs to assume an electron density of about 3 $10^{20}$ $cm^{-3}$ . At such densities it is also impossible to interpret a high value of the j/y ratio in the recombination regime of the plasma since to explain a high value of the q/j satellites it is necessary to assume a very low ionization temperature of about 150 eV. In additions, the variations within thermal models remain unclear.

On the other hand assuming a non-thermal model with the presence of a small admixture of about 1% of anisotropic nonMaxwellian electrons allows the interpretation of all features in the spectra mentioned above as well as of the effect of w-line polarization. The enhancement and variations in the 3l/j ratio could be naturally attributed to such electrons with allow cut-off energy close to the excitation energy of n=3 satellite group, i.e. of the order of E =1.4 keV. The decrease of the y/w ratio is then connected to a preferential excitation of the singlet line with respect to the triplet lines due to the differences in the energy dependence of the excitation cross- sections due to electron impact. The q/j and q/a ratios become also in quantitative agreement while suggesting an ionization temperature of about 250 eV.

The electron temperature being reduced to the value of about 350eV come close to the ionization temperature. Such a difference in these temperatures is quite natural since the electron density in this model should be less then $10^{20}$ $cm^{-3}$ and therefore the ionization equilibrium can lag behind the electron temperature.

Assumptions of the model described above make it possible also to derive the parameters of the non-thermal electrons from the polarization measurements by means of eqs (6)-(8). Calculations show that for explaining the measured value of polarization of the w-line it is necessary to assume the average pitch angle near the maximum of the energy of the non-thermal spectrum of order of $\alpha_0 \approx 50^0$.

## IV.CONCLUSION.

The application of X-ray polarization spectroscopy in the investigation of micropinches in vacuum spark plasmas made it possible to reveal the presence of anisotropic nonMaxwellian electrons. A polarization degree of $P_0$=0.12 for the resonance AlXII ion line was derived. The analysis of the spectra provided information for the formulation of a self-consistent model. Thus the parameters of the energy spectrum and of the anisotropy of the beam in the plasma were obtained.

Acknowledgments. Authors are greatly thankful to Dr. J. Dubau for a participation in the atomic calculations and detailed discussions. The work was supported by the grants of INTAS-RFBR 95-875, the RFBR 97-02-16919 and the DFG.

**References**

[1] Fujimoto T, and Kazantsev S A, 1997, Plasma Phys.Control.Fusion. 39,1267 .

[2] Urnov A, 1998, "Historical overview of PPS". Present proceedings.

[3] Veretennikov V A, Gurii, A E, Dolgov A N, Korneev V V, and Semenov O G, 1987, Russian: Pis'ma v Zh.Exp.Teor.Fiz. 47, 29.

[4] Kieffer J C, Matte J P, Chaker M, Beaudon Y, Chien C Y, Coe S, Mourou G, Dubau J, and Inal M K, 1993, Phys.Rev.E. 48, 4648.

[5] Blum K, 1981, Density matrix theory and applications, NY, London, Plenum Press.

[6] Zhitnik I A, Korneev V V, Krutov V V, Oparin S N, and Urnov A M, 1987, Russian: Trudi FIAN, 179,39. English translation: Proceedings of P N Lebedev Physical Institute (N G Basov, edt). v. 179 (Sobelman I I, edt), p.51, Nova Science publ. co., New York.

[7] Schulz A, Hebach M, Kunze H-J, Rosmej F R, and Walden F, 1994, J.Quant. Spectrosc. Radiat. Transfer 51, 341.

[8] Haug E, 1981, Solar Phys. 71, 77.

[9] Vinogradov A V, Urnov A M, and Shlyaptseva A S, 1989, Russian Trudi FIAN, 195, 89. English translation: Proceedings of the Lebedev Physics Institute of Russian Academy of Sciences Vol.192, edited by I.I.Sobelman (Nova Science, Commack, NY, ) p.93.

[10] Beigman I L, Oparin S N, Urnov A M, ibid. p.51.

# Alignment creation in atomic ensembles by elastic electron scattering; the case of $^{138}Ba$ (...6s6p $^1P_1$) atoms

S. Trajmar[†◆], I. Kanik[†‡], M. A. Khakoo[‡], L. R. LeClair[†o], I. Bray[*], D. Fursa[*] and G. Csanak[x]

† *California Institute of Technology, Jet Propulsion Laboratory, Pasadena, CA 91109, USA*

◆ *California Institute of Technology, Division of Chemistry and Chemical Engineering, Pasadena, CA 91109, USA*

‡ *California State University, Department of Physics, Fullerton, CA 92634, USA*

* *Electronic Structure of Materials Centre, The Flinders University of South Australia, G.P.O. Box 2100, Adelaide 5001, Australia*

x *University of California, Los Alamos National Laboratory, Los Alamos, NM 87544, USA*

o *Present address: MPB Technologies, Pointe Claire, Quebec H9R 1E9, Canada*

The questions whether elastic electron scattering by initially isotropic atomic ensembles can lead to alignment and to what degree, have been raised recently in connection with plasma polarization spectroscopy by Petrashen et al. (1984), Dashevskaya and Nikitin (1987), Fujimoto (1996) and Kazantsev (1996). For a discussion of plasma polarization spectroscopy, see Kazantsev and Henoux (1995). Until now, there have been no experimental data available to answer these questions and calculations based on various scattering approximations have failed to address these issues.

Here, we describe some of our results from a joint experimental and theoretical program concerning elastic electron scattering by $^{138}$Ba (...6s6p $^1P_1$) atoms. From the experimental results, we derived various scattering parameters and magnetic sublevel specific differential elastic scattering cross sections at impact energy ($E_0$) of 20.0 eV and at scattering angles ($\theta$) of 10°, 15°, and 20°. The same parameters and cross sections were calculated by the convergent close coupling (CCC) approximation and compared to the experimental results. An excellent agreement, found for the two sets of data, gave us confidence in the CCC method and allowed us to extend the angular and energy ranges for the purpose of generating integral elastic scattering cross sections needed for the deduction of the alignment creation cross sections. The integral cross sections needed here are related to the process $^{138}Ba$ *(...6s6p* $^1P_1$*; isotr)* + $e^-(E_o)$ → $^{138}Ba$ *(...6s6p* $^1P_1$*;* $M_f$*)* + $e^-(E_o)$ and will be denoted as $Q(M_f)$ where $M_f$ refers to the final magnetic sublevel quantum number. The alignment creation cross section, $Q^{[2]}_{CR}$, for this case is given by Kazantsev et al. (1988) as:

$$Q^{[2]}_{CR} = (2/3)^{1/2}[Q(M_f = 1) - Q(M_f = 0)].$$

Calculations were carried out at $E_o$ = 2.8, 20.0 and 97.8 eV in the full 0° to 180° angular range in one degree steps and the results indicate that alignment can be created to a significant degree by elastic electron scattering.

In the following, we are going to describe briefly the experimental and theoretical methods, show the comparison of some experimental and theoretical results and present the values obtained for $Q(M_f)$ and $Q^{[2]}_{CR}$ as well as several other integral elastic cross sections for the purpose of comparison.

The experimental arrangement has been described earlier by Zetner et al. (1990). A collimated atomic Ba (naturally occurring isotopic mixture) beam was crossed at 90° by a nearly monoenergetic ($\Delta E_{1/2} \approx 0.08$ eV) electron beam. The interaction region was illuminated by a linearly polarized laser beam which was located in the scattering plane and was produced from a ring laser, operating in single mode. The laser wavelength was tuned to excite the $^{138}$Ba (...6s$^2$ $^1S_o$ → ...6s6p $^1P_1$) transition. (See Fig. 1 for the energy level scheme.) The elastic scattering signal was measured at a fixed ($E_o$, $\theta$) for fixed laser geometries, with respect to the laboratory frame ($\theta_v$, $\phi_v$), as a function of the linear polarization angle ($\psi$) with respect to the scattering plane.

The measured count rates in the elastic scattering experiment include contributions from background, from elastic scattering by ground state atoms of all isotopes, and from elastic scattering by coherently excited $^1P_1$

($I_{cP}^{el}$) and cascade populated $^3D_2$ and $^1D_2$ metastable $^{138}Ba$ atoms. In order to assure identical experimental conditions for the modulation measurements, to separate $I_{cP}^{el}$ from other contributions to the measured signal and to obtain various parameters and absolute cross sections from the experiments, we needed to carry out 116 measurements for each fixed ($E_0$, $\theta$) case. These measurements involved the inelastic ($^1S_0 \rightarrow {}^1P_1$), the superelastic ($^1P_1 \rightarrow {}^1S_0$) and the elastic scattering channels. Scattering intensities for various combinations of the Ba beam and laser beam turned ON and OFF, at two laser positions (laser in the scattering plane and laser displaced by about 4 mm parallel to the scattering plane upstream of the Ba beam) and for four laser geometries ($\theta_v = 45°$ and $90°$, both with $\phi_v = 0°$ and $180°$) were measured and the modulation of the elastic and superelastic scattering intensities as a function of $\psi$ was determined. Normalization of the $I_{cP}^{el}(\psi)$ signal to the corresponding differential cross section, $DCS_{cP}^{el}(\psi)$, was achieved by measuring the ratio of this elastic scattering signal to the signal associated with ($^1S_0 \rightarrow {}^1P_0$) inelastic scattering and utilizing the derived population fractions and the ($^1S_0 \rightarrow {}^1P_0$) inelastic differential cross section values of Wang et al. (1994).

At this stage, we have [for a fixed ($E_0$, $\theta$) case ] a modulation equation of the type

$$DCS_{cP}^{el}(\psi) = \tfrac{3}{4}\, DCS_{P}^{el} \{ A + B \cos 2\psi \}$$

for each laser geometry (Zetner et al., 1990). The values of A and B were obtained from least squares fitting of the experimental data. They contain factors related to the laser geometry and parameters related to the physics of the electron-atom collision. Measurements with several laser geometries were needed to obtain these parameters and various cross sections. We denote here the differential cross sections associated with scattering processes where the initial atomic states are prepared by coherent excitation to the $^1P_1$ state with a particular laser geometry and polarization as $DCS_{cP}^{el}(\psi)$. For differential cross sections associated with processes where the initial and/or final magnetic sublevel is specified (or averaged-over incoherently), we use the notation $DCS_P^{el}(M_i, M_f)$, $DCS_P^{el}(M_i = M)$, $DCS_P^{el}(M_f = M)$ and $DCS_P^{el}$. Omission of $M_i$ and/or $M_f$ implies averaging (summation) over those magnetic sublevel quantum numbers. M can take the values of -1, 0 or +1. (We select for the quantization axis for the magnetic sublevel cross sections the incoming electron momentum vector.) Since the spin of the scattering electrons was not selected or detected in the present measurements, averaging over initial and summation over final spin quantum numbers are always assumed.

The modulation equation can be used in two different ways: (i) to obtain EICP's and differential cross sections for the hypothetical "inverse" process, i.e. for elastic scattering by an isotropic, incoherent state of $^{138}Ba$ (...6s6p $^1P_1$) atoms, (ii) to obtain collision parameters and differential cross sections for elastic scattering by the coherently prepared $^{138}Ba$ (...6s6p $^1P_1$) atoms.

For evaluation of the modulation equations in terms of the hypothetical "inverse" process (based on the

theory of Macek and Hertel,1974), we have for the modulation coefficients (Zetner et al. 1990):

$$A = 1 + \cos^2\theta_n + \lambda(1-3\cos^2\theta_n) + (\lambda - 1)\cos\varepsilon\sin^2\theta_n + \kappa\sin 2\theta_n\cos\phi_n$$

$$B = (3\lambda - 1)\sin^2\theta_n + (1 - \lambda)\cos\varepsilon(1 + \cos^2\theta_n) + \kappa\sin 2\theta_n\cos\phi_n$$

where

$$\kappa = 2\sqrt{\lambda(1-\lambda)}\cos\chi = 2\sqrt{\lambda(1-\lambda)}\cos\Delta\cos\tilde{\chi}\ .$$

In the present experiments, $\theta_n = \theta_v + \theta\cos\phi_n$ and for scattering to the left we have $\phi_v = 180°$ and $\phi_n = \phi_v - \pi = 0°$ and for scattering to the right we have $\phi_n = \phi_v = 180°$. The modulation equations involve the four EICP's ($\lambda$, cos $\varepsilon$, cos $\Delta$ and $\tilde{\chi}$) as defined by da Paixao et al.(1980) and applied to the Ba superelastic scattering by Zetner et al. (1990). From our laser-in-plane measurements we can extract only $\lambda$, cos $\varepsilon$ and $\kappa$. These EICP's can be obtained by solving any set of three equations defining A or B for laser geometries with $\theta_v = 45°$ and 90°. There are 16 meaningful such combinations, each yielding a set of EICP's. We took the average of these 16 sets as our experimental values. Definition of these EICP's and their relations to various cross sections and scattering amplitudes for a ($^1S_0 \rightsquigarrow {}^1P_1$) process is given by Zetner et al. (1990). The only difference here is the generalization from the ($^1S_0 \rightsquigarrow {}^1P_1$) to the ($^1P_1 \rightsquigarrow {}^1P_1$) transition which requires averaging over the initial magnetic sublevels of the $^1P_1$ level. From $\lambda$ and $DCS_P^{el}$, we obtained $DCS^{el}(M_f = 0)$. From $DCS^{el}(M_f = 0)$ and $DCS_P^{el}$, the $DCS^{el}(M_f = 1)$ values were calculated. $DCS_P^{el}$ was obtained by taking the average of $DCS_{\alpha P}^{el}(\psi_m)^+$ and $DCS_{\alpha P}^{el}(\psi_m)^-$ where $\psi_m$ is the polarization magic angle satisfying the condition $\cos 2\psi_m = 1/3$ and the superscript +(-) refers to $\phi_n = 0°(180°)$.

The present $e^-$-Ba scattering calculations have been performed by using the CCC method in the non-relativistic LS-coupling framework (see Fursa and Bray, 1997 and 1998 for details). In brief, the barium atom was considered to have two active valence electrons above an inert Hartree-Fock core. Phenomenological one-electron and two-electron polarization potentials have been added to account for the core polarization. Configuration-interaction (CI) expansions have been used to obtain the Ba wave functions. One electron orbitals have been obtained from the diagonalization of the $Ba^+$ Hamiltonian in the Sturmian (Laguerre) basis. This allowed us to obtain good description of the Barium discrete states and to achieve square-integrable discretization of the Ba continuum. All negative-energy states (relative to the $Ba^+$ ground state) and a large number of positive energy states (representing coupling to the ionization continuum) have been included in the CCC calculations.

The total number of states used in the present calculations was 115. They consisted of 14 $^1$S, 17 $^1$P°, 19 $^1$D°, 19 $^1$F°, 7 $^3$S, 9 $^3$P°, 9 $^3$D°, 9 $^3$F° and two each of $^{1,3}$P°, $^{1,3}$D° and $^{1,3}$F° states.

Selected values of the large set of the measured and calculated cross sections and parameters are shown in Figs. 2 and 3, respectively. The estimated experimental error limits for these quantities are 30% for the differential cross sections and $\lambda$ parameter and 40% for the cos $\varepsilon$ parameter.

In Fig. 2, three theoretical differential cross sections are shown over the full angular range and compared to the experimental results. The experimental and theoretical results agree well within the estimated experimental error limits. The values for these cross sections drop almost five orders of magnitude between 0° and 70°. It is clear from the present study that the cross sections at high scattering angles are very small and their measurement would be extremely difficult. Therefore, one will have to rely on the theoretical calculations in these regions. A "shoulder" with an inflexion point at around 35° and two deep minima at around 72° and 134° appear in the theoretical curves. The calculations show that the various $DCS_P^{el}$ ($M_i$, $M_f$) values differ by more than an order of magnitude but these differences are eliminated, to a large extent, in the averaging processes. The difference in $DCS_P^{el}$ ($M_f = 1$) and $DCS_P^{el}$ ($M_f = 0$) values, which determines the alignment creation cross section, is, however, significant at most scattering angles.

In Fig. 3 the EICP's, $\lambda$ and cos $\varepsilon$ are shown. Not surprisingly, very good agreement between experiment and theory is found for $\lambda$ since it represents the ratio of two cross sections which both show, separately, good agreement between experiment and theory. Somewhat less satisfactory is the agreement for cos $\varepsilon$. While no significant features appear in the $\lambda$ curve, the cos $\varepsilon$ curve shows a deep minimum at around 22° and two sharp maxima at around 72° and 135°. These maxima are associated with the deep minima in the $DCS_{\alpha P}^{el}$ ($M_f = 1$) which appear as the denominator in the definition of cos $\varepsilon$. The deviation of cos $\varepsilon$ from the value of unity for the theoretical curve is strictly due to the averaging over $M_i$ which causes the loss of coherence between the $M_f = 1$ and $M_f = -1$ scattering amplitudes. For the experimental value, some loss of coherence may also be due to spin-orbit coupling effects and this may account to some extent for the less satisfactory agreement between experiment and theory.

Considering the complexity of the experiments and the fact that the theoretical calculations neglect spin-orbit coupling effects, the general agreement between theory and experiment is surprisingly good for the $E_0 = 20$ eV, $\theta = 10°, 15°, 20°$ cases. This agreement indicates that extended scattering volume effects (see Zetner et al., 1990) are not important in the present measurements and that the CCC calculational scheme, used here, is applicable to elastic scattering by Ba ($^1P_1$) atoms. The rate of convergence and the importance of the ionization channels in our calculations were investigated by also performing calculations with 55 discrete states in the expansion. The results of these calculations were found to be in reasonably good agreement with those described here (which included 115 states and accounted for coupling to the target ionization continuum). The reason for this agreement is that the dipole polarizability for the Ba (6s6p $^1P_1$) state is dominated by the discrete spectrum.

The neglect of spin-orbit coupling in our calculations is justified by the good agreement between experiment and theory. The major effect of spin-orbit coupling in our case manifests itself in singlet-triplet mixing for the target atom. It is well-known, however, that the mixing coefficient for the $^3P_1$ LS term is small (see e.g. Bauschlicher Jr. et al. 1985).

With the assurance given by the good agreement between experiment and theory, we extended the CCC calculations to other scattering angles and impact energies to obtain the various integral elastic scattering and the alignment creation cross sections. Some of these cross sections are listed in Table I, which also shows for purpose of comparison $Q(M_i)$ values as well as experimental and calculated integral elastic scattering cross-sections for ground state Ba atoms at $E_o$ = 20 eV. This table shows that alignment can be created by elastic scattering and gives us some indication concerning the magnitude of the alignment creation cross section.

## Acknowledgments

The authors acknowledge the financial support by NSF, NASA, NRC and DOE. Support of the South Australian Centre for High Performance Computing and Communications is also acknowledged. We wish to express our gratitude to T. Fujimoto and S. A. Kazantsev for calling our attention to the question of alignment creation in elastic scattering and for valuable discussions. We also acknowledge important communications with P.W. Zetner and D.C. Cartwright.

## References


Bauschlicher Jr., C. W., Jaffe, R. L., Langhoff, S. R., Mascarello, F. G. and Partridge, H., 1985 *J. Phys. B,* **18,** 2147.

Dashevskaya E. I. and E. E. Nikitin, E. E., 1987 *Sov. J. Chem. Phys.*, **4** 1934.

Fujimoto, T. (private communication, 1996).

Fursa, D. V. and Bray, I. (to be published, 1998)

Fursa, D. V. and Bray, I., 1997 *J. Phys. B,* **30** 5895.

Kazantsev, S. A. and Henoux, J. C. Polarization Spectroscopy of Ionized Gases, Kluwer Academic Publishers, Dordrecht 1995.

Kazantsev, S. A. (private communication, 1996).

Kazantsev, S. A., Polinovskaya, N. Ya, Pyatritskii, L. N. and Edelman, S. A., 1988 *Sov. Phys. Usp.*, **31** 785.

Macek, J. and Hertel, I. V., 1974, *J. Phys. B,* 7 2173.

Paxio, F. J. de, Padial, N. T., Csanak, Gy. and Blum K. 1980 *Phys. Rev. Lett.*, **41** 749.

Petrashen, A. G, Rebane, V. N. and Rebane, T. K., 1984 *Opt. Spectrosc. (USSR),* **55** 492.

Wang, S., Trajmar, S. and Zetner, P. W., 1994 *J. Phys. B.*, **27** 1613.

Zetner, P. W., Trajmar, S. and Csanak, G., 1990 *Phys. Rev. A,* **41** 5980.

## Figure Captions

1. Energy level diagram for Ba. On the right hand side the isotopic and hyperfine structure of the ....6s6p $^1P_1$ level is shown with the energy scale in MHz units.

2. Elastic differential electron scattering cross sections for $^{138}$Ba ($^1P_1$) atoms at $E_0$ = 20 eV. Lines represent the results of CCC calculations. The corresponding experimental values are indicated by symbols. Experimental error limits are also shown.

3. The EICP's ($\lambda$ and cos $\varepsilon$) for elastic electron scattering by $^{138}$Ba ($^1P_1$) atoms at $E_0$ = 20 eV. • indicates the present experimental results with error limits, the lines are from the present CCC calculations.

Table I. Integral cross sections for elastic electron scattering by $^{138}Ba$ (...6s6p $^1P_1$) atoms (in $10^{-16}$ cm$^2$ units).

| | 2.8 eV | 20.0 eV | 97.8 eV |
|---|---|---|---|
| Q (1, 1) = Q (-1, -1) | 119.7 | 36.6 | 18.1 |
| Q (1, 0) = Q (-1, 0) | 2.0 | 0.74 | 0.054 |
| Q (1, -1) | 4.6 | 1.6 | 0.37 |
| Q (0, 0) | 89.3 | 28.5 | 14.7 |
| Q (0, -1) = Q (0, 1) | 1.2 | 0.62 | 0.054 |
| | | | |
| $Q(M_f = 0)$ | 31.1 | 10.0 | 4.9 |
| $Q(M_f = 1) = Q(M_f = -1)$ | 41.8 | 12.9 | 6.2 |
| | | | |
| $Q(M_i = 0)$ | 91.6 | 30.0 | 14.8 |
| $Q(M_i = 1) = Q(M_i = -1)$ | 126.3 | 39.0 | 18.5 |
| | | | |
| Q | 114.7 | 35.9 | 17.3 |
| $Q^{[2]}_{CR}$ | 8.7 | 2.4 | 1.0 |

$Q(^1S_0 \rightarrow {}^1S_0)$ at $E_0$=20 eV

Experiment [(a)]: 26.7
CCC calculation [(b)]: 29.4

(a) Wang et al (1994)
(b) Fursa and Bray (1997)

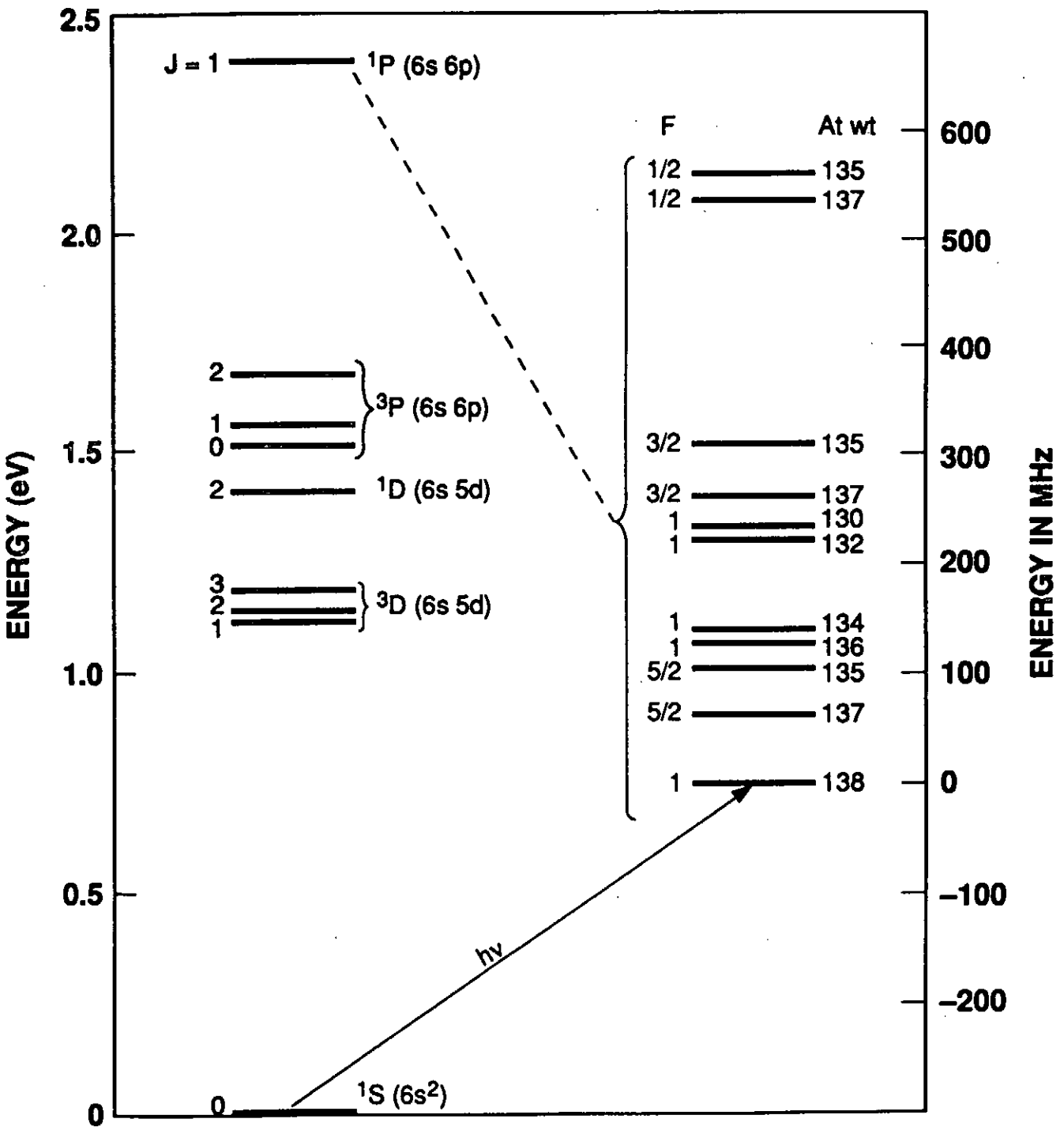
2.5
2.0
1.5
1.0
0.5
0
ENERGY (eV)
J = 1
1P (6s 6p)
2
1
0
3P (6s 6p)
2
1D (6s 5d)
3
2
1
3D (6s 5d)
0
1S (6s2)
hν
F
At wt
1/2
135
1/2
137
3/2
135
3/2
137
1
130
1
132
1
134
1
136
5/2
135
5/2
137
1
138
600
500
400
300
200
100
0
–100
–200
ENERGY IN MHz

Fig. 1

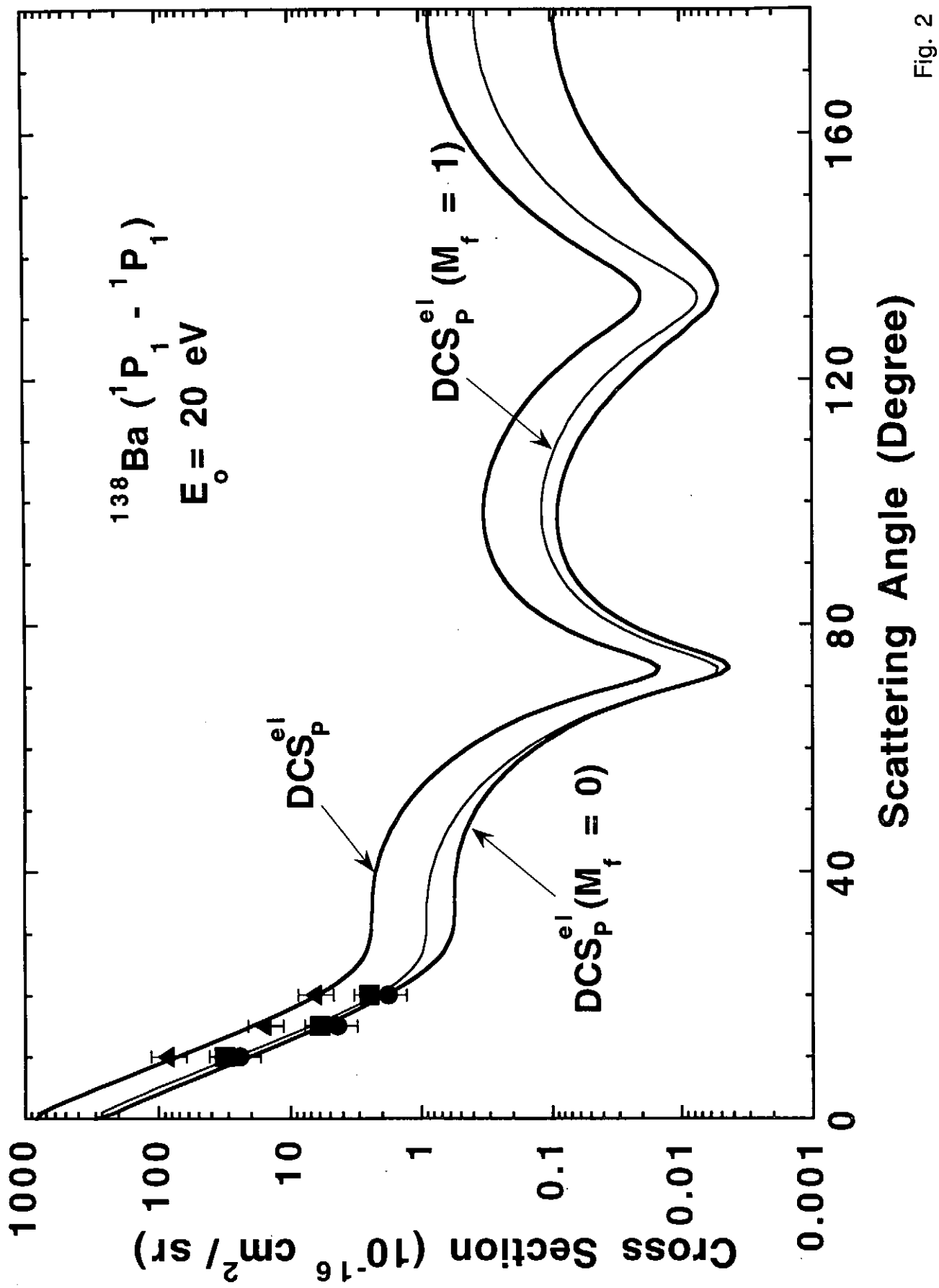
$^{138}Ba$ ($^1P_1$ - $^1P_1$)
$E_o$ = 20 eV
$DCS_P^{el}$
$DCS_P^{el}$ ($M_f$ = 1)
$DCS_P^{el}$ ($M_f$ = 0)
Cross Section ($10^{-16}$ $cm^2$/ sr)
Scattering Angle (Degree)
1000
100
10
1
0.1
0.01
0.001
0
40
80
120
160

Fig. 2

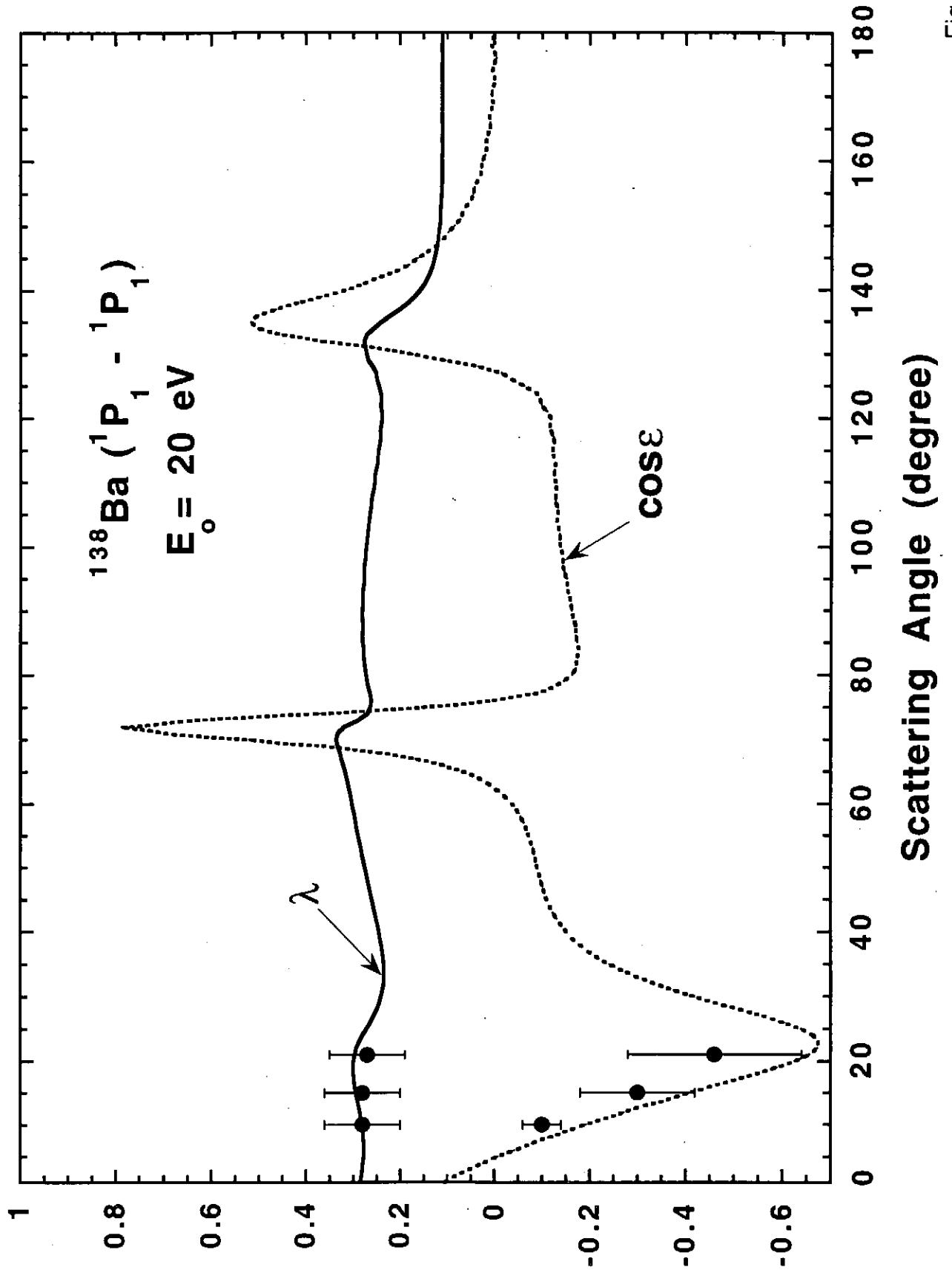
$^{138}$Ba ($^1$P$_1$ - $^1$P$_1$)
E$_o$ = 20 eV
λ
cosε
Scattering Angle (degree)
1
0.8
0.6
0.4
0.2
0
-0.2
-0.4
-0.6
0
20
40
60
80
100
120
140
160
180

Fig. 3

# Population Analysis for Atomic Cascade Decay Processes

Keiko Suto, Takashi Kagawa and Kaoru Futaba
Department of Physics, Nara Women's University, Nara 630-8506, Japan

**Abstract**

Down-stream cascade decay processes in atomic systems are analyzed by solving a coupled rate equation for which an analytical solution for a population in each excited state is obtained. Some typical numerical examples for populations to interpret the decay passes connecting to features of optical or electron spectra observed in various collision experiments are also given.

## 1. Introduction

Analysis of down-stream cascade decay processes from a highly excited state in atomic systems is important to explain optical or electron spectra observed in various experiments such as the beam-foil spectroscopy, ion-atom or ion-solid collision ones because the spectra contain physical informations such as a dominant decay pass or time-dependent populations in each upper state in the system. Populations for excited states in a decay process can be obtained by solving a coupled rate equation and be used not only to construct a feature of spectra observed but to make a decay model for a system under consideration. If accurate transition rates for all transitions related to decay streams in consideration in a system and initial populations in each excited states are known, time-dependent populations for any lower states can completely be estimated. On the other hand, using accurate transition rates and a set of time dependent intensities for selected spectra observed, it is also possible to obtain initial populations in each excited states. Especially for down-stream cascade decays an analytical solution of populations for the rate equation can be obtained [1,2].

Here we present an alternative analytical expression for the solution of a coupled rate equation by introducing *cascade coefficients* which give increment of the population for a state under consideration due to the transitions from upper states. These *cascade coefficients* can be calculated with a recursion formula for them.

Numerical results for populations in some typical down-stream decay processes in atomic systems are given. A possibility of obtaining initial populations from the cascade spectra is also discussed.

## 2. A solution of a coupled rate equation for down-stream cascade transitions

The population $N_k(t)$ for the $k$ state at time $t$ in each decay step can be obtained by

solving a coupled rate equations written as

$$\frac{dN_k(t)}{dt} = -\alpha_k N_k(t) + \sum_{m(>k)} \Gamma_{m\to k} N_m(t), \tag{1}$$

where $\alpha_k$ is a decay constant (inverse of the life time) for the $k$ state and $\Gamma_{m\to k}$ is a transition rate for the $m \to k$ transition from an upper $m$ state. $\alpha_k$ is a sum of transition rates for all transitions from the $k$ state under consideration to lower $l$ states given by

$$\alpha_k = \sum_{l(<k)} \Gamma_{k\to l}. \tag{2}$$

We also give an alternative analytic solution for the rate equation in Eq. (1) by introducing *cascade coefficients* described below. We start with $N_k(t)$ written as

$$N_k(t) = C_k(t) e^{-\alpha_k t}, \tag{3}$$

and rewrite Eq. (1) for $N_k(t)$ as that for the coefficients $C_k(t)$,

$$\frac{dC_k(t)}{dt} = \sum_{m(>k)} \Gamma_{m\to k} C_m(t) e^{\alpha_{km} t}, \tag{4}$$

where

$$\alpha_{km} = \alpha_k - \alpha_m. \tag{5}$$

Now we can write $C_k(t)$ in terms of *cascade coefficients* $a_{m,k}$ and an initial population $N_k(0)$ at $t = 0$ for the $k$ state in the following form,

$$C_k(t) = N_k(0) + \sum_{m(>k)} a_{m,k}(e^{\alpha_{km} t} - 1), \tag{6}$$

In order to obtain a recursion relation for *cascade coefficients* $a_{m,k}$, the coefficients $C_k(t)$ in Eq. (6) is inserted into Eq.(1). By using an initial condition for the uppermost state denoted by $p$ as

$$a_{p+1,p} = 0, \tag{7}$$

and

$$N_p(t) = C_p(t) e^{-\alpha_p t} = N_p(0) e^{-\alpha_p t}, \tag{8}$$

the equation for them is solved step by step starting from the uppermost $p$ state so that a recursion formula for $a_{m,k}$ is obtained in the form as

$$a_{m,k} = \frac{1}{\alpha_{km}} \left[ \Gamma_{m\to k} \left( N_m(0) - \sum_{j=m+1}^{p} a_{j,m} \right) + \sum_{j=k+1}^{m-1} \Gamma_{j\to k} a_{m,j} \right]. \tag{9}$$

If all the transition rates including $\Gamma_{m\to k}$ and initial populations $N_k(0)$ at $t = 0$ are given, *cascade coefficients* $a_{m,k}$ for the system are determined completely. Therefore the population $N_k(t)$ in an analytical form is obtained in terms of $a_{m,k}$ as

$$N_k(t) = \left( N_k(0) - \sum_{m=k+1}^{p} a_{m,k} \right) e^{-\alpha_k t} + \sum_{m=k+1}^{p} a_{m,k} e^{-\alpha_m t}. \tag{10}$$

This is an alternative analytical form of a solution for the rate equation for a down-stream decay in an atomic system among those reported before by other people [1,2].

## 3. Calculated results

Now we show numerical results for populations in typical three decay processes: The first one is populations due to radiative cascade decay transitions in hydrogen-like atoms and the second is populations for excited states in $Ne^{2+}$ produced through the Auger transition from a K-hole state in Ne and the last is those for hollow atomic states in Ar ions produced by collisions between $Ar^{17+}$ and a solid surface, where a multistep-capture-and-loss (MSCL) model is used.

### (a) Populations due to radiative cascade transitions in hydrogen-like atoms:

Because hydrogen-like systems are a basic model for atomic systems for which one can use exact values for physical quantities such as energies and transition rates, they are suitable to test the theory with various assumptions for the experimental situation. Here to see the difference of a time-dependent population for a lower state due to an initial population in a different higher state, we calculate the $N_{2p_{3/2}}(t)$ as a function of $t$ for hydrogen-like systems with $Z = 10$ when an initial population in one of the $n = 4$ states is set, that is, $N_{4s}(0) = 1$, $N_{4p_{1/2,3/2}}(0) = 1$, $N_{4d_{3/2,5/2}}(0) = 1$, $N_{4f_{5/2,7/2}}(0) = 1$, where we use values of relativistic transition rates for all the electric dipole (E1) transitions in the decay model.

In Fig. 1 and 2, the population $N_{2p_{3/2}}(t)$ for the $2p_{3/2}$ state as a function of time with an initial population of the n=4 states with $\kappa < 0$ and $\kappa > 0$ in $Z = 10$ are shown, respectively, where $\kappa$ is the relativistic quantum number given by $\kappa = \mp|j + 1/2|$ when $j = l \pm 1/2$. It is seen from the figures that the $4d_{5/2,3/2} \to 2p_{3/2}$ transitions occur very fast, while the results for the $N_{4s}(0) = 1$ and $N_{4f_{5/2,7/2}}(0) = 1$ show that the decay curve of $N_{2p_{3/2}}$ at large $t$ does not decrease rapidly. These come from the smallness of the transition rate for the $4s \to 2p_{3/2}$ transition in the case of $N_{4s}(0) = 1$, and from the cascade transitions of the $4f_{5/2,7/2} \to 3d_{3/2,5/2} \to 2p_{3/2}$ for the $N_{4f_{5/2,7/2}} = 1$ case leading to a superposition of two different exponential functions with the decay constants for the $4f_{5/2,7/2} \to 3d_{3/2,5/2}$ and $3d_{3/2,5/2} \to 2p_{3/2}$ transitions. On the other hand no contribution from the $N_{4p_{1/2,3/2}}(0) = 1$ to the $N_{2p_{3/2}}(t)$ is observed because the direct transition from the $4p_{1/2,3/2}$ state to the $1s$ state is dominant and fast for the $4p_{1/2,3/2}$ state compared

to the cascade transitions of $4p_{1/2,3/2} \rightarrow (3s \text{ or } 3d_{3/2,5/2}) \rightarrow 2p_{3/2}$. However life time in these excited states is too short, namely $10^{-12}$ second, to observe the decay curves for them experimentally at present.

**(b) Populations in excited states in $Ne^{2+}$ due to Auger transitions :**

In light atomic systems, the fluorescence yield for inner-hole states such as the $K$-hole one is very small so that ionization process due to the Auger transitions becomes dominant for the inner-hole states in an atomic system. So the transition rate for the Auger transitions from a mother atomic system to its daughter one can be inferred by measuring line intensities as a function of time due to the cascade decay transitions in the daughter system.

Here we calculate time-dependent populations for states in $Ne^{2+}$ produced by Auger transitions for K-hole state in Ne atom to look into how line intensities in the spectra in the ion are observed. In the calculation of the populations for states in $Ne^{2+}$, we set an initial population for a K-hole state in $Ne^{+}$, that is, the uppermost excited level in the system under consideration as $N_{K-hole}(0) = 1$ . We use values of transition rates for all Ne K Auger transitions obtained with experiment by Ablibetz [3] and theoretical RCI calculations by Ikeda et. al. [4]. The decay constant for the K-hole state in $Ne^{+}$ is obtained with the theoretical fluorescence yield $\omega_K$ of McGuire [5], that is, $\omega_K = 0.0182$ and the total KLL Auger rate of Ablibetz, which is $9.9 \times 10^{-3}$ in atomic units.

Fig. 3 shows the populations for four states in $Ne^{2+}$ picked, that is, $KL_{23}L_{23}(^1D_2)$, $KL_1L_{23}(^3P_0)$, $KL_1L_{23}(^1P_1)$, $KL_1L_1(^1S_0)$, when an initial population of $N_{K-hole}(0) = 1$. The lower state $KL_{23}L_{23}(^1D_2)$ is a quasi-stable state, so that most of the $K$-hole population $N_{K-hole}(0)$ is accumulated in the state when $t$ increases, which is seen in Fig. 3.

**(c) The MSCL model for decay processes in hollow atomic Ar ions**

In recent collision experiments between slow highly-charged ions and solid surfaces, neutralization of a projectile ion due to the multielectron transfer from a target leads to formation of various hollow atomic states in the ion, where there is no core electron in the innermost shells such as the K and/or L shells for an ion. The hollow atom stabilizes through successive Auger or radiative transitions so that the mechanism on the formation of hollow atoms in the experiments can in principle be traced through analysis of the x-ray or Auger electron spectra observed. Recently various satellite lines for the K x-ray spectra emitted from Ar hollow atoms above or below the surface of a solid target have been observed in the collision experiments between the ion and a solid surface by Briand et. al. [6].

We use the multistep capture and loss (MSCL) model to describe decay processes for an Ar hollow ion produced below the surface of a solid target in order to obtain

relative intensities for satellite lines of the K x-ray spectra for Ar ions observed. The MSCL model, in which a set of coupled rate equations for a down-stream cascade decay is solved, has effectively been applied to the analysis of Auger electron spectra emitted from Ne hollow atoms below the surface of a solid target by Page et. al. [7]. Our MSCL model used is similar to that of Page et. al.. Decay of a hollow atomic state for an Ar projectile ion having an initial electron configuration of $K^{n_K}L^{n_L}M^{n_M}$ proceeds through the $KLL$, $KLM$、 $KMM$, $LMM$ Auger transitions and collisional electron captures from the conduction band to the $M$-shell in each steps of the decay, where $n_K$, $n_L$ and $n_M$ are occupation numbers for the $K$, $L$ and $M$ shells, respectively. We calculate the populations for Ar hollow atomic states having a single $K$ hole produced as a result of cascade decays through both the electron loss and capture processes in a solid target. Starting from the $KM^4$ configuration for Ar ion produced below the surface of the target, time integrated populations for $K$-hole states with configurations expressed by $KL^{n_L}M^{n_M}$ are calculated by solving the rate equation.

Here we only show a result of simulated spectra emitted Ar hollow atoms below the surface to demonstrate the effectiveness of the population analysis by mean of a coupled rate equation because of the limited space in the proceedings. In Fig. 4 the relative K x-ray effective population versus emitted K x-ray energy obtained with the Dirac-Hartree-Fock-Slater method [8,9] for the states which can emit K x-rays are listed, where the fluorescence yield for the K x-ray emission for all the K hole states are taken into account. If the transition rate for the $L \rightarrow K$ transition for all the states considered are the same, the relative effective population for the states considered can directly be compared to the K x-ray spectra observed by Briand et. al.. One can see from Fig. 4 that a good agreement between our theoretical spectra and their experimental one is observed. The material on the analysis for K x-ray satellite spectra in Ar hollow ions will be submitted elsewhere soon.

## 4. Discussion

As has been mentioned above, initial populations in various excited states can, in principle, be obtained by observing line intensities of the spectra for all transitions needed in cascade decay processes, although difficulties may lie in obtaining absolute values of intensities of various spectra with different wavelengths experimentally.

Now we consider a radiative decay process as an example for possibilities to obtain the initial populations in higher excited states from observations of line intensities in the cascade decay spectra. For a line intensity $I_{k\rightarrow l}(t)$ for the $k \rightarrow l$ transition is written with $N_k(t)$ in Eq. (13) as

$$I_{k\rightarrow l}(t) = N_k(t)A_{k\rightarrow l} = \left[\left(N_k(0) - \sum_{m=k+1}^{p} a_{m,k}\right) e^{-\alpha_k t} + \sum_{m=k+1}^{p} a_{m,k} e^{-\alpha_m t}\right] A_{k\rightarrow l} \quad (11)$$

where it is assumed that the uppermost excited state in a system is the pth state. Life time for some states in the system is not always long enough to be measured in the experiments such as the beam-foil spectroscopy. In this case in obtaining initial populations with the cascade decay spectra, time integrated intensities of them can also be used. By performing the integration from $t = t_0$ to $t = t_1$ for both sides of Eq. (33), an initial population $N_k(0)$ for the $k$th state can be expressed with a time-integrated intensity of the spectra for the $k \to l$ transiton in the following,

$$N_k(0) = \frac{\alpha_k}{e^{-\alpha_k t_0} - e^{-\alpha_k t_1}} \left[ \frac{1}{A_{k\to l}} \int_{t_0}^{t_1} I_{k\to l} dt - \sum_{m=k+1}^{p} a_{m,k} \left( \frac{e^{-\alpha_m t_0} - e^{-\alpha_m t_1}}{\alpha_m} \right) \right] + \sum_{m=k+1}^{p} a_{m,k}. \quad (12)$$

To obtain an initial population $N_k(0)$ for a kth excited state with the Eq. (34), all $a_{m,k}$ and a line intensity of the time-integrated experiment data for the $k \to l$ transition are needed. Since $a_{m,k}(m > k)$ in Eq. (14) contains an initial population $N_m(0)$ for the $m$th excited state, initial populations for all higher excited states than a $k$th excited state under consideration must be determined in order to obtain the $N_k(0)$: One has to start from the estimation of $N_p(0)$ for the uppermost pth state with a line for one of the $p \to l$ transitions and go down to the next lower state step by step. However, at present it may be a hard task to obtain a set of line intensities needed enough by experiment because of weekness of lines or degenerate energy levels such as those for hydrogenic systems in which less independent lines than needed are observed.

In the present proceedings we have not discussed on the analysis of polarization effects in atomic spectroscopy. However, it will certainly be interesting to study down-stream decay transitions from highly excited atoms in connection with the polarization because cascade effects on the polarization for lines in plasma spectroscopy are expected to be large as discussed in this workshop.

This work was supported in part by a Grant-in Aid from the Japanese Ministry of Education (Grant No.05238102).

## References

[1] E. Segre, *Nuclei and Particles* (Benjamine, New York, 1964).
[2] L.J. Curtis, Amer. J. Phys. **36**, 1123 (1968).
[3] A. Albiez, et. al., Z. Phys. D**16**, 97 (1990).
[4] A. Ikeda, K. Futaba, I. Sasaki and T. Kagawa, (unpublished).
[5] E.J. McGuire, Phys. Rev. A**2**, 273 (1970).
[6] J.-P Briand, et. al., Phys. Rev. A**54**, 4136 (1996).
[7] R. Page et.al., Phys. Rev. A**52**, 1344 (1995).
[8] S. Kiyokawa et. al., Phys. Rev. Lett. **54**, 1999 (1985).
[9] S. Kiyokawa et. al., AIP Coference Proceedings Series, **136**, 176 (1985).

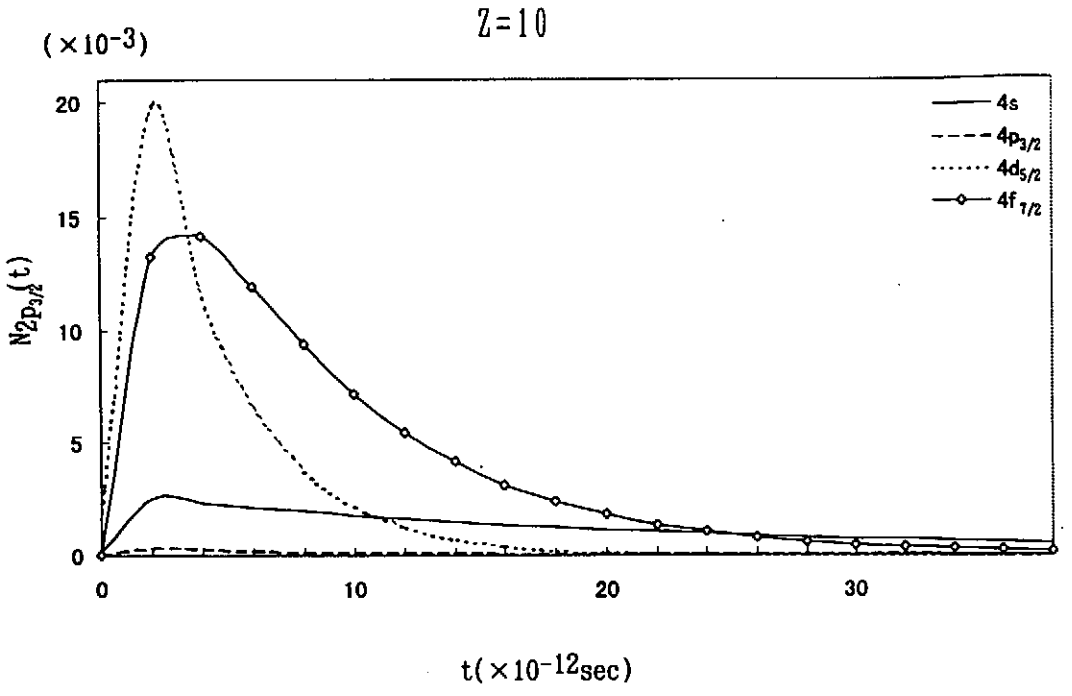


Fig. 1. Population $N_{2p_{3/2}}(t)$ for the $2p_{3/2}$ state as a function of time in hydrogen-like Ne atom (Z=10) with an initial population of the n=4 states with $\kappa < 0$ ; $N_{4s}(0) = 1$, $N_{4p_{3/2}}(0) = 1$, $N_{4d_{5/2}}(0) = 1$ and $N_{4f_{7/2}}(0) = 1$.

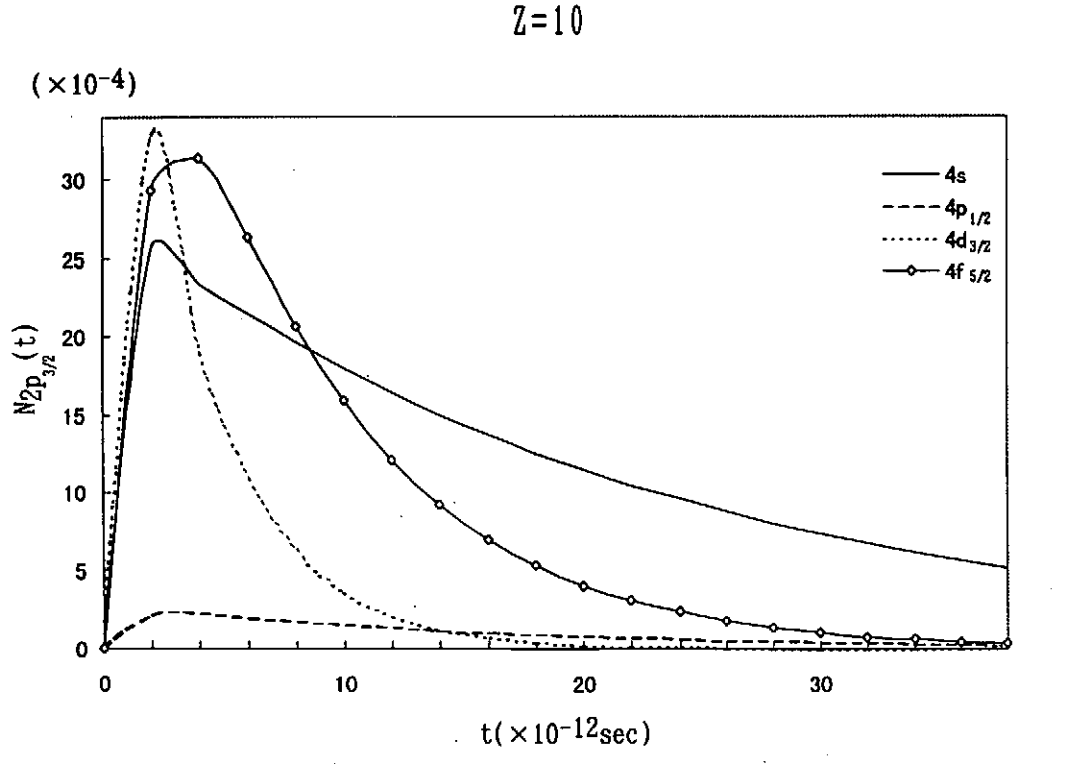


Fig. 2. Population $N_{2p_{3/2}}(t)$ in hydrogen-like Ne atom (Z=10) with an initial population of the n=4 states with $\kappa > 0$ including the 4s state; $N_{4s}(0) = 1$, $N_{4p_{1/2}}(0) = 1$, $N_{4d_{3/2}}(0) = 1$ and $N_{4f_{5/2}}(0) = 1$.

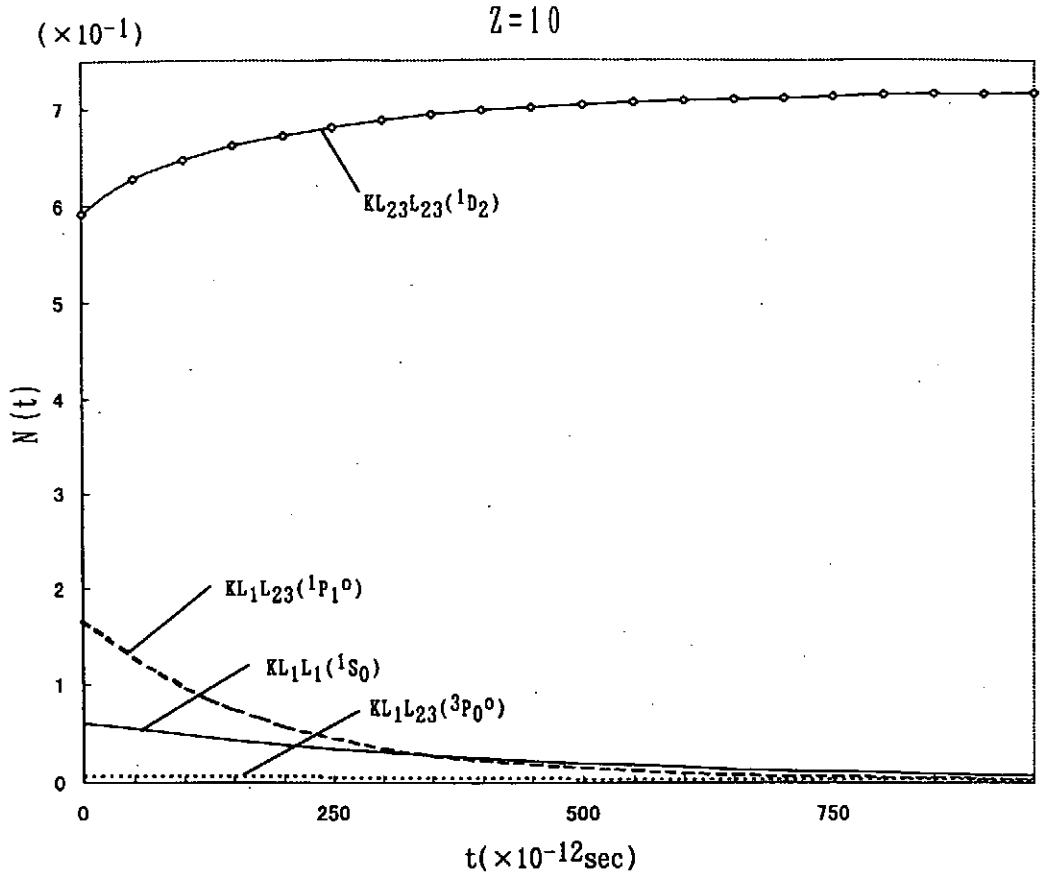


Fig. 3. Populations for four $KLL$ Auger states of $KL_{23}L_{23}(^1D_2)$, $KL_1L_{23}(^3P_0)$, $KL_1L_{23}(^1P_1)$ and $KL_1L_1(^1S_0)$ in $Ne^{2+}$ with an initial population of $N_{K-hole}(0) = 1$.

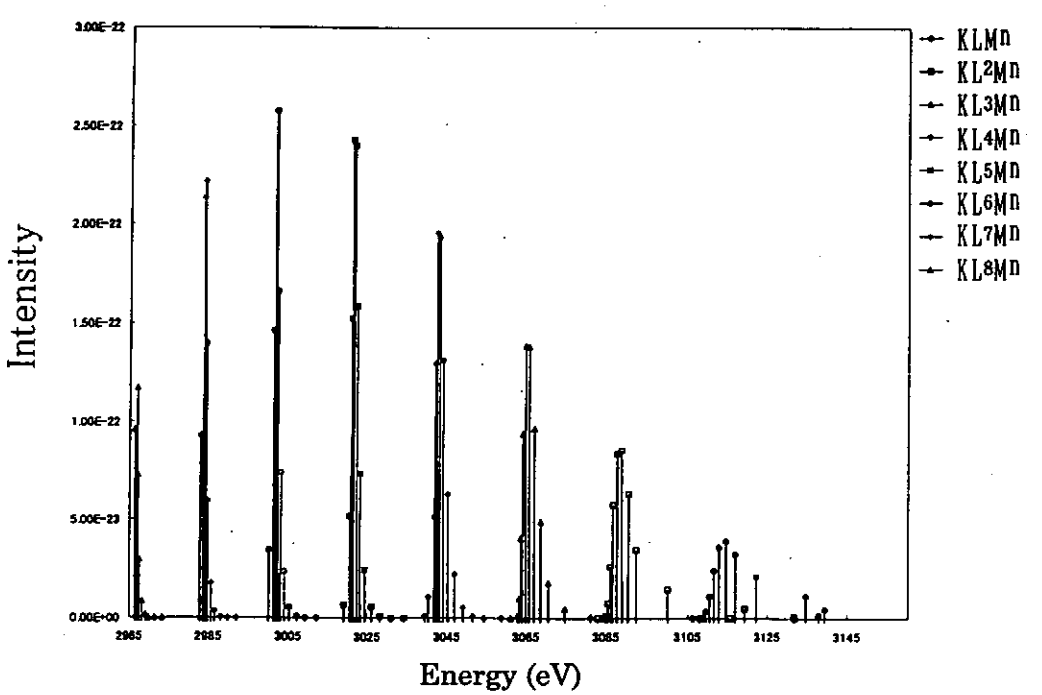


Fig. 4. Relative Intensities for the satellite lines for the K x-ray spectra emitted from Ar ions calculated with the MSCL model starting from the initial $KM^4$ state whose population is unity.

# A Rate-Equation Model for Polarized Laser-Induced Fluorescence to Measure Electric Field in Glow Discharge He Plasmas

K. Takiyama, M. Watanabe and T. Oda

*Department of Applied Physics and Chemistry, Faculty of Engineering, Hiroshima University, Higashi-Hiroshima 739, Japan*

Possibility of applying polarized laser-induced fluorescence (LIF) spectroscopy for measuring the electric field in a plasma with a large collisional depolarization has been investigated. A rate equation model including the depolarization process was employed to analyze the time evolution of LIF polarization components. The polarized LIF pulse shapes observed in the sheath of a He glow discharge plasma were successfully reproduced, and the electric field distribution was obtained with high accuracy.

## 1. Introduction

Importance of sheath electric field distribution in discharge plasmas has been well recognized, since it plays an essential role in the charged particle behaviors and in dynamics of the discharge. Several direct measurements have been made in the sheath regions, using laser-induced fluorescence (LIF) techniques [1,2]. In previous reports, we proposed an improved high-sensitive LIF method combined with plasma polarization spectroscopy [3,5]. This method is to observe merely polarization of LIF due to the forbidden excitation of the He metastable atom ($2^1S$-$n^1D$) which is caused by the Stark mixing of $n^1P$ to $n^1D$ in the electric field and also by the electric quadrupole moment (QDP), as shown in Fig.1.

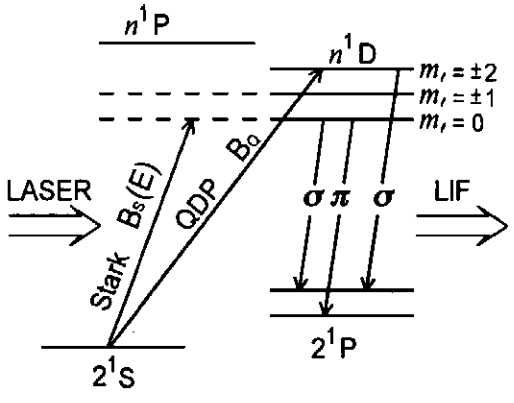


Fig. 1: Partial energy level diagram of HeI and forbidden excitation of metastable atoms by laser polarized linearly parallel to the electric field without magnetic field, relevant to the polarized fluorescence.

The excited atoms decay with intense allowed fluorescence ($n^1D$-$2^1P$). The intensity $I_F$ is written as a function of electric field strength $E$ as follows:

$$I_F \propto n_{2S}\rho_L[B_S(E)+B_Q] , \qquad (1)$$

where $\rho_L$ is a laser power density, $n_{2S}$ is the metastable atom density, $B_S(E)$ is the absorption coefficient for the Stark transition ($B_S(E) \propto E^2$), and $B_Q$ is the absorption coefficient for the QDP transition. The observed fluorescence is usually polarized,

because anisotropic population between sublevels in the excited states (alignment) is achieved with the linearly-polarized laser excitation [6]. The polarization of the Stark component is quite different from that of the QDP (for example, see Fig. 1) [3]. Considering the alignment and the selection rules for the allowed transition ($n^1$D-2$^1$P), the ratio $B_S(E)/B_Q$ is a function of the polarization degree $P$ in a given observation geometry and the electric field is simply described in the following:

$$E = C\sqrt{B_S(E)/B_Q} = C\sqrt{f(P)}\,. \qquad (2)$$

Here, $C$ is the electric field strength at $B_S(E)=B_Q$, which can be quantum-mechanically calculated. When the laser polarization $e_L$ is parallel to the $z$-axis in our observation geometry (see section 3), f($P$) in two cases without magnetic field and with magnetic field are simply given by $6P/(3\text{-}5P)$ and $(3\text{-}9P)/(10P\text{-}6)$, respectively.

In plasmas with higher particle density (electrons, ions and atoms), however, the decay of polarization becomes faster and the LIF waveform is considerably modified by the frequent collisions of the aligned $n^1$D atoms with the plasma particles (collisional depolarization). In such cases it will become difficult to estimate $E$ straightforwardly from the experimental $P$. To evaluate $E$ accurately, we analyze temporal evolution of polarized LIF by using a rate-equation model involving the depolarization process of aligned atoms in this report. Specifically, the following factors determine the waveform: De-population of $n^1$D states, collisional transfer between magnetic sublevels in $n^1$D states (disalignment), laser pulse profile, and time response of detection system. All of these should be included in the model.

## 2. Rate-equation model

We assume that polarization decay is caused by the collisional transfers between three Stark sublevels $m_\ell$ of $n^1$D state specified by magnetic quantum numbers 0, $\pm1$ and $\pm2$, respectively, as shown in Figs. 1, 2. The rate coefficients for collisional transfers from $m_\ell$ to $m_\ell'$, $R(m_\ell, m_\ell')$, are defined considering the detailed balance in the following:

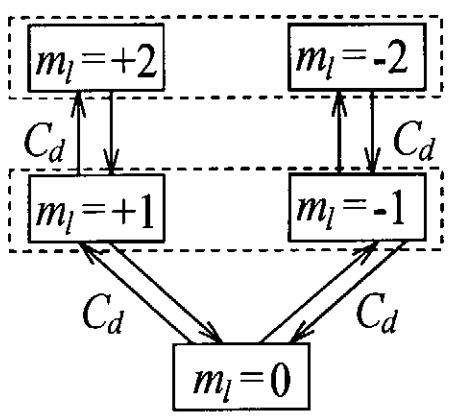


Fig. 2: Three Stark sublevels in $n^1$D state and collisional depolarization mechanism.

$$
\begin{aligned}
&R(0,\pm1) = 2C_d,\\
&R(\pm1,0) = C_d,\\
&R(\pm1,\pm2) = C_d,\\
&R(\pm2,\pm1) = C_d.
\end{aligned}
\qquad (3)
$$

Here, $C_d$ denotes the transfer rate between adjacent Zeeman sublevels, as shown in Fig.2. The temporal evolution of the population density $n_{m_\ell}(t)$ of a sublevel $m_\ell$ in $n^1$D level can be written as a set of rate-equations:

$$
\begin{aligned}
\frac{dn_{m_\ell}}{dt} = &-n_{m_\ell}\left(\sum_{k<m_\ell} A_{m_\ell k} + \sum_k n_{e,a}\langle\sigma_{e,a}v\rangle_{m_\ell k} + \sum_{m_\ell'} R(m_\ell,m_\ell')\right)\\
&+\left(\sum_{k>m_\ell} n_k A_{km_\ell} + \sum_k n_k n_{e,a}\langle\sigma_{e,a}v\rangle_{km_\ell}\right) + \sum_{m_\ell'} n_{m_\ell'} R(m_\ell',m_\ell)\\
&+ I_{\ell m_\ell}(t)(n_\ell B_{\ell m_\ell} - n_{m_\ell} B_{m_\ell \ell}),
\end{aligned}
\qquad (4)
$$

where $A_{m_\ell k}$ is the radiative transition probability from level $m_\ell$ to level $k$, $n_{e,a}$ is the electron or atom density, $\langle\sigma_{e,a}v\rangle_{m_\ell k}$ the excitation or de-excitation rate coefficient by electron or atom impact. The last term on the right-hand side corresponds to laser pumping of $2^1$S to $m_\ell$, where $B_{\ell m_\ell}$ is the absorption coefficient in the forbidden transition ($\ell \rightarrow m_\ell$).

By solving numerically a set of rate equations for each levels from $n$=1 to 6 with the Runge-Kutta method, the temporal behaviors of population are obtained. Parallel and perpendicular components of LIF ($I_{//Z}$ and $I_{\perp Z}$) are reconstructed from the calculated sublevel populations of $n^1$D considering the quantization axis, the selection rules of the transition from the sublevels of $n^1$D to those of $2^1$P, and also the instrumental time response function. Then, the time evolution of LIF polarization is given by

$$
P(t) = \frac{I_{//Z}(t) - I_{\perp Z}(t)}{I_{//Z}(t) + I_{\perp Z}(t)}. \qquad (5)
$$

## 3. Experimental

The observation geometry is shown in Fig. 3. The plasma was produced in helium gas between a pair of plane-parallel disk electrodes (diameter of 4 cm and separation of 1 cm) with discharge voltage of 1 kV and current of 15 mA at gas pressure of 2 Torr. The $z$-axis was taken to be perpendicular to the electrode surface, i.e., parallel to the electric field in the sheath, and its origin was the center of the gap. An electric probe measurement showed that almost all the

discharge voltage was applied over the dark space with width of ~6 mm and the electron temperature and density were ~1 eV and ~1x10$^{11}$ cm$^{-3}$, respectively, at the center of the negative glow when $B$=0.

A laser beam exciting the forbidden transition (2$^1$S-3$^1$D, 504.2 nm) with pulse width of 5 ns was injected into the plasma along the $y$-axis, and the polarized LIF (3$^1$D-2$^1$P, 667.8 nm) was observed along the $x$-axis. Spatial distribution of LIF was measured by scanning the plasma vessel along the $z$-axis.

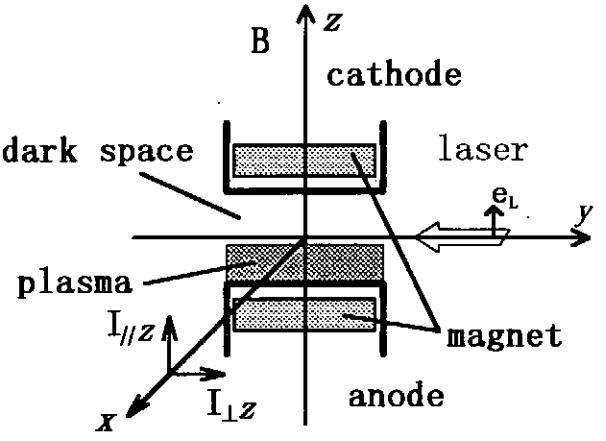


Fig. 3: Geometry of LIF observation and the cross section of glow discharge vessel

## 4. Results and Discussion

Polarization components of 667.8 nm fluorescence (3$^1$D-2$^1$P) , $I_{//z}$ and $I_{\perp z}$, induced by laser with $e_L \perp z$ were observed at the plasma region ($z$=−1mm) in the vicinity of the sheath, where only the QDP transition occurs, since the electric field is negligibly small, as shown in Fig 4 (a). Using eq. (5) temporal polarization $P$ obtained from experimental $I_{//z}$ and $I_{\perp z}$ is depicted by open circles in Fig. 4 (b). The polarization at the earlier stage is ~−0.8 very close to unity, reflecting a feature of polarized LIF due to the QDP excitation. Since the quantization axis for QDP excitation is always perpendicular to the polarization plane of laser without magnetic field, the direction turns to $z$-axis and the atoms are selectively excited to the sublevels $m_l$=±2 in 3$^1$D [3]. Excited atoms subsequently decay down to the 2$^1$P state with allowed σ-fluorescence of 667.8 nm. We are supposed to observe perfectly negative polarization of the fluorescence in our

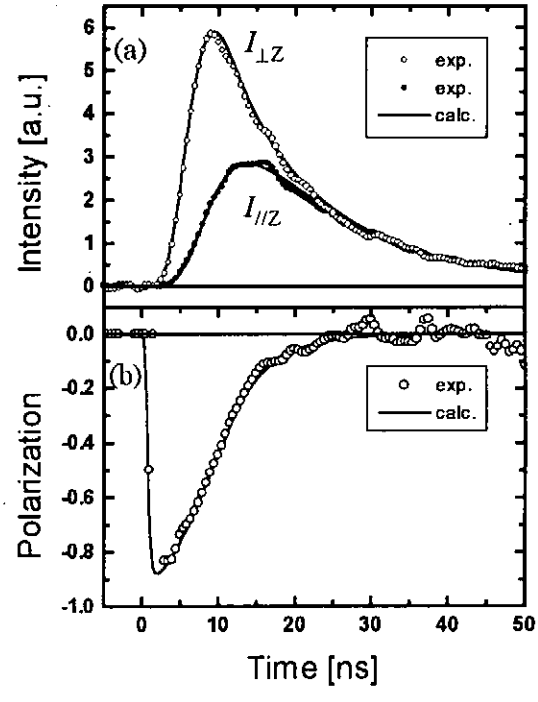


Fig. 4: Calculated waveforms fitted to the experimental ones observed by laser excitation ($e_L \perp z$) at the negative glow region.

geometry. However, considerable depolarization due to collisional disalignment was observed. The disalignment and de-population rates are estimated to be $2.1 \times 10^8$ s$^{-1}$ and $0.7 \times 10^8$ s$^{-1}$, respectively, from the slopes of semi-logarithmic plots of time evolution of longitudinal alignment and population.

In our fitting procedure between the calculated curves with the experimental LIF ones (open and closed circles in Fig. 4), we took the transfer rate ($C_d$) as a fitting parameter. When $C_d = 1.5 \times 10^8$ s$^{-1}$, the best-fit curves of $I_{//Z}$, $I_{\perp Z}$ and $P$ were obtained, as represented by solid lines in Fig. 4 (a), (b).

Figure 5 (a) shows polarization components $I_{//Z}$ and $I_{\perp Z}$ of LIF observed at $z$=4mm in the sheath region under excitation by laser with $e_L//z//E$. The temporal polarization is also depicted by open circles in Fig. 5 (b). In the sheath electric field a polarized laser simultaneously excites both Stark and QDP transitions. The quantization axis for Stark excitation can be taken to the direction of electric field ($//z$) independently to the laser polarization and the value of $P$ is always positive. On the other hand QDP component is unpolarized in this excitation geometry. Remarkable positive value of $P$ at the earlier stage shows that in LIF the Stark component is dominantly included rather than the QDP one: Most of excited atoms populate in the sublevel $m_\ell$=0 in $3^1$D. The disalignment and de-population rates estimated in the similar way described above were the same values as ones obtained at $z$=−1mm in the plasma region near the sheath. This means that $C_d$ as well as plasma parameters are almost the same in the observed region from $z$=−1 mm to cathode. Using $C_d$ obtained above, we can determine uniquely the electric field $E$ by fitting the calculated curves to the experimental ones observed in the sheath region. The best-fit curves, solid curves in Fig.5 (a), (b), are obtained when $E$=2.7kV/cm.

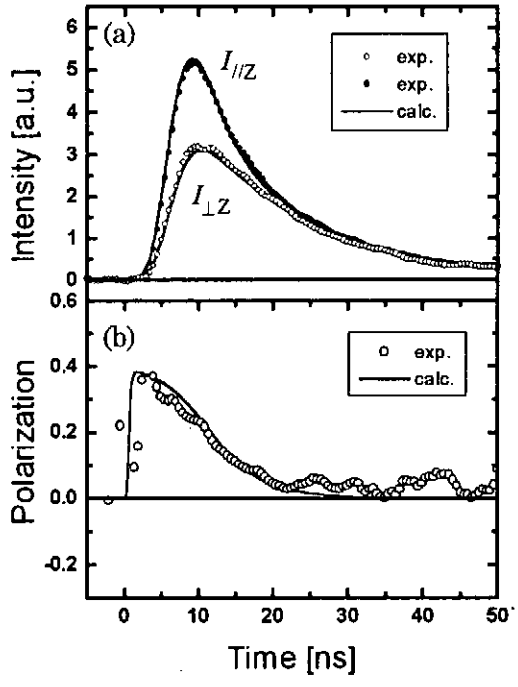


Fig. 5: Calculated waveforms fitted to the experimental ones observed by laser excitation ($e_L//z$) at the sheath region.

For the case of $B$=200G, same procedures are also carried out to reconstruct the polarized LIF.

Spatially resolved LIF signals were obtained by scanning the plasma vessel. Using the same procedure as described above, spatial profiles of $E$ in the sheath region of both plasmas with $B$=0 and $B$=200 G were obtained as shown in Fig. 6, in which electric field is increasing linearly toward the cathode surface. From the profiles, sheath thickness $d$ and cathode-fall potentials $V_C$ were obtained, as presented in Table I with experimental conditions. It should be noted that the potentials for both cases are in good agreement with one obtained by the electric probe. The proportionality between the transfer rate $C_d$ and the He gas pressure suggests that the strong depolarization process is dominantly caused by collisions of aligned $3^1D$ atoms with ground state He atoms for the present cases.

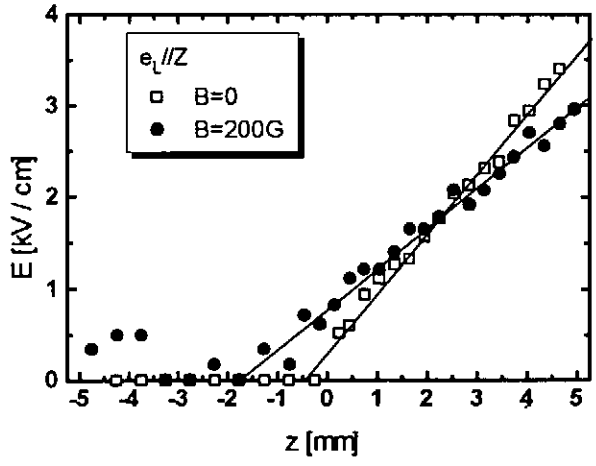

Fig. 6: Spatial distribution of electric field

Thus, the polarized laser-induced fluorescence spectroscopy was successfully applied to measure the electric field profiles in the sheath of the plasma with higher He gas pressure and of magnetized plasma with the aid of the rate-equation analysis. The sensitivity of this method is increased by exciting the higher $n$ level. At $n$=5, the electric field of a few tens V/cm can be measured.

Table I Summary of the LIF and electric probe measurements

| Discharge condition | | | LIF | | | Electric probe |
|---|---|---|---|---|---|---|
| | He Pressure (Torr) | Discharge current (mA) | Magnetic field B(G) | Transfer rate $C_d(s^{-1})$ | Sheath thickness d(mm) | Cathode-fall potential $V_C$(kV) | Cathode-fall potential $V_C$(kV) |
| (a) | 3 | 15 | 0 | $1.5\times10^8$ | 5.6±0.2 | 1.03±0.05 | 1.0 |
| (b) | 2 | 15 | 200 | $1.0\times10^8$ | 6.9±0.5 | 1.06±0.10 | 1.0 |


## Acknowledgements

This work was supported in part by a Grant-in-Aid for Scientific Research (C) from the Ministry of Education, Science, Sports and Culture, and by Electric Technology Research Foundation of Chugoku.

**References**


[1] H. Sakai, K. Takiyama, et al., J. Nucl. Mater. **196-198** (1992) 1135.

[2] M. D. Bowden, Y. W. Choi and K. Muraoka, Appl. Phys. Lett. **66** (1995) 1059.

[3] K. Takiyama, et al., *Proc. 6th Int. Sympo. Laser- Aided Plasma Diagnostics,* Bar Harbor, Maine, Oct. 25-28, 1993, p.43.

[4] T. Oda and K. Takiyama, *Proc. 7th Int. Sympo. Laser-Aided Plasma Diagnostics*, Fukuoka, Dec. 5-8, 1995, p.227.

[5] K. Takiyama et al., Rev. Sci. Instrum. **68** (1997) 1028.

[6] T. Fujimoto and A. Kazantsev, Plasma Phys. Control. Fusion **39** (1997) 1267

# Line Width and Alignment

**Volkmar Helbig**

Institut für Experimentelle und Angewandte Physik
Universität Kiel, D 24098 Kiel, Germany

## I. Introduction

In spectroscopic investigations there is a certain need for disalignment rates for the interpretation of data taken e.g. by means of plasma polarization spectroscopy. Hirabayashi et al. [1] pointed out that there is a similarity between disalignment and line width. The collisional destruction of alignment appears to be a process closely related to the impact broadening of spectral lines which is often well approximated by the dephasing of the upper level only. It would be very desirable to have a theoretical formalism at hand to convert disalignment rates to line widths and vice versa. Especially the latter direction would be of great importance because there are numerous papers in literature that contain line broadening data that could be used in this case for the calculation of disalignment rates. There have been reported only few direct measurements of these rates. For a very useful compilation of line broadening data see e.g. Fuhr and Lesage [2].

We have carried out a number of different experiments in our group at the university of Kiel to further investigate the mentioned similarity. In this paper measurements are described that have been carried out in Neon. In high and low pressure discharges Stark- and van der Waals broadening have been studied. Disalignment rates have been obtained in experiments with CW and pulsed lasers.

## II. Pressure broadening at low densities

The shift and the broadening of the neon line at 588.2 nm by neutral neon have been determined in [3]. The measurements were carried out in a low pressure glow discharge using Doppler-free polarization spectroscopy. The pressure broadening parameters were extracted from the raw data by a least squares computer routine accounting for competing broadening mechanisms like residual Doppler broadening, saturation broadening and the finite laser line width.

## III. Stark and pressure broadening at high densities

In a cascade arc discharge running in neon at atmospheric pressure the Stark widths and shifts of a number of neon lines have been determined using a high resolution grating monochromator [4]. For the plasma analysis LTE was assumed and the electron density was determined by a two wavelength laser interferometer. A careful investigation of the density dependence of the linewidths revealed that pressure broadening by the neutral neon atoms was not negligible. From the known pressure and the neutral gas temperature the neutral particle density could be obtained. Since for given pressure a high temperature corresponds to a low neutral density and a high electron density and vice versa it is possible to separate the influence of the electrons and the neutrals and to obtain constants for both broadening mechanisms from the same set of data.

## IV. Disaligment rates measured in a DC gas discharge

In a pump and probe experiment using two narrow bandwidth dye lasers running on different wavelengths corresponding to neon lines disalignment rates for the upper level of one of the lines have been determined in neon and helium gas discharges at low pressure [5]. A V-shaped excitation scheme has been applied for the linearly polarized pumping laser and the probing laser that had a direction of polarization that was set at 45° with respect to the pumping laser. Figure 1 shows the type of spectra obtained for different pressures in the discharge. The polarization signal starts with a Doppler-free peak on a pedestal caused by collisions. With increasing pressure the height of the Doppler-free peak decreases, changes the sign and increases again. From the spectra the presssure for zero signal can be interpolated. Solving the system of rate equations that describe the process it is possible to extract the disalignment rate from the measurements.

## V. Disalignment rates measured in a pulsed laser experiment

The time-resolved laser-induced fluorescence observed after excitation of an atomic beam with a pulsed laser is influenced by collisions and polarization effects [6]. This has to be taken into account in lifetime measurements. While collisional depopulation will still result in a single exponential decay curve, the alignment induced by the polarization of

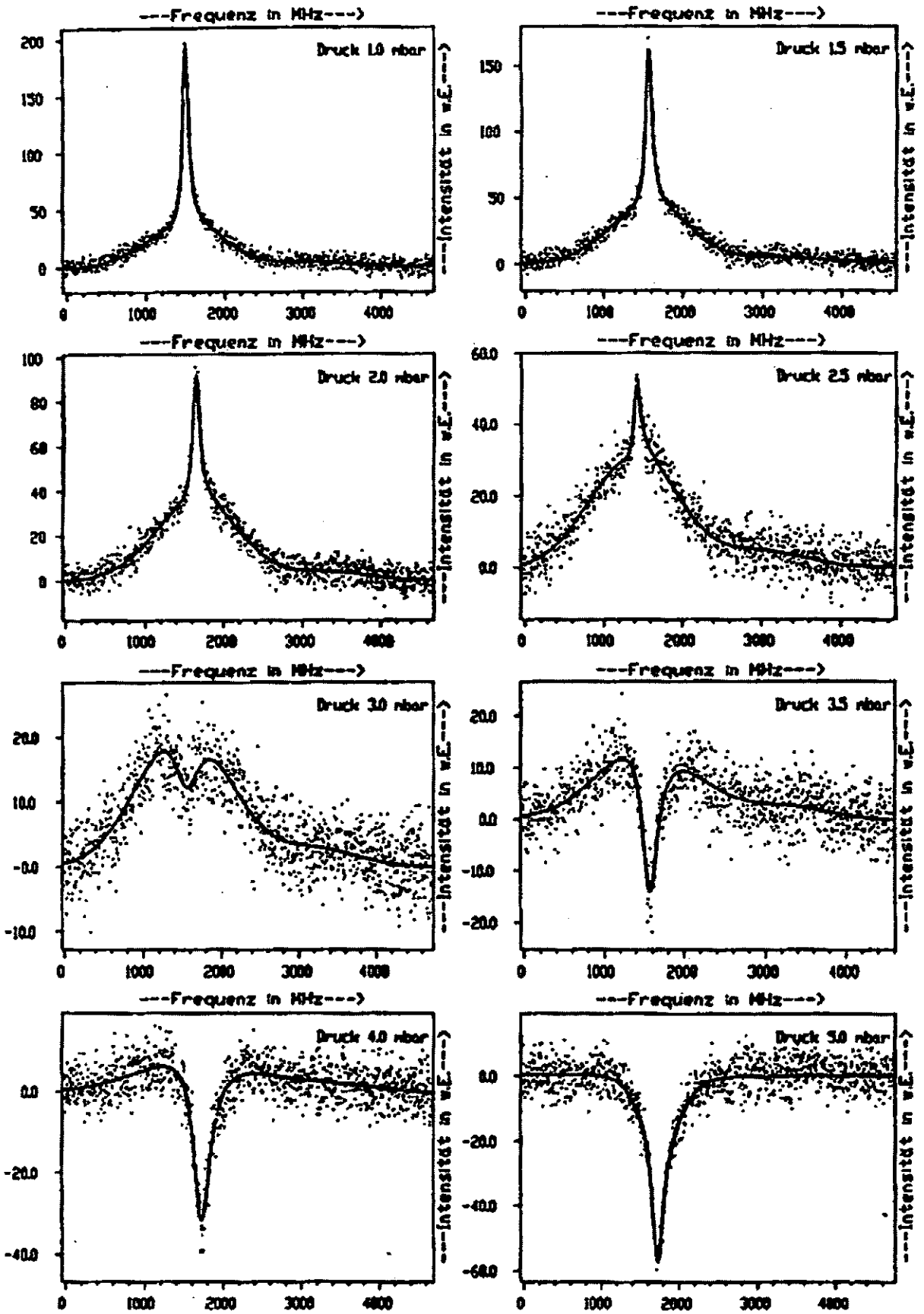


**Fig. 1:** *Polarization spectra for different pressures in the discharge. The wavelengths of the pumping and the probing laser are 650.7 and 603.0 nm, respectively.*

the exciting laser will change the shape of the decay curve, depending on the angle between polarization in the excitation and in the observation arm. Only under magic angle conditions the alignment effects will cancel out and a single exponential decay curve is obtained again. In [6] two sets of experiments have been carried out. By using the magic angle and collecting decay curves for different pressures it is possible to obtain the rate for collisional depopulation from a Stern-Vollmer plot. Extrapolation to zero pressure will yield the lifetime. By setting the angle at a different value it is possible to extract the rate for disalignment from the shape of the observed decay curves.

## VI. Conclusions

Taking the data from the different experiments it is possible to calculate in a very coarse approximation widths from the rates and vice versa. While this procedure reproduces the order of magnitude for the respective data it is not surprising that the agreement is not very good. Starting from the theoretical cross sections given for instance by Schuller and Behmenburg [7] it should be possible to develop a theory for a better transformation of the widths to the rates.

## VII. References


[1] A. Hirabayashi, Y. Namba, M. Hasuo and T. Fujimoto, "Disalignment of excited neon atoms due to electron and ion collsions", Phys. Rev. A 37, 83 (1988).

[2] J.R. Fuhr and A. Lesage, "Bibliography on Atomic Line Shapes and Shifts", NIST Special Publication 366, Suppl. 4, Washington (1993).

[3] J. Röhe-Hansen, K. Jeß and V. Helbig, "Study of the pressure broadening of the 587.6 nm helium and the 588.2 nm neon lines", J. Phys. B 20, 4993 (1987).

[4] A. Döhrn and V. Helbig, "Stark broadening and shift of selected neutral neon lines", Phys. Rev. E 53, 6581 (1996).

[5] J. Kruse, Diploma thesis Kiel (to be published).

[6] W. Schade, L. Wolejko and V. Helbig, "Influence of polarization and magnetic fields on time-resolved laser-induced fluorescence measurements", Phys. Rev. A 47, 2099 (1993).

[7] F. Schuller and W. Behmenburg, "Pertubation of spectral lines by atomic interactions", Physics Reports 12, 273 (1974).

# Polarization spectroscopy for ionizing and recombining plasma produced by ultra-short-pulse laser

Hitoki Yoneda, Noboru Hasegawa, Shu-ichi Kawana, Hiroshi Asai and Ken-ichi Ueda
Institute for Laser Science, University of electro-communications

**abstract**

A large anisotropy of the electron distribution function (EDF) was observed in high density plasma. The plasma was created by a 2ps TW KrF laser system in which a prepulse energy was well controlled with a saturable absorber. The observed electron density at the emission area with He-like F ions was $0.7\sim1.5\times10^{22}cm^{-3}$. It is clarified with our experiments that, even with these high collisionality, the anisotropy of EDF was driven by the laser field. That means the anisotropy will become a parameter instead of temperature in the high density plasma which was far from the equilibrium states. However, the quantitative estimation of the anisotropy of EDF is not simple in the laser produced plasma because the upper states of the observed resonant line emission was created both with the excitation from the ground state and the deexcitaion or the recombination from higher n states or higher-ionized ions. To overcome this difficulty, we selected the experimental condition carefully to separate these emission area in space and time. With this technique, the anisotropy of EDF was estimated with help of a cascade model for the recombining plasma and the usual polarization theory for ionizing plasmas.

## 1. Introduction

For understanding interaction physics of ultra-short-pulse lasers and plasmas, it is important to investigate the energy transport process from the laser field to the electrons and ions. Especially, it has to be considered that the created plasma will be far from the equilibrium condition for its ultra-short-pulse duration. In other words, there is no way to define the 'temperature'. To treat these phenomena with accuracy, the electron distribution function (EDF) has to be measured directly and analyzed. In the lower density plasma which was created from the gas medium, it can be measured by the laser Thomson scattering method[1]. However, there is no laser beam for probing the high density plasma due to its large absorbance and refractivity. A new diagnostic method would be useful since most interesting features will be obtained in high density plasmas which starts from the solid state condition or in the compressed core plasma of ICF experiments.

In these plasmas, initially, the incident laser field oscillates the inside electrons, which subsequently drive processes such as collective plasma waves or thermal conductive flux. The EDF has a large anisotropy which is determined by the applied laser field in the initial phase. After enough collisions have occurred, this anisotropy decreases and may disappear, and the plasma will be thermalized finally. That is to say the applied laser field gives not only energy to the electrons but also anisotropy to them. The anisotropy of the EDF itself can be considered as one of the parameters to denote these plasma behaviors.

In this paper, the anisotropy of a high density plasma was investigated for understanding the energy transport process in the ultra-short-pulse laser produced plasma. Since the collision process randomly redistribute the coherent or alignment motion of the electrons, this density is scaled by the collisionality of the objective electrons. A ninety-degree deflection time by the electron-ion collisions is given by,

$$\tau_{90} = \frac{m_e^{\,2}\, v_e^{\,3}}{8\pi n_e Z e^4 \ln\Lambda}$$

In this formula, e is the electron charge, $\ln\Lambda$ is the Coulomb logarithm, $n_e$ is the electron density, $v_e$ is the electron velocity, $m_e$ is the electron mass and Z is the ion charge. The dominant velocity of the electrons for the excitation of the ions depends on Z, because the rate

of excitation and polarization of the emission are maximum at just above the threshold energy which was dependent on $Z^2$. If the dependence of the electron density on the laser wavelength can be scaled by the critical density, the collisionality of the created plasma is proportional to $\tau_{90}^{-1} \sim n_e v_e^{-3} Z \sim \lambda^{-2} Z^{-2}$. To simulate a collisional "high density" plasma, the shorter wavelength of the laser and the lower Z number of the tracer ions are required. In this study, a deep-ultra-violet KrF($\lambda$=0.248μm) laser was used and F ions (Z=9) were chosen as the tracer. The contour plot of the collisionality is shown in **Fig.1** with the parameters of the electron energy and the electron density. The created electron density will be a few times $10^{22}cm^{-3}$ and is as high as only one-tenth of the so-called solid-state density. In addition, the anisotropy of EDF in this experimental condition simulates that of 2.6keV electrons in solid density plasma. The intensity where the quiver energy $E_{os}$ is equal to the excitation energy $E_{ex}$ is estimated to be $I=2x10^{17}W/cm^2$. All the experiments in this study were performed below this intensity.

## 2. Experiments

The experiments were carried out with our 2TW KrF laser system [2] at the Institute for Laser Science of the University of Electro-communications. While the maximum output power of this laser is 2TW/beam with 500fs pulses, the longer 2ps duration pulse was used to achieve the larger ratio of the collision time and the laser pulse duration. This also reduced the undesirable dispersion and nonlinear absorption in the windows of the KrF laser amplifiers and the target chamber. The amplified beams were focused on the target with an F/3 aspherical lens and the intensity on the targets was changed from $10^{14}W/cm^2$ to $10^{16}W/cm^2$ with changing its position near the best focusing point. In the KrF laser system, amplified spontaneous emission from the early-stage amplifiers is a main source of the pre-pulse energy, and its reduction is a key for achieving a high contrast laser pulse. The saturable absorber filters of Acridine in methanol[3] were introduced between the every amplifier. After careful control of the concentration of the dye and the gain of the preamplifiers, the power contrast ratio of the prepulse to the main pulse was $10^{-8}$ on the target. There was no plasma emission and no observable damage on the target without the main pulse.

The anisotropy of the EDF can be estimated from the polarization of an resonant line of He like ions. The polarization was measured by a pair of flat KAP crystal spectrometers, which were located at almost the same distance, in the same line of sight and consisted of the same Bragg crystals and UV-cut filters [4]. Because the Bragg reflectivity of curved crystals strongly depend on the condition of its local curvature and surface condition, we selected the flat crystals in spite of their low efficient detectability. To compensate the small difference between the two spectrometers, which was mainly caused by the non-unity aspect ratio of the target plasma (expansion length vs. plasma width), the intensity of the H-like Lα line was used for calibration. This line was considered to be unpolarized[5]. One cleaved surface of the Bragg crystal was aligned to reflect the x ray having the e-vector to be parallel to the target normal ($I \parallel$) and the other aligned to the perpendicular one ($I \perp$). The polarization of the emission was estimated by the ratio of the spectral intensity between each spectrometer signal. In several shots of these studies, a knife edge was introduced between the target plasma and the spectrometer for obtaining the spatial profile of the emission. The spatial resolution of this measurements is 20μm.

The nominal incidence angle of the laser beam on the target was 40 degrees for all experiments in this paper. According to our previous experiments[6], the optimum angle of the resonant absorption was 55 degrees at $I=10^{14}W/cm^2$ and it was not dominate with in the 40 degree incident angle condition.

## 3. Experimental results and discussion

Typical spectra from the polarized spectrometers are shown in **Fig. 2**. A series of lines of He and H like F ions were observed. The polarization degree of the Heα line was determined by

$$P = \frac{I_{ii} - I_{\perp}}{I_{ii} + I_{\perp}}.$$

The polarization of Heα in the **Fig.2** spectrum was estimated to be +0.25. If the $P_0$=0.6 (the polarization for the monoenergetic electron beam) was assumed[6] and the upper level of this line emission was considered to be created only with electron colisional excitation from the ground state, this polarization denotes evidence for a large anisotropy of the EDF ($f_2/f_0$=2.0, $f_0$: isotropic part of EDF, $f_2$: second-order anisotropy.) in this plasma. The electron density of the emitting plasma was estimated by Stark broadening of the Heβ line whilst considering the plasma size and the instrumental broadening effects. The observed electron density is $0.7\sim1.5\times10^{22}cm^{-3}$. The ratio of the pulse duration and the collision time is greater than one hundred in this case. Even in such 'high density' plasma, a large beam-like anisotropy of the EDF has been observed. In comparing the longer wavelength experiments[7], the sign of polarization is opposite and the absolute value of polarization is large though the electron density is greater than the turning point of the laser field ($n_e > n_c \cos^2\theta$).

To investigate the driving force for the anisotropy, the dependence of the polarization on the intensity of the incident laser was measured (**Fig. 3**). In this figure, the error bar of each data denotes the estimation error of the polarization from the x-ray spectral intensity. At both $10^{14}W/cm^2$ and $10^{16}W/cm^2$ irradiances, a strong dependence on laser polarization was observed and little dependence on the laser intensity. The axis of the observation of the beam-like anisotropy was parallel to the laser electric field direction. While a large positive polarization was observed in p-polarized laser, the negative but weak polarization was observed in s-polarized laser.

It is known that the resonant absorption process and the related wave dumping generate fast non-thermal electrons, in longer pulse experiments. However, in our experiments, the absolute intensities of the He- and H-like lines were not dependent on the polarization of the lasers. Therefore, the resonant absorption was not the main absorption process for exciting the He-like F ions. The incident angle was detuned from the maximum absorption one in this irradiation condition[6]. In addition, the density which was estimated by Stark broadening of the Heβ line was almost the same in both the s- and the p- polarized laser case. These results also highlight the difficulty in explaining the laser-polarization dependence of the anisotropy of the EDF by normal resonant absorption theory.

In the previous paper[7], the anisotropy of the EDF was explained by the short scale length properties. Because the scale length of the created plasma may depend on the intensity more strongly than the laser polarization, their model can not explain our experimental results. In addition, they observed a pancake-like EDF(P<0), while a beam-like EDF(P>0) was observed in our p-polarized laser shots. To consider that the small but negative polarization has been observed in the s-polarized laser shots may be due to the same mechanism as previous papers[7], the positive polarization in the p-polarized laser shots denoted here is due to the new mechanism of driving the anisotropy of the EDF. The obliquely incident laser and small pre plasma condition might change the results drastically.

Although the detailed mechanism of the anisotropy of EDF in our experiments has not been determined, the dominant process producing their anisotropy is directly driven by the applied laser field. However, in the laser produced plasma, the plasma parameters were drastically changed with time and space. We assumed only the excitation process from the ground state for above estimation of anisotropy of EDF. Actually, this upper level is also populated with the deexcitation from higher state levels and the recombination from the continuum level. This multiple way cause some uncertainties for quantitative estimation of anisotropy of EDF. To

overcome this difficulty, we tried to find out the experimental condition, where the ionizing and the recombining phase were separated in space each other. The measured results of spatial profile of intensity of Heα, Lα and recombination continuum were shown in **Fig.4** for two typical experimental conditions. In **Fig.4-(a)** the laser focus spot was 200μm diameter and irradiance was $I=1x10^{14}W/cm^2$. In (b), 20μm diameter and $I=1x10^{16}W/cm^2$ were selected. In **Fig.4-(b)**, there are two separated emission peaks of Heα line. It is reasonable to consider that the excitation from the ground states was dominant to create the upper level of Heα line I the first peaks, while the recombination and deexcitaion was dominant in the second peak. This distinguished situation can be obtained because the laser pulse duration was smaller than expansion time and/or the ionization and the recombination time. In **Fig.4-(b)**, we also found that the recombination continuum of He-like ions was also emitted strongly at the second peak. That means the information of the anisotropy of EDF was included in the polarization of the recombination continuum. Of cause, the Bragg angle for continuum emission is not optimum(31 degree). The ratio of the reflectivity of the two linear polarized light was estimated to be 2.2. Even with such small extinction efficiency, the polarization of recombination continuum was observed (**Fig.5**). We've found that polarization for **(b)** condition is about 0.2 (This value was calculated including the effect of the small difference reflection.). This meant the value of $f_2/f_0$ for the recombining electrons were 0.7. To calculate of the polarization of Heα line at recombining plasma, we've used the cascade model[8]. This model included the contribution coming from direct recombination and cascades from higher-energy states. Because the electron collisional excitation affected the alignment of the higher energy levels even in the recombining plasma, this estimation would give the upper limit of the Heα line polarization. After some modification of the data from the reference, we concluded the polarization of Heα in the recombining phase was 0.1. Finally, we could separate the two phase in the ultra-short pulse laser produced plasma. The estimated value of $f_2/f_0$ for ionizing phase was 1.7~1.9.

## 4. Conclusion

Anisotropy was measured in a high density plasma of lower-Z targets which was produced with a KrF laser system in which the pre pulse was well-controlled. Even though there was a large opportunity for electron-ion collisions during the laser pulse, a large polarization of the resonant line emission has been observed. This positive polarization denoted here is the beam-like EDF with a p-polarized laser interaction. The laser polarization has strong influence on this anisotropy. It is difficult to explain the EDF anisotropy with the normal resonant process, because the absorption of laser light had small dependence on the laser polarization and the incident angle was detuned from the maximum absorption for it. Because it was apparent that this anisotropy was driven by the applied laser field directly, x-ray polarization spectroscopy has become a strong tool for measuring the relaxation from laser energy to thermal energy in high density, non-equilibrium plasmas produced by ultra-short-pulse lasers.

In the laser produced plasma, the upper level of the observed line emission was populated with both of the excitation and deexcitation process. Those complexity resulted in the uncertainties in the estimation of anisotropy of EDF. To overcome this difficulty, we separated the emitting regions in space and time. In first region, the ionization process dominated, while in the second region the recombining one dominated. With the help of the cascade model, the anisotropy of EDF ($f_2/f_0$) in both region were decided. During the expansion, it decreased from 1.7~1.9 in the ionizing phase to 0.1 in the recombination phase.

## References

[1] for example, Offenberger, A.A., Blyth, W., Dangor, A.E., Djaoui, Z.A., Key, M.H., Najmudin, Z., Wark, J.S., Phys. Rev. Lett., vol.71, no.24, 3983-6, 1993

[2] H.Yoneda, T.Miura, Y.Yokota, Y.Motoki, A.Sasaki, K.Ueda, and H.Takuma, Laser and Part. Beams, Vol.11, no.1, 15-23 (1993)

[3] H.Nishioka, H.Kuranishi, K.Ueda, and H.Takuma, Opt. Lett., Vol.14, no.13, 692-694, (1989)

[4] H.Yoneda, N.Hasegawa, S.Kawana, and K.Ueda, Phys. Rev. E, Vol. 56, 988-991, (1997)

[5] M.K.Inal and J.Dubaum J. Phys. B Vol. 22 3329 (1989)

[6] N.Hasegawa, H.Nakagawa, H.Yoneda, K.Ueda, and H.Takuma, Proc. of 12th International Conference on Laser Interaction and Related Plasma Phenomena edited by S.Nakai and G.H.Miley, AIP conference Proc. 369, p660- 665, (1996)

[7] J.Kieffer, J Matte, M.Chaker, Y.Beaudoin, C.Chien, S.Coe, G.Mourou, J.Dubau, and M.Inal, Phys. Rev. E, Vol 48, no.6, p4648-4658, (1993)

[8] J.H.Scofield, Phys. Rev. A, vol.44, p139-143 (1991)

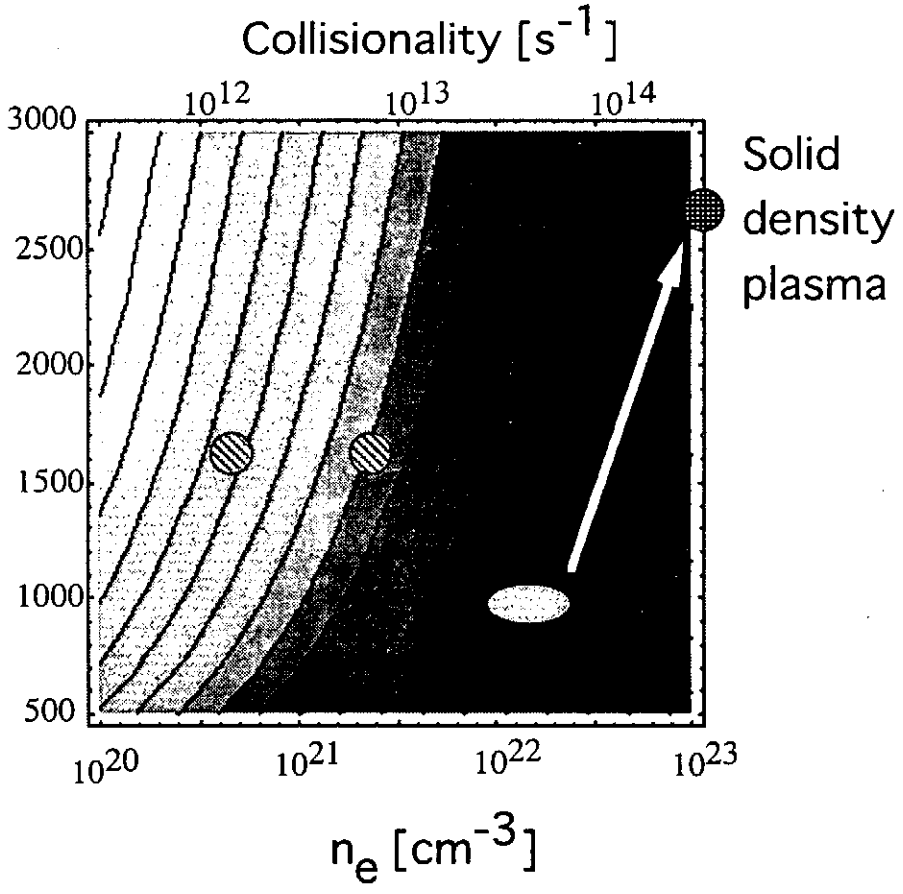


Fig.1 The contour plot of the collisionality was shown as a parameter of the electron energy and the electron density. The created electron density was as high as only one-tenth of the so-called solid-state density. The anisotropy of EDF in this experimental condition simulates that of 2.6keV electrons in solid density plasma.

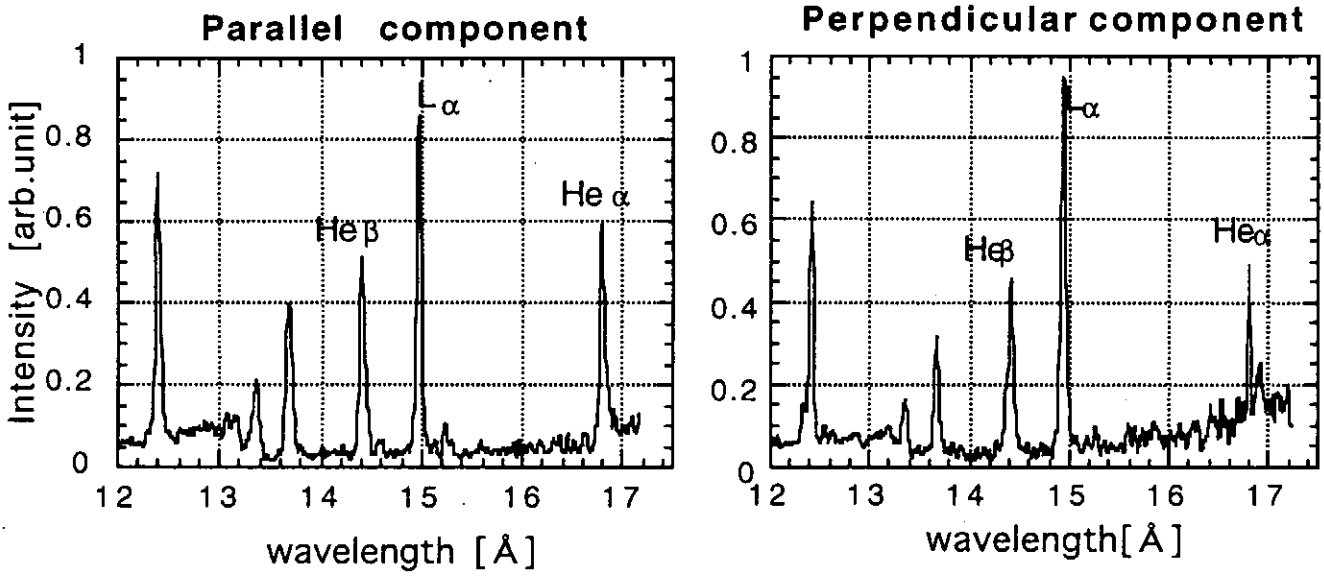


Fig.2 Typical spectra from the polarization spectrometers. He- and H-like resonant lines were observed. The ratio of the Heα line and the Lα line intensity intensities showed a large difference between the perpendicular (a) and the parallel component (b). From this spectrum, the polarization was estimated to be +0.25.

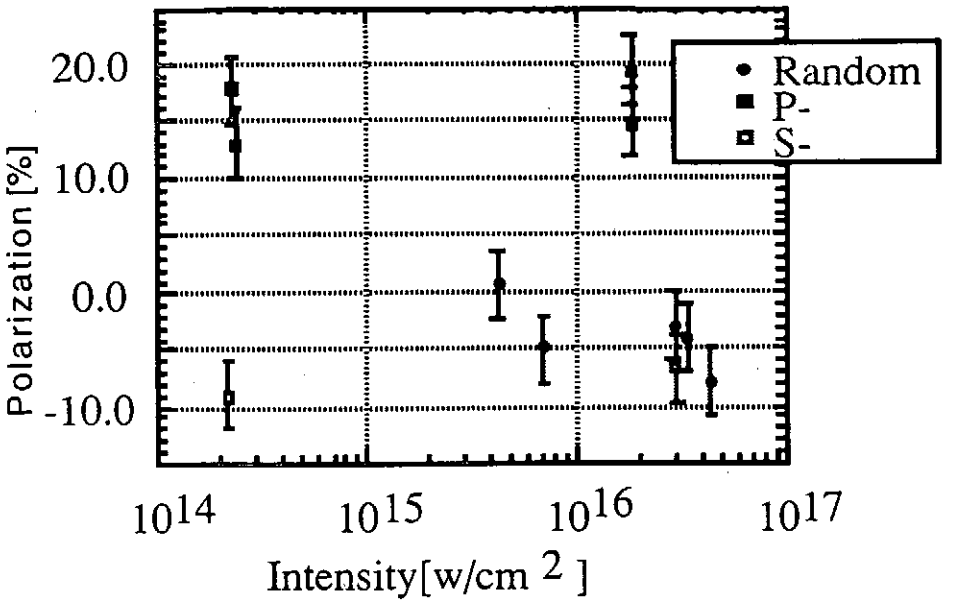


Fig.3 The dependence of the irradiation intensity and the laser polarization on the emitted x-ray polarization. A large difference was observed with the p-polarized laser condition and the s-polarized one. This is the most reliable evidence for the polarization of the x ray of the resonant line, because the setup and the other conditions were the same except for the laser polarization.

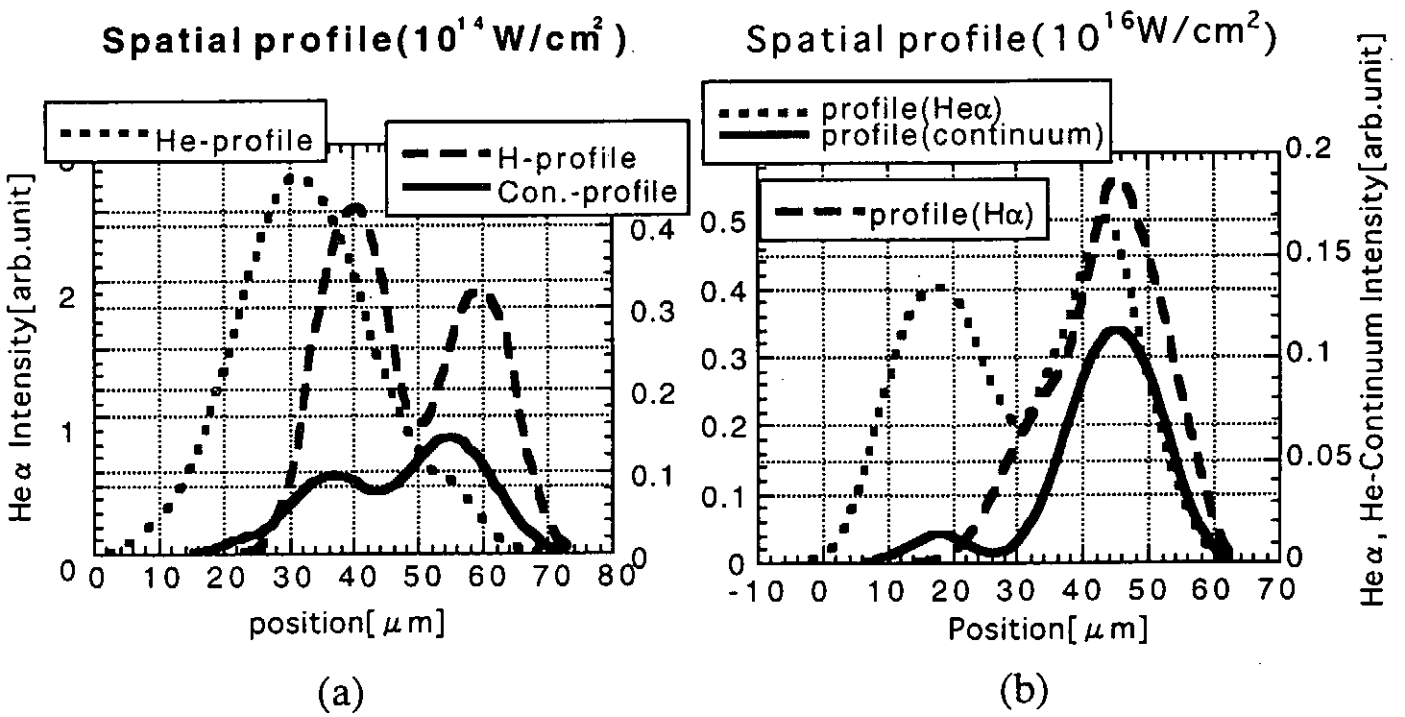


Fig.4 The measured results of spatial profiles of intensity of Heα, Lα and recombination continuum. The data of (a) is for 200μm diameter focus spot and irradiance of I=1x$10^{14}$W/cm$^2$ and that of (b) is for 20μm diameter and I=1x$10^{16}$W/cm$^2$.

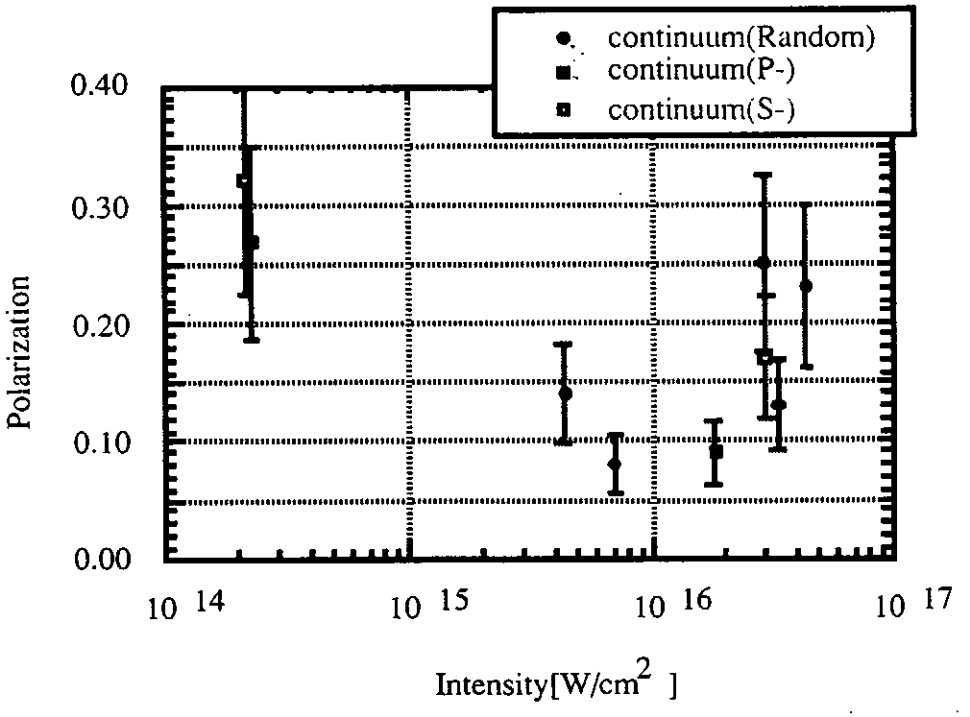


Fig.5 The measured results of the polarization of the recombination continuum as a function of laser intensity.

# X-ray generation by the LULI subpicosecond TW laser chain and perspectives for polarization of x-rays

C. Chenais-Popovics, P. Audebert, M. Fajardo, J.P. Geindre, J.C. Gauthier,
*Laboratoire pour l'Utilisation des Lasers Intenses, CNRS, Ecole Polytechnique, 91120 Palaiseau, France*

P. Sondhauss, I. Uschmann, U. Teubner, E. Foerster,
*X-ray Optics Group, Friedrich-Schiller Universität, Max-Wien Platz 1, D-07743 Jena, Germany*

I. Matsushima,
*Electrotechnical Laboratory , 1-1-4, Umezono, Tsukuba, 3058568, Japan*

R.C. Mancini, A.S. Shlyaptseva,
*Department of Physics/220, University of Nevada, Reno, NV 89557-0058 USA*

## Abstract

A 100 TW Nd-glass laser chain has been developed at LULI laser facility. X-ray spectra of the Al He-like resonance line and Li-like satellites have been recorded by focusing the frequency-doubled 30J, 300fs laser beam on a massive aluminum target. The spectra were emitted in a very high density plasma and exhibit a large amount of high-order Li-like satellite lines with spectator electrons in the n=3 and 4 shells. The measurement of the polarization of X-rays is planned with this laser in conditions optimized to generate a high fast electrons yield.

## 1 . Introduction

The development of subpicosecond terawatt and petawatt laser systems has raised in the context of Inertial Fusion Confinement, with the concept of fast ignition.[1] A number of scientific fields are opening with these lasers. The ultra-high intensity and very short pulses generated raise new fundamental physics problems. Different experiments have proved that a copious amount of very energetic electrons are generated during the interaction of a TW laser with a solid.[2,3] Polarization of X-rays emitted in the presence of high-energy electrons can be expected. This field has been extensively studied from the theoretical point of view.[4,5,6,7] Polarization has been demonstrated and studied experimentally using Electron Beam Ion Traps (EBIT).[8,9] Only a few works have been published concerning the polarization of X-rays emitted by laser-produced plasmas, mainly in femtosecond laser-produced plasmas.[10,11] In plasmas produced in the nanosecond regime, the polarization properties of X-ray lasers have been studied.[12,13]

## 2 . The LULI laser system

The 100 terawatt laser system installed at the LULI laser facility is a Neodymium glass system. It is among the five most powerful Nd-glass systems installed in the world that are located in Lawrence Livermore National Laboratory (USA) , Rutherford Appleton Laboratory (UK), Institute of Laser Engineering (Japan), Centre d'Etudes de Limeil-Valenton (France) and LULI. A scheme of the laser system is shown in Fig.1. A Titanium-Sapphire (Ti-Sa) oscillator is delivering a 100 fs pulse which is stretched in a quadruple-pass grating stretcher and amplified in a regenerative Ti-Sa amplifier. The 1 mJ, 0.7 ns pulse is then amplified in a series of phosphate and silicate glass amplifiers of diameters 16 to 45 mm. This amplification in two types of glasses enables to keep a broadband spectrum. This is the condition to be able to recompress the beam to a subpicosecond pulse.[14] The last amplification step is done in a two-pass phosphate glass disk amplifier. A part of the beam is recompressed in a double pass

grating compressor. The output energy of the subpicosecond pulse is limited by the damage threshold of the compressor gratings to a 100 TW beam, i.e. 30 J in 300 fs. The 50J, 450 ps non-compressed beam can be synchronized to the 100 TW beam in the experimental chamber. Frequency-doubling is done with a crystal set in the compressor chamber with a conversion ratio between 50 and 60%.

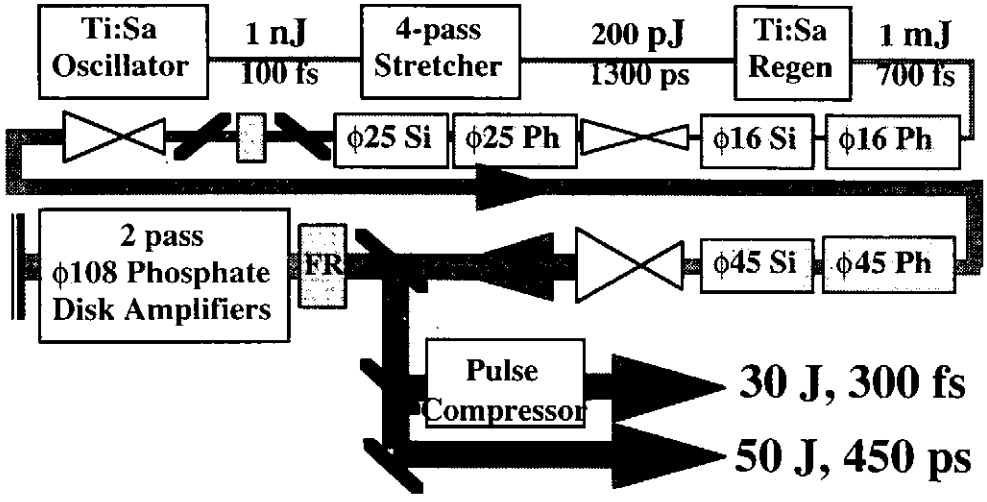


*Figure 1 : The 100 terawatt LULI laser system*

## 3 . Experimental setup for measurement of an X-ray aluminum spectrum

A plasma has been produced by focusing the 100 terawatt laser beam on a massive flat aluminum target at normal incidence. The laser beam was frequency doubled ($\lambda$=0.53 $\mu$m) and focused by a f/8, 750 mm focal length off-axis parabolic mirror (see Fig.2).

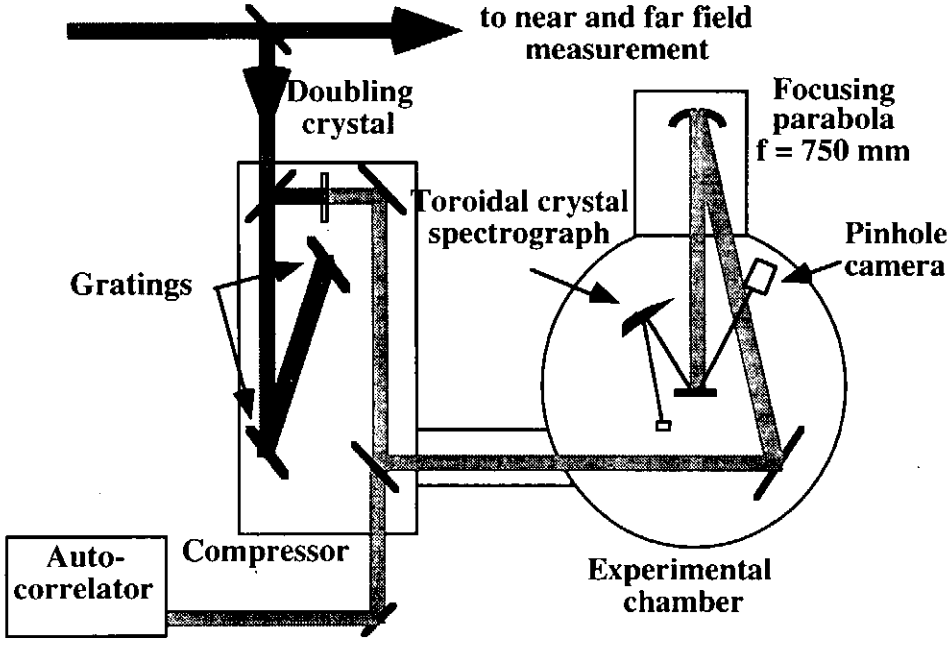


*Figure 2 : Experimental mounting for X-ray measurements.*

The laser was frequency doubled inside the compressor chamber and was directed to the experimental chamber through vacuum tubes. The pulse duration as well as the far-field and

near-field images of the infrared beam were recorded on low energy shots. A calorimeter set before the compressor measured the laser energy at $\lambda = 1.06$ µm. The focal spot obtained on target was measured on low energy shots by imaging the focused 0.53 µm wavelength beam on a CCD camera through a f/5 lens. All these diagnostics have been aligned on low energy shots at 10 Hz repetition rate.

A 35 µm diameter X-ray pinhole camera filtered with 23 µm beryllium recorded the X-ray emitted by the plasma in the keV range. Ultra-high resolution X-ray spectra were recorded with a toroidally bent crystal spectrograph built in Friedrich-Schiller University in Jena. The (10.0) quartz crystal bent to 264 mm in the dispersion plane and 112 mm in the perpendicular plane was set at an angle around 30° from the laser beam. The toroidal geometry enabled to record very high resolution spectra with spatial resolution along the focal spot of the laser. The theoretical resolving power was 6000 and the spatial resolution was 5 µm, limited by the detector, a Kodak DEF film.

## 4. Plasma characterization

### 4.1. Laser pulse duration and focusing.

The laser pulse duration has been measured on low energy shots during the experimental campaign and was 410±20 fs. This is slightly longer than the minimum value of 310 fs measured during the laser construction, in highly optimized conditions of alignment of the compressor gratings. The focal spot obtained on target at 0.53 µm on a low energy shot is shown in Fig. 3a. A 12 µm full width half maximum (FWHM) was measured from this image. From this measurement and from the far-field image, the maximum laser divergence was estimated to 2 to 4 times the diffraction limit. From the pinhole image, only a maximum size of the X-ray image was obtained as the size of the pinhole was much larger than the focal spot: the recorded image had the same diameter of 35 µm as the pinhole size.

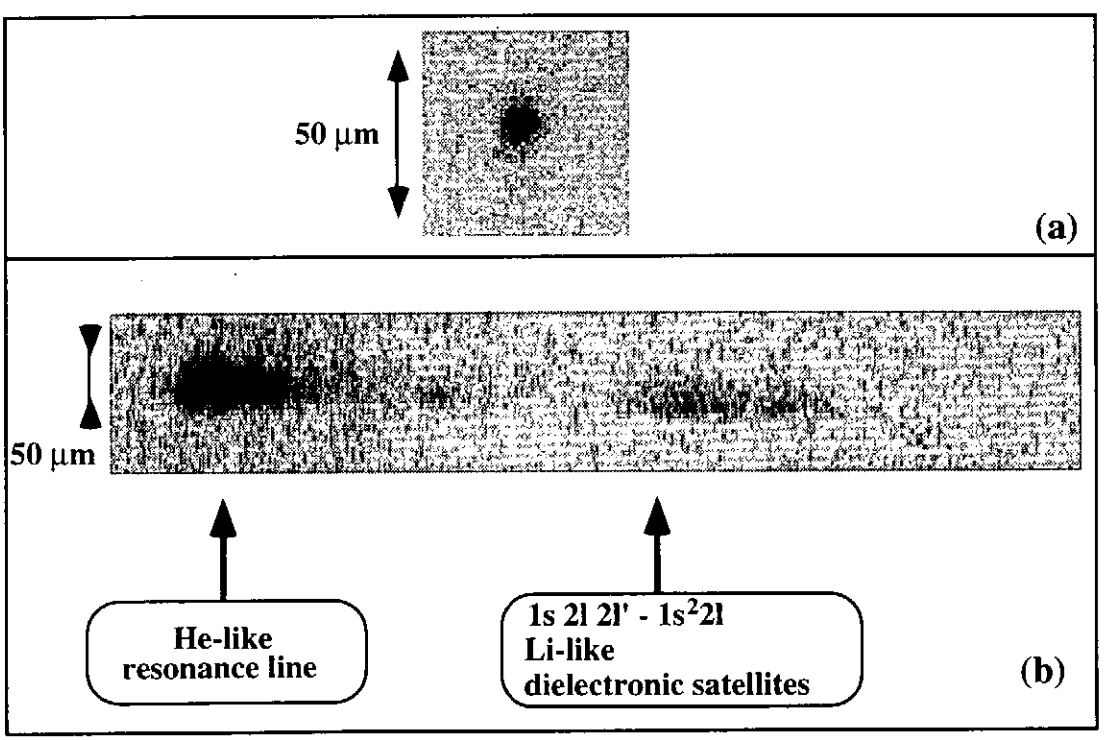


*Figure 3 : (a) Image of the focal spot at 0.53 µm wavelength; (b) raw space resolved Al spectrum*

The X-ray spectra gave a one-dimensional measurement of the plasma X-ray image. A raw spectrum is shown in Fig. 3b. It shows that the plasma expansion is negligible. The FWHM of the plasma given by this spectrum is 19±5 µm. This measurement is obtained on a

full energy shot. So it is compatible with the 12 μm measured with the 0.53 μm image of the focal spot which is recorded at 10Hz on a low energy shot. The intensity on target calculated from these measurements was of the order of $1x10^{19}$ W/cm$^2$.

4.2. Analysis of X-ray spectra.

The high resolution X-ray spectrograph was used to measure the aluminum He-like $1s^2$-1s2p (Heα) transition and its Li-like dielectronic satellites in the spectral range of 1520-1640 eV (i.e. 0. 765-0.815 nm wavelength) as shown in figure 4.

The X-ray signal is of the order of a few photons/μm$^2$. We note that this spectrum has been obtained on a single laser shot. The strong features seen in Fig. 4a are the resonance line strongly broadened towards the low energy, and the Li-like 1s2l2l' - $1s^2$2l. The Be-like satellite lines expected around 1560 eV are very weak. The broadening of the Heα line is attributed to high order Li-like satellite lines involving spectator electrons in the n=3 and n=4 levels.[15,16] The intercombination line stays at a very low level which is characteristic of very high density plasmas. The Li-like structure has been compared to a time-dependent non-LTE model of the doubly excited 1s2l2l' states of Li-like ions including Stark broadening.[17] Fig. 4b shows that the spectrum is well fitted using an electron density of $2*10^{23}$ cm$^{-3}$ and an electron temperature of 500 eV. The Li-like structure is mostly sensitive to the density. Fitting the spectrum gave a measurement of the density, but electron temperature was not measured in the present experiment. However, it has to be noted that Be-like satellite lines are too weak to be measured which could be indicative of a rather high temperature.

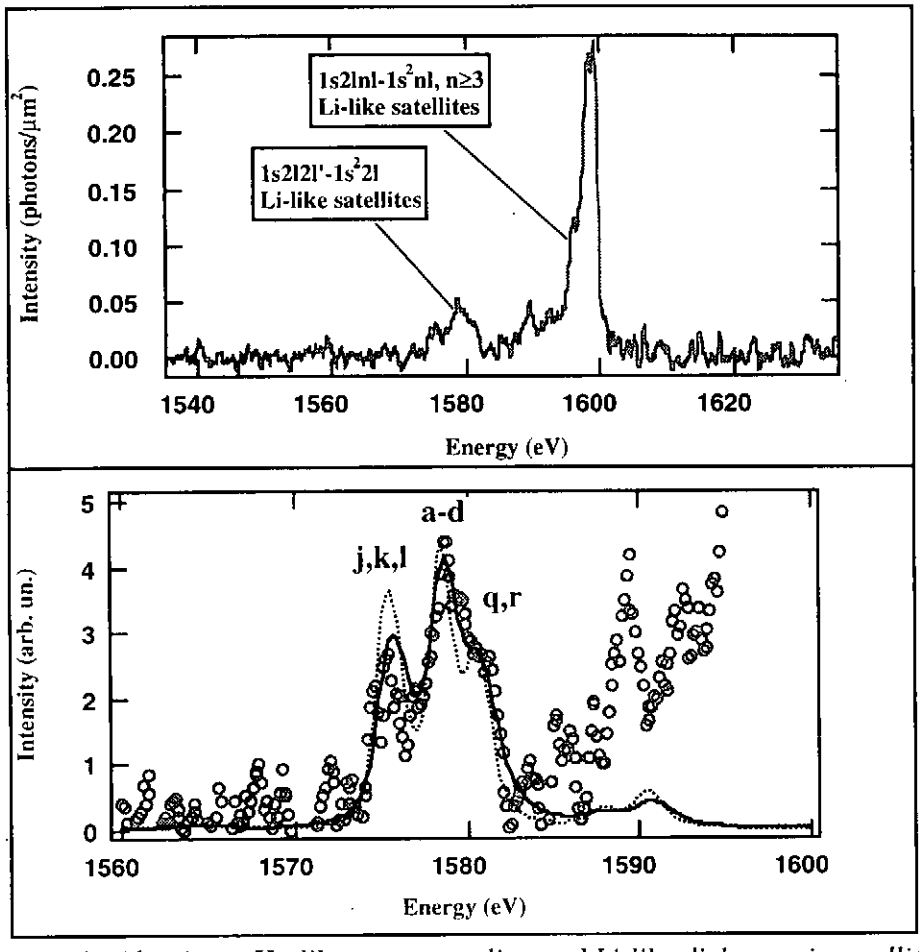


*Figure 4 : Aluminum He-like resonance line and Li-like dielectronic satellites. (a) experimental spectrum; (b) comparison of the experimental Li-like satellite spectrum (circles) to theory calculated for 500 eV temperature and electron densities of $1x10^{23}$ cm$^{-3}$ (dotted line) and $2x10^{23}$ cm$^{-3}$ (full line).*

## 5 . Planned X-ray polarization measurements

A measurement of the polarization of X-rays emitted from a plasma produced with the LULI TW laser system is scheduled during the beginning of 1999. The experiment has to be optimized for a maximum of polarization, i.e. for a maximum emission of supra-thermal electrons during the subpicosecond interaction. The fast electron generation has been extensively studied by a few of us, using the femtosecond laser of the Laboratoire d'Optique Appliquée laser facility.[2] Based on these studies, it is planned to focus the laser on target at an incidence angle around 45° to favor the coupling of the laser energy to high-energy electrons. A laser prepulse controlled in time and intensity will be added before the main pulse. This prepulse controls the density gradient scale length which is of importance in the mechanism of fast electron generation.

The target will be chosen with an even atomic number to avoid the perturbation of polarization due to non-zero nuclear spin of the ions. Silicium could be a good candidate. The setup of two Bragg crystals is under study to optimize the polarization measurement. One crucial point is to observe the same volume of plasma with both crystals. An improvement from the experiment described in ref. [10] comes from the high laser energy available which permits to obtain X-ray spectra on a single shot. Depolarization due to high density conditions is under study.

## 6 . Conclusion

The LULI TW laser is a powerful tool to study X-ray polarization due to fast electrons generation. X-ray measurements already performed with this laser are very promising for the success of an X-ray polarization measurement. In particular, they prove that single shot X-ray spectra can be recorded with Bragg crystals. The optimization of fast electron generation has been done at LOA, and the laser and plasma conditions will be adjusted to have a maximum of fast electrons.

## 7 . Acknowledgments

This work was supported by the European Community under contract n° FMGECT950044 of the Large-Scale Facility TMR program. The X-ray polarization project is supported by the NATO contract CRG 971588.

## References

[1] M. Tabak, J. Hammer, M.E. Glinsky, W.L. Kruer, S.C. Wilks, J. Woodworth, E.M. Campbell and M.D. Perry, Phys. Plasmas **1**, 1628 (1994)

[2] S. Bastiani, A. Rousse, J.P. Geindre, P. Audebert, C. Quoix, G. Hamoniaux, A. Antonetti and J.C. Gauthier, Phys. Rev. E, **56**, 7179 (1997) and references therein

[3] T. Feurer, W. Theobald, R. Sauerbrey, I. Uschmann, D. Altenbernd, U. Teubner, P. Gibbon, E. Foerster, G. Malka, J. L. Miquel, Phys. Rev. E **56** (1997) 4608

[4] M.K. Inal and J. Dubau, J. Phys. B **20**, 4221 (1987)

[5] S. Urnov, in these proceedings, and references therein

[6] J. Dubau in these proceedings, and references therein

[7] T. Fujimoto and S. Kazantsev, Plasma Phys. Control. Fusion, **39**,1267 (1997) and referenceres therein

[8] P. Beiersdorfer, D.A. Vogel, K.J. Reed, V. Decaux, J.H. Scofield, K. Widmann, G. Hölzer, E. Förster, O. Wehrhan, D.W. Savin, L. Schweikhard, Phys. Rev A **53**, 3974 (1996)

[9] A.S. Shlyaptseva, R. Mancini, P. Neill, P. Beiersdorfer, J.R. Crespo Lopez-Urrutia, K. Widmann, Phys. Rev. A, **57**, 888 (1998)

[10] J.C. Kieffer, J.P. Matte,M. Chaker, Y. Beaudoin, C.Y. Chen, S. Coe, G. Mourou, J. Dubau and M.K. Inal, Phys. Rev. E **48**, 4648 (1993)

[11] H. Yoneda, N. Hasegawa, S. Kawana and K. Ueda, Phys. Rev. E **56**, 988 (1997)

[12] T. Kawagashi, K. Murai, G. Yuan, S. Ninomiya, R. Kodama, H. Daido, Y. Kato and T. Fujimoto, Phys. Rev. Letters, **21**, 3826 (1995)

[13] B. Rus, C.L.S. Lewis, G.F. Cairns, P. Dhez, P. Jaeglé, M.H. Key, D.Neely, A.G. MacPhee, S.A. Ramsden, C.G. Smith and A. Sureau, Phys. Rev.A **51**, 2316 (1995)
[14] D. Strickland and G. Mourou, Optics Commun. 56,219 (1985)
[15] R.C. Mancini, A.S. Shlyaptseva, P. Audebert, J.P. Geindre, S. Bastiani, J.C. Gauthier, G. Grillon, A. Mysyrowicz, and A. Antonetti, Phys. Rev. E **54**,4147 (1996)
[16] U. Teubner, T. Missalla, I. Uschmann, E. Foerster, C. Wuelker, W. Theobald, Appl. Phys. B **62**, 213 (1996)
[17] R.C. Mancini, P. Audebert, J.P. Geindre, A. Rousse, F.Falliès, J.C. Gauthier, A. Mysyrowicz, J.P. Chambaret and A. Antonetti, J. Phys. B, **27**, 1671 (1995)

## Publication List of NIFS-PROC Series

NIFS-PROC-1 "*U.S.-Japan on Comparison of Theoretical and Experimental Transport in Toroidal Systems Oct. 23-27, 1989*", Mar. 1990

NIFS-PROC-2 "*Structures in Confined Plasmas –Proceedings of Workshop of US-Japan Joint Institute for Fusion Theory Program–* "; Mar. 1990

NIFS-PROC-3 "*Proceedings of the First International Toki Conference on Plasma Physics and Controlled Nuclear Fusion –Next Generation Experiments in Helical Systems– Dec. 4-7, 1989*" Mar. 1990

NIFS-PROC-4 "*Plasma Spectroscopy and Atomic Processes –Proceedings of the Workshop at Data & Planning Center in NIFS–*"; Sep. 1990

NIFS-PROC-5 "*Symposium on Development of Intensed Pulsed Particle Beams and Its Applications February 20 1990*"; Oct. 1990

NIFS-PROC-6 "*Proceedings of the Second International TOKI Conference on Plasma Physics and Controlled Nuclear Fusion , Nonlinear Phenomena in Fusion Plasmas -Theory and Computer Simulation-*"; Apr. 1991

NIFS-PROC-7 "*Proceedings of Workshop on Emissions from Heavy Current Carrying High Density Plasma and Diagnostics*"; May 1991

NIFS-PROC-8 "*Symposium on Development and Applications of Intense Pulsed Particle Beams, December 6 - 7, 1990*"; June 1991

NIFS-PROC-9 "*X-ray Radiation from Hot Dense Plasmas and Atomic Processes*"; Oct. 1991

NIFS-PROC-10 "*U.S.-Japan Workshop on "RF Heating and Current Drive in Confinement Systems Tokamaks" Nov. 18-21, 1991*, Jan. 1992

NIFS-PROC-11 "*Plasma-Based and Novel Accelerators (Proceedings of Workshop on Plasma-Based and Novel Accelerators) Nagoya, Japan, Dec. 1991*"; May 1992

NIFS-PROC-12 "*Proceedings of Japan-U.S. Workshop P-196 on High Heat Flux Components and Plasma Surface Interactions for Next Devices*"; Mar. 1993

NIFS-PROC-13 「NIFS シンポジウム
「核燃焼プラズマの研究を考える－現状と今後の取り組み方」
1992年7月15日、核融合科学研究所」1993年7月
*NIFS Symposium "Toward the Research of Fusion Burning Plasmas -Present Status and Future strategy-", 1992 July 15, National Institute for Fusion Science*"; July 1993 (in Japanese)

NIFS-PROC-14 "*Physics and Application of High Density Z-pinches*", July 1993

NIFS-PROC-15 岡本正雄、講義「プラズマ物理の基礎」
平成5年度 総合大学院大学1994年2月
*M. Okamoto,*
*"Lecture Note on the Bases of Plasma Pysics"Graduate University for Advanced Studies* Feb. 1994
(in Japanese)

NIFS-PROC-16 代表者 河合良信
平成5年度 核融合科学研究所共同研究
研究会報告書「プラズマ中のカオス現象」
*"Interdisciplinary Graduate School of Engineering Sciences" Report of the meeting on Chaotic Phenomena in Plasma*Apr. 1994 (in Japanese)

NIFS-PROC-17 平成5年度NIFSシンオジウム報告書
「核融合炉開発研究のアセスメント」平成5年11月29日-30日 於 核融合科学研究所
*"Assessment of Fusion Reactor Development" Proceedings of NIFS Symposium held on November 29-30, 1993 at National Insitute for Fusion Science"* Apr. 1994(in Japanese)

NIFS-PROC-18 *"Physics of High Energy Density Plasmas Produced by Pulsed Power"* June 1994

NIFS-PROC-19 K. Morita, N. Noda (Ed.),

"*Proceedings of 2nd International Workshop on Tritium Effects in Plasma Facing Components at Nagoya University, Symposion Hall, May 19-20, 1994*", Aug. 1994

NIFS-PROC-20 研究代表者 阿部 勝憲 (東北大学・工学部)
所内世話人 野田信明
平成6年度 核融合科学研究所共同研究 [研究会] 「金属系高熱流束材料の開発と評価」成果報告書
K. Abe and N. Noda (Eds.),
*"Research and Development of Metallic Materials for Plasma Facing and High Heat Flux Components"* Nov. 1994(in Japanese)

NIFS-PROC-21 世話人:森田 健治 (名大工学部)、金子 敏明 (岡山理科大学理学部)
「境界プラズマと炉壁との相互作用に関する基礎過程の研究」研究会報告
K. Morita (Nagoya Univ.), T. Kaneko (Okayama Univ. Science)(Eds.)
"*NIFS Joint Meeting "Plasma-Divertor Interactions" and "Fundamentals of Boundary Plasma-Wall Interactions" January 6-7, 1995 National Institute for Fusion Science*" Mar. 1995 (in Japanese)

NIFS-PROC-22 代表者 河合 良信
プラズマ中のカオス現象
Y. Kawai,
"*Report of the Meeting on Chaotic Phenomena in Plasma,* 1994" Apr. 1995 (in Japanese)

NIFS-PROC-23 K. Yatsui (Ed.),
"*New Applications of Pulsed, High-Energy Density Plasmas*"; June 1995

NIFS-PROC-24 T. Kuroda and M. Sasao (Eds.),
"*Proceedings of the Symposium on Negative Ion Sources and Their Applications, NIFS, Dec. 26-27, 1994*", Aug. 1995

NIFS-PROC-25 岡本 正雄
新古典輸送概論 (講義録)
M. Okamoto,
"*An Introduction to the Neoclassical Transport Theory" (Lecture note),* Nov. 1995 (in Japanese)

NIFS-PROC-26 Shozo Ishii (Ed.),
"*Physics, Diagnostics, and Application of Pulsed High Energy Density Plasma as an Extreme State*"; May 1996

NIFS-PROC-27 代表者 河合 良信
プラズマ中のカオスとその周辺非線形現象
Y. Kawai ,
"*Report of the Meeting on Chaotic Phenomena in Plasmas and Beyond, 1995*", Sep. 1996 (in Japanese)

NIFS-PROC-28 T. Mito (Ed.),
"*Proceedings of the Symposium on Cryogenic Systems for Large Scale Superconducting Applications*", Sep. 1996

NIFS-PROC-29 岡本 正雄
講義「核融合プラズマ物理の基礎 - I」
平成8年度 総合研究大学院大学 数物科学研究科 核融合科学専攻 1996年10月
M. Okamoto
"*Lecture Note on the Fundamentals of Fusion Plasma Physics - I" Graduate University for Advanced Studies;* Oct. 1996 (in Japanese)

NIFS-PROC-30 研究代表者 栗下 裕明 (東北大学金属材料研究所)
所内世話人 加藤 雄大
平成8年度核融合科学研究所共同研究「被損傷材料の微小体積強度評価法の高度化」研究会 1996年10月 9日 於:核融合科学研究所
H. Kurishita and Y. Katoh (Eds.)
*NIFS Workshop on Application of Micro-Indentation Technique to Evaluation of Mechanical Properties of Fusion Materials, Oct. 9, 1996, NIFS* ; Nov. 1996 (in Japanese)

NIFS-PROC-31 岡本 正雄
講義「核融合プラズマ物理の基礎 - II」
平成8年度 総合研究大学院大学 数物科学研究科 核融合科学専攻 1997年4月
M. Okamoto
"*Lecture Note on the Fundamentals of Fusion Plasma Physics - II" Graduate University for Advanced*

*Studies;* Apr. 1997 (in Japanese)

NIFS-PROC-32 代表者　河合　良信
平成8年度　核融合科学研究所共同研究　研究会報告「プラズマ中のカオスとその周辺非線形現象」

Y. Kawai (Ed)
*Report of the Meeting on Chaotic Phenomena in Plasmas and Beyond, 1996;* Apr. 1997 (mainly in Japanese)

NIFS-PROC-33 H. Sanuki,
*Studies on Wave Analysis and Electric Field in Plasmas*; July 1997

NIFS-PROC-34 プラズマ対向機器・PSI・熱・粒子制御合同研究会報告
平成9年6月27日（金）9:00～16:20　核融合科学研究所・管理棟4F第1会議室
1997年　10月
T. Yamashina (Hokkaido University)
*Plasma Facing Components, PSI and Heat/Particle Control June 27, 1997, National Institute for Fusion Science T. Yamashina (Hokkaido University)* ; Oct. 1997 (in Japanese)

NIFS-PROC-35 T. Watari,
*Plasma Heating and Current Drive*; Oct. 1997

NIFS-PROC-36 T. Miyamoto and K. Takasugi (Eds.)
*Production and Physics of High Energy Density Plasma; Production and Physics of High Energy Density Plasma;* Oct. 1997

NIFS-PROC-37 ( Eds.)T. Fujimoto, P. Beiersdorfer
*Proceedings of the Japan-US Workshop on Plasma Polarization Spectroscopy and The International Seminar on Plasma Polarization Spectroscopy January 26-28, 1998, Kyoto*